AGARD

ADVISORY GROUP FOR AEROSPACE RESEARCH & DEVELOPMENT

7 RUE ANCELLE, 92200 NEUILLY-SUR-SEINE, FRANCE

AGARD REPORT 822

Numerical Unsteady Aerodynamic and Aeroelastic Simulation

(l'Aérodynamique instationnaire numérique et la simulation de l'aéroelasticité)

Papers presented at the 85th Meeting of the AGARD Structures and Materials Panel, held in
Aalborg, Denmark, 14-15 October 1997.

19980514 140

North Atlantic Treaty Organization
Organisation du Traité de l'Atlantique Nord

DTIC QUALITY INSPECTED

The Mission of AGARD*

According to its Charter, the mission of AGARD is to bring together the leading personalities of the NATO nations in the fields of science and technology relating to aerospace for the following purposes:

— Recommending effective ways for the member nations to use their research and development capabilities for the common benefit of the NATO community;

— Providing scientific and technical advice and assistance to the Military Committee in the field of aerospace research and development (with particular regard to its military application);

— Continuously stimulating advances in the aerospace sciences relevant to strengthening the common defence posture;

— Improving the co-operation among member nations in aerospace research and development;

— Exchange of scientific and technical information;

— Providing assistance to member nations for the purpose of increasing their scientific and technical potential;

— Rendering scientific and technical assistance, as requested, to other NATO bodies and to member nations in connection with research and development problems in the aerospace field.

The highest authority within AGARD is the National Delegates Board agardconsisting of officially appointed senior representatives from each member nation. The mission of AGARD is carried out through the Panels which are composed of experts appointed by the National Delegates, the Consultant and Exchange Programme and the Aerospace Applications Studies Programme. The results of AGARD work are reported to the member nations and the NATO Authorities through the AGARD series of publications of which this is one.

Participation in AGARD activities is by invitation only and is normally limited to citizens of the NATO nations.

The content of this publication has been reproduced
directly from material supplied by AGARD or the authors.

Printed on recycled paper

Numerical Unsteady Aerodynamic and Aeroelastic Simulation

(AGARD-R-822)

Executive Summary

Two components are required for analysis of dynamic aeroelastic phenomena, a structural finite element model of the vehicle, and an unsteady aerodynamics model; in current practice linear approximations are used for both models. Although structural nonlinearities possibly play a part in some cases of Limit Cycle Oscillation (LCO), the analysis community is generally content with existing structural modeling methods. The need for accurate and user-friendly advanced aerodynamic methods, however, is generally recognized.

Control surface buzz, a one degree of freedom aeroelastic phenomenon involving shock oscillation, is an example of a problem not susceptible to analysis using linear aerodynamics. The current practice in industry is to use very conservative rules of thumb in hopes of preventing buzz, or simply to ignore the possibility. Obviously, conservatism introduces unnecessary weight and the discovery of a buzz problem during the test program causes delay and an expensive redesign effort.

As computer hardware increases in capability, CFD methods are maturing and becoming available for at least limited use in industry. These methods hold much hope for future improvements in unsteady aerodynamics predictions. More accurate analysis of ordinary flutter in the sub- and supersonic flight regimes as well as the development of transonic analysis methods can result in a reduction of aircraft weight and development cost by reducing the need for conservatism and possibly by eliminating the expense of flutter model testing. Up to the present time, extreme difficulty of use, computational cost and lack of verification against suitable test cases have severely limited use of CFD procedures in industry; codes suitable for analysis of complete aircraft have not been shown to exist.

The papers at this Workshop dealt with methods at the leading edge of current technology as applied in industry, and with more advanced methods which are in the development and checkout process. These papers contribute to the expectation that the time is not far removed when industry will be able to make much increased use of advanced unsteady aerodynamics methods.

L'aérodynamique instationnaire numérique et la simulation de l'aéroélasticité

(AGARD-R-822)

Synthèse

Deux éléments sont nécessaires pour l'analyse des phénomènes aéroélastiques dynamiques; un modèle à éléments finis de la structure du véhicule et un autre concernant l'aérodynamique instable. Des approximations linéaires sont couramment utilisées pour les deux modèles. Bien que des aspects non linéaires de la structure puissent jouer un rôle dans certains cas d'oscillation en cycle limite (LCO), l'ensemble des analystes des phénomènes aéroélastiques dynamiques est globalement satisfait des méthodes de modélisation structurale existantes. Cependant, le besoin de méthodes aérodynamiques conviviales avancées se fait largement sentir.

Le bourdonnement des gouvernes, phénomène aéroélastique avec un seul degré de liberté et qui comporte des oscillations de choc, est un exemple de problème se prêtant mal à l'analyse par le biais de l'aérodynamique linéaire. La pratique adoptée couramment par l'industrie est soit d'appliquer des règles empiriques très conservatrices pour éviter les problèmes de vibration, soit d'éliminer l'éventualité de la vibration. Il va sans dire que cette approche conservatrice entraîne une augmentation inévitable du poids et que la découverte, au cours des essais, d'éventuels problèmes de bourdonnement entraîne des retards et peut même nécessiter la reprise intégrale de la conception, avec les coûts additionnels y afférents.

Avec les performances toujours croissantes de l'informatique, les méthodes CFD s'améliorent et trouvent déjà quelques applications dans l'industrie. Ces méthodes sont porteuses d'améliorations dans le domaine des prévisions de l'aérodynamique instable. L'analyse plus précise du flottement prévisible en régime de vol subsonique et supersonique, associée au développement des méthodes d'analyse transsoniques, pourrait entraîner une diminution de la masse de l'avion et des coûts de développement, en diminuant le besoin d'approches conservatrices et en éliminant le coût élevé des essais des modèles du flottement. Jusqu'à présent, l'emploi des procédures CFD dans l'industrie a été très limité en raison des nombreuses difficultés de mise en œuvre, des coûts du traitement informatique, et du manque de données de vérification établies à partir de cas d'essai représentatifs. L'existence de codes appropriés permettant l'analyse de l'avion complet n'a pas encore été démontrée.

Les communications présentées lors de l'Atelier traitaient de méthodes liées aux derniers développements technologiques, et appliquées dans l'industrie, ainsi que d'autres méthodes, plus avancées, au stade de développement ou de mise au point. Ces communications permettent d'imaginer que l'industrie pourra probablement, dans un avenir relativement proche, tirer profit des méthodes avancées dans le domaine de l'aérodynamique instable.

Contents

Preface

The computation of unsteady aerodynamic forces generated by the vibration of the structure is the heart of the analysis of flutter, aeroservoelastic stability, dynamic response and related phenomena. The objectives of the Workshop were to examine the state of the art in computational unsteady aerodynamics with respect to methods already in use, methods available for use in the short term, and advanced methods which show promise of maturation into usefulness.

The Workshop was conducted in Aalborg, Denmark in October, 1997, and provided an exchange of ideas among industry, academia, and research institutions. Special thanks are due to Ir. Rijkert Zwaan, retired SMP Member from The Netherlands, for suggesting the topic and providing the initial guidance of the Sub-Committee.

J.A. Ellis
Chairman,
Sub-Committee on
Numerical Unsteady Aerodynamic
and Aeroelastic Simulation

Structures and Materials Panel

Chairman: Prof. R. Potter
Business Manager
Structural Materials Center
Griffith Building (A7) Room 1014
DERA Farnborough
United Kingdom

Deputy Chairman: Ir. H. H. Ottens
Head of Structures Department
National Aerospace Laboratory
(NLR)
P.O. Box 153
8300 AD Emmerloord
Netherlands

SUB-COMMITTEE MEMBERS

Chairman: Mr. J. Ellis
LMTAS
P.O. Box 748
Attn. Mail Zone 2851
Fort Worth, TX 76101
USA

Members: L. Chesta   -   IT
A. Humble   -   UK

H. Hönlinger   -   GE
C. Perron   -   CA

PANEL EXECUTIVE

Dr. J.M. CARBALLAL, SP

Mail from Europe:
AGARD-OTAN
92200 Neuilly-sur-Seine
France

Mail from US and Canada:
AGARD-NATO/SMP
PSC 116
APO AE 09777

Tel: 33(0) 1 55 61 22 90 & 92
Telefax: 33(0) 1 55 61 22 99 & 98
Telex: 610175F

TECHNICAL EVALUATION REPORT ON 1997 SPECIALISTS' MEETING ON "NUMERICAL UNSTEADY AERODYNAMIC AND AEROELASTIC SIMULATION"

M. Lacabanne, Aerospatiale, 316 route de Bayonne A/BTE/EG/CA,
31060 Toulouse Cedex 03, France
R. J. Zwaan, formerly NLR P. O. Box 90502, 1006 BM Amsterdam,
The Netherlands

SUMMARY
This paper presents a technical evaluation of the Workshop on "Numerical Unsteady Aerodynamic and Aeroelastic Simulation" held at the 85th meeting of the RTO (formerly AGARD) Structures and Materials Panel on 13-17 October 1997, in Aalborg, Denmark.

ABBREVIATIONS

AIC	Aerodynamic Influence Coefficient
AOA	Angle Of Attack
CUA	Computational Unsteady Aerodynamics
(CAP)-TSD	(Computational Aeroelasticity Program)-Transonic Small Disturbance
CAS	Computational Aeroelastic Simulation
CFD	Computational Fluid Dynamics
DLM	Doublet Lattice Method
EE	Euler Equations
FE	Finite Element
FP	Full Potential
LCO	Limit Cycle Oscillation
MDO	Multi-Disciplinary Optimization
MIMO	Multiple Input/Multiple Output
(TL)NS	(Thin Layer) Navier-Stokes

1. INTRODUCTION
The objectives of the Workshop were:
- Review of the technological readiness of CUA/CAS methods.
- Review of the industrial readiness of these methods in practical applications.

SMP has monitored continually the progress in the development of computational capabilities in unsteady aerodynamics and aeroelasticity. The last meeting in this subject area was the 1991 Specialists' Meeting on "Transonic Unsteady Aerodynamics and Aeroelasticity", San Diego, USA, AGARD-CP-507. Since then many more advances were made in refining mathematical models, applications to more complex aircraft configurations and computational efficiency.

Within SMP, however, the concern grew about in what measure industry could benefit from these advances. Voices were given to the threat that a gap existed between the technological and industrial readiness and that this gap was gradually increasing, manifested e.g. by an enormous over-representation of contributions to conferences and journals from the side of research institutes and universities in comparison with industry.

The need was felt to organize a meeting in which the industrial views could be brought out explicitly, which has led to the present Workshop. A preparatory step was the pilot paper of M. Burt, Military Aircraft Division, British Aerospace Ltd., UK, who expressed the industrial needs and expectations of CUA/CAS.

In accordance with the objectives of the Workshop equal numbers of papers from industry and institutes/universities were pursued and realized. One paper was withdrawn (No. 6) and one paper was replaced (No. 13). In section 2 those issues of the papers are highlighted that were relevant to the subject of the Workshop.

2. OUTLINE OF PAPERS

2.1 J. W. Edwards: "Calculated Viscous and Scale Effects on Transonic Aeroelasticity"
A viscous-inviscid interactive coupling method, CAP-TSDV, is described for the computation of unsteady transonic flow including possible separation and reattachment, occurring in self-exited shock-induced oscillations and transonic flutter. Basic elements are the lag-entrainment integral boundary layer equations and the transonic small disturbance potential code CAP-TSD, coupled with a variable gain, integral control coupling method. Mach scaling is applied to enable the use of validated modelings at wind tunnel model scale to make predictions at full scale flight vehicles.
Results of flutter calculations for the AGARD 445.6 wing show excellent agreement for M<1.0. Numerical experimentation at the transonic dip yields minor scale and Reynolds number effects, but an obvious effect originates from motion amplitude.
Another example deals with wing flutter calculations for a business jet. Good agreement is found with experimental data up to M=0.9 and with results of an NS code at small amplitude motions. At large amplitudes LCO is predicted, which corresponds with wind tunnel observations.

2.2 C. Pétiau, Ph. Nico and B. Stoufflet: "Tendances en CFD pour l'Aéroélasticité"
The evolution is described of using CFD methods within the aeroelastic analysis system ELFINI-AEROELASTICITY. At the present stage the system includes for the "heavy" computations an EE method to determine in combination with an FE model the effects of initial shapes and rigid body motions on the so-called load and aerodynamic bases, according to the concept of ELFINI. Using the results, a linear potential method is applied to calculate the aerodynamic characteristics for all required aircraft configurations and flight conditions. Calibration of the aerodynamic model is achieved by using wind tunnel and flight test data.
Currently two nonlinear CUA methods are explored, focusing on transonic flow:
- The steady method CITRON and unsteady method TCITRON for wings with simple geometry.
- The method using unstructured grids EUGENIE for complex configurations.

These methods can be integrated with FE models to perform CAS analyses. This procedure, however, is very expensive and the reliability of the time responses is uncertain because of the analysis tools requiring linearity. As a way out linarized CFD tools are investigated, also considered by ONERA.

Results presented illustrate the various development stages.

2.3 D. Schuster, M. Smith, B. Buxton, L. Huttsell and E. Turner: "Application of a Three-Dimensional Euler/Navier-Stokes Aeroelastic Method"

This paper discusses two validation cases of the well-known TLNS method ENS3DAE. The method is in development and use since 1989; its present stage of development is explained in the paper.

The first application concerns a 4% thick rectangular semi-span wing with a 25% chord aileron at M=0.7 and a static aileron deflection of 1 deg, using the inviscid EE option of ENS3DAE to calculate the control effectiveness for an increasing dynamic pressure, including control reversal. The results show an excellent agreement with those of CAP-TSD if the same grid is used.

In the second application results of the TLNS option are presented for the BACT model, a 12% thick semi-span rectangular wing with a 25% trailing edge control surface that could be oscillated harmonically. Two chordwise sections with pressure taps were installed at and besides the place of the control surface. Results of static and dynamic calculations for M=0.77 are in very good agreement with wind tunnel data for the subsonic part of the pressure distributions, and are reasonable in the transonic part where discrepancies occur which will be investigated further.

2.4 W. Wegner: "Aerodynamics for Elastically Oscillating Wings Using the Virtual Grid Deformation Method"

A method for dynamic grid generation is described, which can be applied in CFD codes to calculate motion-induced aerodynamic forces. At issue is the technique to transform the basic flow equations into a time-dependent boundary-fitted coordinate system, which in most current grid generators implies a time-consuming recalculation of the grid point locations at each time step. Different from this technique, the author presents an alternative virtual mapping algorithm that uses only the normal vector of the cell faces and the relative velocity of the cell face centers instead of the precise location of the grid points.

He claims that his algorithm is computationally time-efficient, but no quantification is given.

The algorithm can also be used if viscous flow is considered. This is demonstrated by the application of a viscous-inviscid interaction method, developed by the author, to the AMP wing model in fixed position and in pitching motion. Calculated steady and unsteady pressure distributions are compared with wind tunnel data. The agreement is satisfactory, but makes clear that the influence of a body at the wing root and of model flexibility should not be neglected.

2.5 G.D. Mortchéléwicz: "Application des Equations de Euler Linéarisées au Flottement"

A linearized EE method, REELC, is presented for use in flutter calculations at small amplitudes. The unsteady aerodynamic solution is defined as a first-order harmonic perturbation of a steady solution. Consequently, the calculation of the unsteady solution is considered as a complex steady problem. Disadvantage of this procedure is of course the doubling of the required memory, but on the other hand results become available immediately in the frequency domain, while the computation time is independent of the reduced frequency.

Calculated pressure distributions are shown for a pitching NACA 64A010 airfoil at a transonic flow condition, and compared with wind tunnel data. Noteworthy is that the unsteady solution converged very quickly, even before the steady solution was fully converged. Another example deals with a delta wing for which generalized aerodynamic forces are presented for a series of reduced frequencies as well as flutter characteristics using these forces. The author mentions the total computation time for this case and states that the time would have been forbiddingly long if an Euler method were used.

2.6 Paper withdrawn

2.7 C. Farhat: "High Fidelity and High Performance Computational Algorithms for the Solution of Three-Dimensional Static, Transient and Eigen Aeroelastic Problems"

The author highlights the status of the three-field coupled fluid/structure/moving grid method , which he developed with M. Lesoinne, for applications to nonlinear (aerodynamic and structural) cases, including "pathological" features as high AOA and flow separation. This method employs a partitioned procedure for time-integrating the coupled equations, to be used both for explicit and implicit schemes. The primary subject of the paper is the algorithm for first-order time integration in the structural and fluid domain, providing maximum performance of the solution (reduced CPU time) at sufficient accuracy and numerical stability. This algorithm includes subcycling, implying that the structural time step is taken larger than the aerodynamic time step.

The performance is demonstrated by dynamic response calculations for the AGARD 445.6 wing using an EE formulation and an unstructured grid. The CPU time turned out to be a factor 20 less than that of the case without subcycling. An intriguing second example is the time response of a 2-D model of the Tacoma Narrows Bridge, with nonlinearities in both aerodynamics and structure. The result is in qualitative agreement with observations.

In the future applications to buffet problems are foreseen.

2.8 M.L. Baker: "CFD-Based Corrections for Linear Aerodynamic Methods"

The paper presents a method to introduce results of CFD codes into production-type aeroelastic methods through corrections of the initially used linear aerodynamic forces. This method does not imply the usual multiplicative correction factors for AIC's, but makes use of the concept of "local equivalence". This requires only a small number of nonlinear aerodynamic computations, in this way reducing effectively the expenses of the routine aeroelastic computations. The concept is based on defining any arbitrary displacement of the airplane structure as the sum of a "representative" displacement and a residual. The aerodynamics of the "representative" and residual displacements have to be provided by locally linearized CFD solutions and fully linear methods, respectively. The

paper indicates how the concept can be implemented efficiently in AIC calculation codes.

Results of flutter stability curves for the AGARD wing 445.6 model, calculated with the use of the DLM, the CAP-TSD method and the newly presented method show a good agreement for the latter two methods. Further validation for complex configurations, using Euler/NS codes, is ongoing.

2.9 L. Huttsell, J. Tinapple and R. Weyer: "Investigation of Buffet Load Alleviation on a scaled F-15 Twin Model by Means of Blowing and Smart Structures"

A buffet investigation is described on a sting mounted 4.7% scale F-15C twin tail model, which is the first phase of a larger research program. Phase 1 included the experimental study of the buffet characteristics and of the effect of tangential blowing as a means of buffet suppression, computation of the flow field and a comparison of computational and test results. One vertical tail was flexible and was provided with instrumentation to allow pressure measurements. Flow visualization was applied to trace vortical flow initiation. The unstructured EE simulations were performed at one tunnel test condition (M=0.2, AOA=24 deg, side slip angle=-4 deg). In the paper details are given of the methods used for surface and unstructured spatial grid generation and the solver for inviscid and viscous flow. In the present simulation the inviscid mode was used.

RMS values of the measured bending and torsion moments at the root of the flexible tail showed that tangential blowing had little effect. The computed model forces and moments for inviscid flow agreed reasonably well with the test results. The vortical flow was determined to be initiated at the top of the engine inlets, which confirmed the visualization results of the tunnel test. Flow trace and vector plots indicated that the vortices pass the vertical tails very closely at the outer sides, again confirming visualization results.

In a continued research program an EE simulation with a structured grid will be performed.

2.10 S. Schulze: "Transonic Aeroelastic Simulation of a Flexible Wing Section"

A CAS method, SNAP2d, is discussed to analyse flutter characteristics of an airfoil in transonic flow. Its main feature is the use of domain decomposition, i.e. the partitioned solution procedure in which the solvers for fluid motion and structural motion are active alternately, exchanging data only at certain time steps (subcycling). A substantial reduction of the computational effort is found in applying large "global" time steps in the structural domain, favored there by the relatively low frequency content, in comparison with the time steps in the flow domain, which are small as required by stability and accuracy. The theoretical basis of the method is described extensively for an EE modeling in combination with an FE model. Flutter stability curves and time responses are presented for a NACA 64A010 airfoil in three configurations. The stability curves agree mainly well with results from other sources, except for a small second transonic dip which was not predicted earlier. Also the flutter mechanism is analysed, revealing that especially the rapid variation of the out-of-phase component of the torsional moment coefficient

with Mach number effects the shape of the transonic dip region.

2.11 B.J.G. Eussen, M.H.L. Hounjet, J.J. Meijer and B.B. Prananta: "NLR Experience in Unsteady Aerodynamics and Aeroelastic Simulation Applications"

The paper presents the current status and research activities of the CUA/CAS method AESIM. This system has been developed primarily for flutter certification of transport type aircraft, with the aim to become an affordable tool for industry. The solver includes FP, EE or TLNS modelings. The status is illustrated with pressure distributions on the oscillating wing of a fighter type wind tunnel model, calculated with the FP and TLNS options, showing satisfactory agreement with measured data.

Extensions of AESIM are ongoing which are primarily focused on a further reduction of computational effort and user interference, and on increased confidence level:

. The efficient application of MIMO techniques to analyse calculated time responses and determine flutter speeds.

. An on-line prognostic method to continue time responses after the simulation has stopped.

. Large time step coupling procedures in CAS, using prolongations in either aerodynamic or structural domain.

Improved Padé techniques for transforming linear aerodynamics between frequency and time domain.

. LCO simulations with optimal integration of CUA methods and steady and unsteady wind tunnel data.

Preliminary results of these points of investigation are shown. Representative are accurate EE and TLNS unsteady pressure distributions obtained with 8 and 48 time steps per period, respectively, and coupled EE results obtained using 8 time steps per cycle. The 3-D EE and TLNS aerodynamic computations are about 5 and 15 times slower than those with FP.

2.12 M J. de C. Henshaw, D. McKeirnon and C. Mairs: "Flutter Prediction for Complex Configurations"

A modular process is described for the design and qualification of military aircraft to prevent aero(servo)elastic instabilities. A key characteristic is that the utilization is allowed of sophisticated CUA as well as the most effective simple methods, consistent with the particular stage of the design cycle being adressed. The authors state that about 75% of the effort required to qualify flutter aspects is associated with the modeling (major part) and analysis phases, the remaining 25% being involved with validation, qualification and certification (mainly ground and flight testing). On the other hand, 75% of the cost is associated with the validation and qualification phases. Further, the authors point out the strong relationship between the extent of the modeling and analysis effort and the cost savings through reduced flight testing. Also the risk of redesign is reduced. Potential for improving the quality of the modeling and analysis phase is therefore found in the use of advanced CUA codes in relation to transonic flow and complex configurations. The CUA tools at BAe(MA&A) include production tools like inviscid linear methods, and advanced methods like TSD and EE methods; an NS code is being developed. The optimal place of these tools in the design process is

discussed in the paper. Various issues concerning CUA developments are adressed, including the impact of CUA on the design process as a whole. Noteworthy is the authors' suggestion to link the post-processing techniques to determine frequencies and dampings from calculated response data to flutter flight data analysis methods. A case study is presented: the AGARD SMP taileron with a comparison of results obtained with linear, TSD and EE methods. In conclusion, the authors state that CPU time is the major limiting factor for EE and NS methods, and their expectation is that, although the performance of these methods will increase, they will complement and not replace the existing simpler methods.

2.13 W. Luber and J. Becker: "High Incidence Unsteady Aerodynamics for Aeroservoelastic Prediction"

The design of flight control laws for modern fighter aircraft is generally based on an analytical model describing the dynamics of the aircraft structure and the aerodynamic forces generated by the structural vibration modes and control surface deflections. A specific problem is the prediction of stability margins of the vibration modes at high incidences. The authors state that for these cases no theoretical methods exist to predict unsteady aerodynamic forces (including flow separation), and therefore they fall back on a validated semi-empirical method consisting of a linear theoretical method modified by steady and unsteady pressure distributions from wind tunnel tests. The modification has to affect primarily the generalized control surface aerodynamic efficiencies and the vibration mode induced aerodynamic damping forces.
In an application to a delta canard fighter aircraft, predicted open-loop frequncy response functions are compared using the linear theoretical and the semi-empirical method. A validation by flight tests has still to take place.

2.14 C. Chen, D. Liu and D. Sarhaddi: "A Unified Aerodynamic Module for Aeroelastic and MDO Applications"

A unified AIC based unsteady aerodynamics module ZAERO is presented, covering subsonic to hypersonic flow. The integration of the module into the structural optimization method ASTROS is being carried out. The module can also be used as a stand alone system as well as be interfaced with FE methods like NASTRAN MSC. ZAERO consists of four unsteady codes: subsonic and supersonic for aircraft configurations with external stores, transonic for lifting surface systems and hypersonic/supersonic for lifting surface systems and wing-body configurations. In the paper more details about these codes are given.
Numerous validation cases of ZAREO and ZAERO/ASTROS are presented in which calculated results are compared with results from other methods and experimental data. The agreement is generally satisfactory; in some cases departures exist which are explained.
Finally, the authors present as global strategy for computational aeroelasticity in industrial applications: to utilize the AIC methods complimentary to CFD methods.

2.15 B. Franzen, B. Nilsson and B. Winzell: "Experience with Unsteady Aerodynamics for SAAB Military Aircraft"

The authors present an outline of current numerical unsteady aerodynamic and aeroelastic tools used at SAAB. The corner stones are the linear system AEREL for sub/supersonic flow and complete aircraft configurations, an FP aeroelastic simulation code for wings and recently the multipurpose EE/NS program EURANUS which was made time-linearized and extended to a pilot version for aeroelastic simulation.
Various applications are shown dealing with the Gripen and the SAAB 2000 aircraft. Referring to the paper for the details, some relevant experiences are summarized here:

.   Use of CFD tools in project work is almost forbiddingly time-consuming, especially the grid generation, and should be less in next generation codes. Also computing time should be reduced.

.   Linear flutter analysis of the Gripen provides acceptable results and unsteady transonic aerodynamics do not add much to that.

.   In the attempt to get the unsteady aerodynamics in flutter analysis right all other contributions (structure, control system, etc.) should be modeled with corresponding accuracy.

.   The confidence level of the current CFD methods is not high enough to justify their use in an industrial environment. This experience is supported by the results presented of an ongoing unsteady wind tunnel research project with two cropped delta wing models and a flutter analysis for the AGARD 445.6 wing.

.   An indirectly gained experience is the acceleration of the convergence obtained in static aeroelastic calculations by using critical damping.

3. ROUND TABLE DISCUSSION AND EVALUATION

From the technical presentations and discussions, some important points related with CUA/CAS should be noted:

3.1 Progress of CUA/CAS in research institutes and industry

It clearly appears that since the 1991 AGARD Specialists' Meeting on this topic progress has been evidently made in CUA, and also in the application of CUA to predict aeroelastic phenomena.
The Workshop reviewed the whole range of CUA methods, as already defined in the evaluation report of the 1991 Specialists' Meeting. They include the classical small disturbance potential equation, the nonlinear potential equation(both TSD and FP), the Euler equations (EE) and the NS equations (both Full NS and TLNS forms).

Research institutes and universities are continuing to develop CUA methods, mainly TSD, EE, TLNS, and to validate them using public experimental results (e.g. AGARD 445.6 wing, ISOGAI and LANN wing). Most of the correlation between analysis and test is made with the AGARD 445.6 wing flutter test results. Many papers show the capability of the different methods to predict the transonic dip for the AGARD wing.
Aircraft manufacturers commonly use linear methods including correction factors, but they are evolving towards the use of nonlinear CUA or linearized CUA. Industry needs to implement affordable techniques which do not

demand tremendous effort and high computation times, and, at the same time, are accurate in the prediction of aeroelastic phenomena. Industry uses the most advanced techniques only for isolated cases (paper 15 presented by Dr. Winzell of SAAB shows the implementation of EE and NS solutions). Industry will have the responsibility to choose the most suitable methods according to the development stage of an aircraft project.

The need for AIC correction factors still remains, even if nonlinear CUA tends to be used as a "numerical wind tunnel".

Indeed, industry must run a large number of aeroelastic computations, varying Mach numbers, payload and fuel configurations, and cannot afford to compute all the cases with nonlinear CUA. Furthermore, AIC's are still necessary for aeroelastic optimization work.

The cost saving achieved by using CUA in the flutter analysis process needs to be assessed. A trade-off between accuracy, computation cost, manpower effort and cost saving induced by the application of CUA methods to aeroelastic phenomena predictions should be established whenever possible.

3.2 Improvement of CUA techniques

CUA techniques must still be improved so as to reduce computation time. This reduction might be obtained by improvement of algorithms and use of parallel computers. Another challenging aspect of CUA is the problem of grid generation and the choice between use of a fixed grid or moving grid.

Comparisons of solutions using structured or non-structured grids should be made. There is a need to think about checks for grid generation. When using NS equations, good turbulence models should be used so that the solution of these equations involves more physics and not numerical concerns.

3.3 Validation cases of CUA methods

There is still a need for validation cases and for calibration of CUA methods versus experiments. Indeed, the AGARD 445.6 wing which was the test reference in many papers, is not fully appropriate for validating CUA codes because there is no strong transonic effect and because some test results remain questionable. The AGARD wing should only be a case for calibration of methods before performing analysis on more difficult cases.

A lot of work still remains in defining good test cases. There is a consensus in saying that available test cases are not sufficient for calibrating CUA methods and flutter predictions in the transonic regime. Dr. Bahtia of Boeing emphasized this point and proposed that research institutes work on the definition of new standardized cases.

3.4 Additional comments

The CUA tools discussed in the workshop serve typically aeroelastic needs and interests, and their procedures and algorithms are therefore not completely equivalent to those of the CFD tools of "steady" aerodynamic experts. So keeping CUA expertise in the organization of industries and institutes in or very close to the aeroelastic department or group is highly desirable.

It was agreed that viscous effects should be included in computations to predict aeroelastic phenomena like LCO. Dr. Edwards of NASA said that "an expanded concept of

stability for transonic flutter computations and testing "should be defined.

Linearization of Euler equations must be considered as an alternative to the solution of nonlinear EE equations. While capturing nonlinear effects (shocks, etc.) for small motions, linearization of Euler equations allows computation time to be saved.

There is a need for developing post-processing software to derive stability criteria from response time histories.

All the efforts made in CUA will serve to validate the complete aeroservoelastic loop.

4. CONCLUSIONS AND RECOMMENDATIONS FOR FUTURE EFFORTS

There is no doubt that considerable progress has been made since 1991 to predict classical aeroelastic phenomena (e.g transonic dips), but also less classical ones like LCO. Progress is made step by step, both in the research institutes and universities and in the aeronautical industry. While the industry aeroelasticians perform most of the analysis with classical linear methods including weighting factors, they also use CUA methods for some cases. Nevertheless, the use of CUA methods in industry remains marginal because of cost, required implementation effort and the clear need for more validation of the methods versus experiment.

There is a need for new standardized tests which will serve as a basis for further calibration of methods. These cases should be defined by the research institute community. They should cover a wide range of aeroelastic phenomena (static deformation, flutter in the transonic regime, LCO, buffet, etc.). They should address clean wing transonic phenomena, as well as control surface aerodynamics in connection with aeroelasticity concerns.

One of the main challenges of CUA is the grid generation, with a need to represent the details of geometry (e.g missile or underwing stores for military aircraft, nacelles for civil aircraft). The improvement of algorithms, reduction of computation time and implementation effort are necessary. The advanced methods should only be used when they bring in more physics and the aeroelastician should know when he has to be concerned about the numerics.

Up to now, because of insufficient calibration of CUA methods, high cost and the manpower required to implement such methods, industry is not ready to use time domain solutions extensively for analysis of aeroelastic phenomena. Industry still prefers to use, for aeroelastic analysis, linear or linearized solutions including weighting factors which improve AIC's. However, aircraft manufacturers are thinking about the integration of these methods within the complete aeroelastic analysis and validation process. Calibration of the methods versus experiment for classical static and dynamic aeroelasticity and for less conventional aeroelastic phenomena (LCO, buffeting, etc.) remains necessary.

In the technical evaluation report of the 1991 Specialists' Meeting it was mentioned that the "one really new thing" seen in the presentations was the transonic LCO on a fighter aircraft. LCO understanding had been addressed by a semi-empirical method. In the 1997 Workshop papers 1 and 10 have treated the LCO phenomenon through computation and correlation with tests.

Nevertheless, a special effort for understanding and
predicting LCO phenomena is still necessary.
The recommendations included in the same report remain
relevant. The objectives of computational unsteady
aerodynamicists and aeroelasticians should be to continue
jointly the investigation of transonic dip phenomena, do
comprehensive work on LCO for the short term and
medium term and extend studies to buffeting for long-term
studies.

CALCULATED VISCOUS AND SCALE EFFECTS ON TRANSONIC AEROELASTICTY

John W. Edwards*
NASA Langley Research Center
Mail Stop 121
Hampton, Virginia USA 23681–0001

Abstract

A viscous-inviscid interactive coupling method is used for the computation of unsteady transonic flows. A lag-extrainment integral boundary layer method is used with a transonic small disturbance potential code to compute the transonic aeroelastic response for two wing flutter models. By varying the modeled length scale, viscous effects may be studied as the Reynolds number per reference chordlength varies. Appropriate variation of modeled frequencies and generalized masses then allows comparison of reponses for varying scales or Reynolds number. Two wing planforms are studied: one a four percent thick swept wing and the other a typical business jet wing. Calculations for both wings show limit cycle oscillations at transonic speeds in the vicintiy of minimum flutter speed indices.

Introduction

The onset of transonic shock-induced flow separation is known to be associated with a variety of nonclassical aeroelastic instability and response phenomena,[1-13] referred to variously as: single degree of freedom flutter, limited-amplitude flutter, limit cycle oscillations (LCO), control surface buzz, shock induced oscillations (SIO) and buffeting (onset). A characteristic of the "instabilities" involved is a tendency to grow to a constant or bounded "limit amplitude" which can vary from a nuisance level to levels large enough to cause structural failure. In the latter case, the nonclassical response, generically referred to herein as LCO, is typically observed near the flutter boundary, making a distinction between the two response mechanisms difficult. Edwards[14,15] reviewed these features of transonic aeroelasticity, concluding that i.) computational capability for such cases would require modeling of dynamically separating and reattaching viscous boundary layers and ii.) such capability was not yet mature for wings or more complete configurations.
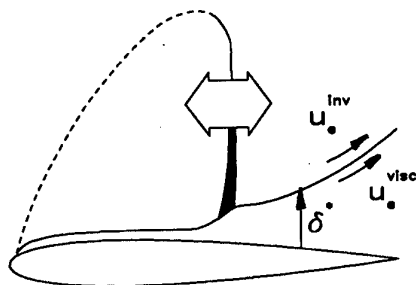

Fig. 1 Sketch of shock-boundary layer interaction.

---

*Senior Research Engineer, Aeroelasticity Branch, Structures Division

Interactive Boundary Layer Modeling (IBLM) provides an alternative to such direct computation of flows involving viscous shear layers. Separate computations are made for an inner viscous boundary layer region and an outer inviscid flow region as illustrated in Fig. 1. Subscript "e" denotes the "edge" of the boundary layer, while superscripts "i" and "v" denote inviscid and viscous variables. Ref. 16 developed an integral boundary layer lag-entrainment method to compute displacement thickness δ^* which was used to update the flow tangency boundary condition of the inviscid solver. This "direct" solution method for the entrainment equation becomes singular at flow separation and "inverse" computation methods[17-22] have been developed in attempts to treat flow separation.

Edwards[23,24] summarizes developments of such inverse computational methods by many authors[17-22,25-33] and extends the inverse method of Howlett[30,33], implemented in the CAP-TSD[31,32] (Computational Aeroelasticity Program-Transonic Small Disturbance) potential equation code, with a new interactive coupling procedure capable of treating transonic Shock Induced Oscillation (SIO) conditions for airfoils. Bartels[12,13] has recently developed an IBLM with a fully unsteady finite-difference boundary layer model interacted with a two-dimensional version of the CAP-TSD code and presents many SIO calculations.

In the present paper, calculations of wing flutter are presented for two cases: a four percent thick swept wing flutter model, and a thicker typical business jet wing flutter model. Viscous effects are shown for both models, including examples of LCO. The effect of model scale, and thus Reynolds number, is studied for both models. Evidence of a significant effect of Reynolds number for flutter and LCO conditions involving separation onset is shown.

Mathematical Method

Details of the inviscid flow equation, the boundary layer equations, the modifications to boundary conditions, and the IBLM coupling procedure are summarized in this section. Further details are given in Refs. 23 and 24.

Inviscid Flow Equation

The CAP-TSD potential equation code is used in this analysis. The CAP-TSD code uses an approximate factorization algorithm for time-accurate solution of the unsteady TSD equation[31,32]

$$\frac{\partial f_0}{\partial t} + \frac{\partial f_1}{\partial x} + \frac{\partial f_2}{\partial y} + \frac{\partial f_3}{\partial z} = 0 \qquad (1)$$

where ϕ is the inviscid-disturbance velocity potential and

$$f_0 = -A\phi_t - B\phi_x \qquad (2a)$$

$$f_1 = E_1\phi_x + F_1\phi_x^2 + G_1\phi_y \qquad (2b)$$

$$f_2 = \phi_y + H_1\phi_x\phi_y \qquad (2c)$$

$$f_3 = \phi_z \qquad (2d)$$

where $A = M^2$, $B = 2M^2$, $E_1 = 1 - M^2$, $F_1 = -\frac{1}{2}[3 - (2-\gamma)M^2]M^2$, $G_1 = -\frac{1}{2}M^2$, and $H_1 = -M^2$. For the 2-D version of the code, $f_2 = G_1 = 0$. The code contains modifications to these coefficients developed by Batina[35] to approximate the effects of shock generated entropy and vorticity.

Lag-Entrainment Boundary Layer Equations

The effect of a turbulent viscous boundary layer is modeled in the quasi-steady manner of Green et al.[16] by solving a set of ordinary differential equations, termed the Boundary Layer Equations (BLE), in x for the integral boundary layer quantities: momentum thickness θ; shape factor $\overline{H}$; and entrainment coefficient C_E. The various closure parameters in these equations are given in Ref. 31. In this form, the equations are suitable for attached flow boundary layers and provide the boundary layer displacement thickness

$$\delta^* = H\theta \qquad (3)$$

This provides a "direct" calculation of the viscous modification to the airfoil shape to be implemented in the boundary conditions discussed below.

At separation, the equations become singular and an alternative "inverse" IBLM is used as described by Howlett[34], Melnik and Brook[18] and LeBalleur[19]. In this form, the equation for θ is replaced by an equation for the viscous edge velocity, u_e^v, and θ and δ^* are obtained from the interactive boundary layer coupling method described below.

Numerical Implementation

From the leading edge of the airfoil, the boundary layer is approximated by the turbulent boundary layer on a flat plate. At a specified point, numerical integration of the inverse boundary layer equations is implemented with a fourth-order Runge-Kutta method. For the Mach number range studied, it was found that the inverse equations, in conjunction with the coupling method described below, converged rapidly for attached flow upstream of regions of flow separation (and also for downstream regions of reattached flow). This obviated the use of the direct boundary layer equations thus circumventing the numerically troublesome switching between the direct and inverse equations in separating flow regions, where the largest parameter gradients occur.

Interactive Boundary Layer Coupling Method

Since the intended applications of the IBLM include cases of wing flutter, including SIO and LCO, the coupling method was developed based on the observation that at the transonic flow conditions of interest, the flowfield is frequently inherently unsteady, displaying oscillating shocks and separating and reattaching boundary layers. The interacting boundary layer method is thus regarded as a simulation of two dynamic systems, the outer inviscid flow and the inner viscous flow, whose coupling requires active control elements in order to minimize the coupling error between the two systems. The elements utilized, illustrated in analog block diagram fashion in Fig. 2, include a variable gain integral control element for the displacement thickness and a first order smoothing filter for the momentum thickness estimate[23,24].

For the 3-D code, the boundary layer and interactive coupling equations are solved independently at each spanwise chord station on the wing. This is accomplished at each time step, within the Newton linearization iteration loop of the approximate factorization solution algorithm of the resulting CAP-TSDV code, where the appended "V" indicates the IBLM capability.
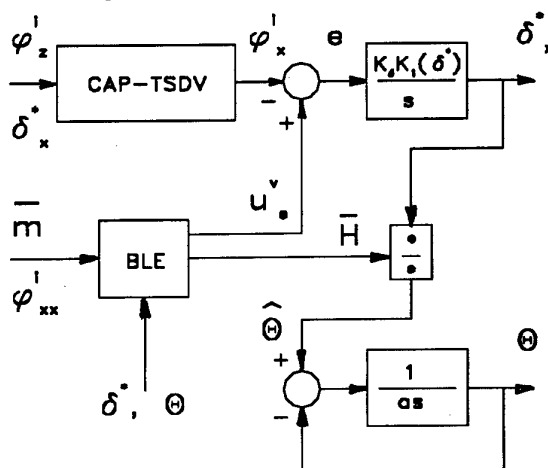

Fig. 2 Schematic diagram of variable gain, integral control, viscous-inviscid interative coupling method.

Scaling and Reynolds Number Modeling

The scaling relations used for flutter models, referred to as Mach scaling,[36,37] are given in Table I. In constructing a flutter model, all of the scaling parameters, λ_i, must be considered. The situation for a computational simulation of Reynolds number effect is much simpler, since there are no constraints on "model" size. Assuming the simulated "model" responses are to be computed for the same gas, same Mach number, same dynamic pressure, and same rel-

Parameter	Symbol	Ratio-model/aircraft
length	λ_l	l_m/l_{ac}
density	λ_ρ	ρ_m/ρ_{ac}
velocity	λ_V	V_m/V_{ac}
mass	λ_m	$\lambda_m\lambda_l^3$
frequency	λ_f	λ_V/λ_l
force	λ_F	$\lambda_\rho\lambda_V^2\lambda_l^2$
torque	λ_T	$\lambda_\rho\lambda_V^2\lambda_l^3$
dynamic pressure	λ_q	$\lambda_\rho\lambda_V^2$
Reynolds number	λ_{Re}	$\lambda_\rho\lambda_V\lambda_l\mu_{ac}/\mu_m$

Table 1 Mach scaling used for flutter model tesing.

ative deflections, we have $\lambda_\rho = \lambda_V = \lambda_q = 1$, leaving the following scaling relations for computational aeroelasticity:

generalized masses: $\lambda_m = \lambda_l^3$

modal frequencies: $\lambda_f = \lambda_l^{-1}$

Reynolds number per root chord: $\lambda_{Re} = \lambda_l$

In cases such as the present, where experimental data from actual wind tunnel models is available and we wish to predict the behavior of a larger flight vehicle, the roles of "aircraft" and "model" in the scaling relations is reversed. For example, if we wish to predict computationally the response of a flight vehicle 20 times larger than the flutter model, the computational aeroelastic analysis should be performed by modifying the aeroelastic equations of motion of the flutter model with: $\lambda_l = 20$, $\lambda_m = 8000$, $\lambda_f = 0.05$, and $\lambda_{Re} = 20$. That is, generalized masses are increased by λ_l^3, modal frequencies are decreased by λ_l, and the Reynolds number increases by λ_l. The procedure for studying the effects of scale or Reynolds number on, e.g. flutter, is thus: determine the computational aeroelastic modal root loci for the two length scales (i.e., modal frequencies and dampings versus dynamic pressure); and then, compare the scaled frequency, $\lambda_l \omega_f$, and damping, ζ, with those obtained from flutter model tests or computation with $\lambda_l = 1$. Also, amplitude effects such as wingtip motion, can be compared using the scaled deflection $\bar{z}_{tip} = z_{tip}/\lambda_l$.

Model Descriptions and Results

Wing Flutter Models

The first wing flutter model, shown in Fig. 3, is the AGARD Standard Aeroelastic Configuration[38,39] which was tested in the Transonic Dynamics Tunnel (TDT) at NASA Langley Research Center. It is a semispan wall-mounted model having a quarter-chord sweep angle of 45 deg., a panel aspect ratio of 1.65, and a taper ratio of 0.66. The wing had a NACA 65A004 airfoil section and was constructed of laminated mahogany. The wing is modeled structurally using the first four natural vibration modes, with natural frequencies ranging from 9.6 Hz for the first bending mode to 91.54 Hz for the second torsion mode. The CAP-TSDV calculations were performed on a 150 x 30 x 80 point computational grid with 100 points along each of 15 spanwise chords on the wing. Other computational conditions were: nondimensional time step $dt = 0.05$, one Newton iteration, and $K_\delta = 0.00030$.

The second wing flutter model, shown in Fig. 4, is a typical business jet configuration also tested in the TDT. The semispan wing-fuselage model was mounted on the wind tunnel sidewall and tested in air, with experimental flutter data obtained for Mach numbers from 0.628 to 0.888. The wing has a taper ratio of 0.29 and a midchord sweep of 23 degrees. The airfoil thickness varies from 13 percent at the symmetry plane (for the extended wing-alone configu-

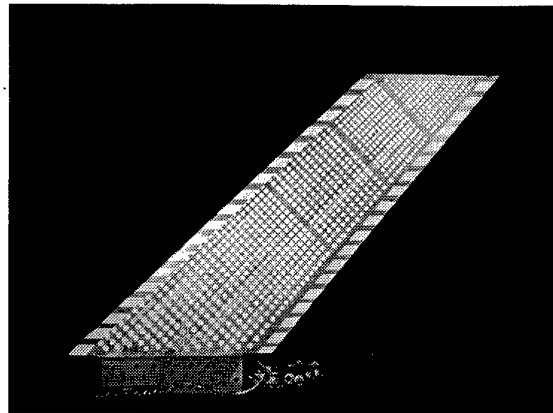ration analyzed) to 8.5 percent at the wing tip. Six natural

Fig. 3 Planview of AGARD Wing 445.6 Standard Aeroelastic Configuration.
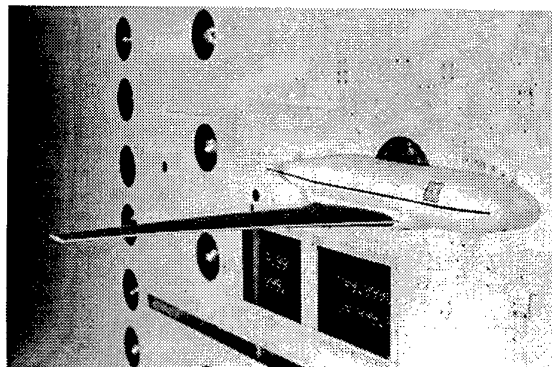

Fig. 4 Business jet flutter model mounted in NASA Langley Transonic Dynamics Tunnel.

vibration modes were included in the calculations, with frequencies ranging from 4.3 Hz to 62.7 Hz. The CAP-TSDV calculations were performed on a 100 x 50 x 80 point computational grid with 45 points along each of 33 spanwise chords on the wing. Other computational conditions were: nondimensional time step $dt = 0.03$, one Newton iteration, and $K_\delta = 0.00010$.
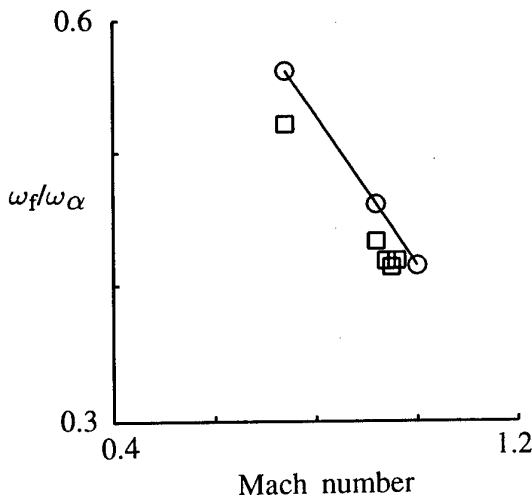
AGARD Wing 445.6 Flutter Calculations

The majority of publushed calculations for this model (actually a series of models with similar planforms) are for the "weakened model #3" tested in air, since this test covered the largest transonic speed range and showed a significant transonic dip effect. Edwards[24] summarizes a number of these calculations from both inviscid and viscous methods. The focus upon this case is unfortunate, in that the model tested in air resulted in unrealistically large mass ratios and small reduced flutter frequencies.

Models tested in heavy gas. It is thus desirable to study results for the "weakened models #5 and #6" which were tested in heavy gas and had more reasonable ranges of mass ratio and frequency. CAP-TSDV calculations for these cases are shown in Fig. 5. Again, for these cases with $M \leq 1.0$, the CAP-TSDV results are in excellent agreement with experiment for $M = 0.74$ and 0.92. Due to issues discussed above for very low supersonic Mach

numbers, calculations have not been attempted for the third experimental Mach number of 1.0. Instead, calculations at $M = 0.90$–0.96 revealed an interesting minimum feature in the flutter speed index parameter at $M = 0.95$. Figure 6 shows flutter boundaries for five values of the scale factor, λ, ranging from 1 to 40 and covering Reynolds number per root chord from 3.5 million to 140 million. Inserts show
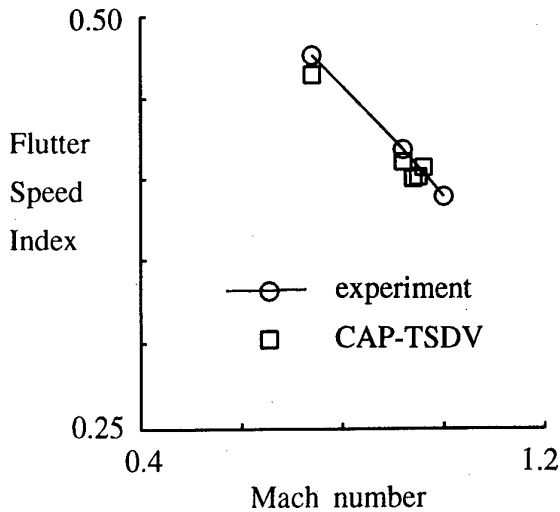
(a) flutter speed index.

(b) frequency.

Fig. 5 Comparison between experimental and calculated flutter speed index and frequency for the AGARD Wing 445.6 tested in heavy gas.

typical time histories for converging and diverging responses from which the stability boundaries were determined. For all the values of λ there is a minimum flutter speed index near $M = 0.95$ seen in the faired curves connecting the data points. For Mach numbers below this minimum, there is a small, monotonic decrease in flutter speed index with increasing Reynolds number. The amount of the decrease is less than one percent. At $M = 0.94$ and 0.96 there is a reversal of this trend, with the flutter speed index for $\lambda = 40$ increasing over that for $\lambda = 20$.

Further numerical experimentation at $M = 0.96$ re-

vealed interesting nonlinear response features. It was found that the estimated damping of the flutter mode was dependent upon the amplitude of the response time history. Figure 7 shows two instances of this behavior on the "backside" of this transonic dip in the flutter boundary for λ's of 1 and 40. In each case, stability boundaries inferred from responses with larger amplitudes of motion lead to lower flutter speed index values. Such amplitude dependent stability behavior is an indication that nonlinear processes are involved, and that nonlinear response mechanisms, such as limit cycle oscillations may be anticipated. This was investigated by calculating a simulated wing "tip rap" response for $M = 0.96$ and $Q = 0.75$ psi., shown in Figure 8. The interpolated flutter dynamic pressure from the experimental data for this Mach number is $Q_f = 0.757$ psi. The early portion of the response indicates positive damping of the flutter mode and also a higher frequency mode. The damping of the flutter mode decreases as the response amplitude decays to approximately 0.12 inches peak-to-peak, where stable limit cycle oscillations persist.
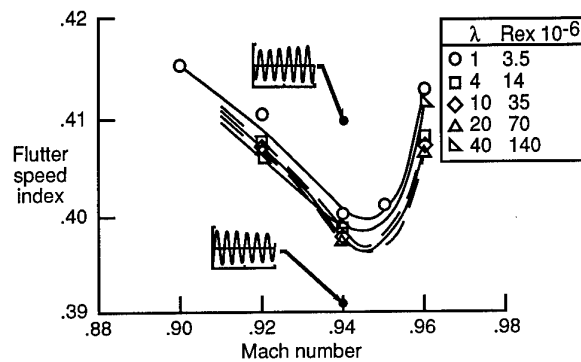

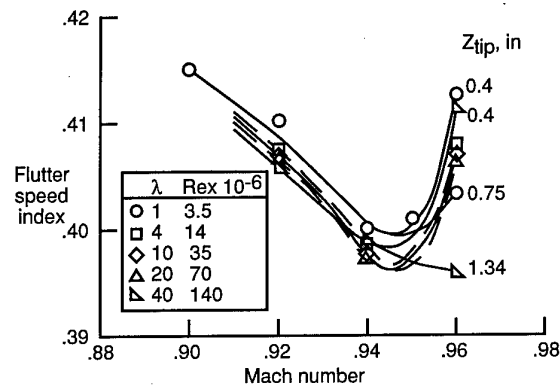**Fig. 6 Calculated effect of Reynolds number on Flutter near minimum transonic flutter speed.**

Fig. 7 Calculated effect of motion amplitude upon "flutter" boundary near minimum transonic flutter speeds.

This limit cycle behavior was further studied by sequentially increasing the dynamic pressure between computed runs from $Q = 0.5$ to 0.81 psi. The resulting tip deflection time history is shown in Figure 9. Twelve computer runs with a total of 24,000 time steps were calculated. The dynamic pressure was incremented as indicated in steps between restarted runs. For $Q \le 0.60$ psi., the response is

damped and for $Q = 0.70$ psi., small neutrally stable oscillations are seen. With Q increased to 0.78 psi., slowly divergent oscillations develop and with further increase to 0.81 psi., the divergent oscillations grow with increased negative damping until the amplitude reaches approximately 0.12 inches peak-to-peak. The growth of the oscillations then quenches and it appears that a limit cycle condition will again develop, although further calculations are needed to fully establish this feature.

This same sequence of increasing dynamic pressure calculations was performed for $\lambda = 10$, or Re = 35 million, and the results are shown in Figure 10. Very similar behavior is shown in Figure 9 for $\lambda = 1$ and Re = 3.5 million. Hence, for this wing geometry and "test" conditions, the nonlinear effect of motion amplitude dominates the effect of Reynolds number.
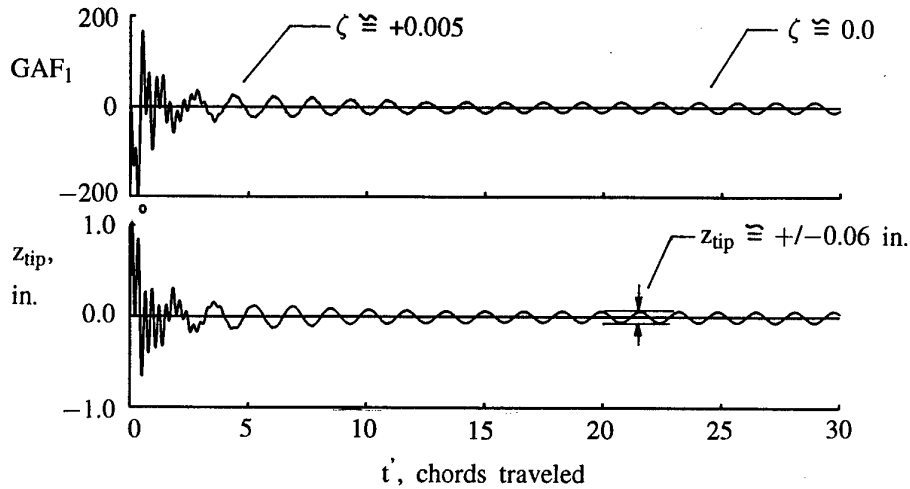
Fig. 8 Calculated AGARD Wing 445.6 tip response in heavy gas for M = 0.96 and Q = 0.75 psi.
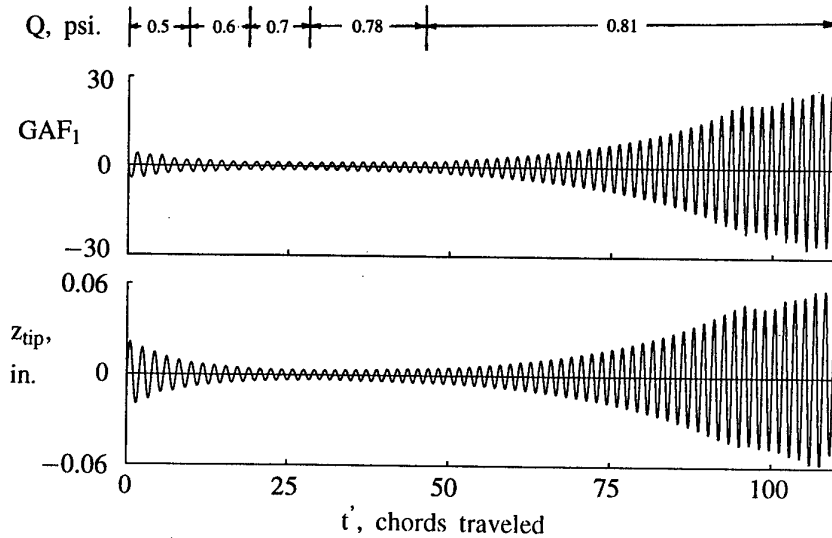
Fig. 9 Calculated AGARD Wing 445.6 response in heavy gas for M = 0.96 and increasing dynamic pressure; $\lambda_i = 1$.
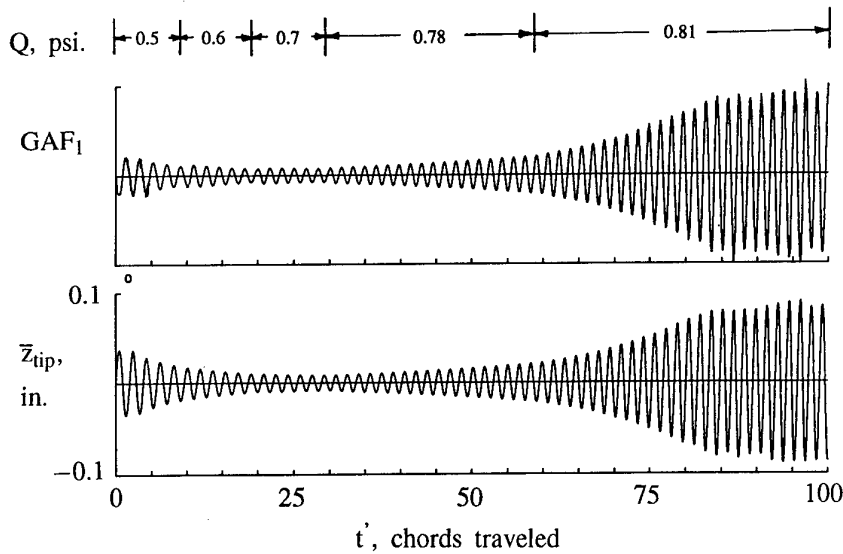
Fig. 10 Calculated scaled AGARD Wing 445.6 response in heavy gas for M = 0.96 and increasing dynamic pressure; $\lambda_t = 10$.

This limit cycle behavior for this model was only observed for the highest calculated Mach number, $M = 0.96$ which lies on the "backside" of the small transonic dip seen in Fig. 5. At this Mach number and for the wing motions calculated, the flow is fully attached with no significant transonic features. The boundary layer coupling method performed well, with well-converged displacement thickness profiles. Numerical flow visualizations of the wing pressure showed details which are possibly key to this nonlinear response behavior. At this Mach number and for this thin wing, significant regions of near sonic flow develop adjacent to the wing upper and lower surfaces as the wing oscillates. Very high frequency upstream moving pressure waves are seen in the visualizations which are consistent with forward propagating Mach waves. At a given point on the wing, the frequency of these pressure waves is 10–20 times the flutter mode frequency for this case. The amplitudes of these calculated limit cycles is small and no mention of such behavior is reported[39]. It is unlikely that such small motions, even if present, would have been detected since they would have been heavily masked by the model response to tunnel turbulence.

One final computational experiment for this case involved perturbing the LCO obtained at the end of the sequence shown in Figure 10. Figure 11 shows this result obtained by restarting from the last sequence with all modal displacements and velocities doubled. Instead of returning to the original LCO state, the response slowly diverges to more than five times the original amplitude. Again, further calculations are needed to establish the final state of the system.
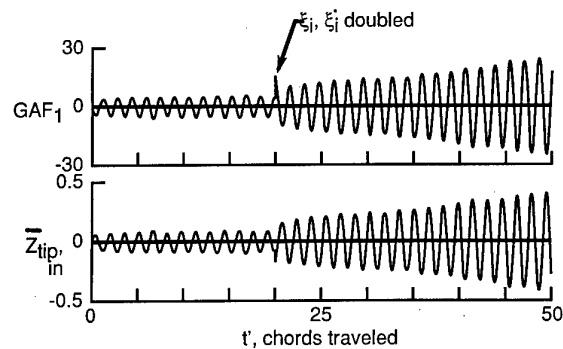

Fig. 11 Effect of perturbation from Limit Cycle Oscillation condition; M = 0.96, λ=10.0, Q = 0.81 psi., heavy gas.

Business Jet Wing Flutter Calculations

The business jet wing flutter model shown in Figure 4 was tested in the Transonic Dynamics Tunnel at NASA Langley Research Center. Gibbons[40] presents flutter calculations for the model including spatial and temporal convergence studies, and surface pressure coefficient comparisons for rigid and statically deformed cases, using TSD, Euler, and Navier-Stokes methods. For the present study, the effects of including viscous effects and varying Reynolds number by varying the model scale were investigated using the CAP-TSDV code.

Wind Tunnel Model Scale, $\lambda = 1$.The model was constructed from aluminum plate with fiberglass wrapped foam

providing the airfoil contour. The wing was mounted low on the side-wall mounted fuselage model which had a circular cross-section with a conical aft end. The wing root angle-of-attack was varied during the test to minimize loading. The maximum angle needed for this purpose was 0.2 degrees at the highest tested Mach number. This root angle was used for the calculations described below. This resulted in calculated static tip deflections (for $\lambda = 1.0$) of -1.33 in. at $M = 0.628$ and $+1.35$ in. at $M = 0.888$. The Reynolds numbers for these two Mach numbers were 2.17 million and 1.14 million respectively, based on the 2.0 ft. root chord. The model had a 4.4 ft. semispan.

Contour plots of the upper and lower wing surface pressure, displacement thickness, and skin friction are shown in Fig. 12 for $M = 0.888$. Note the lower surface leading edge suction peak and mild inboard shock seen in the pressures. The displacement thickness is oriented positive downwards for best visualization of the contour plot. The lower surface displacement thickness is similar to the upper surface with maximum thicknesses below one percent except near the root where the lower surface shock produces a thickness of approximately 1.5 percent root chord. The skin friction reflects these features seen in the displacement thickness and is informative regarding closeness to separation. The lower surface trailing-edge is separated at the root and there is a small separation bubble just inboard of the tip and aft of the leading-edge suction peak. The skin friction coefficient is

low in the trailing-edge region of the upper surface, reaching a minimum near 88 percent span. This region and the upper surface separation bubble are key in the effect of amplitude upon flutter mode response described below.

Calculated flutter speed indices and frequencies versus Mach number are compared with experiment in Fig. 13. The linear CAP-TSD, Euler, and Navier-Stokes resultes are from Gibbons[40] while the four CAP-TSDV data points are new. Comparison of these flutter boundaries leads to similar observations as for the 445.6 wing:

1. Inviscid calculations agree among themselves and are in very good agreement with experiment for the lower Mach numbers. For higher Mach numbers in the vicinity of the transonic dip region, the inviscid codes become increasingly conservative. For this wing, inviscid calculations should not be used for $M > 0.80$.

2. For Mach numbers at and below the minimum transonic flutter speed index, the viscous methods, CAP-TSDV and CFL-3D, are in agreement and both provide good agreement with experiment, largely correcting the deficiency in the inviscid methods.

3. Linear flutter calculations[43] are in excellent agreement with experiment up to $M = 0.85$, but cannot be relied upon for higher transonic Mach numbers. The good agreement in the lower transonic speed range is due to well-known compensating defects of linear theory wherein thickness and viscous effects are neglected.
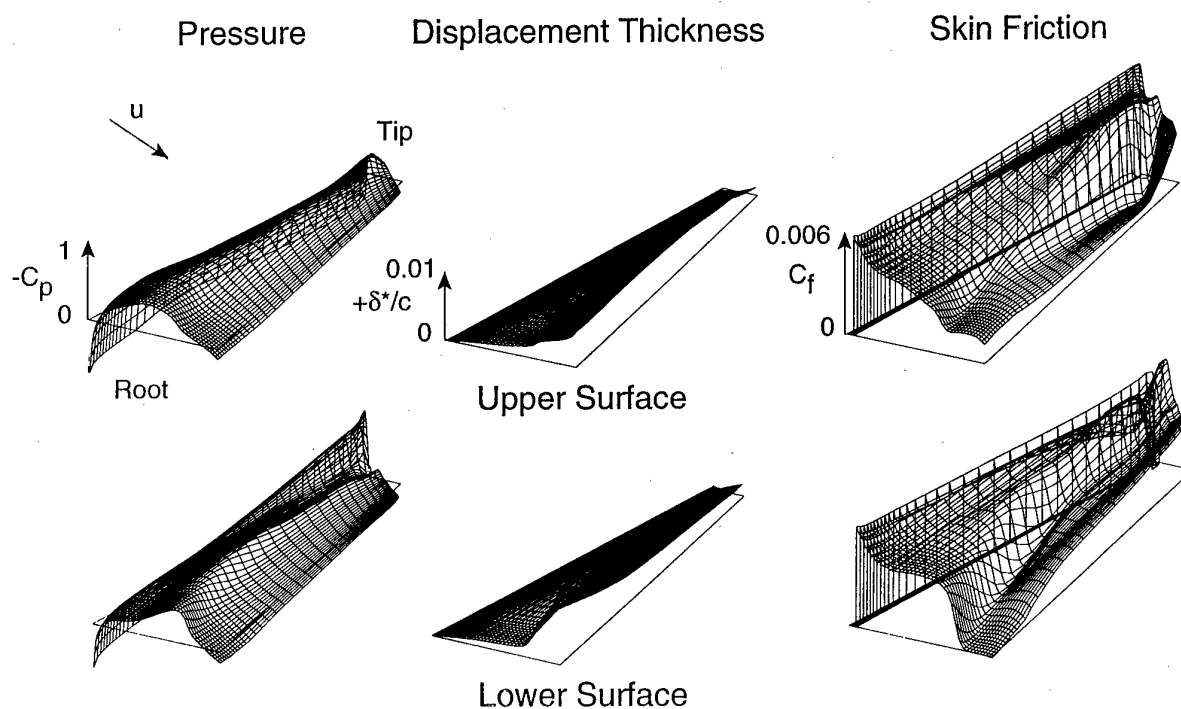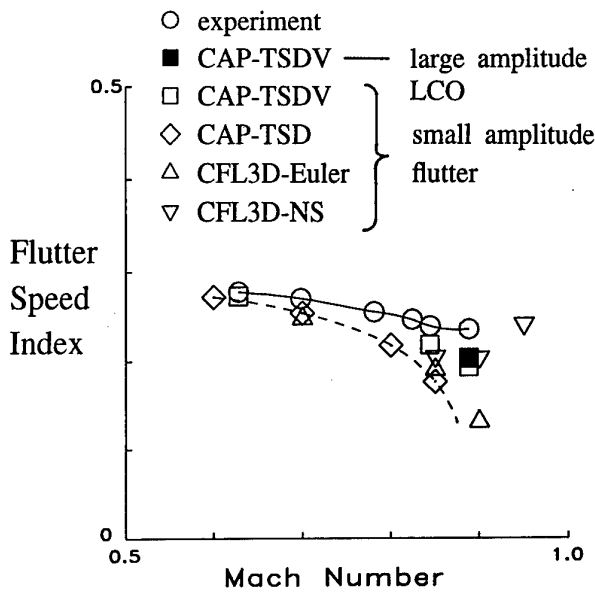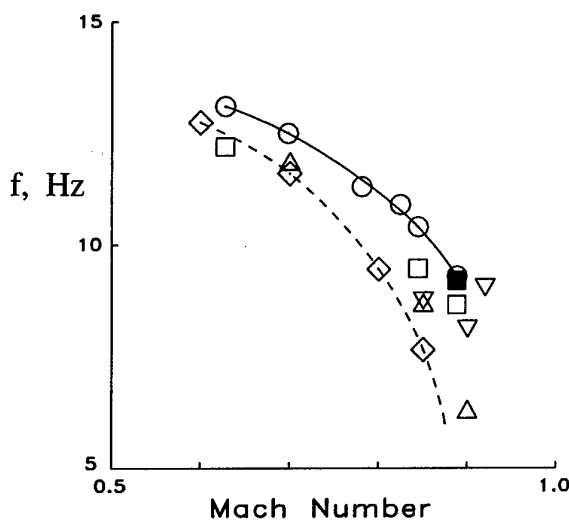

Fig. 12 Contour plots of business jet wing pressure and boundary layer parameters at statically deformed conditions: M = 0.888, Q = 79 psf., $\alpha = 0.2°$, $\lambda = 1$, $Re_c = 1.14$ million.

All of the results discussed thus far were obtained from transient or harmonic responses of small amplitude, that is, wing tip response amplitudes were less than several tenths of an inch. Under these conditions, no large changes of the static aerodynamic loading occurred and transient responses exhibited exponential stability, characteristic of a "locally linear" system behavior. At $M = 0.888$ the CAP-TSDV code was able to calculate large amplitude response motions which demonstrated limit cycle behavior. The motion was calculated for the experimental "flutter" dynamic pressure of 79 lb/ft^2. The conditions for the limit cycle are noted in Fig. 13 by the solid symbol indicating a 0.5 Hz. increase in frequency over the small amplitude value. Figure 14 shows two transient responses confirming the limit cycle behavior. The
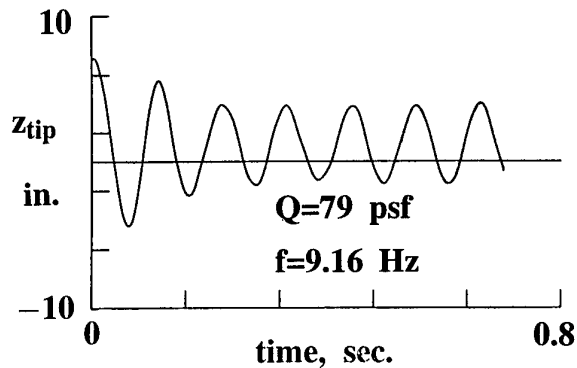
motions were excited from converged statically deformed conditions by multiplying the modal displacements and velocities by factors of 5.0 for Fig. 14a and 0.5 for Fig. 14b. The larger factor simulates a wing tip displacement of about 7 inches, resulting in decaying oscillations to a limit cycle with an amplitude of 5–6 inches peak-to-peak. The smaller factor results in oscillations growing in amplitude to the limit cycle. This behavior is similar to model behavior observed during the test. Video tape of the model motions at the experimental "flutter" conditions for this Mach number shows the model to be undergoing constant amplitude wing oscillations with amplitude of slightly less than one tip chord (6.3 inches) peak-to-peak. This is in very good agreement with the calculated LCO amplitude and frequency shown in Fig. 14. The plate construction of the model provides sufficient strength to allow the model to sustain oscillations of this amplitude without structural failure. Inspection of the wing boundary layer parameters and surface pressures during the calculated limit cycle oscillations confirmed that the flow over the wing was intermittently separating and reattaching in the outboard upper and lower surface regions described above. This apparently provides the mechanism needed to quench the growth of the unstable flutter mode motions.
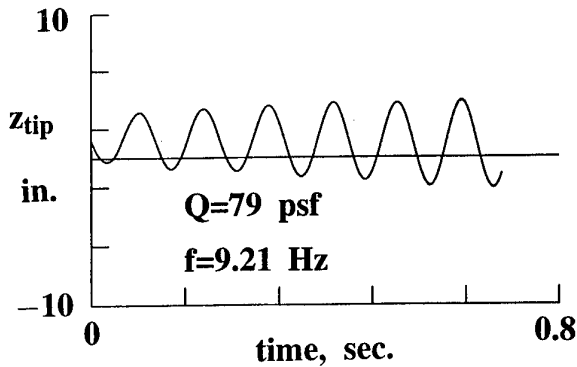

(a) flutter speed index.

(b) frequency.

Fig. 13 Comparison between experimental and calculated flutter speed index and frequency for a business jet flutter model tested in air.
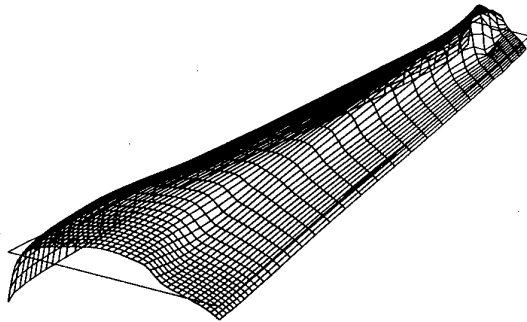

(a) amplitude decaying to limit cycle oscillation.
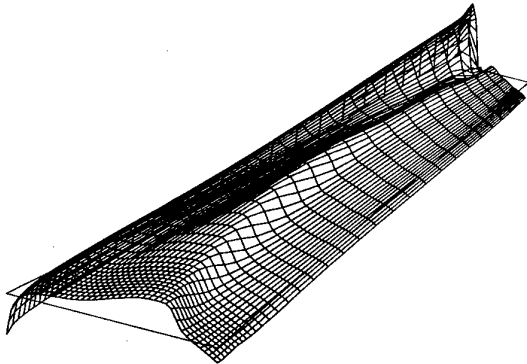

(b) amplitude growing to limit cycle oscillation.

Fig. 14 Calculated limit cycle response for a business jet wing flutter model: M = 0.888, Q = 79 psf., λ = 1.0, Re$_c$ = 1.14 million.

Effect of Reynolds number, $\lambda = 10.0$. A limited study of the effect of Reynolds number on this LCO behavior at $M = 0.888$ was conducted. Figure 15 shows the steady deformed wing pressure contours. Comparison with Figure 12 indicates modest changes in the wing loading for the increased Reynolds number. Boundary layer parameters (not shown) indicate that the displacement thickness over the wing is approximately half that shown for $\lambda = 1.0$,

accounting for the increased gradients seen in c_p in the inboard region of the lower surface and the outboard region of the upper surface in Figure 15. The wing lift and moment coefficients decreased slightly from $C_L = 0.034$ and $C_M = -0.038$ for $\lambda = 1$ to $C_L = 0.017$ and $C_M = -0.027$ for $\lambda = 10$ and the scaled wing tip displacement decreased by several tenths of an inch.

(a) upper surface pressure coefficient.

(b) lower surface pressure coefficient.

Fig. 15 Contour plots of business jet wing pressure at statically deformed conditions: M = 0.888, Q = 79 psf., α = 0.2°, λ = 10, Re_c = 11.4 million.
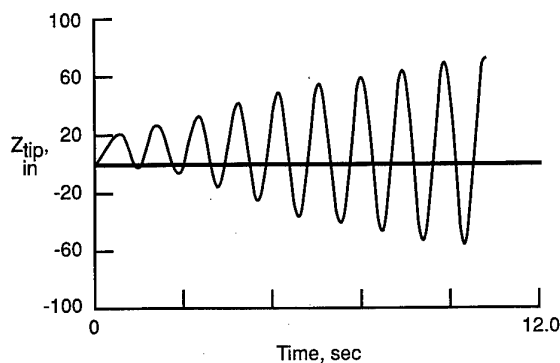

Fig. 16 Calculated limit cycle response for a business jet wing flutter model: M = 0.888, Q = 79 psf., λ = 10.0, Re_c = 11.4 million.

Figure 16 shows the effect of the increased Reynolds number upon the LCO behavior of the wing. If there had been no effect, the wing oscillations would be expected to grow to a LCO condition with wing tip motions of about ± 25–30 inches, whereas the actual motion shown in Figure 16 has reached ± 60 inches and has not yet achieved stable

limit cycle conditions. While the higher Reynolds number leads to increased pressure gradients and hence slightly increased transonic shock strength, the thinner boundary layer is apparently less prone to providing the quenching mechanism for the LCO and larger wing motions are required to induce such quenching. In the present case, LCO motions for the $\lambda = 10$ case are over twice the LCO motions calculated and observed for the wind tunnel model scale which was tested. This might infer that the wind tunnel flutter model test provided an unconservative flutter boundary. On the other hand, the large LCO motions observed during the test were correctly interpreted by the test engineers as "flutter." The ambiguity underlying this discussion of stability for realistic flutter model testing should be interpreted as a requirement for an expanded concept of stability for transonic flutter computations and testing.

Concluding Remarks

A viscous-inviscid interactive coupling method has been described, directed towards the computation of unsteady separating and reattaching transonic flows which must be treated in cases of self-excited shock-induced oscillations and transonic flutter. Lag-entrainment integral boundary layer equations and a transonic small disturbance potential code are coupled with a variable gain, integral control coupling method.

Flutter calculations for the AGARD 445.6 flutter model are in excellent agreement with experiment for $M < 1.0$ for models tested in air and heavy gas. Calculations with the CAP-TSDV code are in excellent agreement with results from a Navier-Stokes code at $M = 0.96$. For Mach numbers below and very near unity, viscous modeling is required for such thin wings in order to achieve acceptable accuracy. In this region, calculations show evidence of small amplitude limit cycle behavior. Effects of scale and Reynolds number for this four percent thick model are small for Mach numbers less than the minimum transonic flutter speed; less than one percent decrease in flutter speed for increasing Reynolds number from 1 to 140 million. For Mach numbers just above the minimum transonic flutter speed, nonlinear amplitude effects are larger than Reynolds number effects for this wing. It is important to note that for this model and test conditions, there are no strong transonic flow features and the flow is completely attached.

Flutter calculations for a business jet wing model also show very good agreement with experiment for the available test data up to $M = 0.9$. For this thicker wing, the requirement for viscous modeling extends to lower transonic Mach numbers. Again, calculations with the CAP-TSDV code are in very good agreement with a Navier-Stokes code at $M = 0.888$ for small amplitude flutter motions. For large amplitude wing oscillations, the CAP-TSDV code predicts limit cycle behavior at this Mach number in very good agreement with that observed during wind tunnel tests of the model. Also, the effect of a tenfold increase in scale or Reynolds number leads to a thinner boundary layer, weaker viscous effects, and limit cycle oscillation amplitude grows to over twice that calculated and observed in wind tunnel flutter tests.

Acknowledgement

The author would like to express his appreciation to Donald F. Keller of the Aeroelasticity Branch, NASA Langley Research Center for valuable discussion regarding the wind tunnel test of the business jet flutter model. Great appreciation is also due Michael D. Gibbons, Lockheed Engineering & Sciences Corp., for valuable discussions of his experience with flutter calculations for that model. His Reference 37, published posthumously, should be used as a model of careful and accurate computational aeroelasticity.

References

1. Cunningham, A. M., "Practical Problems: Airplanes," Chapter 2 in Unsteady Transonic Aerodynamics, ed. by D. Nixon, Vol. 120 in AIAA Progress in Aeronautics and Astronautics, 1989.
2. Mabey, D. G., "Physical Phenomena Associated with Unsteady Transonic Flow," Chapter 1 in Unsteady Transonic Aerodynamics, ed. by D. Nixon, Vol. 120 in AIAA Progress in Aeronautics and Astronautics, 1989.
3. Eckstrom, C. V., Seidel, D. A., and Sandford, M. C., "Unsteady Pressure and Structural Response Measurements on an Elastic Supercritical Wing," AIAA Paper 88-2277, April 1988.
4. McDevitt, J. B., "Supercritical Flow About a Thick Circular-Arc Airfoil," NASA TM-78549, Jan. 1979.
5. McDevitt, J. B., Levy, L. L., Jr., and Deiwert, G. S., "Transonic Flow About a Thick Circular-Arc Airfoil," AIAA Journal, Vol. 14, May 1976, pp. 606–613.
6. McDevitt, J. B., and Okuno, A. F., "Static and Dynamic Pressure Measurements on a NACA 0012 Airfoil in the Ames High Reynolds Number Facility," NASA TP-2485, June 1985.
7. Lee, B. H. K., "Oscillatory Shock Motion Caused by Transonic Shock Boundary-Layer Interaction," AIAA Journal, Vol. 28, pp. 942–944.
8. Hirose, N., and Miwa, H., "Computational and Experimental Research on Buffet Phenomena of Transonic Airfoils," NAL TR-996T, 1988.
9. Edwards, J. W., and Thomas, J. L., "Computational Methods for Unsteady Transonic Flows," Chapter 5 in Unsteady Transonic Aerodynamics, ed. by D. Nixon, Vol. 120 in AIAA Progress in Aeronautics and Astronautics, 1989.
10. Levy, L. L., Jr., "Experimental and Computational Steady and Unsteady Transonic Flows About a Thick Airfoil," AIAA Journal, Vol. 16, June 1978, pp. 564–572.
11. Rumsey, C. L., Sanetrik, M. D., Biedron, R. T., Melson, N. D., and Parlette, E. B., "Efficiency and Accuracy of Time-Accurate Turbulent Navier-Stokes Computations," AIAA Paper 95-1835, June 1995.
12. Bartels, R. E., "Interactive Boundary Layer Computations Using the Improved k-ω Turbulence Model," Proc. of the 9th International Conference on Numerical Methods in Laminar and Turbulent Flow, Pineridge Press 1995.
13. Bartels, R. E., and Rothmayer, A. P., "An IBL Approach to Multiscaled Shock Induced Oscillation," AIAA Paper 95-2157, June 1995.
14. Edwards, J. W., and Malone, J. B., "Current Status of Computational Methods for Transonic Unsteady Aerodynamic and Aeroelastic Applications," Paper No. 1 in Transonic Unsteady Aerodynamics and Aeroelasticity, AGARD CP 507, March 1992.
15. Edwards, J. W., "Technical Evaluation Report on 1991 Specialists' Meeting on Transonic Unsteady Aerodynamics and Aeroelasticity." Paper T in Transonic Unsteady Aerodynamics and Aeroelasticity, AGARD CP 507, March 1992.
16. Green, J. E., Weeks, D. J., and Brooman, J. W. F., "Prediction of Turbulent Boundary Layers and Wakes in Compressible Flow by a Lag-Entrainment Method," R & M No. 3791, British Aeronautical Research Council, 1977.
17. Carter, J. E., "A New Boundary-Layer Inviscid Iteration Technique for Separated Flows," AIAA Paper 79-1450, July 1979.
18. Melnik, R. E., and Brook, J. W., "The Computation of Viscid/Inviscid Interaction on Airfoils With Separated Flow," Third Symposium on Numerical and Physical Aspects of Aerodynamic Flows, California State University, 1985, pp. 1-21–1-37.
19. LeBalleur, J. C., and Girodroux-Lavigne, P., "A Viscous-Inviscid Interaction Method for Computing Unsteady Transonic Separation," Third Symposium on Numerical and Physical Aspects of Aerodynamic Flows, California State University, 1985, (ONERA T. P. No. 1985-5)
20. Houwink, R., and Veldman, A. E. P., "Steady and Unsteady Separated Flow Computations for Transonic Airfoils," AIAA Paper 84-1618, June 1984.
21. Houwink, R., "Computation of Unsteady Turbulent Boundary Layer Effects on Unsteady Flow About Airfoils," Fourth Symposium on Numerical and Physical Aspects of Aerodynamic flows, Jan. 1989 (also NLR TP 89003 U).
22. Thomas, J. L., "Transonic Viscous-Inviscid Interaction Using Euler and Inverse Boundary-Layer Equations," Ph.D. Diss., Mississippi State Univ., Dec. 1983.
23. Edwards, J. W., "Transonic Shock Oscillations Calculated with a New Interactive Boundary Layer Coupling Method," AIAA Paper 93-0777, January 1993.
24. Edwards, J. W., "Transonic Shock Oscillations and Wing Flutter Calculated with an Interactive Boundary Layer Coupling Method," EUROMECH-Colloquium 349, Simulation of Fluid-Structure Interaction in Aeronautics, Gottingen, Germany, Sept. 16–18, 1996.
25. Holst, T. L., "Viscous Transonic Airfoil Workshop Compendium of Results," Journal of Aircraft, Vol. 25, Dec. 1988.
26. Chang, K. C., Alemdarogula, N., Mehta, U., and Cebeci, T., "Further Comparisons of Interactive Boundary-Layer and Thin-Layer Navier-Stokes Procedures," Journal of Aircraft, Vol. 25, Oct. 1988, pp. 89–903.
27. Drela, M., and Giles, M. B., "Viscous-Inviscid Analysis of Transonic and Low Reynolds Number Airfoils," AIAA Journal, Vol. 25, Oct. 1987, pp. 1347–1355.
28. Fenno, C. C., Jr., Newman, P. A., and Hassan, H. A., "Unsteady Viscous-Inviscid Interaction Procedures for Transonic Airfoils Using Cartesian Grids," Journal of Aircraft, Vol. 26, Aug. 1989, pp. 723–730.
29. Kusunose, K., Wigton, L., and Meredith, P., "A Rapidly Converging Viscous/Inviscid Code for Multi-Element Airfoil Configurations," AIAA Paper 91-0177, Jan. 1991.

30. Howlett, J. T., "Efficient Self-Consistent Viscous Inviscid Solution for Unsteady Transonic Flow", *Journal of Aircraft*, Vol. 24, Nov. 1987, pp. 737–744.

31. Batina, J. T., "Unsteady Transonic Algorithm Improvements for Realistic Aircraft Configurations," *Journal of Aircraft*, Vol. 26, Feb. 1989, pp. 131–139.

32. Batina, J. T., "A Finite-Difference Approximate-Factorization Algorithm for Solution of the Unsteady Transonic Small-Disturbance Equation," NASA TP 3129, January 1992.

33. Rizzetta, D. P., "Procedures for the Computation of Unsteady Transonic Flows Including Viscous Effects", NASA CR-155249, Jan. 1982.

34. Howlett, J. T., "Calculation of Unsteady Transonic Flows With Mild Separation by Viscous-Inviscid Interaction," NASA TP-3197, June 1992.

35. Batina, J. T., "Unsteady Transonic Small-Disturbance Theory Including Entropy and Vorticity Effects," *Journal of Aircraft*, Vol. 26, June 1989, pp. 531–538.

36. Regier, A. A.: "The Use of Scaled Dynamic Models in Several Aerospace Vehicle Studies," paper presented at a Colloquium on the Use of Models and Scaling in Shock and Vibration, Winter Annual Meeting of the ASME, Nov. 19, 1963.

37. Dupriex, F.: "Flutter Models, Their Design, Manufacture, and Ground Testing," von Karman Institute for Fluid Dynamics Lecture Series 1992-01, Introduction to Flutter of Winged Aircraft, Dec. 9–13, 1991.

38. Yates, E. C., Jr., "AGARD Standard Aeroelastic Configurations for Dynamic Response. Candidate Configuration I. — Wing 445.6," NASA TM 100492, August 1987.

39. Yates, E. C., Jr., Land, N. S., and Foughner, J. T., Jr., "Measured and Calculated Subsonic and Transonic Flutter Characteristics of a 45 Degree Sweptback Wing Planform in Air and in Freon-12 in the Langley Transonic Dynamics Tunnel," NASA TN D-1616, March 1963.

40. Gibbons, M. D., "Aeroelastic Calculations Using CFD for a Typical Business Jet Model," NASA CR 4753, September 1996.

AEROELASTICITE ET C.F.D.
(AEROELASTICITY AND C.F.D.)

C. PETIAU, B. STOUFFLET, Ph. NICOT
DASSAULT AVIATION
DGT, 78 Quai Marcel Dassault
92214 Saint Cloud Cedex, France

RESUME

Nous présentons l'évolution de l'utilisation des méthodes de C.F.D. dans notre système d'analyse aéroélastique (ELFINI).

Nous sommes partis d'un outil fondé sur le couplage d'un modèle E.F. structural et d'un modèle aérodynamique, issu de la théorie du potentiel linéaire, recalé empiriquement (en particulier sur les essais en vol) ; le caractère linéaire de ces modèles permettant une organisation très efficace des calculs (notions de « base de charges » et de « base aérodynamique »), avec un balayage très peu coûteux de l'ensemble des configurations de vol à étudier (Mach, altitudes, manoeuvres, configuration de masses et d'emports).
Actuellement, en gardant la même organisation, nous utilisons opérationnellement une méthode Eléments Finis Euler pour le calcul des effets de formes « initiales » et de mouvements « rigides ».

Nous poussons maintenant nos développements sur 2 axes principaux :
- méthodes « non linéaires » de couplages statiques et dynamiques directs avec modèles aérodynamiques par méthode de potentiel non linéaire et surtout par méthode Eléments Finis Euler stationnaire et instationnaire,
- méthodes d' « Euler linéarisées » au voisinage des solutions aéroélastiques statiques non linéaires précédentes.

En conclusion, nous évoquons les grandes lignes de notre future organisation des calculs d'aéroélasticité qui devront être plus précis tout en restant à un coût abordable.

ABSTRACT

We present the evolution of the use of C.F.D. methods within our system of aeroelastic analysis (ELFINI).

We started from a tool founded on the coupling of a structural F.E. model and of an aerodynamic model, based on linear potential theory, empirically calibrated (mainly from flight tests) ; the linear character of these models allows a very efficient organization of calculations (notions of « load basis » and of « aerodynamic basis »), sweeping of the whole flight configurations (Mach, altitudes, maneuvers, mass and external store configurations) being inexpensive.

Presently, keeping the same organization, we use an Euler F.E. method for effects of « initial » shapes and of « rigid » motions.

Now we push our developments along two main directions :
- « non linear » methods of direct static and dynamic coupling with aerodynamic model by non linear potential methods and mainly by steady and unsteady F.E. Euler method,

- « linearized » Euler methods, in the neighbourhood of previous non linear static aeroelastic solutions.

As a conclusion, we evoke the main features of our future organization of aeroelasticity analysis which would be more accurate while remaining « affordable ».

1. INTRODUCTION

Au début des années 90 nos outils d'analyse aéroélastique étaient globalement fondés sur le couplage de modèles dynamiques structuraux "Eléments Finis" d'avion complet (voir planche 1) et de modèles aérodynamiques stationnaires et instationnaires issus de l'équation du potentiel linéarisé résolue par méthode de singularité de "doublets" et "sources" (voir références 1, 2, 3), le modèle aérodynamique stationnaire faisant systématiquement l'objet de recalages empiriques (expérience des avions précédents, essais en soufflerie et surtout essais en vol, voir référence 4, 5).

Ces modèles nourrissent l'ensemble des analyses où intervient l'aéroélasticité :

- Analyses de stabilité (divergence statique et flutter)

- Modèle de mécanique du vol "avion souple" et fourniture des opérateurs nécessaires à la mise au point du Système de Commande de Vol (fonctions de transfert entre les déplacements des vérins de commande de vol et les capteurs des mouvements de l'avion, indicateurs de sévérité des charges, ...).

- Calcul des réponses structurales en manoeuvre et sélection des cas de charges dimensionnants.

Une technique particulière, rappelée au §2, permet, à partir de la constitution initiale d'une "base de charges" et d'une "base aérodynamique", de balayer à très faible coût les milliers de configurations à examiner dans le domaine de Mach, altitudes, manoeuvres, configurations de masse et d'emports.

La relative imprécision des modèles aérodynamiques théoriques utilisés, surtout en transsonique, avait deux inconvénients :

- Le risque de découvertes tardives de difficultés au niveau des essais en vol, coûteuses à rattraper.

- La nécessité d'un nombre élevé de ces essais en vol pour assurer la qualification.

L'espoir d'améliorer cette situation est venue de l'émergence de modélisations aérodynamiques plus précises, en particulier les modélisations Eléments Finis EULER, dont les coûts de calcul commencent à être abordables, même pour balayer de multiples configurations d'avion complet avec emports (voir planche 2).

Nous présentons ici la pénétration de ces techniques C.F.D. dans notre processus actuel d'analyse aéroélastique, nous évoquons ensuite les développements en cours.

2. METHODE ACTUELLE OPERATIONNELLE EN AEROELASTICITE

Elle est dans le prolongement de notre approche "classique" supportée par notre logiciel "ELFINI-AEROELASTICITY" (voir référence 1, 2, 3), basée sur le couplage d'un modèle structural "Eléments Finis" de l'avion complet (10000 à 100000 degrés de liberté, exemple planche 1) avec des modèles aérodynamiques "linéarisés" ; ces modèles sont maintenant de provenance mixte :

- Méthode Eléments Finis EULER pour les effets de forme initiale et les mouvements "rigides"

- Méthode de potentiel linéarisé pour les mouvements "souples" et les effets instationnaires.

L'organisation des calculs est résumée planche 3, le principe est d'effectuer les opérations "lourdes" sur le modèle structural et sur les modèles aérodynamiques indépendamment de toutes les configurations de vol à étudier (Mach, altitude, manoeuvres, masse et emports).

Ces opérations lourdes, de constitution des "base de charges" et "base aérodynamique", sont les suivantes :

- Le calcul des déplacements du modèle Eléments Finis pour quelques centaines de chargements de base. Ces chargements de base correspondent à des charges unitaires de pression ou d'inertie par zones ; tout chargement statique ou dynamique peut être représenté par combinaison linéaire des chargements de base.

- La construction du modèle aérodynamique permettant d'exprimer les charges aérodynamiques stationnaires et instationnaires dans la base de charge précédente, en fonction du mouvement de l'avion. Ce mouvement est défini par une combinaison de formes de base aérodynamiques (mouvements rigides et déformés souples) indépendantes des degrés de liberté du modèle élastique. Par les méthodes Eléments Finis EULER, on calcule les effets de formes initiales et de mouvement rigide (linéarisation par différence entre 2 positions), les conditions aux limites de paroi peuvent tenir compte de l'épaisseur de couche limite. Les effets de déformations "souples" stationnaires et les effets instationnaires sont encore calculés par méthode de potentiel linéarisé, les effets instationnaires sont calculés dans le domaine fréquence.

- L'extraction, à partir de ces modèles élastique et aérodynamique encombrants d'opérateurs de base "condensés" contenant les seules données intervenant dans le couplage aéroélastique :

- Matrice de rigidité et matrice de masse réduite dans la base de charge.

- Opérateur de lissage des déformées E.F. de base par les formes aérodynamiques de base.

- "Indicateurs de Sévérité" des charges de base.

A partir de ces opérateurs de base les calculs qui suivent sont très rapides et permettent de balayer des milliers de configurations, ce sont :

- L'élaboration des coefficients des équations de l'aéroélasticité statique ou dynamique pour les configurations de vol et de masse considérée.

- Les analyses de stabilité (Divergence, Flutter).

- Le calcul du mouvement de l'avion, en quasi statique ou en dynamique, avec le suivi des "indicateurs de sévérité des charges".

- La sélection des cas de charges dimensionnants.

Le modèle aérodynamique continue à pouvoir être recalé sur les essais en soufflerie et surtout sur les essais en vol à partir de mesures de jauges de contraintes (voir méthode d'identification de modèle présentée dans les références 4 et 5).

Une technique de "linéarisation par zone" permet de prendre en compte les non linéarités aérodynamiques dues aux grands mouvements rigides (principalement sur l'effet d'incidence et les braquages de gouverne).

Nous présentons planche 4 des comparaisons de résultats de ces modèles à des résultats dérivés des mesures en vol ; elles sont globalement satisfaisantes pour les configurations quasi statiques stationnaires.

Avec cette approche la présence de non linéarité mécanique (exemple : jeux, effets de membrane, grandes rotations des gouvernes, non linéarités hydrauliques des servocommandes, ...) se traite par intégration directe dans le domaine temps après "rationalisation" (approximation par équations différentielles) des forces aérodynamiques instationnaires initialement exprimées dans le domaine fréquence (méthode validée pour le calcul du flutter en présence de jeux mécaniques).

3. PRINCIPAUX DEVELOPPEMENTS EN COURS

Nous donnons la priorité à l'analyse du domaine transsonique, grand badin et donc incidences modérées qui est le plus critique pour les phénomènes d'aéroélasticité et pour lequel nous avons un bon espoir de développer des outils précis à coût d'utilisation abordable.

Nous travaillons sur 2 familles d'outils.

3.1 Couplage aéroélastique avec C.F.D. non linéaire

On explore 2 techniques de C.F.D. :

- Formulation de potentiel non conservatif avec modèle de différences finies (méthode de Jameson, voir références 6 et 7), avec nos outils stationnaires CITRON et instationnaires TCITRON ; les calculs sont rapides mais ne traitent que des ailes de forme simple. Ces outils nous servent à la fois pour les benchmark de comparaison avec les méthodes plus lourdes et surtout pour la compréhension générique des phénomènes.

- Formulation d'EULER conservative avec modèle d'Eléments Finis non structuré (voir référence 8) avec notre code EUGENIE qui se positionne comme notre outil de base permettant de traiter les formes les plus complexes (interaction des emports des avions

militaires, des nacelles moteurs des avions civils).

Dans les 2 techniques, les conditions aux limites, correspondant aux mouvements paroi et à l'épaisseur de couche limite, sont modélisées par une technique de "transpiration" évitant un traitement de la déformation des maillages.

Pour le couplage le comportement dynamique de la structure est condensé par la construction d'un ensemble d'opérateurs linéaires, fournis par ELFINI, donnant le déplacement des noeuds du maillage aérodynamique à la paroi en fonction des pressions aux facettes de la paroi du maillage C.F.D.

En statique la condition au limite de paroi est actualisée périodiquement au cours des itérations de l'algorithme de résolution des équations C.F.D.; en dynamique elle l'est à chaque pas de temps d'intégration ; dans les 2 cas le coût d'actualisation est négligeable.

En statique comme en dynamique les opérateurs structuraux représentent simultanément les mouvements solides (avions et gouvernes) et ceux des modes "souples". En statique ils incluent le calcul de l'équilibre en mécanique du vol pour les manoeuvres considérées. En dynamique ils peuvent intégrer la représentation du Système de Contrôle de Vol, ils peuvent être adaptés à tout schéma d'intégration implicite désiré.

Nous présentons planche 5 un résultat type de calcul d'aéroélasticité statique avec CITRON ; un point remarquable est que le surcoût est nul par rapport à un calcul paroi rigide, la réactualisation de la condition au limite de paroi pour l'aéroélasticité accélérant légèrement la convergence de l'algorithme Jameson dans ce cas.

Planche 6 nous présentons des comparaisons de calculs instationnaires avec les mesures sur l'aile LANN (référence 9) pour des mouvements rigides de paroi ; la non

prise en compte de la couche limite explique en partie l'imprécision relative de la position des chocs.

Planche 7 nous montrons une suite de calculs de réponse dynamique sur une dérive, en deçà et au delà de la vitesse Flutter. On compare les résultats des codes TCITRON et EUGENIE, ainsi que le calcul de l'effet d'une protubérance en haut de dérive avec EUGENIE.

Pour une utilisation systématique en analyse de Flutter, supportant des itérations de conception d'un avion, l'utilisation des simulations dynamiques avec C.F.D. non linéaires est confrontée à 2 difficultés :

- Le coût des calculs actuels et mêmes futurs, quand on envisage des analyses d'avion complet avec emports (maillage de l'ordre du million de noeuds) et le balayage d'un domaine assez large de configurations (Mach, altitude, manoeuvres, configurations massiques et emports, ...).

- Le diagnostique précis de l'instabilité de Flutter à partir de l'examen de réponses temporelles, sachant que les méthodes actuelles (méthodes "polyréférences") utilisées pour l'analyse des mesures en vol présument a priori la linéarité des phénomènes et nécessitent des échantillons de mesure de plusieurs centaines de fois la période des modes de vibration surveillés.

C'est le besoin de contourner ces 2 difficultés qui nous a conduits à étudier les méthodes de C.F.D. "linéarisée" que nous présentons maintenant.

3.2 C.F.D. "linéarisée"

Ces méthodes que nous préconisions dans la référence 3 sont maintenant bien défrichées par l'ONERA (voir présentation de G.D.Mortchelevicz dans ce workshop). L'idée directrice est qu'il peut exister autour d'un état d'équilibre statique un domaine de petites perturbations stationnaires ou instationnaires dans lequel les équations C.F.D. sont linéarisables (développement au 1er ordre des termes des équations au voisinage de la solution statique, voir principes en encadré).

Principe général de linéarisation en analyse numérique non linéaire

Système d'équations non linéaires à résoudre initialement

$$① \quad R\,(W, \lambda) = 0$$

W = Vecteur d'état
λ = Vecteur des « paramètres »
(ex. paramètres de formes en C.F.D.)

Souvent on s'intéresse à des quantités s fonctions de W et λ, soit : $② \quad s\,(W, \lambda)$

Petites perturbations au voisinage de la solution de ① et ② $W(\lambda),\ s(\lambda)$

$$\frac{\partial R}{\partial W}\,dW + \frac{\partial R}{\partial \lambda}\,d\lambda = 0 \quad ③$$

$$ds = \frac{\partial \Delta}{\partial W}\,dW + \frac{\partial s}{\partial \lambda}\,d\lambda \quad ④$$

→

$$ds = \left\{\frac{\partial s}{\partial \lambda} - \frac{\partial s}{\partial W}\left[\frac{\partial R}{\partial W}\right]^{-1}\frac{\partial R}{\partial \lambda}\right\} d\lambda$$

ou

$$ds = \left\{\frac{ds}{\partial \lambda} - \left(\left[\frac{\partial R}{\partial W}\right]_t^{-1}\frac{\partial s}{\partial W_t}\right)\frac{\partial R}{\partial \lambda}\right\} d\lambda$$

- Avec la formule ③, la partie coûteuse des calculs est l'opération $\left[\frac{\partial R}{\partial W}\right]^{-1}\frac{\partial R}{\partial \lambda_t}$

$\left[\frac{\partial R}{\partial W}\right]^{-1}$ est « gratuit » si ① a été résolu par méthode de Newton - on a autant de seconds membres que de paramètres λ

- Avec la formule ④, la partie coûteuse des calculs est l'opération $\left[\frac{\partial R}{\partial W}\right]^{-1}\frac{\partial s}{\partial W_t}$ - on a autant de seconds membres que de quantités suivies s

* Nécessite que $R\,(W, \lambda)$ et $s\,(W, \lambda)$ soient continues/dérivables au voisinage du point W, λ (par exemple qu'on ne soit pas très près d'une bifurcation)

Nous développons cette technique à partir de notre outil EUGENIE ; nous présentons planche 8 une comparaison de résultats entre ces méthodes "linéarisées" et des calculs non linéaires "complets".

En instationnaire, on calcule directement dans domaine fréquence l'ensemble des réponses pour des mouvements harmoniques des formes aérodynamiques de base (déformées polynominales avec ELFINI); cela au voisinage d'un équilibre aéroélastique statique calculé en non linéaire ; à partir de là, la suite des calculs de Flutter est menée dans le cadre de l'outil ELFINI-AEROELASTICTY standard.

Une variante de cette approche linéarisée est développée pour le calcul des "sensibilités" (dérivées des performances aérodynamiques par rapport à des paramètres de forme, voir principe en encadré page précédente), en vue d'intégration à notre outil d'optimisation des formes aérodynamiques.

4. CONCLUSION

Nous voyons poindre une nouvelle génération d'outils pour l'aéroélasticité transsonique avec l'utilisation industrielle des codes couplés Eléments Finis élastiques EULER, réellement en support de la conception de nos avions.

Pour le balayage de l'ensemble des configurations de vol, l'organisation des calculs restera proche de l'organisation actuelle ELFINI-AEROELASTICITY.

L'outil EUGENIE "rigide" donne les effets de forme initiale et l'outil EUGENIE linéarisé stationnaire et instationnaire remplacera progressivement les méthodes de singularités pour les effets de mouvements des formes aérodynamiques de base.

Pour les points critiques on approfondira l'analyse par des calculs quasi statiques non linéaires avec couplage direct Elasticité-

Mécanique du Vol - C.F.D. EULER (calcul pas plus coûteux qu'un calcul rigide) ; autour de ces points d'équilibre aéroélastique statique non linéaire la stabilité dynamique (Flutter) sera analysée à partir de forces aérodynamiques instationnaires calculées avec EULER linéarisé.

On fera appel aux méthodes dynamiques non linéaire "complètes" si on redoute des phénomènes engendrant des mouvements de moyennes ou grandes amplitudes comme des oscillations à cycles limites liées aux mouvements de chocs. Il faut cependant noter que, si on travaille en support de la conception des formes, ce type de phénomène pathologique est plutôt à contourner en changeant le dessin qu'à analyser finement ; pour la compréhension "générique" de ces phénomènes, l'outil rapide TCITRON peut être pratique.

Un point important à traiter est la prise en compte des phénomènes visqueux, pour l'instant on effectue en statique une correction de la forme paroi de l'épaisseur de couche limite en jouant sur la condition de transpiration ; la validité de cette approche est à vérifier pour les calculs instationnaires, linéarisés ou non.

Nous développons aussi, à plus longue échéance, le couplage aéroélastique avec les codes Navier-Stokes instationnaires, les premières applications visées sont les interactions entre structure et écoulement décollé.

REFERENCES

1. C. PETIAU, S. BRUN
    Tendances Actuelles de l'Analyse Aéroélastique des Avions Militaires. AGARD conférence proceedings n° 403 - Athènes 1986

2. Ph. NICOT, C. PETIAU
    Aeroelasticity Analysis using Finite Elements Models
    Proceedings of European Forum ou Aeroelasticity : Aix la Chapelle 1989 - Edited by DGUR

3. C. PETIAU
    Aéroélasticité et Vibrations des Structures, Etat de l'Art et Tendances
    Forum International Aéroélasticité et Dynamique des Structures AAAF Strasbourg 1993

4. C. PETIAU & M. DE LAVIGNE
    Analyse Aéroélastique et Identification des Charges en Vol. AGARD conferences proceeding n° 375 - « Operational Loads Data » - Sienne 1984

5. C. PETIAU, Ph. NICOT
    A General Method for Mathematical Model Identification in Aeroelasticity. International Forum on Aeroelasticity and Structural Dynamics, Royal Aeronautical Society - Manchester 1995

6. A. JAMESON & D.A. CAUGHEY
    A Finite Volume Method for Transonic Potential Flow Calculations. AIAA Paper 75-635

7. S. GUILLEMOT & J.P. ROSENBLUM
    Modélisation d'Ecoulements Instationnaires par une Approche Potentielle Non-Conservative en Différences Finies. Dassault Aviation Document DGT n° 36172

8. A. DERVIEUX, L. FEZOUI, M.P. LECLERCQ, and B. STOUFFLET
    A General upwind Formulation for Compressible Flows on Multi-Element Meshes, in Numerical Methods for Fluid Dynamics 4, M.J. Baines and K.W. Morton eds., Oxford Science Publications, 1993

9. AGARD CP 374
    Transonic Unsteady Aerodynamics and its Aeroelastic Applications

Planche 1

Maillage général d'un avion de combat

Réponses des jauges de contrainte en vol
Comparaison calcul-essais
(manoeuvre de tonneau)
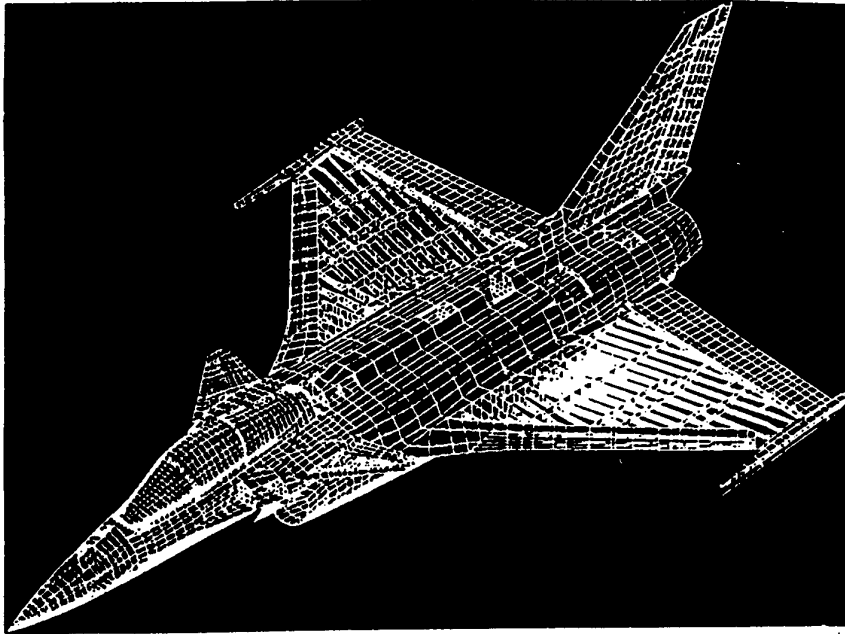
Déformées
aéroélastiques
Mach 0,9

Emplanture dérive

Facteur de charge 9g
x 5
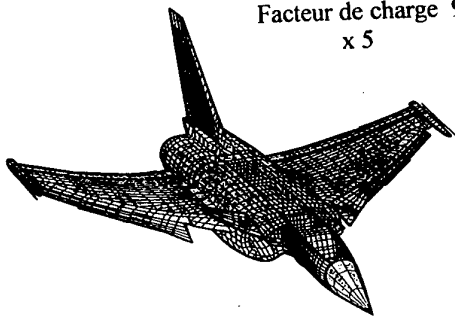
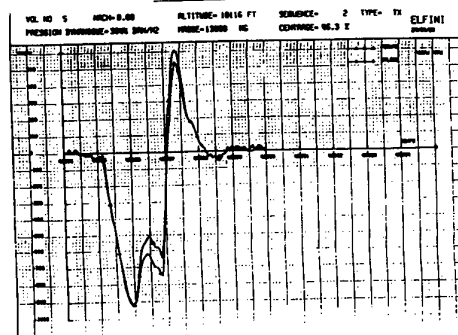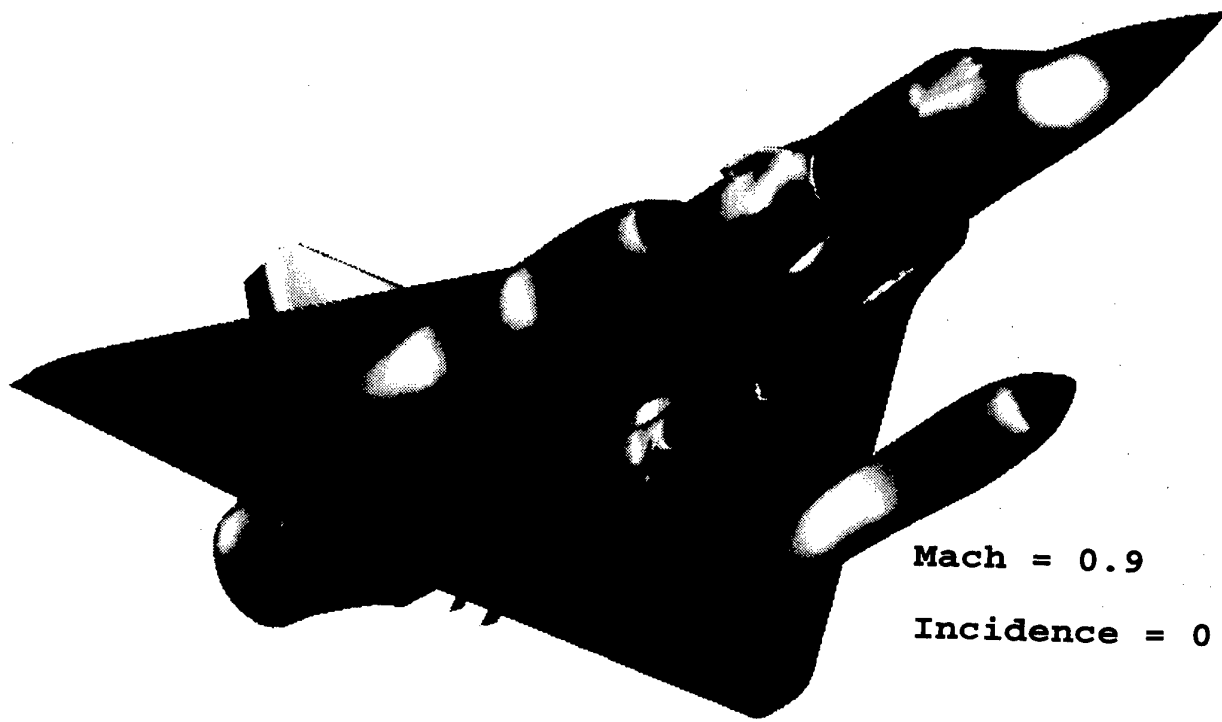Rail de bec de B.A.

Roulis stabilisé 260°/s
x 8
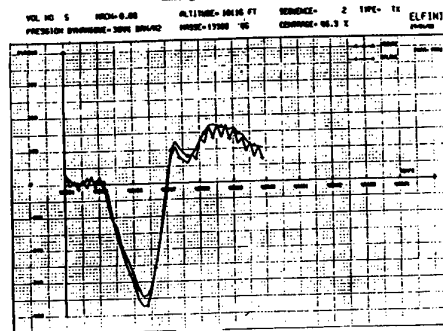
PLANCHE 2
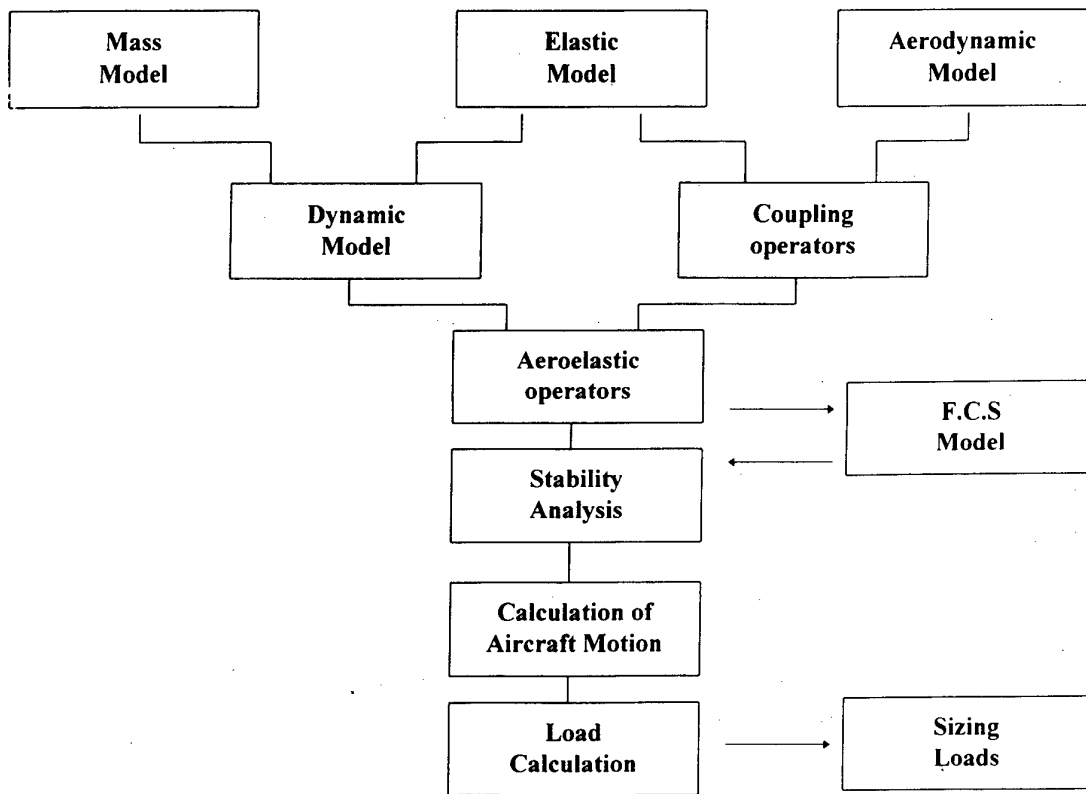CALCULS EULER AVION COMPLET

Mach = 0.9

Incidence = 0
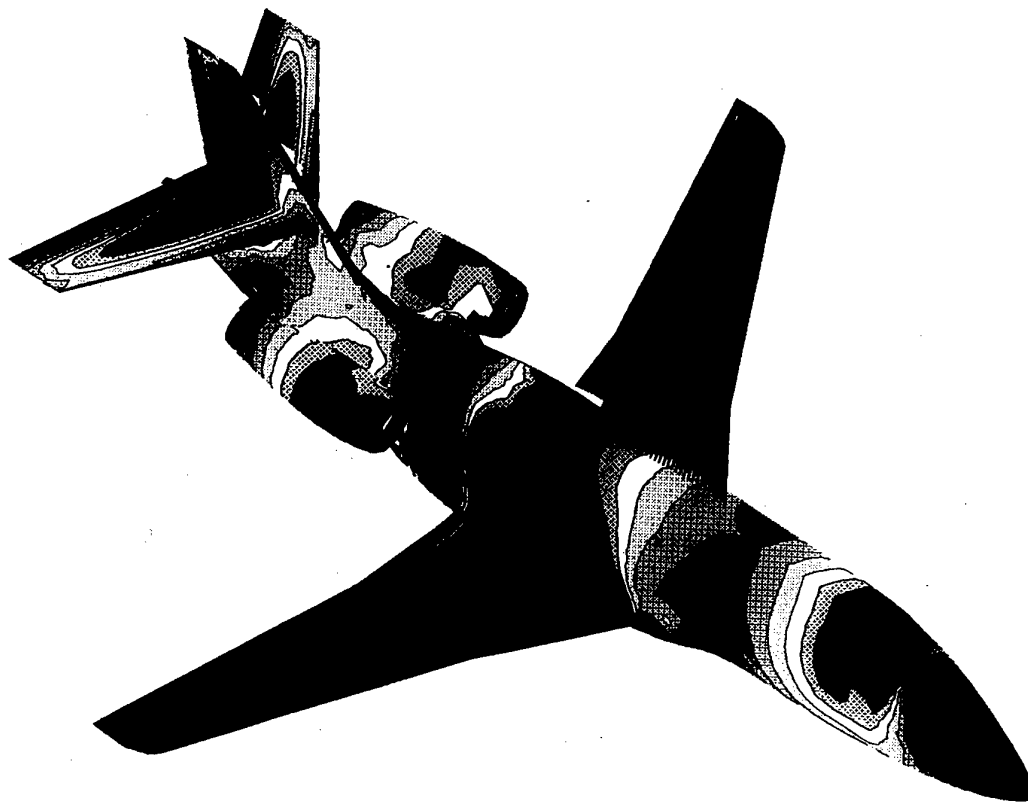
PLANCHE 3

« ELFINI AEROELASTICITY » ORGANIZATION
(DIRECT COUPLING OF STRUCTURE F.E.A. AND C.F.D. TOOLS)

```
┌──────────┐      ┌──────────┐      ┌──────────────┐
│  Mass    │      │ Elastic  │      │ Aerodynamic  │
│  Model   │      │  Model   │      │   Model      │
└──────────┘      └──────────┘      └──────────────┘

        ┌──────────┐          ┌──────────┐
        │ Dynamic  │          │ Coupling │
        │  Model   │          │operators │
        └──────────┘          └──────────┘

              ┌──────────────┐
              │  Aeroelastic │         ┌──────────┐
              │  operators   │ ──────▶ │  F.C.S   │
              └──────────────┘         │  Model   │
              ┌──────────────┐ ◀────── └──────────┘
              │  Stability   │
              │  Analysis    │
              └──────────────┘
              ┌──────────────┐
              │ Calculation of│
              │ Aircraft Motion│
              └──────────────┘
              ┌──────────────┐         ┌──────────┐
              │    Load      │ ──────▶ │  Sizing  │
              │ Calculation  │         │  Loads   │
              └──────────────┘         └──────────┘
```

PLANCHE 4
COMPARAISONS CALCUL - VOL
(EFFETS DE FORME INITIALE ET DE MOUVEMENT RIGIDE CALCULE PAR EULER)

alpha = 1 rad
mx voilure (m3)

calcul Euler
recalage

alpha = 1 rad
my voilure (m3)

calcul Euler
recalage

alpha = 1 rad
x voilure (m)

calcul Euler
recalage

alpha = 1 rad
y voilure (m)

calcul Euler
recalage

alpha = 1 rad
fz voilure (m2)

calcul Euler
recalage
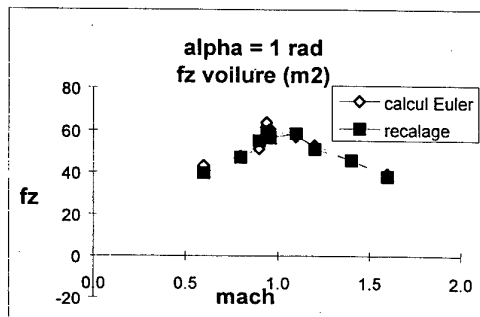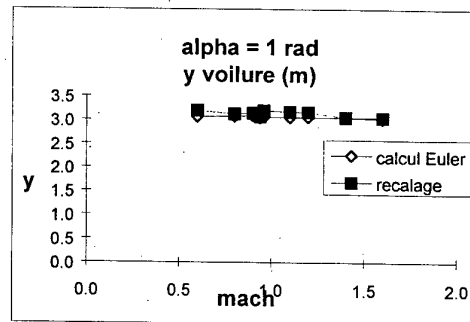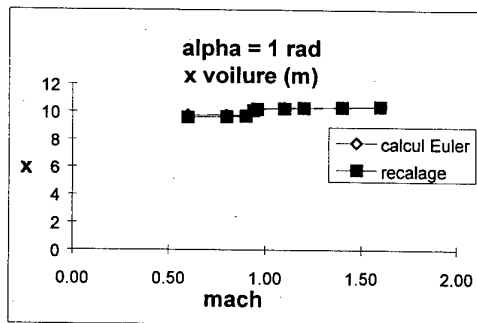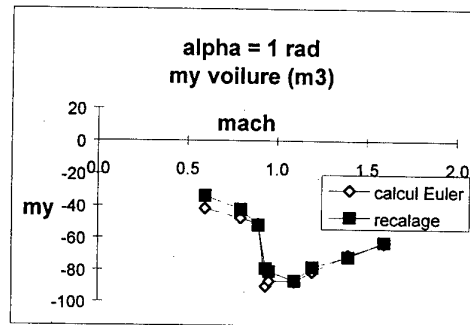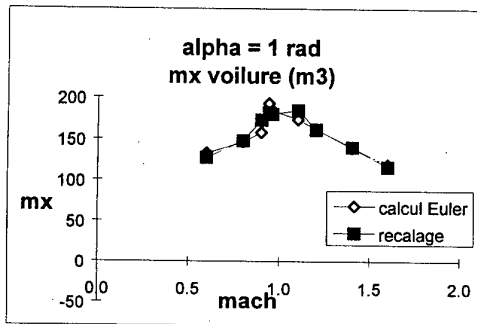
PLANCHE 5
AEROELASTICITE STATIQUE AVEC CITRON
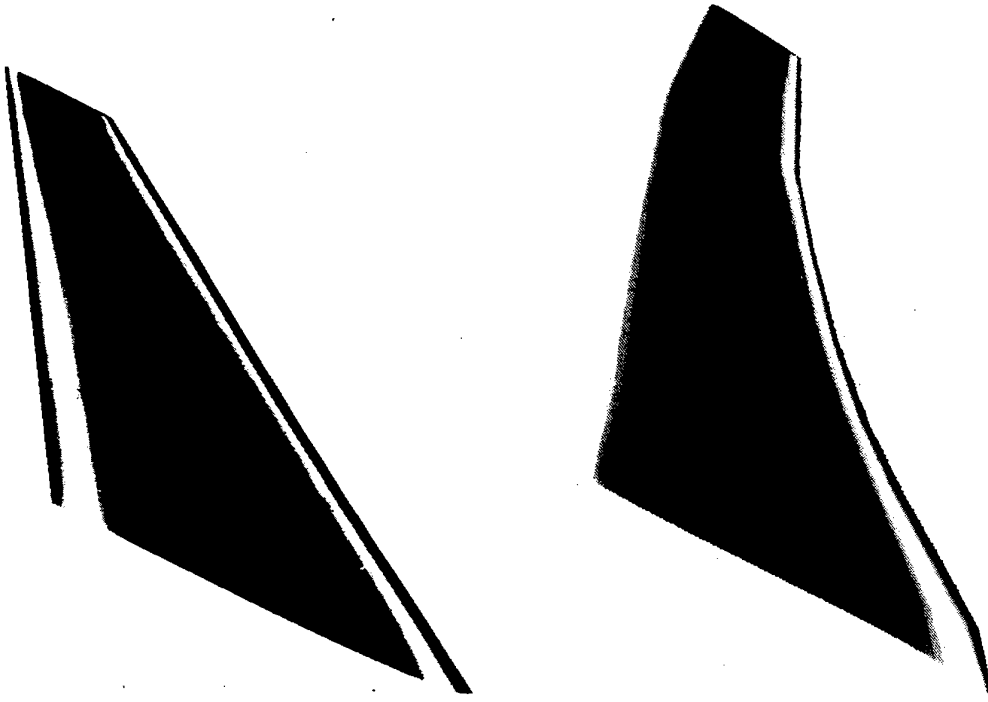
Calcul	Type de convergence	Arrêt après	Temps moyen
Sans Couplage	convergence ➢	236 Iters	64.9s
Avec Couplage	convergence ➢	216 Iters (**-8.5%**)	62.1s (**-4.3%**) ☺

Tableau 2 : Temps CPU d'un calcul Citron avec et sans couplage, avec écriture sur fichier. Conditions : M=0.8. Inc=3 deg. PSA= 1Atm. Frequence de Couplage = 20 Iters. Critère de convergence = 5e-6 . Calcul sur un noeud du SP2.

✍ Le Couplage Aéroélastique n'implique pas de coûts supplémentaires.

PLANCHE 6
COMPARAISONS AILE LANN
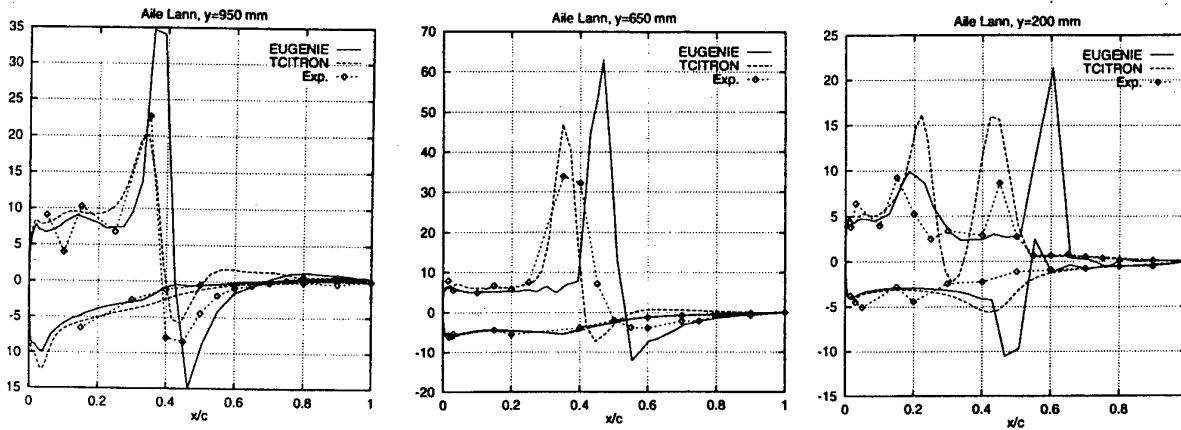
Partie réelle des K_p complexes (aile Lann), $M_\infty = 0.822, f = 24hz$
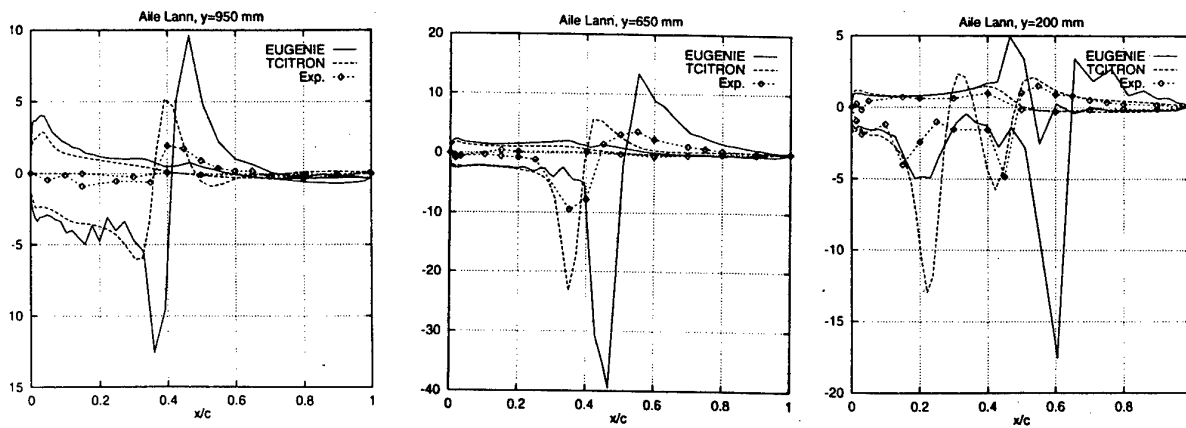
Partie imaginaire des K_p complexes (aile Lann), $M_\infty = 0.822, f = 24hz$

PLANCHE 7
COUPLAGE DYNAMIQUE AVEC C.F.D. NON LINEAIRE
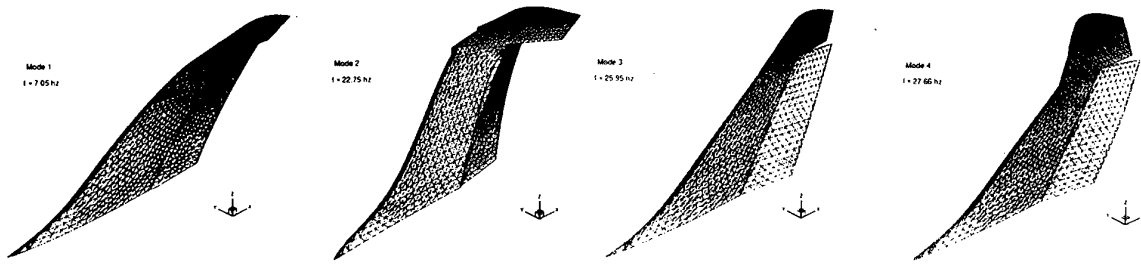
Modes structuraux 1 à 4, dérive sans pod de contre-mesure
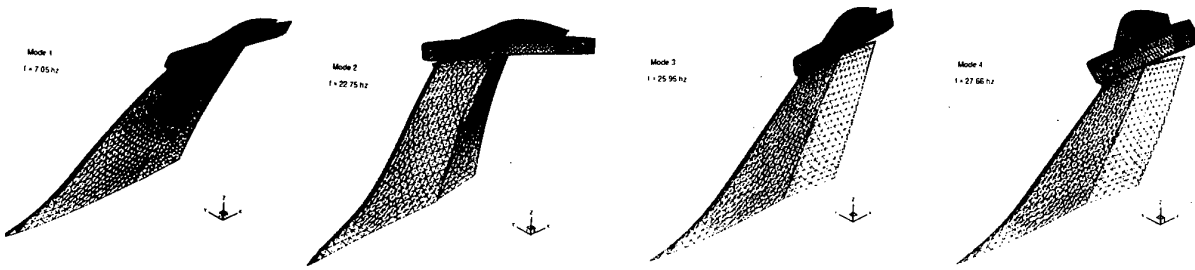
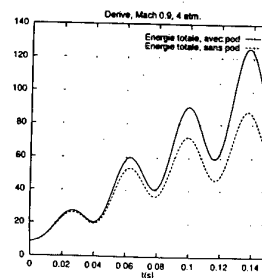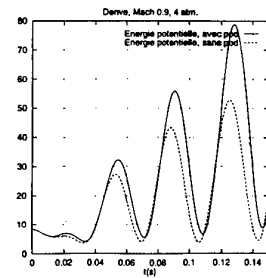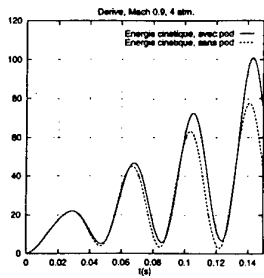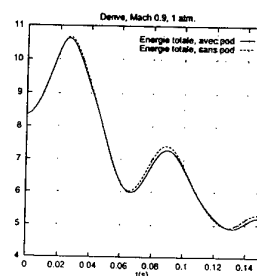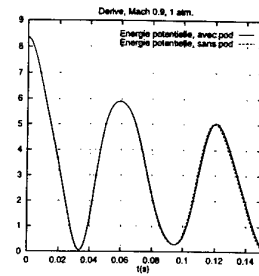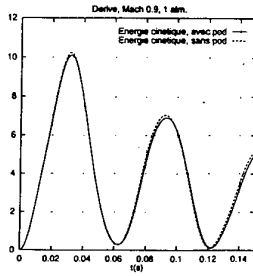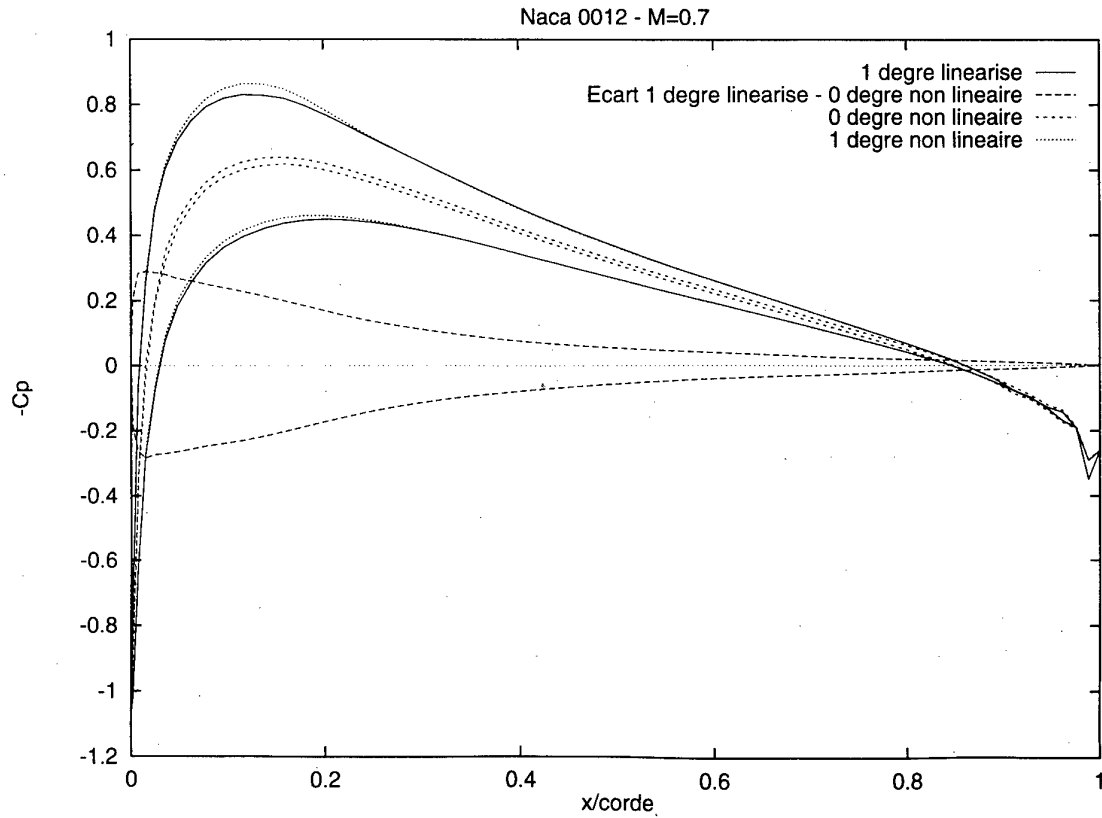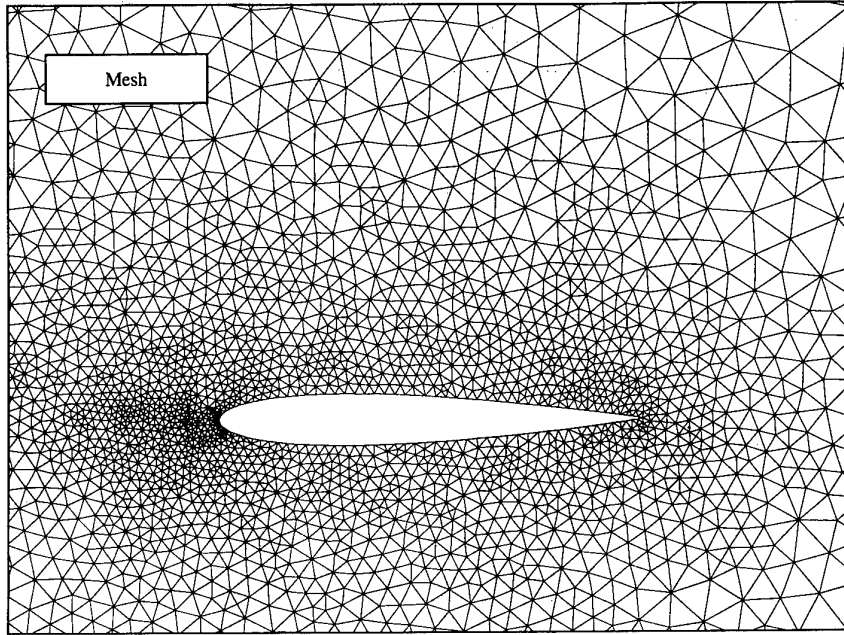Modes structuraux 1 à 4, dérive avec pod de contre-mesure

PLANCHE 8
C.F.D. LINEARISEE

Centered Peraire-Stoufflet (second order) - given incidence

(3469 Nodes ; 6807 Elements)

(122 Steps ; .0000E+00 Run Time)

Mesh

Naca 0012 - M=0.7

1 degre linearise ———
Ecart 1 degre linearise - 0 degre non lineaire -----
0 degre non lineaire ·······
1 degre non lineaire ········

-Cp

x/corde

Application of the ENS3DAE Euler/Navier-Stokes Aeroelastic Method

David M. Schuster
NASA Langley Research Center
Aeroelasticity Branch, MS 340
Mail Stop 371, Hampton, Virginia 23681-0001 USA

Philip S. Beran
Air Force Institute of Technology
Wright Patterson AFB, Ohio 45433-7542 USA

Lawrence J. Huttsell
Air Force Research Laboratory
Wright Patterson AFB, Ohio 45433-7542 USA

SUMMARY

This paper discusses recent applications of the ENS3DAE computational aeroelasticity method. In particular, it describes aeroelastic and unsteady aerodynamics calculations performed on wings with trailing edge control surfaces. These simulations include the investigation of control reversal for a structurally flexible wing with a deflected control surface, and a static and dynamic analysis of a rigid wing with an oscillating control surface. The two sets of calculations were performed independently on different wings using different grid topologies. The control reversal simulation represents an inviscid Euler static aeroelastic analysis of a thin wing with a rectangular planform. The geometry of this wing makes it suitable for computations using more approximate, inviscid aerodynamics methods. Thus, the results of the present Euler computations are compared with numerical data generated by a validated computational aeroelasticity code which uses a simpler aerodynamic formulation. The second illustrated case involves the simulation of a significantly more complex flowfield and the static and dynamic analyses of this geometry were performed using the viscous Navier-Stokes equation option in ENS3DAE. Results of both the steady and unsteady calculations on this wing are compared with existing experimental data.

INTRODUCTION

The ENS3DAE aeroelastic method[1] has been in development and use since 1989 when it was delivered to the Air Force Wright Laboratory by the then Lockheed Aeronautical Systems Company. Since that time, a number of static and dynamic, rigid and aeroelastic test cases have been analyzed using the program and the code has been validated against existing computational and experimental data. Research using the code has focused on applying the method to problems whose geometric and/or aerodynamic complexity are suited to analysis using the Euler/Navier-Stokes equations[2,3]. Flows involving shock waves interacting with boundary layers, generation of vortices and separated boundary layers are among those that can and should be addressed using this class of method. These types

of flows can be generated by vehicles operating deep in the transonic speed regime or at high angles-of-attack, or simply by geometric anomalies in the surface of the vehicle. An example of this latter mechanism is a deflected control surface.

Nonlinear aeroelasticity with control surface deflection has been investigated by Batina, et al.[4] and Guruswamy and Tu[5], both using inviscid transonic small disturbance potential flow theory as their aerodynamic basis. Pitt and Fuglsang[6] also investigated aileron reversal using this type of method. These simulations were performed on wings with thin airfoil sections and control surface deflections of one-half degree or less, thus avoiding violation of the inviscid small disturbance assumptions inherent in the aerodynamic analysis. The first application described in this paper examines the static aeroelastic deformation of a thin wing with a small control surface deflection. Control effectiveness and reversal is predicted using the Euler equation option of ENS3DAE and results are compared with those of Andersen, et al.'s[7] CAP-TSD[8] transonic small disturbance equation analyses.

Larger control surface deflections and thicker wing sections require higher-order aerodynamic simulations since inviscid methods classically overpredict the effectiveness of the control surface for these cases. Under these conditions, strong shocks and separated flow can form on the control surface. In addition, the sharp edges of the control surface combined with its increased loading can form local vortices which can interact with the rest of the lifting surface flowfield. In general, prediction of these features requires a viscous simulation. Obayashi[9,10] has investigated a semispan wing and a full-span wing/fuselage configuration with oscillating control surfaces using three-dimensional Navier-Stokes aerodynamics. Both of these simulations modeled a thin wing with a trailing edge control surface. The full-span computations involved large control surface deflections, and complex interactions between the wing and control surface vortices were observed. The second case presented in this paper uses ENS3DAE to perform a viscous calculation for a wing with a simpler planform and a thick

airfoil section. Both static and oscillating trailing edge control surface deflections are simulated, and the unsteady computations are performed at a much lower reduced frequency than the referenced computations. These computations are compared with experimental benchmark data. Of particular importance are detailed comparisons of the unsteady pressure distributions due to control surface oscillation with unsteady experimental pressure data.

ENS3DAE AEROELASTIC METHOD

ENS3DAE solves the full three-dimensional compressible Reynolds averaged Navier-Stokes equations using an implicit central finite difference approximate factorization algorithm. The method accepts either single or multiple block curvilinear grid topologies and can be run in a steady state or time-accurate mode. Turbulence characteristics are predicted using the Baldwin-Lomax algebraic turbulence model or the Johnson-King model. For the present calculations, the Baldwin-Lomax model is used with transition assumed to be at the leading edge of the wing. A multigrid option for steady flows has recently been added to the method and the code has been explicitly written to take advantage of vectorization. Directives for parallel operation on shared memory processors are also included in the programming.

A linear generalized mode shape structural model is closely-coupled with the aerodynamic method to analyze structurally flexible vehicles. Since dynamic aeroelastic and oscillating control surface simulations require grid models that deform in time, a Geometric Conservation Law (GCL) patterned after that recommended by Thomas and Lombard[11] has also been incorporated in the code.

In the interest of brevity, the details of the numerical algorithm will not be discussed in this paper, and the reader is referred to Reference 1 and Reference 2 for a detailed description of the method.

WING GEOMETRIES

The wing geometries chosen for these studies are shown in Figure 1. Both have a rectangular planform and constant airfoil section from root to tip with no twist. The wing used for the static aeroelastic calculations is patterned after the so-called heavy Goland wing.[12] In this paper, the wing is simply referred to as the rectangular wing. This wing has a semispan of 20 feet and a chord of 6 feet. It includes a 25% chord trailing edge control surface, designated by the shaded area in the figure, that extends from the wing midspan to the tip. The airfoil for this wing is a 4% thick symmetrical parabolic arc section.

The oscillating control surface case was performed on the NASA Langley Benchmark Active Controls Technology (BACT)[13] wing. The BACT model is also a rectangular wing with a NACA 0012[14] airfoil section. The wing has a semispan of 32 in., and a chord of 16 in. It is fitted with a trailing edge
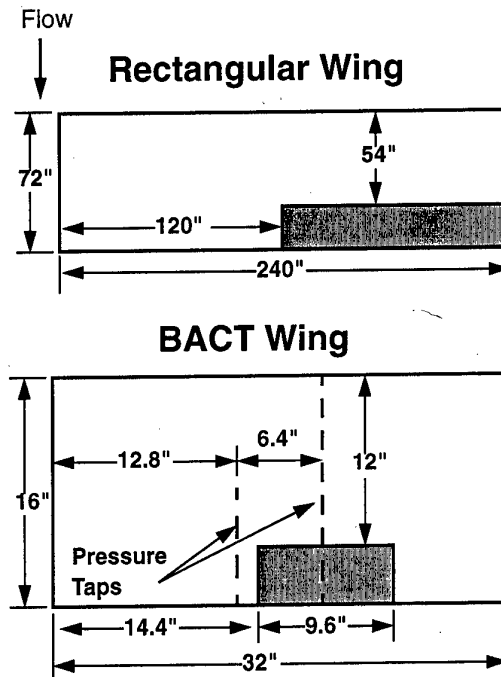

Figure 1.   Planform views of rectangular and BACT wings.

control surface which extends from 45% span to 75% span and has a chord of 25% of the wing chord. The wind tunnel model also had upper and lower surface spoilers which are not depicted in the figure and were not simulated in this analysis. Experimental data for this wing included overall wing forces and moments as well as unsteady pressures. A row of pressure taps were located on the upper and lower surfaces of the wing at 60% span, which coincides with the spanwise center of the aileron. Pressures were measured from the wing leading edge to the trailing edge at this wing station. In addition, a second row of pressures were located at 40% span. At this location, upper and lower surface pressures were measured from 60% chord to the wing trailing edge.

Geometry Modeling and Grid Generation

Due to the differences in airfoil section, different grid topologies were used to model the two wings. Since the rectangular wing has a thin sharp-edged airfoil, a multizone H-H grid topology is employed for this lifting surface. A planform view of the grid for this configuration is shown in Figure 2. This figure is arranged vertically so that the wing root is at the bottom of the figure and the wing tip is at the top. The wing is modeled using two grid zones, one for the flowfield above the wing surface and the other below the wing.

Each zone consists of 120 points in the streamwise direction with 61 points distributed from the wing leading edge to the trailing edge. There are a total of 41 spanwise points with 33 of those stations extending from the wing root to the wing tip. Each zone uses 50 points normal to the wing surface to
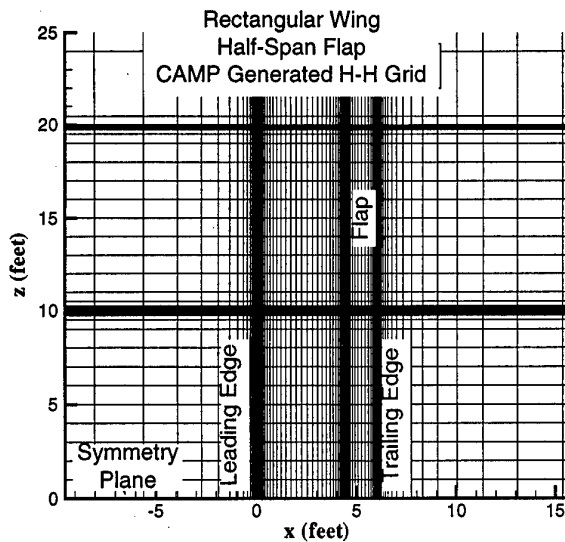
Figure 2. Planform view of rectangular wing grid.

complete the flowfield model. Thus a total of 492,000 grid points are used for this Euler simulation. The spanwise distribution of points was taken from the CAP-TSD grid used in Reference 7 so that a direct comparison could be made between ENS3DAE and CAP-TSD.

Figure 3 displays a section of the H-grid through the middle of the flap on the rectangular wing with the flap deflected one degree. Grid points are clustered at the wing section leading and trailing edge as well as near the control surface hinge line. The first grid line parallel to the airfoil surface is placed 0.0025 chords from the surface which is sufficiently close to the wing for the inviscid calculations to be performed on this geometry.
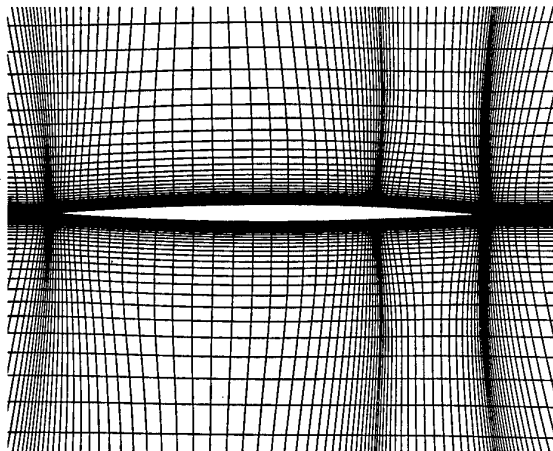

Figure 3. H-grid through rectangular wing section.

Since the BACT wing has a blunt leading edge, twelve percent thick airfoil section, a C-H grid topology is used to model this configuration. This grid consists of a total of 332,469 grid

points distributed with 153 points in the wraparound or "C" direction, 53 points in the spanwise, or "H" direction, and 41 points from the wing surface to the outer boundary. An isometric view of the BACT surface grid with the aileron deflected -5° is presented in Figure 4. The grid lines are placed in the spanwise direction so as to accurately define the edges of the trailing edge control surface. In addition, there is a grid line precisely at 40% and 60% span so that a direct comparison can be made with available experimental data. The streamwise distribution of grid points is also tailored to accurately model the aileron hinge line.
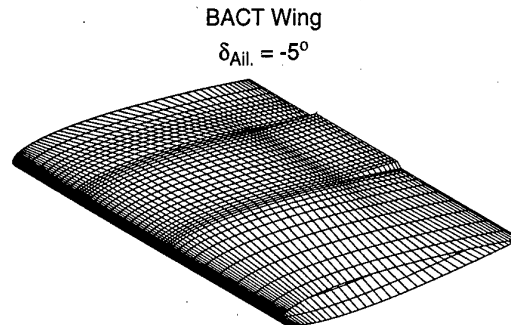

Figure 4. Isometric view of BACT wing surface grid, $\delta_{Ail.}$ = -5.0°.

A side view of the viscous grid through the 60% span station is shown in Figure 5. The nominal wall spacing normal to the wing surface is 0.0002 chords at the leading edge, linearly increasing to 0.003 chords at the trailing edge. This spacing generates y^+ values less than 6 over the entire surface of the wing. This ensures that at least one grid point will be within the laminar sublayer of the boundary layer, which is required for accurate application of the turbulence model. The aileron deflection for the static cases is obtained by preprocessing the airfoil sections used to define the wing surface. A rigid body rotation of the trailing edge portion of the airfoil sections at the inboard and outboard edges of the control surface is performed to define new airfoil contours at these wing stations. The airfoils just inboard and just outboard of the aileron are left unchanged. The flowfield grid is then generated about this modified geometry using the same techniques as for the case where the aileron is not deflected. This effectively shears the baseline grid in the vicinity of the aileron to define the deflected control surface geometry. This method is simple and very efficient to implement. However, it results in a model which does not have gaps between the control surface and the main wing. This is not a significant problem in this analysis since these gaps are very small on the BACT model. This approximation also is more significant when large control surface deflections are to be simulated, but in this analysis our deflections have been limited to five degrees or less.

For cases where the aileron is oscillated, a mode shape describing the aileron deflection is input directly into the ENS3DAE program. The undeflected grid is used as the basis for the aerodynamic solution. The grid is deformed in time by
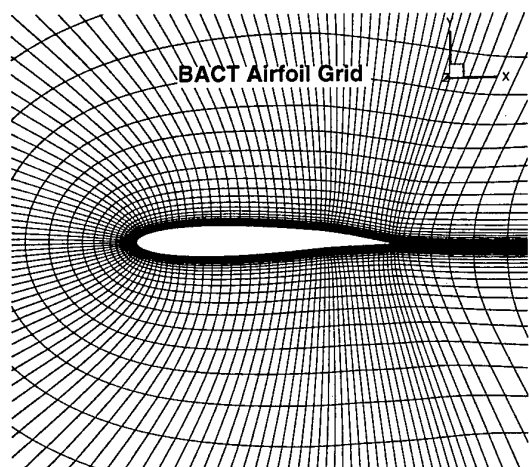
Figure 5.   BACT airfoil section grid, $\delta_{Ail.} = 5.0°$.

superimposing the aileron deflection mode shape on the baseline grid and using ENS3DAE's built-in grid motion capability to deflect the grid. Again, this method effectively shears the grid in the vicinity of the aileron and control surface gaps are not simulated. The mode shape is also defined as a deflection only in the vertical direction, so the chord of the control surface is stretched as the aileron is deflected. For small deflections, this stretching is negligible.

RESULTS

Static Aeroelastic Analysis of the Rectangular Wing

The rectangular wing was analyzed using the inviscid Euler equation option in ENS3DAE. The flow conditions for the analysis are Mach 0.7, zero degrees angle-of-attack and a static control surface deflection of one degree. The beam structural model of Reference 7 was used for all structurally flexible calculations performed on this wing.

An initial static rigid calculation was performed at the reference conditions to establish a basis for aileron control effectiveness. A series of structurally flexible simulations were then performed at steadily increasing dynamic pressure. The rolling moment at each dynamic pressure was computed and the ratio of the flexible rolling moment to the rigid rolling moment was calculated. A plot of this ratio as a function of dynamic pressure is presented in Figure 6. Included on this figure are CAP-TSD results from Reference 7. Control reversal occurs when the control effectiveness ratio becomes negative, as shown in the figure. ENS3DAE predicts a control reversal dynamic pressure of approximately 310 pounds per square foot (psf) compared to CAP-TSD's prediction of 335 psf or an eight percent difference. The ENS3DAE and CAP-TSD results were computed with the same spanwise grid distributions, and similar streamwise grid point distributions. However, ENS3DAE's vertical grid resolution in the vicinity of the wing surface was finer than that used in the original CAP-TSD analysis shown as the upside down triangles in the figure. The CAP-TSD computation was rerun for dynamic pressures of

250 and 300 psf using the Euler analysis normal grid distribution. These results are shown as the diamonds in the figure. For this grid, CAP-TSD predicts an estimated reversal dynamic pressure of 319 psf which compares to within three percent of the Euler results. These results illustrate that grid refinement plays a significant role in this analysis and further investigation into these effects are under way.

Figure 7 compares the ENS3DAE and CAP-TSD pressure distributions as a function of the streamwise coordinate along the midspan of the flap for the 300 psf dynamic pressure. The Euler analysis is depicted by the solid line, while the CAP-TSD analysis is shown by the symbols. These pressure distributions were chosen since they are near the point of reversal. The CAP-TSD and Euler calculations compare very closely for this case, as would be expected for this configuration at these flight conditions. In general, the Euler analysis predicts sharper, deeper pressure peaks in the vicinity of the wing leading and trailing edges, and at the control surface hinge line. These results provide confidence that the ENS3DAE method is predicting accurate results for relatively benign flight conditions, and we are ready to apply the method to more challenging problems. Transonic and low supersonic calculations are currently being computed using ENS3DAE, and these data will be similarly compared with CAP-TSD results.

BACT Wing Static Analyses

Static and dynamic rigid calculations were performed on the BACT wing with ENS3DAE providing viscous full Reynolds-averaged Navier-Stokes simulations. These calculations were compared with experimental data acquired in heavy gas in NASA Langley Research Center's Transonic Dynamics Tunnel (TDT). The nominal flight conditions for these calculations are Mach 0.77 and a Reynolds number of 280,000/ft., which coincide with the test data acquired in the TDT.

Prior to computing the flowfield for the wing with the deflected aileron, a number of calculations were performed on the basic wing without control surface deflection. Inviscid Euler and viscous Navier-Stokes calculations were performed on the wing for both nonlifting and lifting cases. Detailed description of the Euler computations have been omitted from this discussion, but there are several notable features of the Euler analysis which should be addressed. As expected, shock strength was greater for the inviscid calculations, and the shock was displaced aft of the viscous analysis. Viscous effects were also clearly visible in the surface pressure distribution near the trailing edge of the wing. In this region, the inviscid pressures recovered to a significantly higher stagnation pressure than their viscous counterparts. This difference is due to the thickening of the boundary layer near the trailing edge, which tends to flatten the curvature of the airfoil in this region. This effect is even more pronounced when the control surface is deflected, and is the primary reason why inviscid methods cannot generally be applied to this problem.
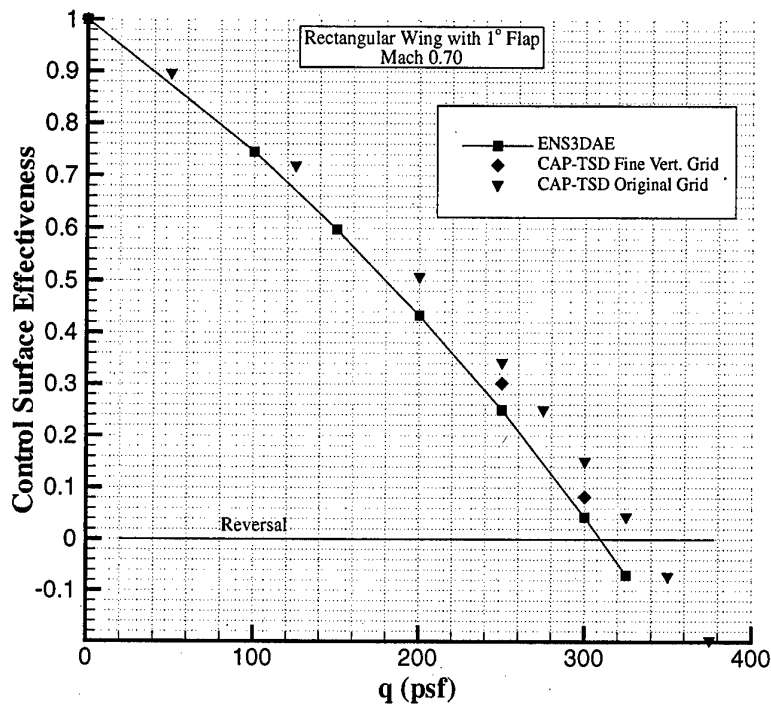
Figure 6. Aileron control effectiveness as a function of dynamic pressure for the rectangular wing, M=0.7, α=0.0°, $\delta_{Ail.}$=1.0°.
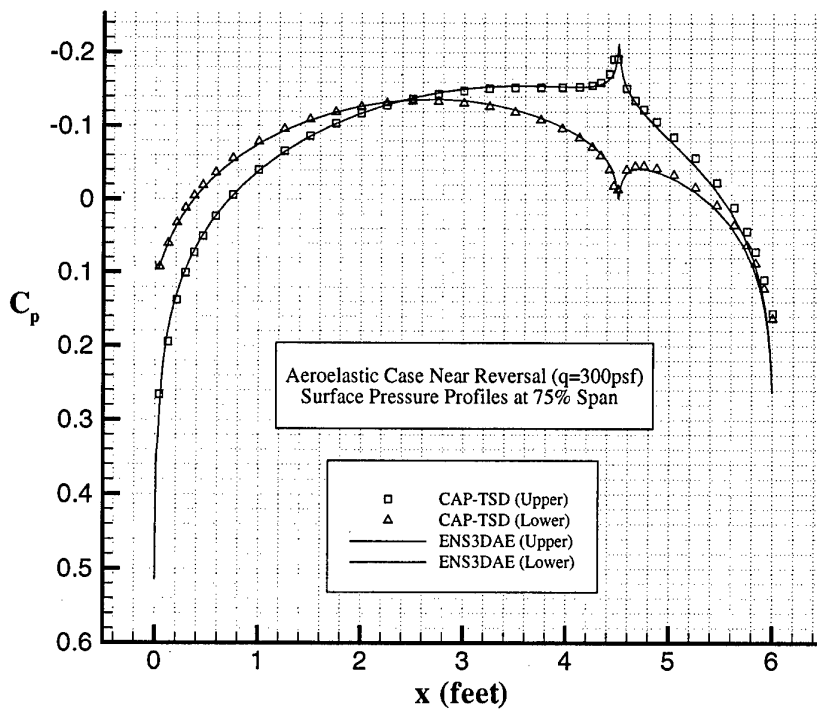

Figure 7. Rectangular wing pressure distribution near reversal, M=0.7, α=0.0°, $\delta_{Ail.}$=1.0°, q=300 psf.

Figure 8 presents the viscous computation of the flow at M=0.77, and zero degrees angle-of-attack. For this nonlifting case, the computations compare relatively well with the experimental data acquired in the TDT. The theory predicts a slightly lower pressure on the forward portion of the wing at the 60% span station, but the pressures on the remainder of the wing are in good agreement with the experimental data.

ENS3DAE calculations are compared with experimental data at M=0.77 and α=3° in Figure 9. At these conditions, a shock on the upper surface is clearly visible in both the theoretical and experimental data. The lower surface pressure distribution and the pressures behind the shock are accurately predicted by the theory. However, the pressure distributions do not compare well on the forward portion of the wing upper surface. This area is usually insensitive to viscous effects since the boundary layer is thin and the flow is experiencing a favorable pressure gradient. However, a sharp increase in the experimental pressure is observed on the 60% span upper surface at 5% chord. This sudden increase is speculated to be due to the transition strip on the model, and the strip could be affecting the flow downstream. The theory accurately predicts the pressure forward of 5% chord. A second possibility for this poor correlation is aerodynamic interactions between the model and the wind tunnel which are not accounted for in the analysis. In addition to the wind tunnel walls, there are several model support components including a splitter plate, and an instrumentation housing which add to the blockage of the tunnel. All computations to date have been performed without modeling the wind tunnel walls or support structure.

Static calculations were also performed with aileron deflection. Figure 10 shows the pressure distribution for an ENS3DAE Navier-Stokes calculation at M=0.77, α=0.0°, and $\delta_{Ail.}$=5.0°. At these conditions, lift is generated by the wing due to the flap deflection. Once again, the theoretical and experimental pressures agree well on the aft portion of the wing, and on the entire lower surface. However, as with the previous lifting cases, the upper surface pressure on the forward portion of the wing does not agree well with the experimental data. The theory predicts a consistently lower pressure on this part of the wing.

ENS3DAE was run for a total of 2000 iterations for these steady Navier-Stokes analyses, and the L-2 norm of the density residual is reduced by approximately 2.5 orders of magnitude during this period. By iteration 2000, oscillations in the lift and pitching moment coefficient have reduced to a very small amplitude and can be considered at a steady state for this analysis. Noticeable oscillations in the drag coefficient were still present at this point in the solution. To further investigate the convergence characteristics of this problem, a viscous solution at α=2° was run a total of 4000 iterations and the drag was shown to reach a steady state at approximately 2500 iterations. The differences in the pressure distributions between 2000 and 4000 iterations were virtually indiscernible. Therefore, for the purposes of this study, all static simulations were assumed to be at a steady state after 2000 iterations.

BACT ENS3DAE Analysis
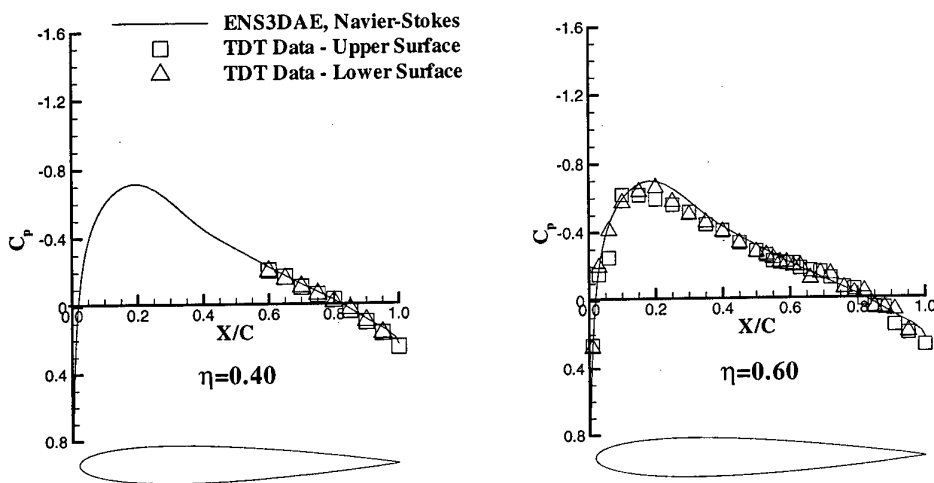## M=0.77, α=0.0°, $\delta_{ail.}$=0.0°

Figure 8.   Steady viscous pressure distribution on BACT wing at M=0.77, α=0.0°, $\delta_{Ail.}$=0.0°.

BACT ENS3DAE Analysis
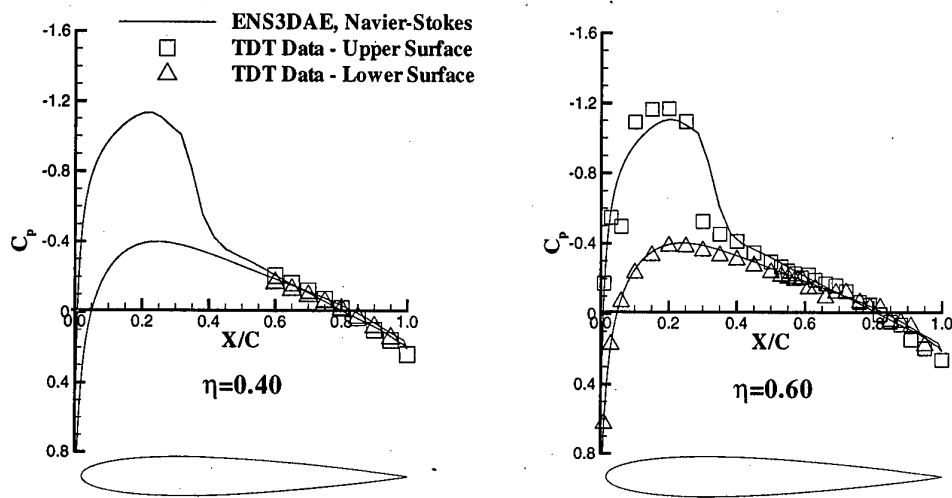## $M=0.77$, $\alpha=3.0^\circ$, $\delta_{ail.}=0.0^\circ$

Figure 9.   Steady viscous pressure distribution on BACT wing at
M=0.77, α=3.0°, $\delta_{Ail.}$=0.0°.

BACT ENS3DAE Analysis
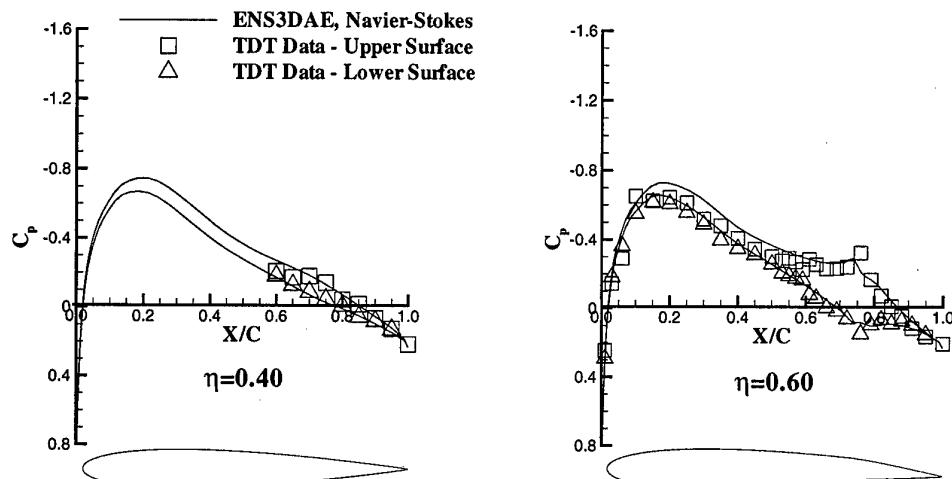## $M=0.77$, $\alpha=0.0^\circ$, $\delta_{ail.}=5.0^\circ$

Figure 10.   Steady viscous pressure distribution on BACT wing at
M=0.77, α=0.0°, $\delta_{Ail.}$=5.0°.

Unsteady Analysis of BACT Wing with Oscillating Aileron

Unsteady simulations have been performed by harmonically oscillating the BACT aileron at a specified frequency. The unsteady computations are performed by using a steady solution about the baseline condition without aileron deflection, then impulsively starting the aileron oscillation. The solution is allowed to run until a total of three cycles of aileron oscillation are completed. For the simulations presented in this paper, the aileron is oscillated sinusoidally with an amplitude of two degrees at a frequency of five Hertz (Hz), which corresponds to a reduced frequency of 0.056 based on wing semichord.

An initial calculation was performed using a nondimensional time step of 0.1172 which for this problem is a CFL number of approximately 90 based on the global minimum time step for this grid. This CFL number is well beyond where we had previously run the code, and we felt that these conditions might be near the algorithm's stability limit. With this time step, one cycle of aileron oscillation at 5 Hz requires 10,000 time steps. Thus, it required 30,000 time steps to complete the three cycles of motion. Once this initial transient was successfully completed, we searched for the largest time step we could take and have the code remain stable. We were ultimately able to double the time step to 0.2344, which gave us a CFL number of 180 and reduced our run time to 5,000 time steps per cycle of aileron oscillation. Upon comparing these two analyses, no noticeable differences in the results were observed.

Figure 11 shows the unsteady pressure at 60% span and 23% chord for the 5,000 time step per cycle simulation. The pressure is plotted against nondimensional time, and the aileron deflection angle as a function of time is included at the bottom of the figure. Following an initial transient due to the impulsive start of the aileron oscillation, the pressure at this station quickly becomes sinusoidal and by the end of the first cycle of aileron oscillation, it has stabilized into a clean periodic form. The pressure distributions due to the second and third cycles of aileron motion are virtually identical giving us good confidence that the solution has reached a stable periodic response by the end of the second cycle of aileron deflection. Pressure distributions at other wing stations show similar character.

The unsteady pressures at the 40% and 60% span station were analyzed by taking the Fast Fourier Transform (FFT) of the pressures during the third cycle of aileron motion and scaling the real and imaginary components by the amplitude of the aileron deflection. In the following figures, the real component of the unsteady pressure represents the pressure perturbation that is in-phase with the aileron motion, while the imaginary component represents the pressure perturbation whose phase lags the aileron motion by ninety degrees. In addition, the mean pressure coefficient has also been extracted from the unsteady pressure.

BACT Unsteady Pressure Data
M=0.77, α=0.0°, $\delta_{Ail.}$=2.0°, f=5 Hz.
X/C = 0.23, η=0.60

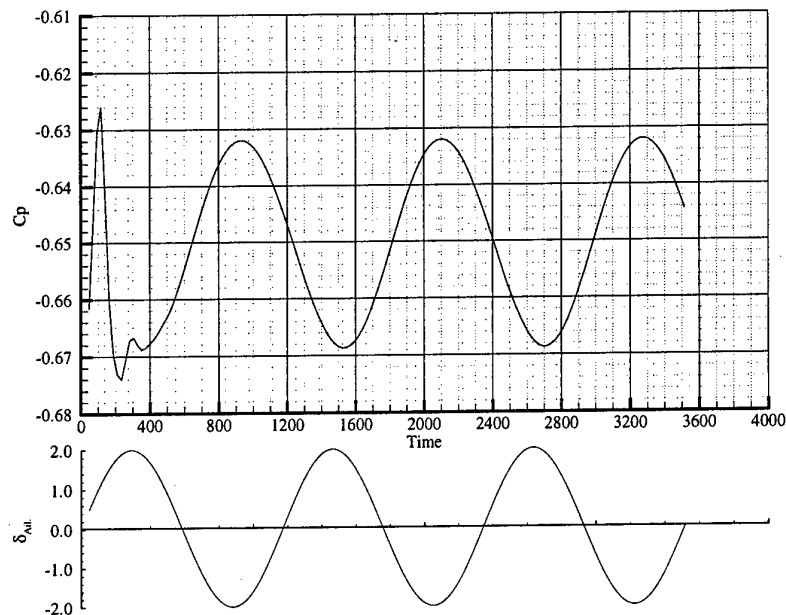
Figure 11.   Unsteady BACT pressures M=0.77, α=0.0°, $\delta_{Ail.}$=2.0°, f=5 Hz.

Figure 12 compares the predicted mean pressure coefficient for the unsteady analysis with the TDT experimental data. The agreement for this case is similar to that obtained for the steady analysis. This figure is significant since this is a comparison of mean values extracted from the unsteady pressure data. This pressure distribution is an important contributor to the overall pressures computed by the analysis method, which is often overlooked when evaluating unsteady simulations. The favorable mean pressure comparison with experimental data is the first indicator that the computational method is providing an accurate temporal simulation. If there were errors in the temporal algorithm they would very likely be uncovered by this comparison.

Figure 13 compares the in-phase and out-of-phase perturbation pressures at the 40% span, while Figure 14 presents this same comparison at 60% span. Both of these figures show that the pressure coefficient response to the aileron deflection is primarily in-phase with the aileron motion since the real components of the pressures are noticeably larger in amplitude than the imaginary components. The comparison of both the real and imaginary components of pressure with the experimental data are very good at the 40% span station. The comparison is also good for the real pressure at 60% span from 60% chord aft. In Figure 14 a definite jump in the experimental real component of the pressure can be seen at 60% chord. The aileron extends from 75% chord aft, and the agreement between theory and experiment on this portion of the wing is excellent. The BACT also has a deployable spoiler at this

station which extends from 60% chord to 75% chord. The pressure distribution comparison in this area is also very good. The wing ahead of 60% chord is fixed and does not house any control surfaces. It is in this area that the theory and experiment do not compare well. The sharp jump in the experimental data at 60% chord combined with the excellent agreement between theory and experiment on the spoiler and oscillating aileron suggest that there may be an anomaly in the experimental data where the model transitions from the fixed portion of the wing to the control surfaces. However, a preliminary investigation into the experimental data has not uncovered any obvious deficiencies. Investigations with other numerical methods may provide further insight into these differences, and these calculations are planned for the near future.

CONCLUSION

The ENS3DAE computational aeroelasticity program has been applied to the static aeroelastic and the unsteady aerodynamic analysis of two rectangular wings. Both wings included trailing edge control surfaces, which were deflected during the analysis. The static aeroelastic calculations investigated control reversal on a thin wing with a parabolic arc airfoil. Results of this study have been compared with results obtained using the CAP-TSD computational aeroelasticity program, which is based on transonic small disturbance potential flow aerodynamics. Detailed comparisons of the pressure distributions at the mid-span of the control surface show

Unsteady BACT ENS3DAE Analysis
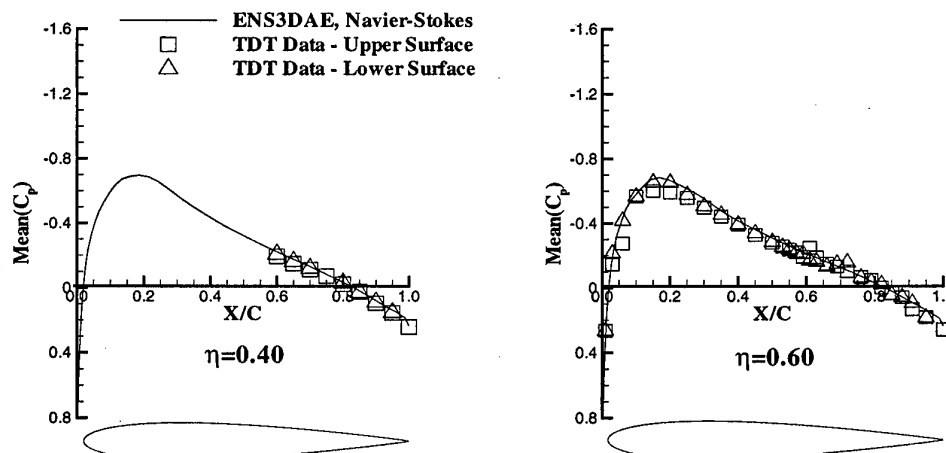## $M=0.77$, $\alpha=0.0°$, $\delta_{ail.}=2.0°$, $f=40$ Hz.

Figure 12. Mean unsteady BACT pressures, $M=0.77$, $\alpha=0.0°$,
$\delta_{Ail.}=2.0°$, $f=5$ Hz.

Unsteady BACT ENS3DAE Analysis
M=0.77, α=0.0°, $\delta_{Ail.}$=2.0°, *f*=5 Hz.
η = 0.40
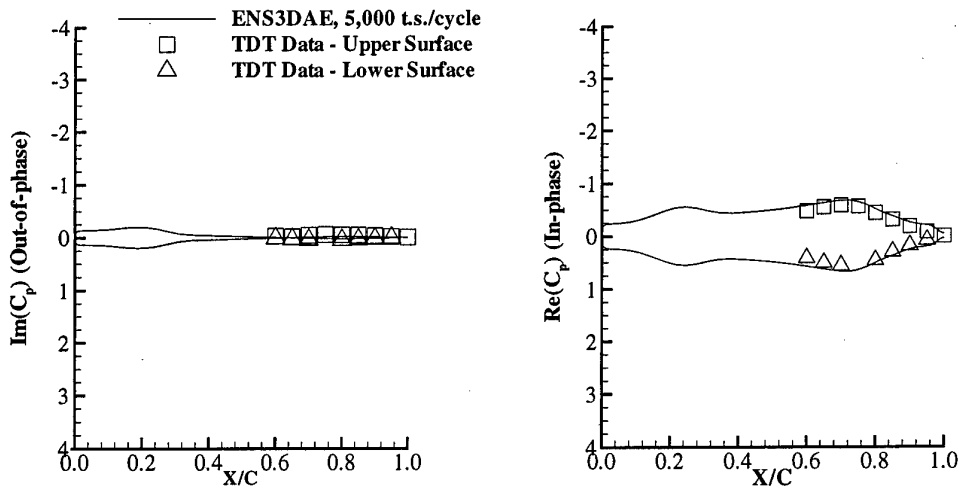
Figure 13.   Unsteady BACT pressures M=0.77, α=0.0°, $\delta_{Ail.}$=2.0°,
             f=5 Hz, η=0.40.

Unsteady BACT ENS3DAE Analysis
M=0.77, α=0.0°, $\delta_{Ail.}$=2.0°, *f*=5 Hz.
η = 0.60
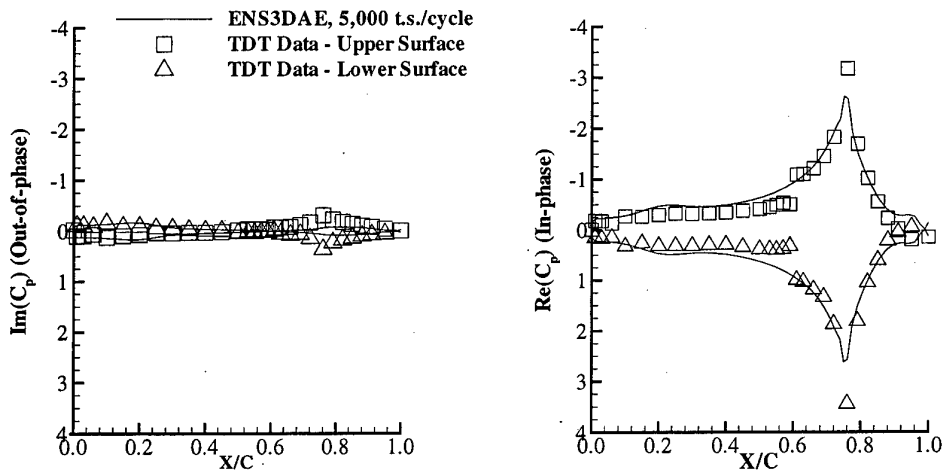

Figure 14. Unsteady BACT pressures M=0.77, α=0.0°,
           $\delta_{Ail.}$=2.0°, *f*=5 Hz, η=0.60.

expected excellent agreement between the ENS3DAE Euler equation analysis and CAP-TSD. The control reversal dynamic pressure predicted by ENS3DAE is approximately three percent lower than that computed by CAP-TSD. This parameter has been shown to be sensitive to the distribution of grid points in the CAP-TSD analysis and further grid resolution studies on both methods are currently underway.

Steady and unsteady Navier-Stokes equation calculations were performed on the BACT wing with a fixed and oscillating trailing edge control surface. Computed results have been compared with experimental data obtained in NASA Langley's Transonic Dynamics Tunnel. Cases where the flow is primarily subsonic over the entire surface of the wing section compare very well with experimental data. However, cases involving transonic flow show a discrepancy in the pressures on the forward portion of the airfoil upper surface and in the shock strength and location. Transonic pressures ahead of shock waves are typically well-predicted by computational methods, leading us to believe that there may be complex interactions between the wind tunnel and the model that are not accurately accounted for in our numerical analysis. Mean pressures from the unsteady aileron deflection analysis compare very well with the experimental data. The in-phase component is the main contributor to the unsteady pressure perturbation, and these computations compare closely with the TDT data from 60% chord aft. Differences on the forward portion of the wing similar to those observed in the steady analysis are also present in the unsteady perturbation pressures. The out-of-phase pressure component is considerably smaller in magnitude than the in-phase component, and given these small values, the comparison between theory and experiment is reasonable. Further calculations modeling the wind tunnel walls and support structure are required to investigate the transonic differences between the theoretical and experimental data.

ACKNOWLEDGEMENTS

REFERENCES

1. Schuster, D. M., J. Vadyak, and E. Atta, "Flight Loads Prediction Methods for Fighter Aircraft," WRDC-TR-89-3104, November, 1989.

2. Schuster, D. M., J. Vadyak, and E. Atta, "Static Aeroelastic Analysis of Fighter Aircraft Using a Three-Dimensional Navier-Stokes Algorithm," *Journal of Aircraft*, Volume 27, Number 9, September, 1990, pp. 820-825.

3. Schuster, D. M., "Application of Navier-Stokes Aeroelastic Methods to Improve Fighter Wing Performance," *Journal of Aircraft*, Volume 32, Number 1, January-February, 1995, pp. 77-83.

4. Batina, J. T., et al., "Unsteady Transonic Flow Calculations for Realistic Aircraft Configurations," *Journal of Aircraft*, Volume 26, Number 1, January, 1989, pp. 21-28.

5. Guruswamy, G. P. and E. L. Tu, "Transonic Aeroelasticity of Fighter Wings with Active Control Surfaces," *Journal of Aircraft*, Volume 26, Number 7, July, 1989, pp. 682-684.

6. Pitt, D. M., and D. F. Fuglsang, "Aeroelastic Calculations for Fighter Aircraft Using the Transonic Small Disturbance Equation," AGARD-CP-507, March, 1992, pp. 16-1 - 16-11.

7. Andersen, G., R. Kolonay, and F. Eastep, "Control Reversal in the Transonic Regime," AIAA Paper 97-1385, 38th AIAA/ASME/ASCE/AHS/ASC Structures, Structural Dynamics, and Materials Conference and Exhibit, Kissimmee, FL, April, 1997.

8. Batina, J. T., "A Finite-Difference Approximate-Factorization Algorithm for Solution of the Unsteady Transonic Small Disturbance Equation," NASA Technical Paper 3129, January, 1992.

9. Obayashi, S. and G. P. Guruswamy, "Navier-Stokes Computations for Oscillating Control Surfaces," *Journal of Aircraft*, Volume 31, Number 3, May-June, 1994, pp. 631-636.

10. Obayashi, S., I.-T. Chiu, and G. P. Guruswamy, "Navier-Stokes Computations on Full Wing-Body Configuration with Oscillating Control Surfaces," *Journal of Aircraft*, Volume 32, Number 6, November-December, 1995, pp.1227-1233.

11. Thomas, P. D., and C. K. Lombard, "Geometric Conservation Law and Its Application to Flow Computations on Moving Grids," *AIAA Journal*, Volume 17, Number 10, October, 1979, pp. 1030 - 1037.

12. Borland, C. J., "XTRAN3S - Transonic Steady and Unsteady Aerodynamics for Aeroelastic Applications," AFWAL-TR-85-3214, Air Force Wright Aeronautical Laboratories, Wright-Patterson AFB, OH, January, 1986.

13. Scott, R. C., et al., "The Benchmark Active Controls Technology Model Aerodynamic Data," AIAA Paper 97-0829, 35th Aerospace Sciences Meeting and Exhibit, January, 1997.

14. Abbott, I. H. and A. E. Von Doenhoff, *Theory of Wing Sections*, Dover Publications, Inc., New York, NY, 1959.

Aerodynamics for Elastically Oscillating Wings Using the Virtual Grid Deformation Method

W. Wegner

German Aerospace Research Establishment (DLR)
Institute of Aeroelasticity (23200)
Bunsenstrasse 10, 37073 Göttingen, Germany

Abstract

A new, efficient, and at the same time most precise calculation method for unsteady aerodynamics is presented in this paper. It is called the "virtual grid deformation" method. The time-dependent grid deformation is observed virtually and without restriction, meaning that this method is also valid for high deflections and large amplitudes, respectively. This method is applicable to the conservation laws of fluid flows which are solved by a finite volume scheme and by a time-stepping procedure. Numerical results of a standard wing in steady and unsteady flow are compared with available measurements.

Symbols and Definitions

a	speed of sound
A	wing surface
c_l, c_m	local lift and momentum coefficient
C_l, C_m	total lift and momentum coefficient
$c_p = \frac{p - p_\infty}{\frac{1}{2}\rho_\infty V_\infty^2}$	pressure coefficient
$c_\Pi = \frac{P}{\frac{1}{2}\rho_\infty V_\infty^3 l}$	local power coefficient
$C_\Pi = \frac{P}{\frac{1}{2}\rho_\infty V_\infty^3 A}$	total power coefficient
e	total energy
F, G, H	flux vectors in the x, y, z directions
J	Jacobian of a functional matrix
l	local profile length
l_R	characteristic length, root profile chord
$l_\mu = \frac{S}{A} \int_S^0 l^2 dy$	characteristic length, mean aerodynamic chord
$M = \frac{V}{a}$	Mach number
$N = [N_x, N_y, N_z]$	normal vector to a coordinate surface
p	pressure
P	power
q, r	interpolation functions
Re	Reynolds number
s	semi span width

$[T]$	rotational matrix
U	vector of the conservative variables
$V = [u, v, w]$	vector of the Cartesian velocity components
$V_{kin} = [\dot{x}, \dot{y}, \dot{z}]$	relative velocity in fixed reference system
$x = \frac{\bar{x}}{l_R}, \quad y = \frac{\bar{y}}{l_R},$ $z = \frac{\bar{z}}{l_R}$	non-dimensional Cartesian coordinates
x_R, z_R	coordinates of the rotation axis
α, β, γ	rotational angles around the y,z,x axis
α_0	steady angle of attack
α_1	pitch amplitude
ρ	density
$\tau = \frac{V_\infty}{l_\mu} t$	non-dimensional time
ω	circular frequency
$\omega^* = \frac{l_\mu}{V_\infty} \omega$	reduced frequency

Subscripts

0	lower or left boundary
1	upper or right boundary
i, j, k	spatial indices
∞	undisturbed free-flow condition

Superscript

n	time level

1 Introduction

In the following, a theoretical flow procedure which occurs in the transonic speed range of modern commercial aircraft is researched. One main point is the calculation of periodic motion-induced air forces in order to identify unwanted aerodynamic instabilities for an entire configuration as well as for individual components. The goal is to integrate the aerodynamic stability of the wings of future commercial aircraft at

an early stage in the design. The requirement for this is a systematic study of the geometry and the elastic mode shapes of the wing and its influence on aerodynamic stability.

Transformation of the basic equations of fluid dynamics into a time-dependent boundary-fitted coordinate system enables the calculation of flows around any body which has time-dependent surfaces. This, in particular, enables the simulation of elastically oscillating wings in transonic flow.

Of particular interest is the implementation of the grid motion in the numerical algorithm. A natural procedure arises when computational grids are generated with regard to the time-dependent boundary conditions. They can be made available in two different manners:

- The grid is generated at each time step by sufficient iteration steps.

- The grid is generated for the extreme positions of deflections, and the positions in between are interploated.

In these general methods, all of the metric terms and corresponding vector products have to be recalculated for each time step, which is time consuming. This major disadvantage holds true even in the case of restricting the grid generation to the extreme positions of deflection. These methods of dynamic grid implementation are the basis for the current numerical algorithm for unsteady fluid dynamic and aeroelastic problems. It was realized for two-dimensional meshes by Batina [2], Hoffren [6], and Voss, Carstens [16] and was extended to three-dimensional meshes by Anderson, Thomas, Rumsey [1].

An alternative procedure is explained in this paper: Extracted from the grid motion are those values which express the temporal changes of the metric terms. The extracted values are represented analytically as a function of the spatial coordinates of the computational domain and of time with regard to the time-dependent boundary conditions. These are taken into account in the numerical solution algorithm at every time step.

In this new method only the information of the moving grid required for the numerical algorithm is used. Detailed information on the geometric positions is not necessary. This is quite understandable: The basic equations are those of differential equations and the metric terms always appear as differentials. Since the time-dependent positions of the grid points are not taken into account in the numerical algorithm, the grid motion can be regarded as virtual mapping. For this reason, the method is advantageous:

- The basic grid is always the same boundary-fitted grid of the initial steady state solution
- The numerical algorithm is computationally time efficient and does not limit the quality of the solution.

The solution algorithms of both methods are different in the case of a dynamically deforming grid, yet their solutions are identical.

2 Basic Equations

Basically, first-order hyperbolic conservation laws which are derived from physical principles of conservation and which can be written in the so-called strong conservation law form below are considered:

$$\frac{\partial U}{\partial t} + \frac{\partial F}{\partial x} + \frac{\partial G}{\partial y} + \frac{\partial H}{\partial z} = 0 \qquad (1)$$

The transformation from Cartesian into time-dependent, boundary-fitted coordinates

$$
\begin{array}{ll}
x = x(\xi,\eta,\zeta,\tau) & \xi = \xi(x,y,z,t) \\
y = y(\xi,\eta,\zeta,\tau) \leftrightarrow & \eta = \eta(x,y,z,t) \quad , \tau \\
z = z(\xi,\eta,\zeta,\tau) & \zeta = \zeta(x,y,z,t)
\end{array} \qquad (2)
$$

is a unique mapping if the Jacobian J of the transformation at each location is not equal to zero:

$$J = \frac{\partial(x,y,z)}{\partial(\xi,\eta,\zeta)} = \begin{vmatrix} x_\xi & x_\eta & x_\zeta \\ y_\xi & y_\eta & y_\zeta \\ z_\xi & z_\eta & z_\zeta \end{vmatrix} \neq \qquad (3)$$

Then the transformation again leads to a system of strong conservation law form:

$$\frac{\partial \hat{U}}{\partial t} + \frac{\partial \hat{F}}{\partial \xi} + \frac{\partial \hat{G}}{\partial \eta} + \frac{\partial \hat{H}}{\partial \zeta} = 0 \qquad (4)$$

The transformed equations can be expressed by the following relations:

$$
\begin{aligned}
\hat{U} &= J \cdot U \\
\hat{F} &= J \cdot [F,G,H] \cdot N(\xi) + J \cdot U \cdot \xi_t \\
\hat{G} &= J \cdot [F,G,H] \cdot N(\eta) + J \cdot U \cdot \eta_t \\
\hat{H} &= J \cdot [F,G,H] \cdot N(\zeta) + J \cdot U \cdot \zeta_t
\end{aligned} \qquad (5)
$$

which again will be emphasized in the following statement:

The transformation of hyperbolic conservation laws into curvilinear coordinates is represented as the local Jacobian J, as the normalized normal vectors JN which belongs to all of the tangential areas of the curvilinear coordinates ξ, η, ζ, and as their normalized relative velocities.

The components of the co- and contravariant basis vectors are:

$$
\begin{array}{lll}
\xi_x = \frac{y_\eta z_\zeta - z_\eta y_\zeta}{J} \;; & \eta_x = \frac{z_\xi y_\zeta - y_\xi z_\zeta}{J} \;; & \zeta_x = \frac{y_\xi z_\eta - z_\xi y_\eta}{J} \\
\xi_y = \frac{z_\eta x_\zeta - x_\eta z_\zeta}{J} \;; & \eta_y = \frac{x_\xi z_\zeta - z_\xi x_\zeta}{J} \;; & \zeta_y = \frac{z_\xi x_\eta - x_\xi z_\eta}{J} \\
\xi_z = \frac{x_\eta y_\zeta - y_\eta x_\zeta}{J} \;; & \eta_z = \frac{y_\xi x_\zeta - x_\xi y_\zeta}{J} \;; & \zeta_z = \frac{x_\xi y_\eta - y_\xi x_\eta}{J}
\end{array} \qquad (6)
$$

as well as

$$\xi_t = -\xi_x x_\tau - \xi_y y_\tau - \xi_z z_\tau$$
$$\eta_t = -\eta_x x_\tau - \eta_y y_\tau - \eta_z z_\tau \qquad (7)$$
$$\zeta_t = -\zeta_x x_\tau - \zeta_y y_\tau - \zeta_z z_\tau$$

(1) Examples of fluid flow modelling

As a particular example, the Euler equations, the basic equations of inviscid fluid motion, are regarded. Then U describes the vector of the so-called conservative flow variables and F, G, H describe the fluxes in all coordinate directions, the components of which are developed by the conservation laws of mass, momentum, and energy:

$$U = \rho \begin{bmatrix} 1 \\ u \\ v \\ w \\ e \end{bmatrix} ; \quad F = \rho \begin{bmatrix} u \\ u^2 + p/\rho \\ uv \\ uw \\ [e + p/\rho]\, u \end{bmatrix} ;$$

$$G = \rho \begin{bmatrix} v \\ vu \\ v^2 + p/\rho \\ vw \\ [e + p/\rho]\, v \end{bmatrix} ; \quad H = \rho \begin{bmatrix} w \\ wu \\ wv \\ w^2 + p/\rho \\ [e + p/\rho]\, w \end{bmatrix} \qquad (8)$$

Body forces, which are due to gravitation, and rates of heat, which are due to thermal conduction and diffusion, can be neglected in this particular application of gas dynamics. The necessary closing condition is fulfilled by the equation of state with which a caloric and thermal perfect gas can be assumed.

The representation of the transformed basic equations into a strong conservation form eq.(4) was first achieved by Viviand [15] and Vinokur [14].

(2) Transformation of the normal vector

The transformation of the basic equations into boundary-fitted coordinates can be expressed by the normal vectors of the areas $\xi = const., \eta = const., \zeta = const.$ In this section the time-dependency of the normal vectors is extracted.

In the following, $N(\xi) = grad\,\xi$ denotes a non-normalized normal vector of the area $\xi = const.$ $\hat{N}_1$ denotes a normal vector normalized to the Jacobian J. The standard normalization is integrated as a special case. For example, when regarding the area $\xi = const.$, the following is obtained:

$$N(\xi) = \begin{bmatrix} \xi_x \\ \xi_y \\ \xi_z \end{bmatrix} ; \quad \hat{N}(\xi) = J \cdot \begin{bmatrix} \xi_x \\ \xi_y \\ \xi_z \end{bmatrix} ;$$

$$\hat{N}_1(\xi) = \frac{1}{\sqrt{\xi_x^2 + \xi_y^2 + \xi_z^2}} \begin{bmatrix} \xi_x \\ \xi_y \\ \xi_z \end{bmatrix} \qquad (9)$$

$J \cdot N$ is a normalized form of N because of $\xi_x = \xi_x(1/J)$, $\xi_y = \xi_y(1/J)$, etc. which results from eq.(6).

If the gradients of the normal vector are known at time point $t = 0$, the changes to time point $t > 0$ can be described by angles α, β, γ and, if the need arises, by the change of the Jacobian J. In the following, α, stands for the rotation around the y axis, β for the rotation around the z axis, and γ for the rotation around the x axis.

Then, considering the non-normalized as well as the normalized version, the time-dependent local normal vector can be obtained with a transformation:

$$N(x, y, z, t) = [T](x, y, z, t) \cdot N(x, y, z, t = 0) \cdot \frac{J(x, y, z, t = 0)}{J(x, y, z, t)} \qquad (10)$$

$$\hat{N}(x, y, z, t) = [T](x, y, z, t) \cdot \hat{N}(x, y, z, t = 0) \cdot \frac{J(x, y, z, t = 0)}{J(x, y, z, t)} \qquad (11)$$

This separation approach is the basic idea of the method presented here. Eq.(10) is applicable to the transformed fluxes in eq.(5). Eq.(11) will be needed in the numerical solution algorithm for the determination of the time-dependent change of the finite control volume in chapter 4.

The transformation matrix $[T]$ contains the rotations around the x,y, and z axes:

$$[T] = [T_x] \cdot [T_y] \cdot [T_z] \qquad (12)$$

with the rotation matrix in the x direction:

$$[T_x] = \begin{bmatrix} 1 & 0 & 0 \\ 0 & \cos\gamma & \sin\gamma \\ 0 & -\sin\gamma & \cos\gamma \end{bmatrix} \qquad (13)$$

in the y direction:

$$[T_y] = \begin{bmatrix} \cos\alpha & 0 & -\sin\alpha \\ 0 & 1 & 0 \\ \sin\alpha & 0 & \cos\alpha \end{bmatrix} \qquad (14)$$

and in the z direction:

$$[T_z] = \begin{bmatrix} \cos\beta & \sin\beta & 0 \\ -\sin\beta & \cos\beta & 0 \\ 0 & 0 & 1 \end{bmatrix} \qquad (15)$$

The transformation eq.(12) is non-commutative; it begins with the rotation around the z axis of the steady reference system and ends with the rotation around the x axis. Other sequences are possible which can be achieved by exchanging $[T_x], [T_y]$, and $[T_z]$.

With the aid of [T], the normal vectors of the moving grid are transformed into a fixed area. [T] and, with that, α, β, γ are dependent on the spatial coordinates and on time.

3 Virtual Grid Deformation

The numerical solution algorithm of hyperbolic conservation laws is based on the finite volume scheme and on a time-stepping procedure, and it requires a discretization of the calculation area.

The time-dependent nodal points of each cell element of the computational grid define the geometric positions of the cell face centers, the normal vectors of the cell faces, the cell face areas, the cell volume as well as their time derivatives.

Most of the current solution methods in computational fluid dynamics use the time-dependent geometric positions of the grid points to recalculate the metric terms and the cell volume after every single time step.

However, the hyperbolic conservation laws in time-dependent curvilinear coordinates, when applied to numercal calculations in a discretized area, require no more information than:

- the normal vector of the cell faces and
- the cell volume

as well as the following time derivatives:

- the relative velocity of the cell face centers and
- the change in time of the cell volume.

In chapter 2 it is shown that the transformed basic equations are dependent on the normal vectors of the curvilinear coordinates and on the Jacobian of the coordinate transformation. In chapter 4 it will be shown that the Jacobian J can be interpreted as a cell volume of the discretized area and that the time-dependent cell volume as well as its change in time can be completely determined by the normal vectors and the relative velocities of the corresponding cell faces. Therefore, essentially only the two variables are required:

- the normal vector of the cell faces and
- the relative velocity of the cell face centers.

Only these extracted kinematic values have to be implemented in the numerical algorithm to simulate a time-dependent grid deformation. It is regarded as virtual mapping since the geometric positions of the grid points are not taken into account.

An overview of the method is given in section (1). Theorems for the design of time-dependent normal vectors and the relative velocities are stated in section (2).

(1) Principle algorithms

The transformation into a time-dependent curvilinear coordinate system can be seen as a sequence of two steps:

$$x, y, z \quad \longrightarrow \quad \xi, \eta, \zeta \quad \longrightarrow \quad \xi', \eta', \zeta'$$

The transformation from the Cartesian coordinate system x, y, z into the initial curvilinear coordinate system ξ, η, ζ is described by the mapping eq.(2); the transformation from the initial curvilinear system into the moving curvilinear system ξ', η', ζ' is sufficiently described by the local translations $\bar{x}, \bar{y}, \bar{z}$ and by the rotational angles α, β, γ.
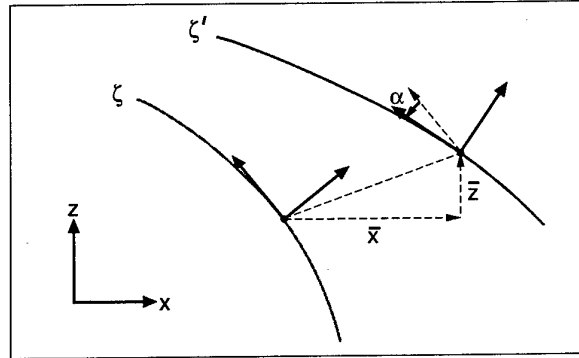

Figure 1: Temporal change of the normal vector of a cell face

Changes of a given curvilinear coordinate system are generally described as a function of its curvilinear coordinates. The changes can particularly be given as a function of a specific coordinate direction ξ or η or ζ. For example, the rotation matrix $[T]$ can be represented by:

$$
\begin{aligned}
T &= T(\xi, \eta(\xi_0), \zeta(\xi_0)) \quad or \\
T &= T(\xi(\eta_0), \eta, \zeta(\eta_0)) \quad or \\
T &= T(\xi(\zeta_0), \eta(\zeta_0), \zeta))
\end{aligned}
\tag{16}
$$

This kind of parametrization is valid without limitation for the application of the virtual grid deformation - it is even advantageous. This will be proved in the next section.

The relation of the boundaries of the transformed computational region to the physical area depends on the chosen topology. Basic two-dimensional types are H-, C-, and O- topologies. Three-dimensional topologies are the result of the combination of these basic types.

Grid motions are always induced at the boundaries. In the following, the boundaries and lines of the computational region are specified with respect to the cause and effect of motion.

Motion-inducing boundaries - as opposed to the remaining boundaries - are not inhibited in their form of motion. Their positions are coupled with the coordinate direction which functionally expresses the spatial grid deformation. For example, the inner and outer motion-inducing boundaries determined by the levels ζ_0 and ζ_1 during the parametization of the grid deformation in the ζ direction.

Motion-induced lines connect the points of the opposite motion-induced boundaries and fulfill their movement. Otherwise, motion is achieved by interpolation. For this, the properties of a unique and smooth mapping are required, which limit the motion possibilities.

Time-dependent boundary conditions arise either because of the form of motion of the body surface or due to the relative motion of the far field boundary and, depending on the topology, can occur in all boundaries of the computational region. Thus they determine the motion-inducing boundaries as well as motion-induced lines on the outer boundaries. In the latter case, the restriction of motion possibilities is irrelevant in practice since, in the physical domain, this is usually a far field boundary.

Motion-inducing boundaries can also be divided into *fixed and free boundaries*. Fixed boundaries are determined by boundary conditions. Free boundaries only have to maintain the motion of their outer points and are totally free in motion otherwise. However, smooth transitions are desirable here as well.

Manifold descriptions can be made of the motion-inducing boundaries and are adjusted to the formulation of the technical requirement. Both of the following exceptions are of particular interest:

1. One of the motion-inducing boundaries is fixed in the steady reference system:

$$
\begin{bmatrix} \dot{x} \\ \dot{y} \\ \dot{z} \end{bmatrix}_0 = 0; \quad \begin{bmatrix} \gamma \\ \alpha \\ \beta \end{bmatrix}_0 = 0 \quad or
$$

$$
\begin{bmatrix} \dot{x} \\ \dot{y} \\ \dot{z} \end{bmatrix}_1 = 1; \quad \begin{bmatrix} \gamma \\ \alpha \\ \beta \end{bmatrix}_1 = 1 \quad (17)
$$

Such a construction is necessary for an unsteady solid boundary interference when, e.g., the flow of an oscillating wing is simulated in a tunnel, whereby tunnel wall interference must be taken into account.

2. The motion-inducing boundaries are coupled in their form of motion. In the case of a rigid-body motion, the identity

$$
\begin{bmatrix} \gamma \\ \alpha \\ \beta \end{bmatrix} (\tau) = \begin{bmatrix} \gamma \\ \alpha \\ \beta \end{bmatrix}_0 = \begin{bmatrix} \gamma \\ \alpha \\ \beta \end{bmatrix}_1 \quad (18)
$$

is appropriate. The angles of the local normal vector are then independent of the spatial coordinates.

Index 0 defines the left or lower boundary, index 1 defines the right or upper boundary.

The design of the functions which describe the virtual grid motion is carried out in 6 steps. This is first
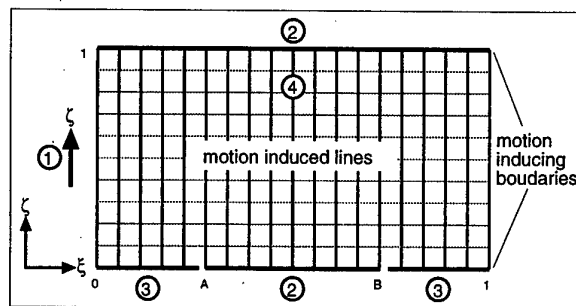

Figure 2: Moving of a two-dimensional curvilinear coordinate system

illustrated for two-dimensional curvilinear coordinates $\xi(x,z), \zeta(x,z)$ in the C-topology in which local relative velocities $V_{kin} = [\dot{x}, \dot{z}]$ and the local rotation angle α occur (see fig.2):

1. Choice of an appropriate coordinate direction for the parametization of the grid changes. In the following example, the essential time-dependent boundary conditions occur at the ζ_0 and ζ_1 boundaries and are defined as motion-inducing boundaries. The parametization is then carried out in the ζ direction.

2. Representation of the fixed boundaries by the local rotation angle $\alpha(\xi, \tau)$ and the local relative velocities $V(\xi, \tau)$. A closed functional description is advantageous.

3. Determination of the changes $\alpha(\xi, \tau), V_{kin}(\xi, \tau)$ of the free boundaries at ζ_0. The values at the positions $(\xi_A, \zeta_0), (\xi_B, \zeta_0)$ correspond with the outer values of the fixed boundary. They correspond in the physical domain with the trailing edge of the given profile.

4. Determination of the changes $\alpha(\zeta, \tau), V_{kin}(\zeta, \tau)$ of the motion-induced lines in the ζ direction. The foot points lie on a free or fixed motion-inducing boundary which, formally speaking, does not make any difference.

5. Inverse transformation of the local Cartesian velocity components $V_{kin} = [\dot{x}, \dot{z}]$ from the virtually moved coordinate system ξ', η', ζ' into the initial curvilinear coordinate system ξ, η, ζ:

$$
\dot{x}(\xi', \zeta', \tau) \cos \alpha(\xi', \zeta', \tau) - \dot{z}(\xi', \zeta', \tau) \sin \alpha(\xi', \zeta', \tau)
$$
$$
\rightarrow \dot{x}(\xi, \zeta, \tau)
$$
$$
\dot{z}(\xi', \zeta', \tau) \cos \alpha(\xi', \zeta,' \tau) + \dot{x}(\xi', \zeta', \tau) \sin \alpha(\xi', \zeta', \tau)
$$
$$
\rightarrow \dot{z}(\xi, \zeta, \tau) \quad (19)
$$

6. Determination of α and V_{kin} for the points (ξ_i, ζ_k) of the discretized computational region and for

the centers of the cell lines by arithmetical means:

$$\alpha_{i+\frac{1}{2},k} = \frac{1}{2}\left[\alpha_{i,k} + \alpha_{i+1,k}\right] \quad,$$

$$\alpha_{i,k+\frac{1}{2}} = \frac{1}{2}\left[\alpha_{i,k} + \alpha_{i,k+1}\right] \quad etc. \qquad (20)$$

A spatial three-dimensional grid motion is achieved when steps 2,3,4 are successively expanded in the η direction. The principle of parametrization in the ζ direction does not change. In step 5, the rotational angles in all coordinate directions are to be considered in the given sequence; see eq.(12). In step 6, the arithmetical mean is applied to the cell face centers of the control volume.

The previous steps show that the analytical description of the motion-induced lines is possible when following the methods of differential geometry. This will be substantiated in the next section. The transition into the discretised coordinates of the computational grid is carried out in only one last step.

(2) Theorems of unique and smooth grid deformations

The analytical description of the time-dependent grid deformation developed here is based on the following prerequisite:

Prerequisite. The boundary-fitted coordinates eq.(2) of the initial grid are based on a unique and smooth mapping.

In the following, only the time-dependent changes of the initial grid are observed. They must be also a unique and smooth mapping. Then, an overlapping of grid lines is excluded and the grid quality of the initial grid is maintained.

Definition 1. The mapping on curvilinear coordinates is unique when it is locally regular.

Definition 2. Curvilinear coordinates are smooth when there are minimum spatial changes in their tangential vectors and when taking into consideration the constraints of defined tangential vectors at the boundary.

The smoothness of the discretized computational grid also follows the smoothness of the cuvilinear coordinates: There are minimum spatial changes in the angles and in the distances between the lines when taking into consideration the constraints of the defined angles and distances at the boundary. Orthogonality at the boundaries specifically produces boundary-fitted coordinates.

The generation of smooth grids is possible by means of variation approaches, several of which lead to the so-called elliptic grid generation: see Godunov and Provkopov [5], Steger and Sorensen [11], Thompson [13], Roache and Steinberg [9], Neisius [8]. A mathematical description for smoothness, however, has not yet been determined in the literature.

Theorem 1. If the changes of a curvilinear coordinate system is angular conform in every point ξ, η, ζ, i.e., if all local tangential vectors are rotated by α, β, γ, then the following applies:

1. The mapping is locally unique
2. The mapping is locally smooth
3. The changes α, β, γ can be parametrized by one characteristic direction ξ or η or ζ.

The uniqueness follows from the separation approach eq.(10) or eq.(11) which also applies to the functional matrix and leads to the identity $det[T] = 1$. The smoothness directly results from definition 2. The parametrization follows from the reduction

$$\alpha_{,\xi} = \alpha_{,\eta} = \alpha_{,\zeta} = \alpha \quad ; \quad \beta_{,\xi} = \beta_{,\eta} = \beta_{,\zeta} = \beta \quad ;$$
$$\gamma_{,\xi} = \gamma_{,\eta} = \gamma_{,\zeta} = \gamma$$

During the transition to a discretized computational grid the values are obtained in the cell face centers by arithmetical means of the values in the discrete points (ξ_i, η_j, ζ_k); see eq.(20). The local mapping is then no longer angular conform, however, as is necessary, it is smooth as according to definition 2.

Theorem 1 presumes the existence of angular conform mapping which still needs to be found in the form of a function of one of the coordinates ξ or η or ζ. During parametrization in the ζ direction, the mapping is generally as follows:

$$\begin{bmatrix} \dot{x}(\zeta) \\ \dot{y}(\zeta) \\ \dot{z}(\zeta) \end{bmatrix} = [1 - Q(\hat{\zeta})]\begin{bmatrix} \dot{x} \\ \dot{y} \\ \dot{z} \end{bmatrix}_0 + Q(\hat{\zeta})\begin{bmatrix} \dot{x} \\ \dot{y} \\ \dot{z} \end{bmatrix}_1$$
$$+ [1 - Q_R(\hat{\zeta})]\begin{bmatrix} \Delta\hat{x} \\ \Delta\hat{y} \\ \Delta\hat{z} \end{bmatrix}_0 \times \begin{bmatrix} \dot{\gamma} \\ \dot{\alpha} \\ \dot{\beta} \end{bmatrix}_0$$
$$+ Q_R(\hat{\zeta})\begin{bmatrix} \Delta\hat{x} \\ \Delta\hat{y} \\ \Delta\hat{z} \end{bmatrix}_1 \times \begin{bmatrix} \dot{\gamma} \\ \dot{\alpha} \\ \dot{\beta} \end{bmatrix}_1 \qquad (21)$$

$$\begin{bmatrix} \gamma(\zeta) \\ \alpha(\zeta) \\ \beta(\zeta) \end{bmatrix} = [1 - R(\hat{\zeta})]\begin{bmatrix} \gamma \\ \alpha \\ \beta \end{bmatrix}_0 + R(\hat{\zeta})\begin{bmatrix} \gamma \\ \alpha \\ \beta \end{bmatrix}_1$$
$$- R_Q(\hat{\zeta})\begin{bmatrix} 1/\Delta\hat{x} \\ 1/\Delta\hat{y} \\ 1/\Delta\hat{z} \end{bmatrix}_{01} \times \begin{bmatrix} \bar{x} \\ \bar{y} \\ \bar{z} \end{bmatrix}_0$$
$$+ R_Q(\hat{\zeta})\begin{bmatrix} 1/\Delta\hat{x} \\ 1/\Delta\hat{y} \\ 1/\Delta\hat{z} \end{bmatrix}_{01} \times \begin{bmatrix} \bar{x} \\ \bar{y} \\ \bar{z} \end{bmatrix}_1 \qquad (22)$$

with the relative arc length:

$$\hat{\zeta} = \hat{\zeta}_0 \frac{\zeta - \zeta_0}{\zeta_1 - \zeta_0} \qquad (23)$$

the transformed distances:

$$\Delta\hat{X}_0 = \Delta X_0 - \bar{X} \cdot \hat{\zeta}_0$$
$$\Delta\hat{X}_1 = \Delta X_1 - \bar{X} \cdot \hat{\zeta}_1 \qquad (24)$$
$$\Delta\hat{X}_{01} = \Delta X_{01} - \bar{X}$$

and the following abbreviations:

$$\Delta X_0(\zeta) = X(\zeta) - X_0 \quad , \qquad (25)$$

$$\Delta X_1(\zeta) = X(\zeta) - X_1 \quad , \quad \Delta X_{01} = X_1 - X_0 \quad (26)$$

Indexes 0 and 1 characterize the points of the lower and upper motion inducing boundaries ζ_0 and ζ_1.
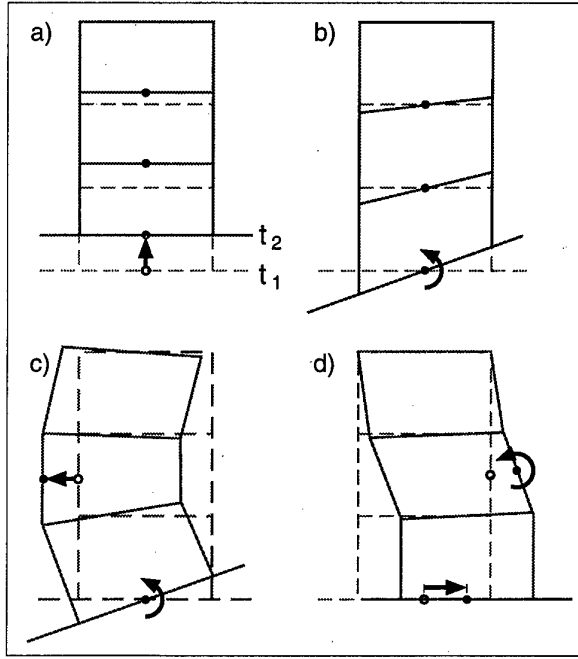

Figure 3: Basic steps for the analytical design of the virtual grid deformation

The interpolation functions $Q(\hat{\zeta}), Q_R(\hat{\zeta})$ and $R(\hat{\zeta}), R_Q(\zeta)$ are dependent on the relative arc length $\hat{\zeta}$. The influences are depicted in fig.3 for a two-dimensional form of motion. Q, R are associated with the direct forms of motion, and Q_R, R_Q with the coupled forms of motion. The cross products describe the relative velocities due to the angular velocities and the rotation due to the shear.

In general, each component of the interpolation function is individually specified which has to be expressed by diagonal matrices, for example:

$$[Q] = \begin{bmatrix} q_x & 0 & 0 \\ 0 & q_y & 0 \\ 0 & 0 & q_2 \end{bmatrix} \qquad (27)$$

The translations $\bar{x}, \bar{y}, \bar{z}$ and the angular velocities $\dot{\alpha}, \dot{\beta}, \dot{\gamma}$ at the boundaries ζ_0 and ζ_1 can be seen as auxilary values for the determination of the motion-induced lines of the moving grid. They are not needed for the numerical solution of the conservation laws.

Theorem 2. The mapping eq.(21) and eq.(22) is unique if the interpolation functions Q, Q_R and R, R_Q meet the following necessary conditions:

1. $Q(\zeta_0) = R(\zeta_0) = Q_R(\zeta_0) = R_Q(\zeta_0) = 0$ for the lower boundary
2. $Q(\zeta_1) = R(\zeta_1) = Q_R(\zeta_1) = 1, R_Q(\zeta_1) = 0$ for the upper boundary
3. $q_x = q_y = q_z = q$; $q_{rx} = q_{ry} = q_z = rq$; $r_x = r_y = r_z = r$; $r_{rx} = r_{ry} = r_z = rq$; for all $\hat{\zeta}$
4. $q(\hat{\zeta}) = q_r(\hat{\zeta})$ for all $\hat{\zeta}$
5. $q(\hat{\zeta})$ is monotonic for $0 \leq \hat{\zeta} \leq 1$

The first two conditions fulfill the time-dependent boundary conditions of the motion-inducing boundaries. The identity of the individual components and the identity of the interpolation functions q and q_r follows the parametrization; it guarantees local angular conform mapping. The monotonic condition becomes clear in the example shown in fig.3a) and b), taking into consideration that the grid lines do not overlap.

Of particular interest is the linkage between the local relative velocities and the local rotational angles in the field, i.e., the relation between the interpolation functions q, q_r and r, r_q.

Theorem 3. If the interpolation functions q and q_r, respectively, are given in the polynomial representation to the mth degree $q(\hat{\zeta}) = c_0 + c_1\hat{\zeta} + c_2\hat{\zeta}^2 + \cdots + c_m\hat{\zeta}^m$, then the following holds for all $\hat{\zeta}$:

1. $r(\hat{\zeta}) = d_0 + d_1\hat{\zeta} + d_2\hat{\zeta}^2 + \cdots + d_i\hat{\zeta}^i$
   with $d_i = 0$ for $c_i = 0$
   $d_i = \frac{1}{[i+1]c_i}$ for $c_i \neq 0$
2. $r_q(\hat{\zeta}) = -\frac{1}{2}\left[c_1 + 2c_2\hat{\zeta} + 3c_3\hat{\zeta}^2 + \cdots + mc_m\hat{\zeta}^{m-1}\right]$
3. $c_0 = c_1 = 0$

The proof of theorem 3 and a more detailed explanation of the method will be presented in an upcoming paper.

4 Changes in the Finite Volume Scheme

The numerical solution algorithm requires the discretization of the spatial coordinates ξ, η, ζ into $i = 1, ..I; j = 1, ..J; k = 1, ..K$ intervals. Similar to differential equation(4), the difference equation

$$\left[\frac{\Delta[JU]}{\Delta_\tau} + \frac{\Delta\hat{F}}{\Delta_\xi} + \frac{\Delta\hat{G}}{\Delta_\eta} + \frac{\Delta\hat{H}}{\Delta_\zeta}\right]^{n+\frac{1}{2}}_{i,j,k} = 0 \qquad (28)$$

must also satisfy the conservation laws in its integral form for all $I \times J \times K$ cells which yields a finite volume scheme. The term $J_{i,j,k}$ in eq.(28) corresponds to the volume of cell i, j, k. The cell face centers are the reference points for the flux transport and therefore also for the grid velocities.

A generalized finite volume scheme is derived from the integral form of conservation laws and thus is in no way restricted to any specific form of the control volume. In the following, however, a structured mesh with octahedron-shaped control volumes are focused on, and therefore the volume scheme given in eq.(28) becomes applicable. In this case, the unique mapping eq.(2) of the curvilinear coordinates directly correlates with the grid points of the control volumes, and the solution scheme for a virtual grid deformation can be described in a computationally efficient manner.

The time integration has to reflect the hyperbolic character of the differential equations, i.e., the solution $U(\tau)$ is always successively computed from the previous time step for all $n = 0, 1, 2, ..$ time levels. The representation of the time level $n = \frac{1}{2}$ is dependent on the type and order of time integration.

The numerical solution depends on the initial data at $\tau = 0$ and on the time-dependent boundary conditions at the boundaries of the computational domain.

The application of the virtual grid deformation method is independent from the type of flux differencing as well as from the type of time integration. It can be combined with central or upwind schemes and with explicit or implicit algorithms. Only the volume change $\Delta J / \Delta \tau$ in eq.(28) has to be taken into account which, in turn, is solved by the so-called geometric conservation law.

(1) Geometric conservation law

The geometric conservation law - first demonstrated by Thomas and Lombard [12] - results from the hyperbolic conservation laws, eq.(4), for constant variables $U = U_\infty$ and any grid velocity. Then the constant variables can be separated and a determination of the temporal change of the control volume follows:

$$\left[\frac{\Delta J}{\Delta \tau} + \frac{\Delta \dot{\xi}}{\Delta \xi} + \frac{\Delta \dot{\eta}}{\Delta \eta} + \frac{\Delta \dot{\zeta}}{\Delta \zeta}\right]^{n+\frac{1}{2}}_{i,j,k} = 0 \qquad (29)$$

The discrete representation of the time level $n + \frac{1}{2}$ is dependent on the type and order of the time integration, examples of which are shown as follows:

1. first-order explicit

$$\frac{J^{n+1} - J^n}{\Delta \tau} + \left[\frac{\Delta \dot{\xi}}{\Delta \xi} + \frac{\Delta \dot{\eta}}{\Delta \eta} + \frac{\Delta \dot{\zeta}}{\Delta \zeta}\right]^{n}_{i,j,k} = 0 \qquad (30)$$

2. first-order implicit

$$\frac{J^{n+1} - J^n}{\Delta \tau} + \left[\frac{\Delta \dot{\xi}}{\Delta \xi} + \frac{\Delta \dot{\eta}}{\Delta \eta} + \frac{\Delta \dot{\zeta}}{\Delta \zeta}\right]^{n+1}_{i,j,k} = 0 \qquad (31)$$

3. second-order implicit

$$\frac{1.5 J^{n+1} - 2 J^n + 0.5 J^{-1}}{\Delta \tau} + \left[\frac{\Delta \dot{\xi}}{\Delta \xi} + \frac{\Delta \dot{\eta}}{\Delta \eta} + \frac{\Delta \dot{\zeta}}{\Delta \zeta}\right]^{n+1}_{i,j,k} = 0 \qquad (32)$$

We gain the insight that the temporally changing control volume has to be determined only by the relative velocities of the cell face centers. Then the geometric conservation law eq.(29) is consistent with the hyperbolic conservation laws eq.(4). Due to infinitesimal rotations of the cell surfaces around its center points, higher-order terms are not to be taken into account. This statement is valid for the first-order hyperbolic conservation laws regarded here and for all corresponding numerical solution schemes. It is also valid when additional viscous terms are included.

(2) Determination of the change in volume

The description of eq.(29) is primarily dependent on the order of the time integration, however, it can always be expressed as a recurrence formula:

$$J^{n+1} = J^n + \Delta \tau \dot{J}^{n+\frac{1}{2}} \qquad (first\ order) \qquad (33)$$

$$J^{n+1} = \frac{4}{3} J^n - \frac{4}{3} J^{n-1} + \frac{2}{3} \Delta \tau \dot{J}^{n+\frac{1}{2}} \qquad (second\ order) \qquad (34)$$

It is applied for the determination of the time-dependent volumes J^{n+1} and is obtained successively, starting from the well-known initial state $J^{n=0}$. With regard to eq.(7) and eq.(9), the term $\dot{J}$ follows from eq.(29):

$$\dot{j}^{n+\frac{1}{2}} = \frac{\Delta}{\Delta \xi}\left[\hat{N}_\xi \begin{bmatrix} \dot{x} \\ \dot{y} \\ \dot{z} \end{bmatrix}\right]^{n+\frac{1}{2}} + \frac{\Delta}{\Delta \eta}\left[\hat{N}_\eta \begin{bmatrix} \dot{x} \\ \dot{y} \\ \dot{z} \end{bmatrix}\right]^{n+\frac{1}{2}}$$
$$+ \frac{\Delta}{\Delta \zeta}\left[\hat{N}_\zeta \begin{bmatrix} \dot{x} \\ \dot{y} \\ \dot{z} \end{bmatrix}\right]^{n+\frac{1}{2}} \qquad (35)$$

Eq.(35) with the transformation eq.(9) is dependent only on the Cartesian grid only velocities $\dot{x}, \dot{y}, \dot{z}$ and on the rotation angles α, β, γ as well as on the well-known metric terms of the initial state. All of these values are already provided by the determination of the motion-induced lines either for time level n or $n + 1$; see chapter 3. To the right of eq.(35), cell volume only J is not contained implicitly.

The computation of the volume change with the help of equations (33) and (34) is advantageous because the evaluation of a recurrence formula is adequate and efficiently applicable in combination with a time-stepping algorithm.

5 Numerical Results

In the following, the AMP model wing documented by Zingel, Jajes, Vogel [18] is examined. The theoretical results of a steady flow configuration and of a real unsteady mode shape are represented and compared with the measurements. In addition, the influence of the body is pointed out.

A computational C-H type grid with $200 \times 43 \times 32$ grid points in the ξ, η, ζ directions is used. The elliptic grid generation by the method of Steger and Sorensen [11] is based on an initial grid which is generated algebraically by the method of Smith and Erikson [10], and which is carried out by Neisius [8]. The distance of the wing to the outer grid line is 10 root profile lengths. Sectional views of the grid are emphasized in fig.4. Unsteady grid deformations are virtually simulated, as stated in this paper.

The virtual grid deformation method can also be applied for all kinds of conservation laws when viscous terms are taken into consideration. In these numerical examples, a viscid-inviscid interaction method developed by the author is used in which three-dimensional separation bubbles are simulated. In this context, only the validation with the measurements is important. Then, the influence of the elasticity of the wing on the aerodynamic forces can be judged in a correct manner and the importance of a grid deformation method is pointed out.

(1) Steady results

Fig. 5 shows pressure distributions in several span sections for the steady flow configuration $M_\infty = 0.78, Re = 3.49 \cdot 106, \alpha_0 = 2.85.$ The wind tunnel interference is taken into account by a reduction of the angle of attack of $0.5°$. The static elastic deformation is correctly represented by the grid generation. Theoretical and experimental data agree sufficiently.

The influence of the body on the wing should not be ignored in transonic flow. The shock is reduced and is positioned further upstream by the body. This effect appears in the spanwise direction up to the outer area of the wing. The shock line on the wing can be seen as a characteristic line on which disturbances are transported without damping.

(2) Unsteady results

An actual mode shape of the AMP model wing in transonic flow is regarded. It results from a pitching motion around the rotation axis $x_R = 0.39$, stimulated at the wing root by:

$$M_\infty = 0.78 \quad ; \quad Re = 3.49 \cdot 106 \quad ;$$
$$\alpha(\tau) = 2.35° + 0.22° sin(w^*\tau) \quad ; \quad \omega^* = 0.41$$

All of the deflections of the mode shape are very small values which correspond to the pitching amplitude of the wing root. The mode shape contains a phase lag of the wing motion in the spanwise direction. In addition, a rigid pitching motion without any elastic deformation - a simple mode shape approximation - is investigated.

Fig.6 and fig.7 show the first harmonics of pressure distributions at several profile sections of the wing and the first harmonics of the local lift and momentum distributions over the span for the rigid pitching motion and for the real elastic mode shape. In this case of low amplitude, the higher harmonics hardly apppear. It can be seen that the behavior in the outer area of the wing is different for both forms of motion especially in the imaginary parts. Therefore the elasticity should not be ignored for an aeroelastic analysis. The agreement between theory and experiment is more consistent than in the case of pure inviscid calculation; see Wegner [17].

The contrast between both forms of motion can also be seen in the change in the local aerodynamic coefficients of several span sections; see fig.8, and in the local mean power distribution over the span; see fig.9. The damping is relatively high during rigid pitching motion and there is no aerodynamic damping during the actual vibration mode. However, this does not yet indicate flutter instability.

The differences between theory and experiment in the inner area of the wing are mainly due to the body which is shown in the last figure. On the other hand, the body does not essentially influence the unsteady flow characteristics in the outer wing area, but nevertheless it influences the aerodynamic damping of the whole wing; see fig.9.

6 Conclusions

Elastic grid deformations are taken into account by a newly-presented calculation method of the unsteady conservation laws. The only prerequisite for this is that the intial computational grid is unique and smooth. The method is time efficient, especially for a physically time-dependent calculation. The simulation of an elastically moving wing allows for the prediction of aerodynamic instabilities. It cannot be approximated by rigid-body motion.

References

[1] Anderson, W.K., Thomas, J.L., Rumsey, C.L.: Extension and Applications of Flux-Vector Splitting to Unsteady Calculations on Dynamic Meshes, AIAA, Paper 87-1152, 1987.

[2] Batina, J.T.: Unsteady Euler Airfoiles Using Unstructured Dynamic Meshes, AIAA Journal, Vol. 28, No. 8, 1990.

[3] Brenneis, A., Eberle A.: Evaluation of an Unsteady Implicit Euler Code Against Two and Three-Dimensional Standard Configurations, AGARD-CP-507, San Diego, 1991.

[4] Försching, H.: New Ultra High Capacity Aircraft (UHCA) - Challenges and Problems from an Aerolastic Point of View, ZFW, Vol. 18, No. 4, pp. 219-231, 1994.

[5] Godonov, S.K., Propokov, G.P.: The Use of Moving Meshes in Gas-Dynamical Computations, USSR Comp. Math 12, 1972.

[6] Hoffren, J.: Unsteady Navier-Stokes Simulations of Airfoil Flows, Numerical Methods in Laminar and Turbulent Flow, Vol. 3, edited by C. Taylor, Pineridge Press, pp. 1065-1076, 1993.

[7] Jameson, A.: Time-Dependent Calculations Using Multigrid with Applications to Unsteady Flows Past Airfoils and Wings, AIAA paper 91-43675, Honolulu, 1991.

[8] Neisius, D.: Adaptive Netzgenerierung, DLR Forschungsbericht 96-09, Göttingen, 1996.

[9] Roache, P.J., Steinberg, S.: A New Approach to Grid Generation Using a Variational Formulation, AIAA paper 85-1527, 1985.

[10] Smith, R.E., Erikson, L.E.: Algebraic Grid Generation, Comput. Meth. in Appl. Mech. Eng. 64, 1987.

[11] Steger, J.L., Sorenson, R.L.: Automatic Mesh Point Clustering Near a Boundary in Grid Generation via Elliptic Partial Differential Equation, J. Comput. Phys. 33, 1979.

[12] Thomas, P.D., Lombard, C.K.: Geometric Conservation Law and its Application to Flow Computations on Moving Grids, AIAA Journal, 17 no. 10, pp. 1030-1037, 1979.

[13] Thompson, J.F., Wasi, Z.U.A., Martin, C.W.: Numerical Grid Generation, Elsevier, New York, 1985.

[14] Vinokur, M.: Conservation Equations of Gas-Dynamics in Curivilinear Coordinate Systems, J. Comp. Phys.14, pp. 105-125, 1974.

[15] Viviand, H.: Conservative Forms of Gas Dynamic Equations, La Recherche Aérospaciale No. 1974-1, pp. 65-688, 1974.

[16] Voss, R., Carstens, V.: Computation of Unsteady Transonic Flows Around Oscillating Airfoils Using Full Potential and Euler Equations, International Symposium of Aeroelasticity and Structural Dynamics, Aachen, 1989.

[17] Wegner, W.: Prediction of Unsteady Aerodynamic Forces for Elastically Oscillating Wings Using CFD Methods, CEAS Int. Forum on Aeroelasticity and Structural Dynamics, Manchester, 1995.

[18] Zingel, H., Jajes, U., Vogel, S.: Aeroelastisches Modellprogramm, Stationäre und Instationäre Luftkräfte, Deutsches Airbus DA/BRE/91-11, 1991.
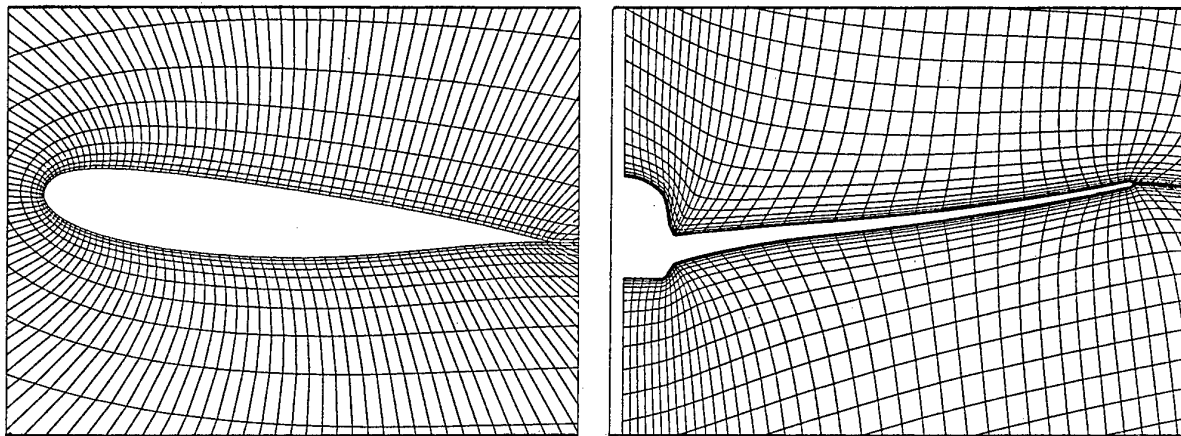
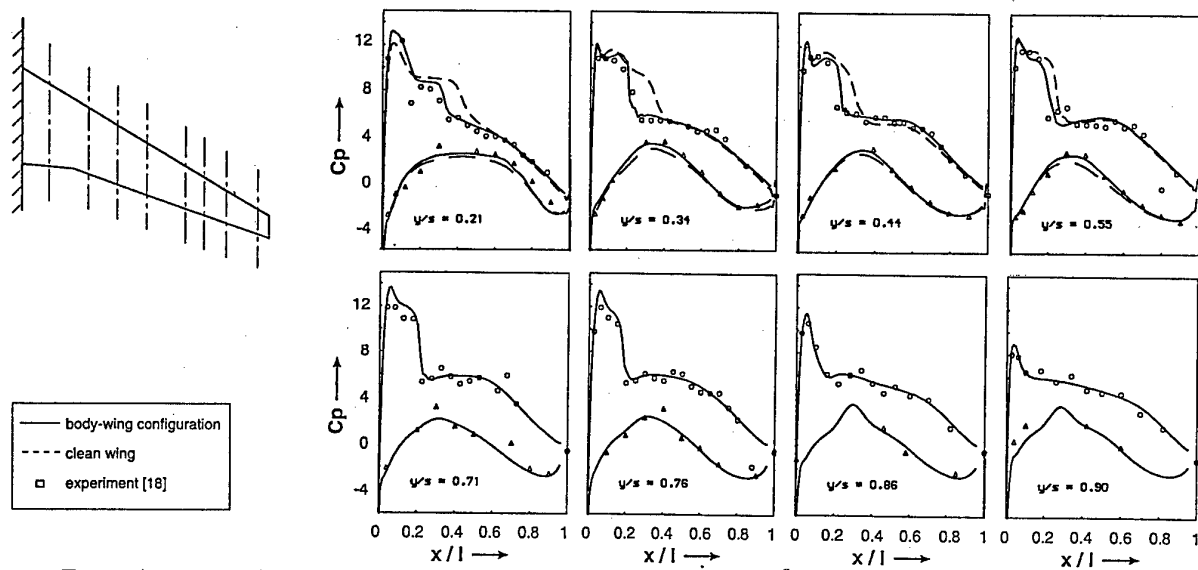Fig.4: AMP model wing; C-H type grid; $200 \times 43 \times 32$ cells.

body-wing configuration

- - - clean wing

□ experiment [18]

$\psi/s = 0.21$ $\psi/s = 0.34$ $\psi/s = 0.44$ $\psi/s = 0.55$

$\psi/s = 0.71$ $\psi/s = 0.76$ $\psi/s = 0.86$ $\psi/s = 0.90$

Fig.5: AMP model wing in steady flow; $M_\infty = 0.78$; $Re = 3.49 \cdot 10^6$; $\alpha_0 = 2.35°$

(AMP mode shape No. 574)

- - - - rigid pitching

elastic pitching

□ experiment [18]

re
im

$\psi/s = 0.57$ $\psi/s = 0.77$ $\psi/s = 0.86$ $\psi/s = 0.92$
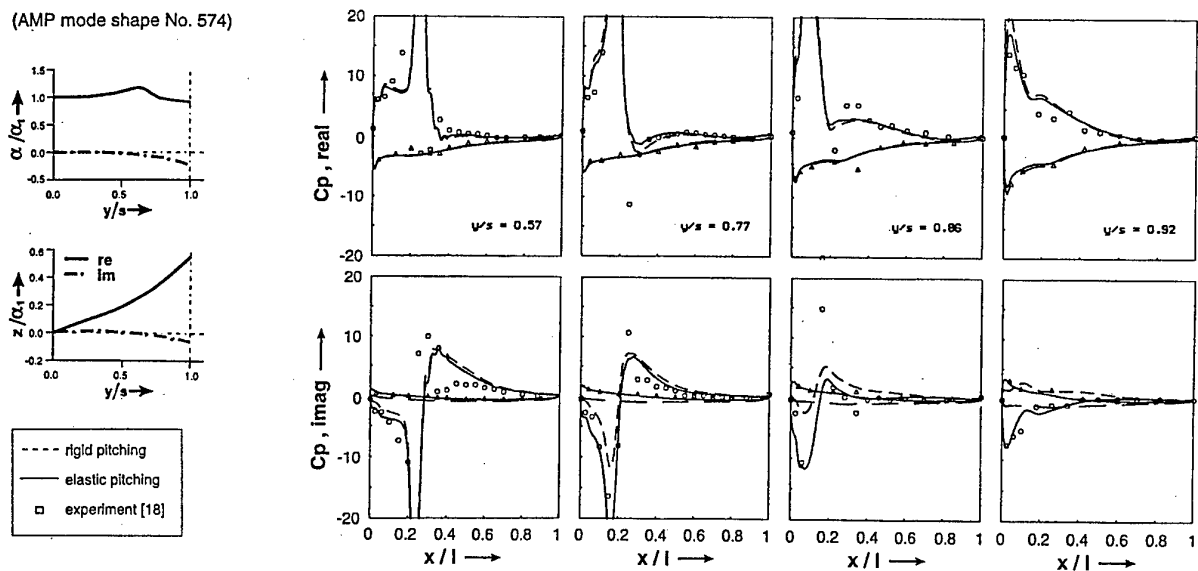
Fig.6: AMP model wing in harmonic pitching motion; first harmonics of pressure;
$M_\infty = 0.78$; $Re = 3.49 \cdot 10^6$; $\alpha_0 = 2.35°$; $\alpha_1 = 0.22°$; $\omega^* = 0.41$

(AMP mode shape No. 574)

- - - - rigid pitching
———— elastic pitching
□   experiment [18]
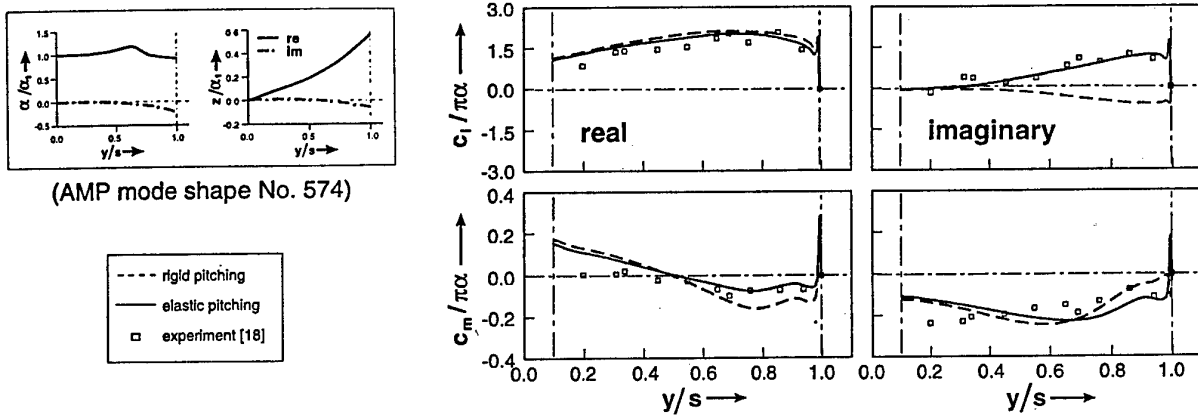
Fig.7: AMP model wing in harmonic pitching motion; lift and momentum distributions;
$M_\infty = 0.78$; $Re = 3.49 \cdot 10^6$; $\alpha_0 = 2.35°; \alpha_1 = 0.22°; \omega^* = 0.41$

- - - - rigid pitching
———— elastic pitching
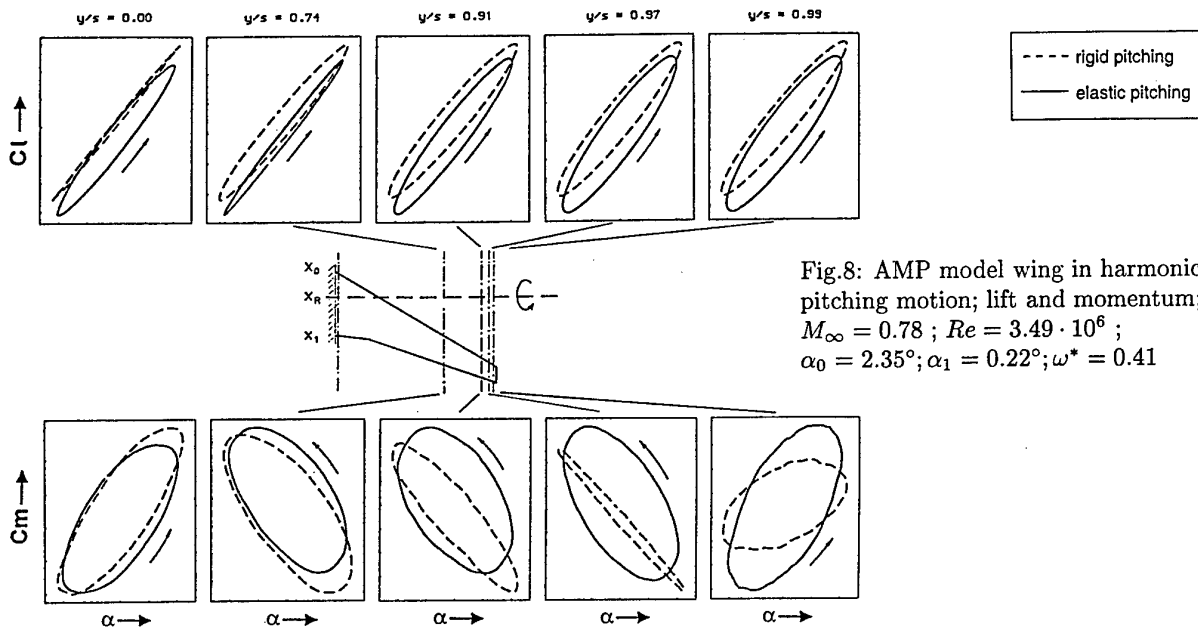
Fig.8: AMP model wing in harmonic pitching motion; lift and momentum;
$M_\infty = 0.78$; $Re = 3.49 \cdot 10^6$;
$\alpha_0 = 2.35°; \alpha_1 = 0.22°; \omega^* = 0.41$
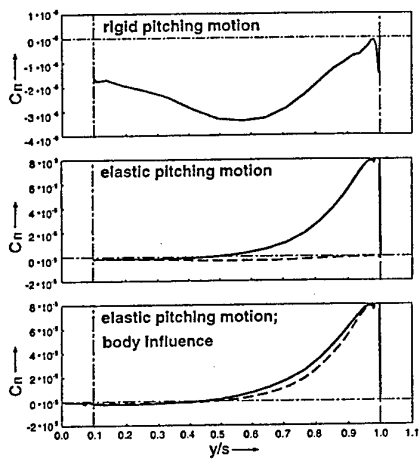
Fig.9: AMP model wing in harmonic pitching motion; mean power distributions
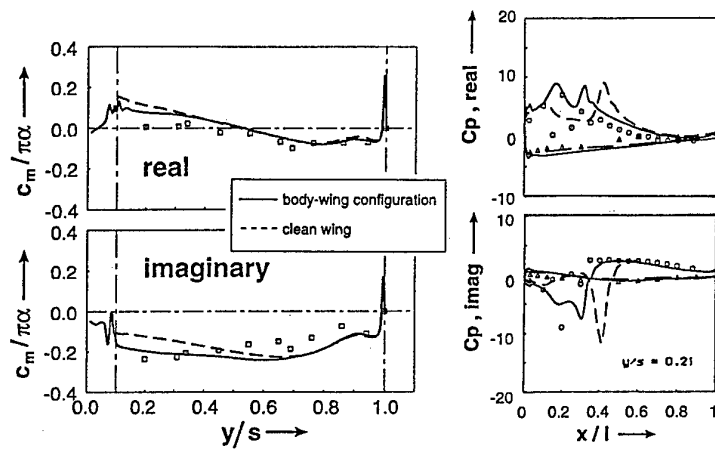
Fig.10: AMP model wing in harmonic pitching motion; influence of the body

APPLICATION DES EQUATIONS D'EULER LINEARISEES A LA PREVISION DU FLOTTEMENT

G.D. Mortchéléwicz

ONERA

29, Avenue de la Division Leclerc

92 322 Chatillon Cedex

France

1. SOMMAIRE

L'utilisation des équations d'Euler linéarisées dans le cadre d'excitations harmoniques des modes structuraux permet de calculer les forces aéroélastiques dans le domaine fréquentiel pour un coût calcul réduit, bien inférieur à celui obtenu par la méthode classique de simulation temporelle utilisant les équations d'Euler. Des exemples numériques permettent d'illustrer cette approche.

2. INTRODUCTION

La prévision de la stabilité aéroélastique des avions s'effectue en résolvant le système couplé aérodynamique structure dans le domaine fréquentiel et nécessite par conséquent la détermination des forces aéroélastiques sur la base modale de l'avion. Cette approche classique et opérationnelle avec l'utilisation de codes linéaires subsoniques ou supersoniques, devient particulièrement onéreuse dans le cadre des équations d'Euler malgré l'utilisation d'une condition de débit à la paroi en instationnaire, permettant de garder un maillage fixe au cours du temps (Réf 1). Le problème du flutter consistant en la recherche du début de l'instabilité, l'amplitude des mouvements simulés est faible. Cette hypothèse complémentaire permet d'envisager la linéarisation des équations d'Euler autour de la solution stationnaire, en considérant le mouvement du mode de structure comme une perturbation du premier ordre. Cette approche a été étudiée depuis de nombreuses années dans le cadre des turbomachines (Réf 2,3,4,5,6,7). Différentes excitations temporelles des modes structuraux peuvent être réalisées conduisant à des problèmes distincts :

- l'excitation est une fonction "large bande" (sa transformée de Fourier est à support compact dans l'intervalle $[-F_{max}, F_{max}]$, une solution instationnaire réelle peut être calculée dont la transformée de Fourier est à support compact dans le même intervalle (Réf 8) ;
- l'excitation est une exponentielle divergente, comme le propose Hounjet (Réf 9), une solution stationnaire d'un problème réel, doit être calculée ;
- l'excitation est harmonique en temps, une solution stationnaire d'un problème complexe, doit être calculée.

Après avoir présenté l'obtention du modèle des équations d'Euler linéarisées et les différentes approches liées à l'excitation temporelle des modes structuraux, le schéma utilisé est développé. Des applications numériques illustrent ces développements.

3. LES ÉQUATIONS D'EULER LINÉARISÉES

Les équations d'Euler s'écrivent sous la forme :

$$\frac{\partial}{\partial t}W + \frac{\partial}{\partial x}(f) + \frac{\partial}{\partial y}(g) + \frac{\partial}{\partial z}(h) = 0$$

où :

$$W = {}^t(\rho, \rho u, \rho v, \rho w, \rho E)$$
$$f = {}^t(\rho u, \rho u^2 + p, \rho uv, \rho uw, (E + p)u)$$
$$g = {}^t(\rho v, \rho uv, \rho v^2 + p, \rho vw, (E + p)v)$$
$$h = {}^t(\rho w, \rho uw, \rho vw, \rho w^2 + p, (E + p)w)$$

ρ désigne la masse volumique, (u, v, w) le champ de vitesse, $E = \rho e$ l'énergie.

Le champ instationnaire W est décomposé en un champ stationnaire W_s et une perturbation du premier ordre $\delta(W)$ dûe au mouvement de faible amplitude. En effectuant un développement limité au premier ordre, on obtient l'équation suivante pour le champ $\delta(W)$:

$$\frac{\partial}{\partial t}(\delta(W)) + \frac{\partial}{\partial x}(A(W_s)\delta(W)) + \frac{\partial}{\partial y}(B(W_s)\delta(W))$$

$$+ \frac{\partial}{\partial z}(C(W_s)\delta(W)) = 0$$

où $A(W_s)$, $B(W_s)$, $C(W_s)$ désignent les matrices jacobiennes des flux f , g , h , calculées pour le champ stationnaire.

Les conditions aux limites utilisent principalement les relations de compatibilité (Réf 10, 11). Elles sont écrites pour les cellules ayant au moins une face sur une frontière. Les valeurs prédites sont prises au centre de la cellule (extrapolation à l'ordre zéro). Les conditions aux limites principalement utilisées dans le cadre des équations d'Euler sont :

- une condition de glissement ;
- une condition de transpiration instationnaire permettant la simulation de déformations ou mouvement du profil au cours du temps. Cette condition aux limites consiste à écrire les quatre premières relations de compatibilité sur la base instantanée, et à compléter par la relation de glissement instationnaire $V.n(t) = V_p(t).n(t)$, où $n(t)$ et $V_p(t)$ désignent la normale et la vitesse instantanée du profil. La normale instationnaire de la face est obtenue en déplaçant chaque point de la frontière du déplacement instantané et en recalculant la normale à partir de cette position fictive des points ;

- à l'infini on privilégie la condition de non réflexion. Celle-ci consiste à considérer d'une part un domaine extérieur pour lequel l'état du fluide sont connues, et d'autre part le champ interne. L'application des relations de compatibilité entre ces deux domaines permet le calcul du champ frontière, et ce sans avoir besoin de spécifier le type de la frontière (amont ou aval), ou l'état du champ (subsonique ou supersonique).

Les conditions aux limites à appliquer, dans le cadre des équations d'Euler linéarisées, sont déduites de celles imposées pour les équations d'Euler par linéarisation au premier ordre. Pour la condition de glissement, la normale instationnaire doit être également linéarisée.

4. LES DIFFÉRENTES APPROCHES

Les modes de structure ont une évolution en temps et en espace définie par :

$$H(M,t) = H_s(M)f(t)$$

où $f(t)$ désigne une fonction temporelle, et $H_s(M)$ un mode structural.

4.1 Excitation large bande

La fonction $f(t)$ prend la forme :

$$f(t) = \frac{\sin(\omega_0\, t)}{\pi t}$$

La transformée de Fourier de cette fonction vaut 1 sur l'intervalle $[-\omega_0, \omega_0]$.

Les équations d'Euler linéarisées sont intégrées sur l'intervalle de temps $[-T_1, +T_2]$, $-T_1$ désigne un temps (négatif) où la fonction $f(t)$ est négligeable, et T_2 le temps où l'énergie transmise au système a été récupérée. Du fait de la linéarité des équations, le champ $\delta(W)$ a sa transformée de Fourier à support compact dans l'intervalle $[-\omega_0, +\omega_0]$. Il en est de même pour le coefficient de pression et les forces aéroélastiques. Une transformée de Fourier discrète (Réf 8) permet de les calculer. La résolution fréquentielle est donnée par la relation : $\Delta f = \frac{1}{T}$, $T = T_1 + T_2$.

Cette méthode pose les problèmes suivants :
- obligation d'utiliser un pas de temps uniforme pour résoudre les équations d'Euler linéarisées. En général les maillages tridimensionnels présentent quelques mailles dégénérées qui obligent à diminuer le pas de temps ;
- le temps d'intégration étant fixé par la finesse de la résolution fréquentielle de la transformée de Fourier, ceci conduit en général à un coût calcul prohibitif.

4.2 Excitation exponentielle divergente

La fonction $f(t)$ prend la forme :

$$f(t) = \exp(st)$$

Ceci conduit au problème stationnaire réel :

$$s\delta(W) + \frac{\partial}{\partial x}(A(W_s)\delta(W)) + \frac{\partial}{\partial y}(B(W_s)\delta(W))$$

$$+\frac{\partial}{\partial z}(C(W_s)\delta(W)) = 0$$

Les propriétés intrinsèques de cette méthode sont présentées avec le cas de l'excitation harmonique.

L'utilisation, proposée par Hounjet, de cette approche consiste à lisser par des fractions rationnelles les forces aéroélastiques ainsi obtenues et à étendre au domaine complexe le lissage obtenu.

4.3 Excitation harmonique

La fonction $f(t)$ prend la forme :

$$f(t) = \Re(\exp(\imath\omega t))$$

Ceci nous conduit à résoudre le problème complexe stationnaire suivant :

$$\imath\omega\delta(W) + \frac{\partial}{\partial x}(A(W_s)\delta(W)) + \frac{\partial}{\partial y}(B(W_s)\delta(W))$$

$$+\frac{\partial}{\partial z}(C(W_s)\delta(W)) = 0$$

Ce problème est résolu par une méthode pseudo instationnaire :

$$\frac{\partial}{\partial t}(\delta(W)) + \imath\omega\delta(W) + \frac{\partial}{\partial x}(A(W_s)\delta(W))$$

$$+\frac{\partial}{\partial y}(B(W_s)\delta(W)) + \frac{\partial}{\partial z}(C(W_s)\delta(W)) = 0$$

L'intérêt de cette approche est d'obtenir directement la valeur des forces aéroélastiques désirées dans le domaine complexe. Cependant ceci conduit à un doublement de la place mémoire nécessaire du fait de la nécessité de travailler en complexe.

Ces deux dernières approches permettent l'utilisation des techniques classiques d'accélération de la convergence : méthode du pas de temps local, méthode multigrille. Seule la première technique a été mise en oeuvre dans le travail présenté.

5. SCHÉMA NUMÉRIQUE UTILISÉ

Le schéma de Jameson-Lerat, développé par Liamis (Réf 12) dans le cadre du code CANARI (Réf 13), est utilisé pour résoudre ces équations. Ce schéma s'établit de la manière suivante :
- un maillage structuré multi blocs du domaine de calcul est réalisé ;
- une discrétisation spatiale des équations par une méthode de volume finie de type Jameson (Réf 14) est mise en oeuvre. Les inconnues sont prises au milieu des cellules. Le flux au travers d'une face s'obtient comme moyenne des flux de part et d'autre de cette face ;
- on obtient ainsi un système d'équations du premier ordre en temps que l'on intègre par un schéma de type Runge Kutta en ligne à K pas :

$$w^{(n,0)} = w^n$$

$$w^{(n,l)} = w^{(0)} + \alpha_l\Delta t\frac{\partial w}{\partial t}^{(n,l-1)} \quad, l = 1, ..., K$$

$$avec: \quad \alpha_l = \frac{1}{K - l + 1}$$
$$w^{n+1} = w^{(n,K)}$$

avec : $K \geq 2$.

Pour des problèmes non linéaires cette intégration n'est précise qu'à l'ordre 2. Par contre elle est précise à l'ordre K pour des problèmes linéaires à condition de définir les instants intermédiaires par :

$$t^{(l)} = (n + \alpha_l)\Delta t \quad , l = 0, 1, ..., K \quad , \alpha_0 = 0$$

- une viscosité artificielle dite "dépendant du pas de temps" est introduite, mettant en oeuvre des opérateurs du deuxième ordre pour capturer les chocs, et du quatrième ordre pour rendre le schéma dissipatif au sens de Kreiss. Cette viscosité est basée sur un senseur pression. Des conditions aux limites particulières, introduites par Eriksson (Réf 15), permettent de conférer à la viscosité de bonnes propriétés ;

- une phase implicite précise au second ordre, de type rayon spectral développée originellement par Lerat, Sidès, Daru (Réf 16) permet une augmentation significative du critère de stabilité de Courant-Friedrichs-Lewy (CFL), critère limitant le pas de temps par rapport au pas d'espace. Cependant dans les deux derniers cas une condition de stabilité conditionnelle demeure. Les formules suivantes ont pu être établies pour les excitations de type :

- exponentielle divergente : $\Delta t_{max} \leq \dfrac{1.767}{T_{nz}s}$;

- harmonique : $\Delta t_{max} \leq \dfrac{0.8}{\omega T_{nz}}$;

où T_{nz} désigne le facteur d'adimensionalisation en temps.

6. EXEMPLES D'APPLICATIONS

La présentation ci-dessus a été concrétisée avec le développement du code REELC, Résolvant les Équations d'Euler Linéarisées en Complexe, dans le cadre de l'excitation harmonique.

Le temps de calcul par pas de temps et par cellule sur le CRAY YMP de l'ONERA est de $3.033 \ 10^{-5}$ secondes.

Pour les applications considérées le nombre CFL est pris égal à 8.

6.1 Cas bidimensionnel : profil NACA 64A010

Ce cas test concerne le profil NACA 64A010 en écoulement infini pour un nombre de Mach amont de 0.796, à incidence nulle. Un mouvement de tangage quart avant est simulé. L'amplitude du mouvement est de 1.01 degré, la fréquence d'excitation est de 34.4 Hz. Ce cas test a été étudié expérimentalement par Davis (Réf 17). Du fait d'une légère dissymétrie entre le profil extrados et intrados la répartition du coefficient de pression stationnaire, figure 1, n'est pas parfaitement symétrique. La comparaison des évolutions de convergence entre les forces aéroélastiques et le champ stationnaire est présentée à la figure 2. L'obtention d'un état stationnaire pour les forces aéroélastiques, figures 3 et 4, est atteint rapidement : 200 à 300 itérations, alors que le champ stationnaire, lui, n'est pas convergé. Ce contexte favorable est à l'origine du gain de temps conséquent obtenu et permet ainsi l'utilisation du code pour des applications complexes. Le premier harmonique du coefficient de pression est comparé à la solution expérimentale à la figure 5.

6.2 Application industrielle au cas d'un avion militaire

Le calcul de flottement est effectué pour une aile Delta. Le maillage réalisé est de faible dimension (105780 cellules). Seize modes structuraux sont pris en compte. Deux nombres de Mach : 0.9 et 1.2 sont simulés. Les incidences sont ajustées de manière à obtenir une portance d'environ 90 000 Newton. Les matrices de forces aéroélastiques sont calculées pour treize fréquences réduites $k = \frac{\omega}{V}$:

$0., 0.001, 0.1, 0.2, 0.3, 0.4, 0.5, 0.65, 0.8, 1.0, 2.0, 3.0, 4.0$

La qualité de convergence n'est pas affectée par les valeurs des fréquences réduites considérées.

Pour les deux nombres de Mach considérés, les effets transsoniques sont négligeables, et les résultats obtenus peuvent être comparés à ceux obtenus par des méthodes linéaires. La figure 6 présentent cette comparaison sur le terme diagonal des matrices de forces aéroélastiques pour les deux nombres de Mach considérés. La simulation du flottement est donnée à la figure 7.

Le temps calcul a été limité à 600 secondes par configuration de calcul. Une matrice de forces aéroélastiques (16 modes, 1 fréquence) coûte 9600 secondes de temps CPU. Chaque calcul de flottement (13 fréquences) a nécessité 124800 secondes, soit pratiquement 35 heures.

Deux remarques doivent être faites :

- le code REELC permet le calcul de la fréquence nulle ;

- un tel calcul serait inenvisageable en simulant les équations d'Euler dans le temps et en simulant 4 périodes pour chaque fréquence et chaque mode.

7. CONCLUSIONS

L'utilisation des équations d'Euler linéarisées pour la simulation du flottement a été démontrée dans le cadre de l'excitation harmonique.

Les limitations de cette méthode sont liées au champ stationnaire qui ne peut évoluer :

- chocs et sillages figés ;

- mouvements de faibles amplitudes.

L'efficacité de la méthode développée est due :

- à l'utilisation de la méthode de pas de temps local ;

- à la possibilité (non traitée ici) de l'utilisation de méthodes multigrilles ;

- à la possibilité d'arrêter le calcul lorsqu'un niveau de convergence suffisant est obtenu sur les forces aéroélastiques généralisées ;

- à l'indépendance du temps de calcul en fonction de la fréquence de calcul.

REFERENCES

1. Sens, A.S. and Mortchéléwicz, G.D., "Implicit schemes for unsteady Euler equations on unstrucured meshes", International Forum on Aeroelasticity and Structural Dynamics, Strasbourg (France), May 24-26, 1993.

2. Hall, K.C., "A linearized Euler analysis of unsteady flows in turbomachinery", Rapport GTL 190, 1987.

3. Hall, K.C. and Crawley, E.F., "Calculation of unsteady flows in turbomachinery using the linearized Euler equations", AIAA Journal, Vol. 27, No 6, pp. 777-787, 1989.

4. Usab , W.J. and Verdon, J.M., "Advances in the numerical analysis of linearized unsteady cascade flows", ASME 90-GT-11, 1990.

5. Verdon, J.M. and Hall, K.C., "Development of a linearized unsteady aerodynamic analysis for cascade gust response predictions", Rapport NASA CR 4308, 1990.

6. Lindquist, D.R., "Computation of unsteady transonic flowfields using shock capturing and the linear perturbation Euler equations", Rapport GTL 207, 1991.

7. Hall, K.C. and Lorence, C.B., "Calculation of three-dimensional unsteady flows in turbomachinery using the linearized harmonic Euler equations", ASME 92-GT-136, 1992.

8. Soize, C., "Méthodes mathématiques en analyse du signal", Masson, 1993.

9. Hounjet, M.H.L., "How to make your aerodynamics in flutter calculations cheaper", NLR MP 85056 U, 1985.

10. Viviand, H., and Veuillot, J.P., " Méthodes pseudo-instationnaires pour le calcul d'écoulements transsoniques", Publication ONERA numéro 1978 4, Octobre 1978.

11. Meauze, G., and Fourmaux, A., "Numerical simulation of flows in axial and radial turbomachines using Euler solvers", cours au VKI, 15-18 juin 1987.

12. Liamis, N., "Méthodes implicites de résolution des équations d'Euler pour des écoulements tridimensionnels instationnaires dans des turbomachines", Université de Paris VI, 4 Octobre 1993.

13. Vuillot, A.M. and Couailler ,V. and Liamis, N., "3D turbomachinery Euler and Navier-Stokes calculation with multidomain Cell-Centered approach", AIAA Paper 93-2576, Monterey, California, June 28-July 1, 1993.

14. Jameson, A. and Schmidt, W. and Turkel, E., "Numerical solution of the Euler equations by finite volume methods using Runge Kutta time stepping schemes", AIAA 14 th Fluid and Plasma Dynamics Conference, Palo Alto, June 1981.

15. Eriksson, L.E., "Boundary conditions for artificial dissipation operators", FFA TN 1984-53, The Aeronautical Research Institute of Sweden, Stockolm 1984.

16. Lerat, A. and Sidès, J. and Daru, V., "An implicit finite volume method for solving the Euler equations", Lecture Notes in Physics, Vol. 16, 1982.

17. AGARD "Compendium of Unsteady Aerodynamic Measurements", AGARD REPORT No 702.

_ extrados   .. intrados   + exp. extrados o exp. intrados
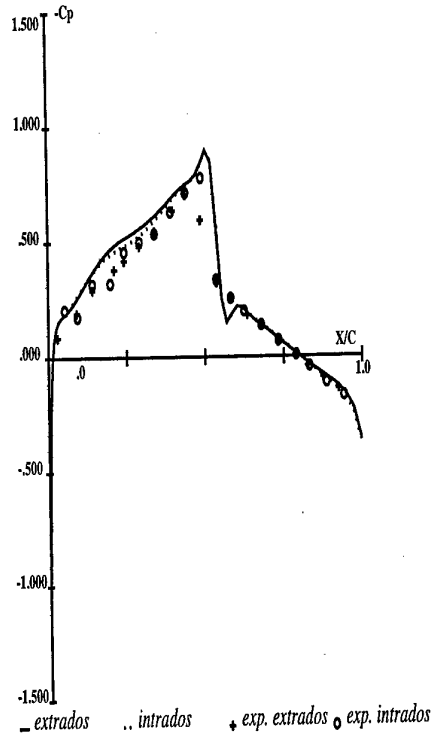
CANARI : Coefficient de pression stationnaire
Profil NACA 64A010
Mach=0.796 Incidence=0
Figure 1
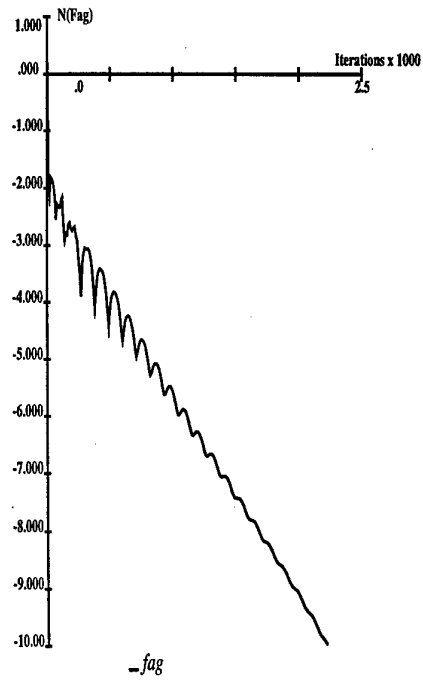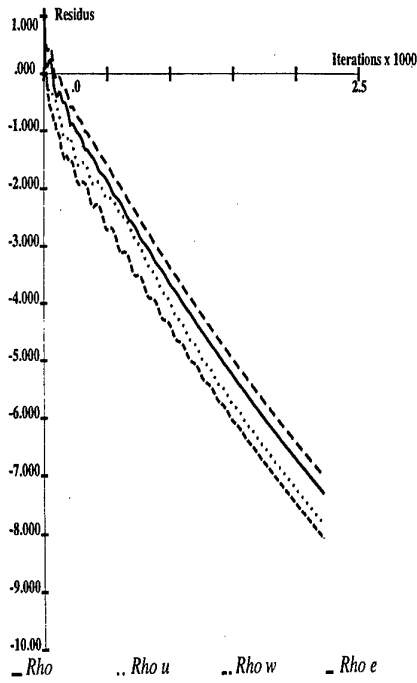
Convergence du champ de perturbation   Convergence des forces aéroélastiques

Profil NACA 64A010, Mach=0.796, incidence=0.
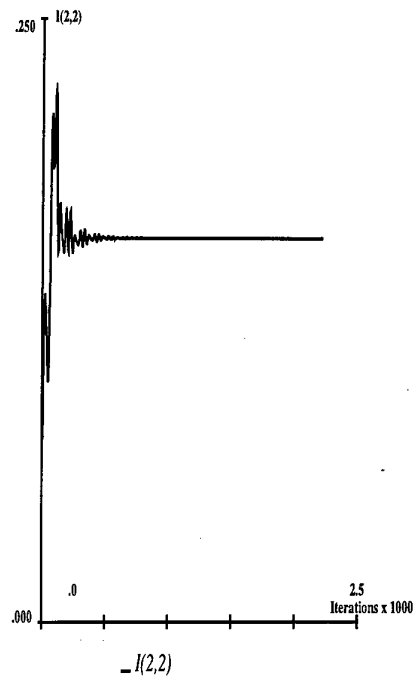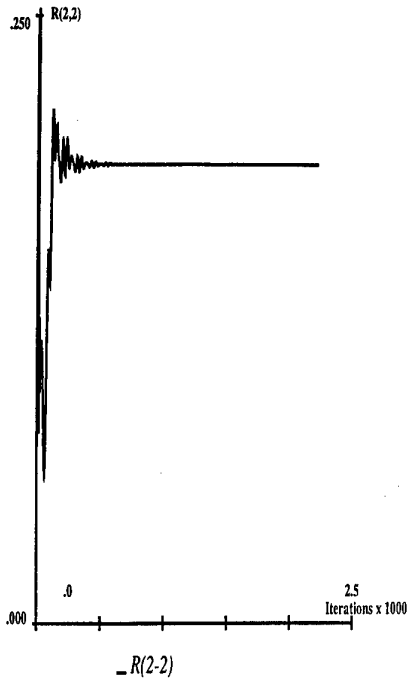REELC : Euler linéarisé, Mode de torsion, 34.4 hz
Figure 2
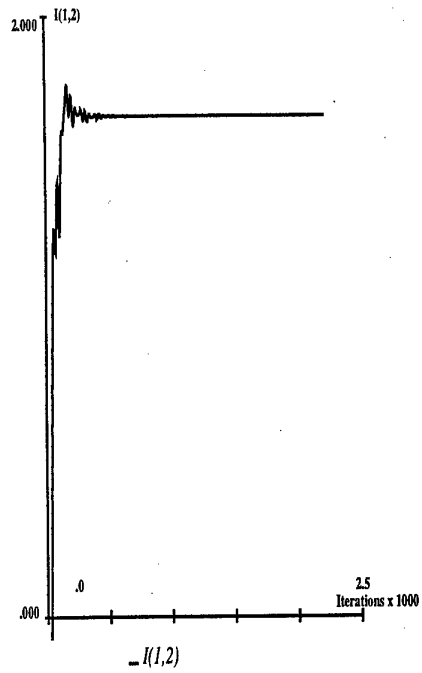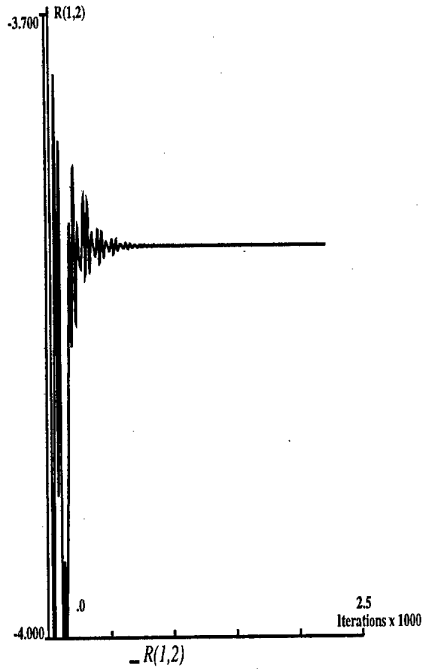
Evolution du terme $\Re(F(2,1))$ Evolution du terme $\Im(F(2,1))$

Profil NACA 64A010, Mach=0.796, incidence=0.
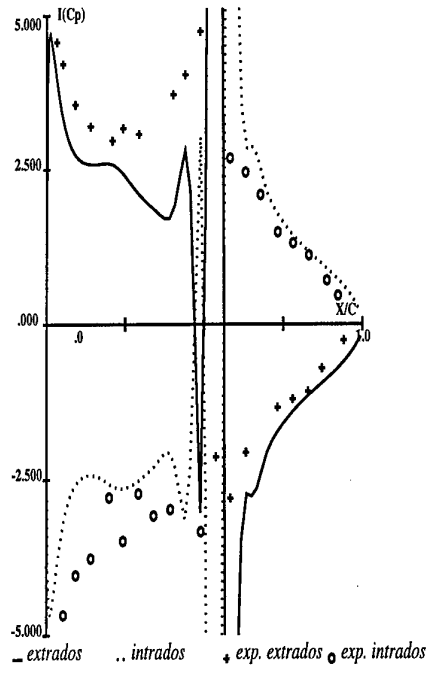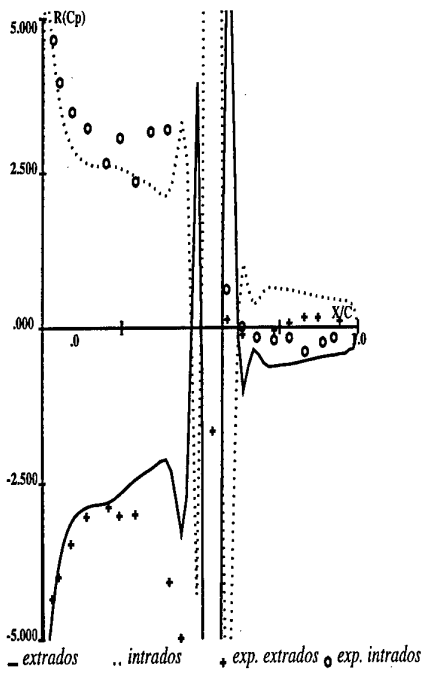REELC : Euler linéarisé, Mode de torsion, 34.4 hz
Figure 3

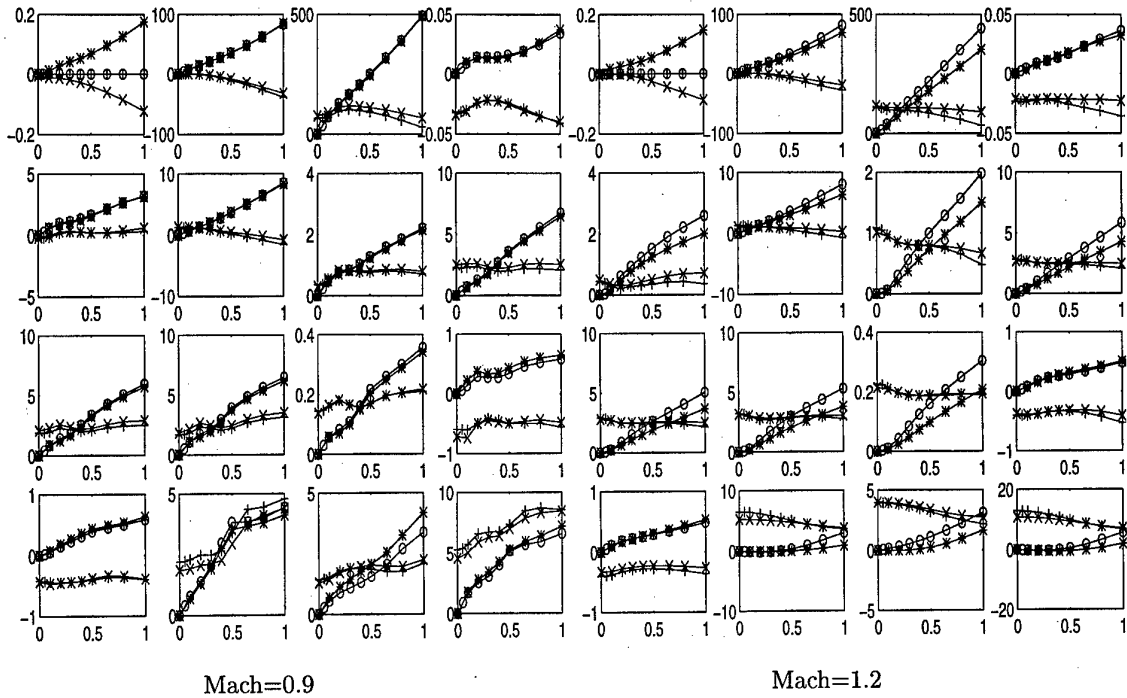Evolution du terme $\Re(F(2,2))$ Evolution du terme $\Im(F(2,2))$

Profil NACA 64A010, Mach=0.796, incidence=0.

REELC : Euler linéarisé, Mode de torsion, 34.4 hz

Figure 4

Partie réelle du premier harmonique   Partie imaginaire du premier harmonique

du coefficient de pression   du coefficient de pression

Profil NACA 64A010, Mach=0.796, incidence=0.

REELC : Euler linéarisé, Mode de torsion, 34.4 hz

Figure 5

Mach=0.9   Mach=1.2

Avion militaire
REELC : évolution du terme diagonal des matrices de forces aéroélastiques en fréquence
Comparaison avec des méthodes linéaires
Figure 6

Mach=0.9   Mach=1.2
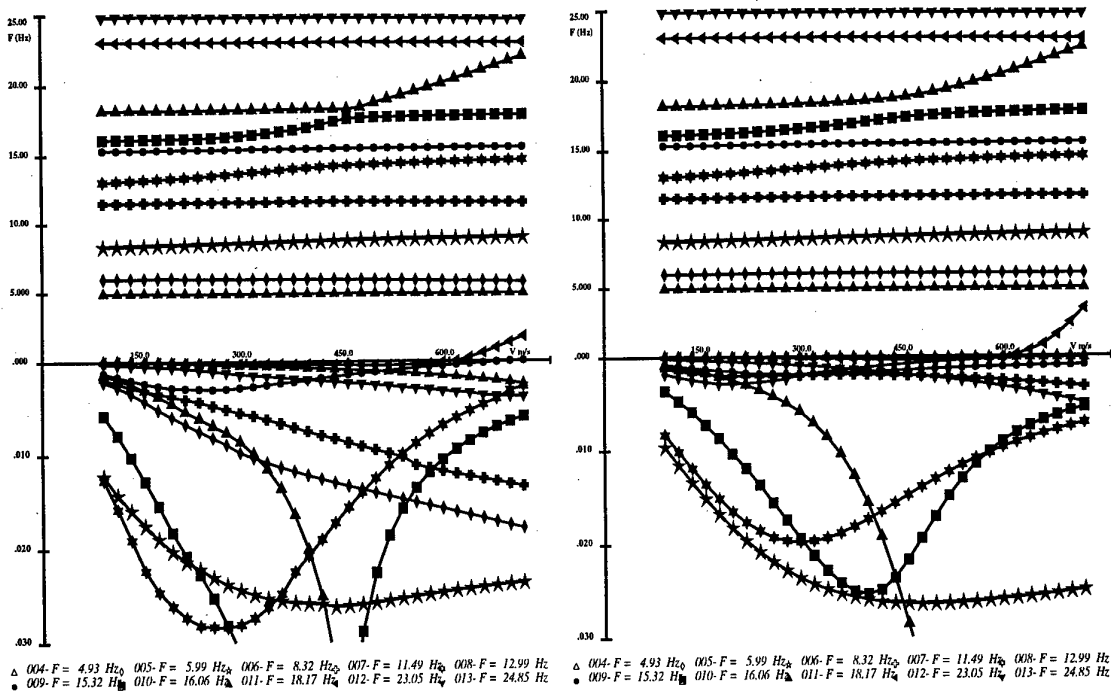
Avion militaire
REELC : Prévision du flottement
Figure 7

Fast Staggered Algorithms for the Solution of Three-Dimensional Nonlinear Aeroelastic Problems

Charbel Farhat *and Michel Lesoinne[†]

Department of Aerospace Engineering and Sciences

and Center for Aerospace Structures

University of Colorado at Boulder

Boulder, CO 80309-0429, U.S.A.

Abstract

We overview two sequential and parallel partitioned procedures that are popular in computational nonlinear aeroelasticity, and address their limitation in terms of accuracy and numerical stability. We propose two alternative serial and parallel staggered algorithms for the solution of coupled transient aeroelastic problems, and demonstrate their superior accuracy and computational efficiency with the flutter analysis of the AGARD Wing 445.6. We contrast our results with those computed by other investigators and validate them with experimental data.

1 Introduction

Several approaches have been proposed in the past for solving fluid/structure interaction problems on moving and deforming meshes, among which we note the two closely related Arbitrary Lagrangian Eulerian (ALE) [1,2] and dynamic mesh [3] methods. In the most general case, all of these methods can be used to formulate the fluid/structure problem of interest as a three-field problem: the fluid, the structure, and the dynamic mesh that is often represented by a pseudo-structural system. For example, in the case of the ALE method, a fluid/structure interaction problem can be described by the following set

*AIAA Associate Fellow
[†]AIAA Student Member

of coupled partial differential equations

$$
\begin{aligned}
\frac{\partial (JW)}{\partial t}\big|_\xi + J\nabla_x.(\mathcal{F}(W) - \dot{x}W) &= J\nabla_x.\mathcal{R}(W) \\
\rho_S \frac{\partial^2 u_S}{\partial t^2} - div(E:\epsilon(u_S)) &= b \\
\bar{\rho}\frac{\partial^2 x}{\partial t^2} - div(\bar{E}:\bar{\epsilon}(x)) &= 0
\end{aligned}
\tag{1}
$$

The first of Eqs. (1) is the ALE nondimensional conservative form of the Navier-Stokes equations and describes viscous flows on dynamic meshes. Here, t denotes time, a dot designates a derivative with respect to time, $x(t)$ denotes the time-dependent position or displacement of a fluid grid point (depending on the context of the sentence and the equation), ξ its position in a reference configuration, $J = det(dx/d\xi)$, W is the fluid state vector using the conservative variables, and $\mathcal{F}$ and $\mathcal{R}$ denote respectively the convective and diffusive fluxes. The second of Eqs. (1) is the classical elastodynamic equation where u_S denotes the displacement field of the structure and ρ_S its density, ϵ and E denote respectively the strain tensor and the tensor of elasticities, and b represents the body forces acting on the given structure. This equation can be replaced by another one describing a nonlinear behavior of the structure without affecting the issues raised and resolved in this paper. Finally, the third of Eqs. (1) governs the dynamics of the fluid moving grid. It is similar to the elastodynamic equation because the dynamic mesh is viewed here a pseudo-structural system. A bar notation is used to indicate that $\bar{\rho}$

is a fictitious density, and $\bar{E}$ is a fictitious tensor of elasticities. The Dirichlet, Neumann, and other boundary conditions intrinsic to each of the fluid and structure problems are omitted for simplicity.

Clearly, the first and third of Eqs. (1) are directly coupled. If u_F denotes the ALE displacement field of the fluid and p its pressure field, σ_S and σ_F the structure stress tensor and the fluid viscous stress tensor, Γ the fluid/structure interface boundary (wet boundary of the structure), and n the normal at a point to Γ, the fluid and structure equations are usually coupled by imposing that

$$
\begin{aligned}
\sigma_S.n &= -pn + \sigma_F.n & \text{on } \Gamma \\
u_S &= u_F & \text{on } \Gamma
\end{aligned}
\tag{2}
$$

The first of these two interface boundary conditions states that the tractions on the wet surface of the structure are in equilibrium with those on the fluid side of Γ. The second of Eqs. (2) expresses the compatibility between the displacement fields of the structure and the fluid at the fluid/structure interface. For inviscid flows, this second equation is replaced by the slip wall boundary condition

$$
\frac{\partial u_F}{\partial t}.n = \frac{\partial u_S}{\partial t}.n \qquad \text{on } \Gamma \tag{3}
$$

The structure and dynamic mesh motions are also coupled by the continuity conditions

$$
\begin{aligned}
x &= u_S & \text{on } \Gamma \\
\frac{\partial x}{\partial t} &= \frac{\partial u_S}{\partial t} & \text{on } \Gamma
\end{aligned}
\tag{4}
$$

The semi-discrete form of Eqs. (1) can be written as

$$
\begin{aligned}
\frac{d}{dt}(\mathbf{AW}) + \mathbf{F}^c(\mathbf{W},\mathbf{x},\dot{\mathbf{x}}) &= \mathbf{R}(\mathbf{W},\mathbf{x}) \\
\mathbf{M}\frac{d^2\mathbf{u}}{dt^2} + \mathbf{Ku} &= \mathbf{f}^{ext}(\mathbf{W}(\mathbf{x},t),\mathbf{x}) \\
\widetilde{\mathbf{M}}\frac{d^2\mathbf{X}}{dt^2} + \widetilde{\mathbf{D}}\frac{d\mathbf{X}}{dt} + \widetilde{\mathbf{K}}\mathbf{x} &= 0
\end{aligned}
\tag{5}
$$

where $\mathbf{x}$ is the displacement or position vector of the fluid moving grid points (depending on the context of the sentence and the equation), $\mathbf{W}$ is the fluid state vector, $\mathbf{A}$ results from the finite element/volume discretization of the fluid equations, $\mathbf{F}^c = \mathbf{F} - \dot{\mathbf{x}}\mathbf{W}$ is the vector of ALE convective fluxes, $\mathbf{F}$ denotes the vector of convective fluxes and $\mathbf{R}$ the

vector of diffusive fluxes, $\mathbf{u}$ is the structural displacement vector, $\mathbf{M}$ and $\mathbf{K}$ denote respectively the finite element mass and stiffness matrix of the structure, $\mathbf{f}^{ext}$ is the vector of external forces acting on the structure, $\widetilde{\mathbf{M}}$, $\widetilde{\mathbf{D}}$, and $\widetilde{\mathbf{K}}$ are fictitious mass, damping, and stiffness matrices associated with the fluid moving grid and constructed to avoid any parasitic interaction between the fluid and its grid, or the structure and the fluid moving grid. For example, $\widetilde{\mathbf{M}} = \widetilde{\mathbf{D}} = 0$ includes as particular cases the spring analogy based mesh motion scheme introduced in [3], and the continuum mechanics based mesh updating strategies advocated by many investigators.

The main objectives of this paper are to overview the solution by partitioned procedures of the semi-discrete Eqs. (5), address the limitations of conventional staggered algorithms that are often employed in computational aeroelasticity, and propose new ones with superior numerical properties and better computational efficiency.

2 Partitioned solution procedures

For simple and small-scale structural problems — for example, for an airfoil with one or two vibrational degrees of freedom — the second of Eqs. (1,5) can be recast in first-order form so that the fluid and the structural equations of motion can be combined into a single formulation (for example, see [4]). In such a case, a "monolithic" fully explicit or fully implicit treatment of the coupled fluid/structure equations of motion is possible. However, for more complex aeroelastic problems, each of the three components of the coupled problem described by Eqs. (1,5) has different mathematical and numerical properties, well-established but distinct numerical solvers, and readily available commercial software. Consequently, the simultaneous solution of Eqs. (1,5) by a monolithic scheme is in general computationally challenging, mathematically and economically suboptimal, and software-wise unmanageable.

Alternatively, Eqs. (1,5) can be solved by a partitioned or staggered procedure [3,5-8,16]. Partitions are spatially and temporally discretized by methods tailored to the underlying mathematical models and geometric complexity; for example finite volumes and a Runge-Kutta scheme for the fluid, and finite elements and a midpoint rule for the structure. The choice may also be influenced by software availability in each individual discipline. As a result, partitions are processed by different programs with interaction

effects treated as external vector inputs. They are advanced with their own time-step exchanging information at synchronization points only, a strategy that simplifies explicit/implicit treatment, subcycling, load balancing, software modularity, and replacements as better models and methods emerge in the fluid and/or structure disciplines. For example, an elementary yet popular partitioned procedure for solving Eqs. (5) goes as follows: (a) advance the structural system under a fluid induced load, (b) transfer the motion of the wet boundary of the structure to the fluid system using Eqs. (4) and the second of Eqs. (2) or Eq. (3), (c) update the fluid dynamic mesh accordingly, (d) advance the fluid system and compute new pressure and fluid stress fields, and (e) convert the new fluid pressure and stress fields into a structural load using the first of Eqs. (2). Clearly, such a partitioned procedure can be described as a loosely coupled solution algorithm. However, if accuracy and/or numerical stability require it, predictor/corrector iterations can be added within each cycle of this five-step staggered scheme, in which case the overall partitioned procedure becomes a strongly coupled solution algorithm. In the latter case, the partitioned solution method can be preferable over a monolithic scheme because of its modular and appealing mathematical and implementation features.

2.1 The conventional serial staggered algorithm

In this paper, the basic staggered algorithm outlined above is referred to as the Conventional Serial Staggered (CSS) procedure. It is graphically depicted in Fig. 1 where $\mathbf{U}$ denotes the structure state vector $(\mathbf{u} \quad \mathbf{u})^T$, $\mathbf{p}$ denotes the fluid pressure, the subscript n designates the n-th time-station, and the equalities shown at the top hold on the fluid/structure interface boundary Γ. The simplicity of the CSS method is attractive and apparently has earned it the highest popularity among partitioned procedures for aeroelastic computations in the time domain (for example, see [3,5,8]).

In most if not all aeroelastic problems, the fluid flow usually requires a finer temporal resolution than the structural vibration. Therefore in such applications, the coupling time-step Δt will be typically dictated by the time-step Δt_F that guarantees a certain accuracy in the flow solution, rather than the time-step $\Delta t_S > \Delta t_F$ that meets the accuracy requirements of the structural field. Using the same

time-step Δt in both fluid and structure computational kernels presents only minor implementational advantages. On the other hand, subcycling the fluid computations with a factor $n_{S/F} = \Delta t_S / \Delta t_F$ can offer substantial computational advantages; these advantages include savings in the overall simulation CPU time because in that case the structural field will be advanced fewer times, and savings in I/O transfers and/or communication costs when computing on a heterogeneous platform because in that case the fluid and structure kernels will exchange information fewer times.

The CSS method can be easily equipped with fluid subcycling as illustrated in Fig. 2.

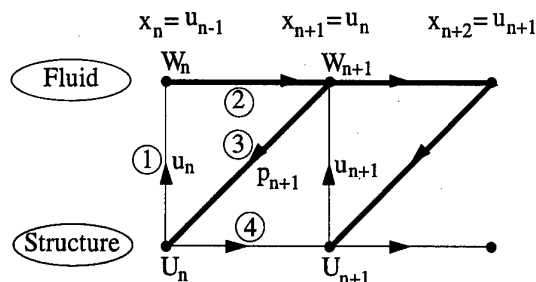Figure 1: CSS: the conventional serial staggered procedure

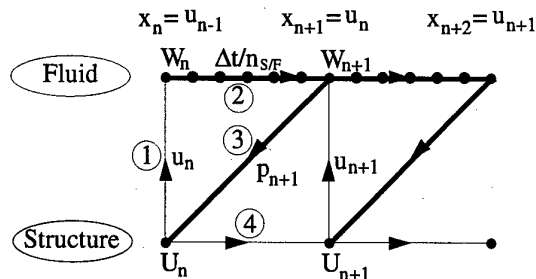

Figure 2: CSS: fluid subcycling

However, as noted for example in [4] and mathematically demonstrated in [7], the CSS procedure has the disadvantage that it is only first-order time-accurate, even when the underlying flow and structural solvers are second-order time-accurate. For this reason, references such as [4] and others advocate fully implicit monolithic solution procedures, and references such as [9] and others recommend full subiterations — that is, iterating on steps 1 to 4 in

Fig. 1 until Eqs. (5) are satisfied before advancing the fluid and structure responses from one coupled time-step to another. While these alternatives certainly remedy the low accuracy issue of the CSS procedure, two reservations can be formulated against them: (a) as stated earlier, monolithic schemes are not realistic for complex aeroelastic problems where the structure is given the same attention and importance as the fluid (i.e., a nonlinear flexible multibody dynamics system and ultimately a linear or nonlinear flexible full aircraft configuration), and b) it has been shown for other classes of fluid/structure interaction problems that the computational cost associated with full subiterations can offset the benefit of the larger time-step they can allow [10]. A third alternative that is presented in this paper is a new subiteration-free staggered algorithm that has the same computational complexity as the CSS procedure, and yet delivers a superior accuracy that is at least similar to that of a monolithic implicit scheme or a strongly coupled (full subiterations) partitioned method. Before discussing this new alternative in details, we overview another partitioned procedure that is gaining popularity on parallel computers.

2.2 A straightforward parallel staggered algorithm

Intra-field parallelism — that is, parallelism within each of the fluid, structure, and mesh motion sub-problems — can be implemented in the CSS procedure as in any Computational Fluid Dynamics (CFD) or computational structural mechanics (CSM) algorithm. However, the CSS method inhibits inter-field parallelism: the structural system cannot be advanced in time until the fluid system is first updated.

Advancing the fluid and structural systems simultaneously and in a loosely coupled manner is appealing because it has the potential of reducing the total aeroelastic simulation time. Recently, the authors of [11] have proposed a partitioned procedure for aeroelastic problems where inter-field parallelism is implemented as shown in Fig. 3. Essentially, the fluid and structure kernels are executed in parallel during the time-interval $[t_n, t_{n+1}]$. Inter-field communication or I/O transfer is needed only at the beginning of each time-interval. In the sequel, we refer to this simple parallel staggered algorithm as the Conventional Parallel Staggered (CPS) procedure. Two of the objectives of this paper are to show that the CPS

method requires relatively small time-steps in order to be numerically stable and sufficiently accurate, and to propose an improved version that has better accuracy properties.
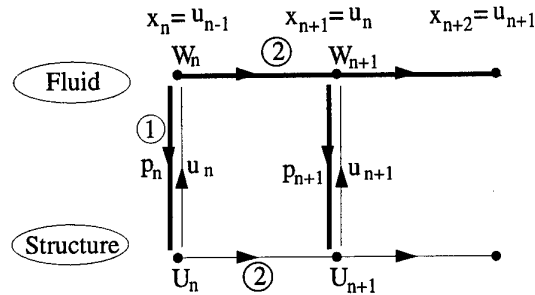

Figure 3: CPS: the conventional parallel staggered procedure

3 An improved serial partitioned solution procedure

Explaining the basic idea behind the improved serial partitioned procedure proposed in this paper requires recalling first an important notion pertaining to flow computations on dynamic meshes.

3.1 Impact of the geometric conservation law

A sufficient condition for a numerical method proposed for the solution of a flow problem on a moving grid to be mathematically consistent is that it predicts exactly a uniform flow. In [12] it was shown that this requirement is satisfied only when the numerical scheme chosen for solving the flow problem, and the algorithm constructed for updating the dynamic mesh, satisfy a discrete Geometric Conservation Law (GCL) that is similar in its principle to the GCL condition that was first pointed out in [13] for structured grids and finite difference schemes. More specifically, it was proved in [12,13] that for first- and second-order time-accurate ALE finite volume

and ALE stabilized finite element methods, the velocity of the dynamic mesh must be computed as

$$\dot{\mathbf{x}} = \frac{\mathbf{x}_{n+1} - \mathbf{x}_n}{\Delta t} \qquad (6)$$

in order to satisfy the GCL.

Note that Eq. (6) is intuitive and has been "naturally" used by several investigators independently from any GCL consideration (for example, see [3]). However, we show next that the impact of Eq. (6) on the solution of Eqs. (5) is significant.

The semi-discrete equations describing the motion of the structure are usually solved by a second-order time-accurate scheme where

$$\dot{\mathbf{u}} \neq \frac{\mathbf{u}_{n+1} - \mathbf{u}_n}{\Delta t} \qquad (7)$$

It follows that if a basic partitioned procedure satisfies the GCL and the first of the continuity equations (4), it violates the second of these interface conditions, as well as the slip condition (3) when the flow is inviscid and discretized by an ALE (or dynamic mesh) formulation. Indeed, if $\mathbf{x} = \mathbf{u}$ is enforced at the fluid/structure interface and the velocity of the dynamic mesh at the interface boundary Γ is computed via Eq. (6), the following holds if the structural equations of motion are time-integrated by a second-order scheme

$$\dot{\mathbf{x}} = \frac{\mathbf{x}_{n+1} - \mathbf{x}_n}{\Delta t} = \frac{\mathbf{u}_{n+1} - \mathbf{u}_n}{\Delta t} \neq \dot{\mathbf{u}} \qquad \text{on} \quad \Gamma \quad (8)$$

In particular, the reader can verify that when the CSS procedure is equipped with Eq. (6) in order to satisfy the GCL and with a second-order structural time-integrator, it violates the continuity of the velocity field across the fluid/structure interface Γ. Hence, under such conditions, the CSS procedure introduces an error in the prediction of the energy exchange between the fluid and the structure on the boundary Γ, which practically limits it to small time-steps to maintain a certain level of accuracy.

3.2 A displacement and velocity conserving staggered algorithm

Here, we propose a staggered algorithm for the solution of the aeroelastic semi-discrete equations (5) that can satisfy the GCL without violating either of the interface continuity conditions (3,4). Hence, unlike the CSS method, this algorithm does not introduce errors in the prediction of the energy exchange

between the fluid and the structure on the interface boundary Γ. We label this method the Improved Serial Staggered (ISS) procedure because, as shown in Section 6, it is capable of computing highly accurate aeroelastic solutions using coupling time-steps that are at least comparable to those afforded by fully implicit monolithic schemes and strongly coupled solution methods.

The description of the ISS method proposed in this paper goes as follows

(1) given some initial conditions $\mathbf{W}_0$, $\mathbf{u}_0$ and $\dot{\mathbf{u}}_0$, initialize the fluid dynamic mesh motion as follows

$$\mathbf{x}_{-\frac{1}{2}} = \mathbf{u}_0 - \frac{\Delta t}{2}\dot{\mathbf{u}}_0 \quad \text{on} \ \Gamma \qquad (9)$$

For $n = 1, ...$

(2a) set

$$\dot{\mathbf{x}}_n = \dot{\mathbf{u}}_n \qquad (10)$$

(2b) update the fluid dynamic mesh as follows

$$\mathbf{x}_{n+\frac{1}{2}} = \mathbf{x}_{n-\frac{1}{2}} + \Delta t \dot{\mathbf{x}}_n \qquad (11)$$

(3) solve the flow problem to obtain the fluid state vector $\mathbf{W}_{n+\frac{1}{2}}$

(4) extract the pressure field on Γ from $\mathbf{W}_{n+\frac{1}{2}}$ and convert it into a structural load

(5) advance the structural system using the second-order time-accurate *midpoint rule*

PROPOSITION 1. Using the ISS procedure, the following relation holds

$$\mathbf{x}_{n-\frac{1}{2}} = \mathbf{u}_n - \frac{\Delta t}{2}\dot{\mathbf{u}}_n \quad \text{on} \ \Gamma \qquad (12)$$

PROOF. Eq. (12) holds for $n = 0$ (see Eq. (9)). Assuming it holds for a given n, Eqs. (10,12) can be substituted into Eq. (11) to obtain

$$
\begin{aligned}
\mathbf{x}_{n+\frac{1}{2}} &= \mathbf{x}_{n-\frac{1}{2}} + \Delta t \dot{\mathbf{x}}_n \\
&= \mathbf{u}_n - \frac{\Delta t}{2}\dot{\mathbf{u}}_n + \Delta t \dot{\mathbf{u}}_n \qquad (13) \\
&= \mathbf{u}_n + \frac{\Delta t}{2}\dot{\mathbf{u}}_n \quad \text{on} \ \Gamma
\end{aligned}
$$

Since the structural problem is solved by the midpoint rule, it follows that

$$\mathbf{u}_{n+1} - \mathbf{u}_n = \frac{\Delta t}{2}(\dot{\mathbf{u}}_n + \dot{\mathbf{u}}_{n+1}) \qquad (14)$$

Finally, from Eqs. (13,14) we derive

$$\mathbf{x}_{n+\frac{1}{2}} = \mathbf{u}_{n+1} - \frac{\Delta t}{2}\dot{\mathbf{u}}_{n+1} \quad \text{on } \Gamma \qquad (15)$$

which completes the proof by induction of *PROPO-SITION 1.*

PROPOSITION 2. The ISS procedure described above satisfies Eq. (6) (implied by the GCL) and both interface continuity equations (4).

PROOF. Define

$$\mathbf{x}_n = \frac{\mathbf{x}_{n-\frac{1}{2}} + \mathbf{x}_{n+\frac{1}{2}}}{2} \qquad (16)$$

Substituting Eq. (11) into Eq. (16) gives

$$\mathbf{x}_n = \mathbf{x}_{n-\frac{1}{2}} + \frac{\Delta t}{2}\dot{\mathbf{x}}_n \qquad (17)$$

and substituting Eqs. (10,12) into Eq. (17) gives

$$\mathbf{x}_n = \mathbf{u}_n \quad \text{on } \Gamma \qquad (18)$$

which concludes the proof of *PROPOSITION 2.*

REMARK 2. From Eq. (13), it follows that updating the fluid dynamic mesh using Eq. (11) is equivalent to updating it using

$$\mathbf{x}_{n+\frac{1}{2}} = \mathbf{u}_n + \frac{\Delta t}{2}\dot{\mathbf{u}}_n \qquad (19)$$

The second proposition summarizes the main idea behind the design of the ISS method, and highlights the major difference between this improved serial staggered procedure and the conventional serial staggered procedure CSS overviewed in Section 2.1.

The ISS method advocated in this paper is illustrated in Fig. 4. It is subiteration-free, has a computational complexity that is similar to that of the CSS method, and exhibits superior numerical properties that are highlighted in Section 6. It can be equipped with fluid subcycling as for the case of the CSS procedure (see Fig. 2).

4   An improved parallel partitioned solution procedure

The mathematical analysis performed in [7] for a linearized aeroelastic model problem suggests that for the CPS procedure, inter-field parallelism is achieved at the expense of amplified errors in the fluid and structure responses. This is not surprising
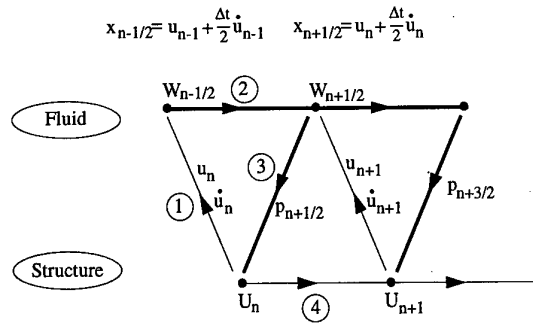
Figure 4: ISS: the improved serial staggered procedure

given that the CPS method does not implement any feedback between the fluid and the structure within one coupled time-step. In order to improve the accuracy of this basic parallel time-integrator, we propose to exchange information between the fluid and structure kernels at half-step. We label the corresponding staggered algorithm the Improved Parallel Staggered (IPS) procedure, and depict it graphically in Fig. 5.
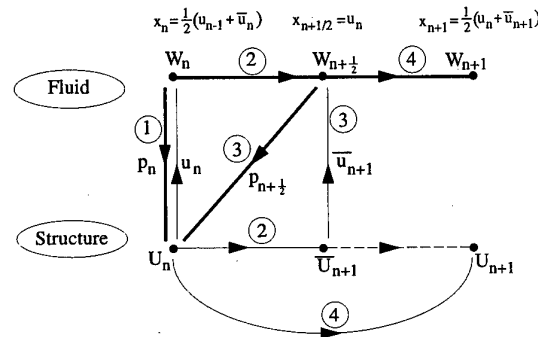
Figure 5: IPS: the improved parallel staggered procedure

The computations performed during the first half of a cycle of the IPS procedure are identical to those that are performed during a cycle of the CPS method, except that the fluid system is advanced only up to $t_{n+\frac{1}{2}}$, while the structure is time-integrated all the way to t_{n+1}. Let $\mathbf{W}_{n+\frac{1}{2}}$ and $\overline{\mathbf{U}}_{n+1}$ denote respectively the fluid and state vectors computed during the first half of an IPS cycle. At $t_{n+\frac{1}{2}}$, the fluid and structure kernels exchange the most recently computed pressure, displacement and ve-

locity information. In the second half of the same IPS cycle, the fluid system is advanced from $t_{n+\frac{1}{2}}$ to t_{n+1} using the structural state vector $\overline{\mathbf{U}}_{n+1}$, and the structural response is simultaneously re-computed using the fluid state vector $\mathbf{W}_{n+\frac{1}{2}}$. Hence, the evaluation of $\overline{\mathbf{U}}_{n+1}$ can be interpreted as a prediction step whose objective is to guess the next position of the fluid/structure boundary Γ in order to update the fluid dynamic mesh using a better information than $\mathbf{U}_n$. Note that the IPS procedure can be equipped with fluid subcycling as for the case of the CSS method (see Fig. 2).

From the results of the mathematical analysis performed in [7] for a linearized aeroelastic model problem, we can expect the IPS method to have a better accuracy than the CPS procedure, at the expense of one additional communication step or I/O transfer during each coupled time-integration cycle, and one additional flow solution if no subcycling is performed (the additional structure solution is performed in parallel and therefore does not consume additional parallel CPU time)

5 Flow, structure, load, and mesh motion solvers

The three-dimensional unsteady implicit flow solver considered in this paper operates on unstructured dynamic tetrahedral meshes. It combines a Roe upwinding scheme for the computation of the convective fluxes with a Galerkin centered approximation for the approximation of the viscous terms. Second-order accuracy is achieved through the use of a piecewise linear interpolation method that follows the principle of the Monotonic upwind Scheme for Conservative Laws (MUSCL). An ALE formulation [2,14] is incorporated into this fluid solver to allow the grid points to displace in a Lagrangian fashion, or be held fixed in an Eulerian manner, or be moved in some specified way to give a continuous and automatic rezoning capability, depending on the needs of the physical problem to be solved. Time-integration is carried out by a second-order implicit backward difference scheme whose implementation satisfies the geometric conservation laws (GCL). This three-dimensional unstructured and unsteady implicit flow solver is parallelized using domain decomposition [14].

In all application problems discussed in the next

section, the structure is represented by a finite element model, and its dynamic behavior is predicted using the *true* displacement, velocity, and acceleration degrees of freedom (d.o.f.) rather than modal or other generalized coordinates. The corresponding semi-discrete equations of dynamic equilibrium are time-integrated with the implicit second-order midpoint rule.

6 Applications

In order to illustrate the issues, support the claims, and validate the new algorithms presented in this paper, we consider the flutter analysis of the AGARD Wing 445.6 [15]. This wing is an AGARD standard aeroelastic configuration with a 45 degrees quarter-chord sweep angle, a panel aspect ratio of 1.65, a taper ratio of 0.66, and a NACA 65A004 airfoil section. The model selected here is the so-called 2.5-ft weakened model 3 whose measured modal frequencies and wind-tunnel flutter test results are reported in [15], and for which computational aeroelastic data can be found in [8,16].

An undamped finite element model of the wing with 800 triangular composite shell elements and 2646 d.o.f. is constructed using the information given in [15]. It yields natural mode shapes and frequencies that are similar to those derived experimentally. More specifically, the frequencies associated with the first four natural modes of this finite element model are respectively 9.83 Hz, 39.54 Hz, 50.50 Hz, and 96.95 Hz. They differ from the experimental ones by only 2.5 %, 3.6 %, 4.5 %, and 5.9 %, respectively. These modal results are included here only for validation purposes; we remind the reader that our flutter analysis is conducted using the true finite element representation of the wing and not its modal coordinates.

Two three-dimensional unstructured tetrahedral CFD Euler meshes are generated. The first one is coarse as it contains 22014 vertices only; it is this mesh that is intended for flutter analysis. The second one is finer: it contains 331233 vertices and is intended only for flutter convergence verification. Note that our first mesh is coarser than the CFD grid with 45180 nodes that was used in [8] and an order magnitude coarser than that with 261129 grid points that was employed in [16] for similar flutter analyses.

All computations discussed next are carried out on an IBM SP2 parallel computer. A single processor

is assigned to the finite element structural model, 3 processors to the coarse CFD mesh, and 40 processors to the fine one.

6.1 Mesh convergence verification

First, the freestream conditions are set to $M_\infty = 0.901$, $\rho_\infty = 1.117 \times 10^{-7}$, and $p_\infty = 10.0$. The last two values are dimensional values with the same units as in [15]. The finite element structural model is perturbed along its first bending mode, and two steady state solutions are computed around the deformed configuration of the wing using both the coarse and fine CFD meshes. Next, this perturbation is used as an initial condition, and the aeroelastic response of the wing is computed using both the coarse and fine CFD meshes, and the ISS procedure with a dimensional coupling time-step $\Delta t = 10^{-3}$ and with $\Delta t/2$. In all cases and for all subsequent aeroelastic computations, the dimensional global fluid time-step is set to $\Delta t_F = \min(5 \times 10^{-4}, \Delta t)$. Hence, the dimensional coupling time-step $\Delta t = 10^{-3}$ leads to a subcycling factor $n_{S/F} = 2$. Note also that this dimensional coupling time-step corresponds to sampling the period of the first torsional mode of the dry wing in 25 points, as usually done for a fully implicit monolithic solution algorithm. The obtained dimensional lift histories are shown in Fig. 7. These results indicate that for the given freestream conditions, the wing does not flutter, which is consistent with the experimental results detailed in [15]. They also show that the spatial resolution of the coarse CFD mesh and the size of the dimensional coupling time-step $\Delta t = 10^{-3}$ are adequate for the aeroelastic analysis in the time domain of the AGARD Wing 445.6. In particular, note that for the coarse CFD mesh, the curves for $\Delta t = 10^{-3}$ and $\Delta t = 5 \times 10^{-4}$ are undistinguishable. Hence, for the sake of efficiency, all subsequent aeroelastic computations are performed using the coarse CFD mesh, and for ISS, a dimensional coupling time-step $\Delta t = 10^{-3}$.

6.2 Benchmark of the improved staggered algorithms

Next, the previous freestream conditions are kept the same and the aeroelastic response of the wing is recomputed using the CSS, CPS, and IPS algorithms and various time-steps.
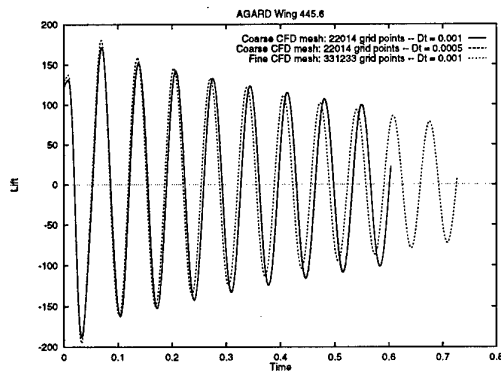
Figure 6: Lift histories predicted by ISS using $\Delta t = 10^{-3}$

The results reported in Fig. 8 show that for a dimensional $\Delta t = 10^{-3}$, CSS predicts an unstable behavior of the wing. However, after reducing the dimensional time-step to $\Delta t = 2 \times 10^{-4}$, CSS reproduces the same stable response as ISS (curves are undistinguishable in Fig. 8). In the absence of a formal theoretical analysis of the solution of the transient nonlinear aeroelastic semidiscrete problem (5) by partitioned procedures, we can conclude that either the domain of numerical stability of the CSS procedure is more restrictive than that of the ISS method, or that the ISS procedure has higher accuracy properties than the CSS method. In any case, this example highlights the superior performance of the proposed ISS procedure which is shown to be capable of reproducing the same result as the CSS method using a coupling time-step that is 5 times larger than can be afforded by the CSS algorithm.

Similarly, the lift histories reported in Fig. 9 and Fig. 10 show that the coupling time-step has to be reduced by a full order magnitude to $\Delta t = 10^{-4}$ before the CPS procedure converges to a stable response, and by a factor of 3 to $\Delta t = 3.3 \times 10^{-4}$ before the IPS method also converges to a stable behavior and reproduces a response that is undistinguishable from that prediced by ISS with $\Delta t = 10^{-3}$. Once again, this demonstrates that inter-field parallelism compromises numerical stability and/or accuracy, and that the improved parallel staggered procedure IPS proposed in this paper has better stability and/or accuracy properties than the conventional parallel staggered method CPS [11]. For $\Delta t = 3.3 \times 10^{-4}$, the IPS procedure performs two flow solutions per staggered cycle (recall that $\Delta t_F = \min(5 \times 10^{-4}, \Delta t) \to n_{S/F} = 1$); on the other hand

for $\Delta t = 10^{-4}$, the CPS method performs only one flow solution per staggered cycle. However, the IPS method allows a time-step that is 3.3 times larger than that of the CPS algorithm, and therefore for this problem, the IPS method is 1.6 times faster than the CPS procedure.
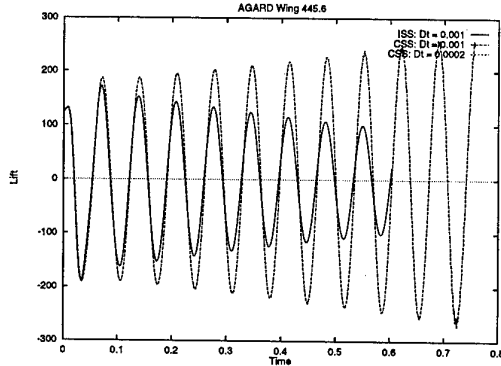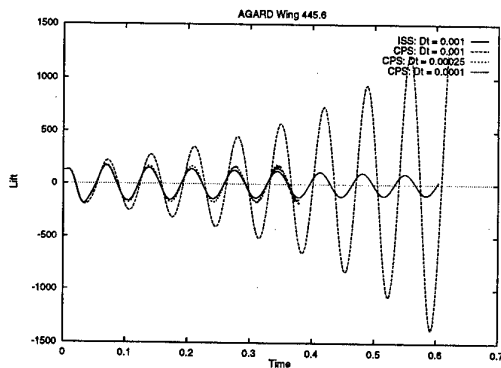

Figure 7: Convergence analysis of CSS

Figure 8: Convergence analysis of CPS

The numerical instability of CSS, CPS, and IPS at the specified coupled time-step $\Delta t = 10^{-3}$ highlights the potential for confusing numerical and physical instabilities when investigating flutter problems in the time domain. Most significant is the fact that the instability exhibited by these methods and shown in Fig. 8–10 is of the "slow" or "weak" type, and therefore does not necessarily strike an analyst as a numerical instability; it could rather mislead him to conclude that a flutter point is reached. This difficulty is intrinsic to flutter analysis in the time-domain, whether a monolithic or staggered algorithm method is chosen for solving Eqs. (5). Adaptive time-stepping (simplified here to a uniform re-
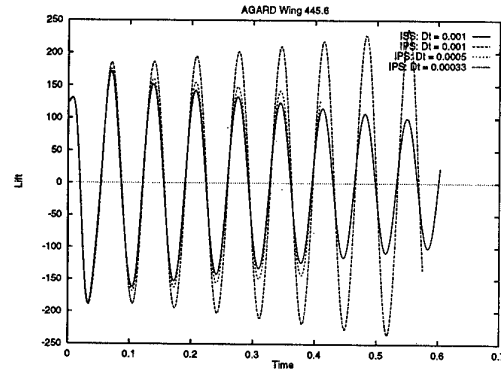
Figure 9: Convergence analysis of IPS

duction of the time-step) is the only feasible cure for this problem that we are aware of. Nevertheless, the results reported herein show that staggered algorithms can be refined to alleviate this problem. They also demonstrate the superiority of the ISS method over the conventional CSS procedure (a factor 5 improvement in the time-step), and the superiority of the IPS method over the CPS algorithm (a factor 3.3 improvement in the time-step). Again, note that the dimensional coupling time-step $\Delta t = 10^{-3}$ corresponds to sampling the period of the first torsional mode of the dry wing in 25 points, and therefore is comparable to the time-step usually selected for the more restrictive fully implicit monolithic algorithms.

6.3 Validation of the improved staggered algorithms
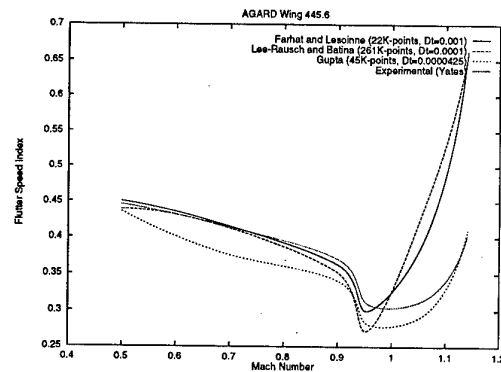
Figure 10: Flutter speed index

Finally, we compute the flutter speed index and flutter frequency ratio as functions of the Mach num-
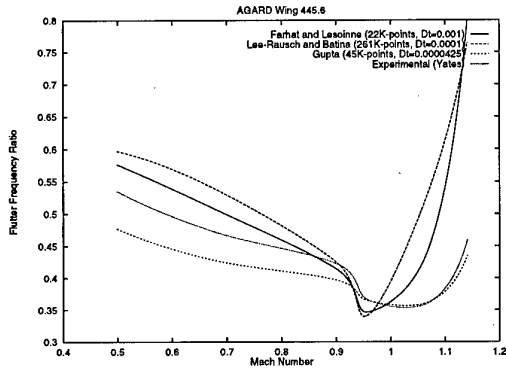
Figure 11: Flutter frequency ratio

bers. More specifically, for each target Mach number, we set the freestream density as in [15] and vary the freestream pressure until we observe the onset of flutter. For this purpose, we employ the coarse CFD mesh with 22014 grid points and the ISS solution method. We set the dimensional coupling time-step to $\Delta t = 10^{-3}$ ($n_{S/F} = 2$). We compare our simulated results with the experimental data published in [15], and with the computational results published in references [8,16]. Both methods used in [8,16] are staggered solution procedures that are similar to the CSS method discussed in this paper, and that use implicit Euler flow solvers with an accuracy comparable to our Euler flow solver. However, both of these references represent the structure by its modal coordinates (reference [16] uses the measured frequencies), and reference [8] includes a 2% modal damping for the dry wing. In reference [8] the CFD mesh has 45180 nodes, the dimensional coupling time-step is set to $\Delta t^{[8]} = 0.0017027/40 = 4.25 \times 10^{-5}$, and no subcycling is used. Hence, our coupling time-step is more than 23 times larger, and our fluid global time-step more than 11 times larger. In reference [16], the CFD mesh has 261129 grid points, the non-dimensional coupling time-step (based on the root chord and the freestream speed of sound) is set to 0.05456, which means that the dimensional coupling time-step is set to $\Delta t^{[16]} = 10^{-4}$, and no subcycling is used. In other words, our mesh is 10 times coarser, our coupling time-step is 10 times larger, and our fluid global time-step 5 times larger than in [16].

The results reported in Fig. 11 and Fig. 12 show that in the range $0.499 \leq M_\infty \leq 0.960$, our computational methodology compares more favorably

with the experimental data than both results published in [8] and [16]. In the supersonic regime, our results compare more favorably with experimental data than those of [16], but less favorably than those of [8]. As a matter of fact, it seems that in the supersonic regime, our computational results validate those of [16]. However, the results reported in this work as well as those reported in [8,16] correspond to Euler flow solutions, and as stated in [16], the modeling of the flow physics by the Euler equations is incomplete. In any case, given that our CFD mesh is coarser than both meshes employed in [8,16], that our ISS algorithm has the same computational complexity as the partitioned procedures used in these references, and that our time-step is at least an order of magnitude larger than both time-steps employed in [8,16], the results shown in Fig. 11 and Fig. 12 not only validate our aeroelastic computational methodology, but also highlight its superior computational efficiency. Furthermore, they demonstrate that, for aeroelastic problems, a well designed staggered algorithm can afford a time-step that is comparable to that of a fully implicit monolithic scheme.

7 Conclusions

It has often been stated that loosely coupled partitioned procedures for the solution of aeroelastic problems in the time domain are inferior to strongly coupled fully implicit monolithic schemes. We do not subscribe to this viewpoint. Partitioned procedures offer the possibility to combine different solution methods that are tailored to the different mathematical models and geometric complexity underlying the fluid and structure problems, can take into account software availability in each individual discipline, simplify mixed explicit/implicit treatment, facilitate subcycling, preserve software modularity, and are the most if not only feasible computational methods when the structural system is more complex than a simple airfoil or a homogeneous flat plate. Partitioned procedures are computationally more economical than fully implicit monolithic schemes. However, they can be less accurate than these methods when they are equipped with the basic staggering algorithm, in which case they often necessitate small time-steps. In this paper, we have shown that better staggered algorithms can be designed to improve the efficiency of partitioned procedures. More specifically, we have presented an enhanced staggered algorithm whose computational

complexity is comparable to that of the basic ones, and yet allows the simplest partitioned procedure to operate with coupling time-steps that are comparable to those afforded by fully implicit monolithic schemes. We have validated this algorithm with the flutter analysis of the AGARD Wing 445.6, and highlighted its superior accuracy and computational efficiency by proving it capable of operating accurately with a coupling time-step that is 10 to 23 times larger, and a fluid global time-step that is 5 to 11 times larger than previously reported in the literature. We have also improved an existing parallel staggered algorithm for the solution of aeroelastic problems. Unless the structural problem is large enough, we recommend the improved serial staggered algorithm as it allows a time-step that is several times larger than the maximum time-step allowed by the parallel variant.

References

[1] J. Donea, An arbitrary Lagrangian-Eulerian finite element method for transient fluid-structure interactions, Comput. Meths. Appl. Mech. Engrg. 33 (1982) 689–723.

[2] C. Farhat, M. Lesoinne and N. Maman, Mixed explicit/implicit time integration of coupled aeroelastic problems: three-field formulation, geometric conservation and distributed solution, Internat. J. Numer. Meths. Fluids 21 (1995) 807–835.

[3] J. T. Batina, Unsteady Euler airfoil solutions using unstructured dynamic meshes, AIAA Paper No. 89-0115, AIAA 27th Aerospace Sciences Meeting, Reno, Nevada, January 9–12, 1989.

[4] S. A. Morton, R. B. Melville, and M. R. Visbal, Accuracy and coupling issues of aeroelastic Navier-Sokes solutions of deforming meshes, AIAA Paper 97-1085, 38th AIAA Structures, Structural Dynamics and Materials Conference, Kissimmee, Florida, April 7–10, 1997.

[5] R. D. Rausch, J. T. Batina and T. Y. Yang, Euler flutter analysis of airfoils using unstructured dynamic meshes, AIAA Paper No. 89-13834, 30th Structures, Structural Dynamics and Materials Conference, Mobile, Alabama, April 3–5, 1989.

[6] C. Farhat, M. Lesoinne, P. S. Chen and S. Lantéri, Parallel heterogeneous algorithms for the solution of three-dimensional transient coupled aeroelastic problems, AIAA Paper No. 95-1290, AIAA 36th Structural Dynamics Meeting, New Orleans, Louisiana, April 10–13, 1995.

[7] S. Piperno, C. Farhat and B. Larrouturou, Partitioned procedures for the transient solution of coupled aeroelastic problems, Comput. Meths. Appl. Mech. Engrg. 124 (1995) 79–11.

[8] K. K. Gupta, Development of a finite element aeroelastic analysis capability, Journal of Aircraft 33 (1996) 995-1002.

[9] J. Mouro, Numerical simulation of nonlinear fluid structure interactions problems and application to hydraulic shock-absorbers, in Proc. Third World Conf. Appl. Computational Fluid Dynamics, Basel World User Days CFD, May 19–23, 1996.

[10] C. A. Felippa and T. L. Geers, Partitioned analysis of coupled mechanical systems, Engineering Computations 5 (1988) 123–133.

[11] S. K. Weeratunga and E. Pramono, Direct coupled aeroelastic analysis through concurrent implicit time integration on a parallel computer, AIAA Paper No. 94-1550, April 1994.

[12] M. Lesoinne and C. Farhat, Geometric conservation laws for flow problems with moving boundaries and deformable meshes, and their impact on aeroelastic computations, Comput. Meths. Appl. Mech. Engrg. 134 (1996) 71–90.

[13] P. D. Thomas and C. K. Lombard, Geometric conservation law and its application to flow computations on moving grids, AIAA J. 17 (1979) 1030–1037.

[14] C. Farhat and S. Lantéri, Simulation of compressible viscous flows on a variety of MPPs: computational algorithms for unstructured dynamic meshes and performance results, Comput. Meths. Appl. Mech. Engrg. 119 (1994) 35–60.

[15] E. C. Yates, AGARD standard aeroelastic configuration for dynamic response, candidate configuration I. – Wing 445.6, NASA TM-100492, 1987.

[16] E. M. Lee-Rausch and J. T. Batina, Wing-flutter boundary prediction using unsteady Euler aerodynamic method, AIAA Paper No. 93-1422, 1993.

CFD Based Corrections for Linear Aerodynamic Methods

Myles L. Baker
The Boeing Company
2401 E. Wardlow Rd, Mail Code 71-34
Long Beach, CA 90807, USA

Abstract

In the past few years, great strides have been made in the analytical prediction of nonlinear flows using computational fluid dynamics (CFD). Coupled with the exponential growth in computer power, this has made it possible to analytically predict the unsteady aerodynamics and aeroelastic motion of complex configurations in nonlinear flow regimes. Unfortunately, these analyses are extremely costly due to the vast amount of computational effort required to compute the requisite time histories. This computational expense limits the use of these nonlinear aeroelastic tools to special cases, and eliminates them from consideration whenever a large number of conditions must be evaluated. Due to this high cost, the aerodynamic tools used in certification analysis and aeroelastic design optimization are usually based on linear lifting surface theory or panel methods. This paper presents a method to bridge this gap, so that the improved accuracy of the expensive nonlinear aerodynamic/aeroelastic methods can be injected into the economical production-type aeroelastic analyses through corrections to the linear aerodynamics. In contrast to techniques based on multiplicative correction factors, the present technique corrects the linear aerodynamics by removing a component of the pressure distribution from the linear theory, and replacing it with a component computed with a nonlinear method using a concept called "local equivalence." This allows a small number of nonlinear analyses to be applied to a large number of aeroelastic analyses. The technique is equally applicable to steady and unsteady aerodynamics. The formulation is such that, if available, steady or unsteady wind tunnel data can also be used in aeroelastic analysis and optimization. The scope of the paper is limited to comparing the results of corrected linear aerodynamics to the available nonlinear data, since many comparisons between nonlinear simulations and experiment are available in the literature. An application of the current technique to the flutter analysis of the AGARD 445.6 wing is shown, along with correlations between direct nonlinear flutter simulations and flutter solutions with corrected aerodynamics.

Introduction and Prior Work

Currently, a great deal of research is being conducted in the solution of the nonlinear unsteady aerodynamic and aeroelastic equations. The techniques being used range from relatively simple nonlinear models based on the transonic small disturbance potential equation [1,2,3,4] to solutions for the full Euler or Navier-Stokes equations [5,6,7,8]. Many of these codes also have the capability of including a model of the structural dynamics of an airplane, allowing the direct simulation of the nonlinear aeroelastic behavior of an airplane.

While these codes provide the most complete and accurate analytical methods for predicting the aeroelastic behavior of airplanes in nonlinear (especially transonic) flight regimes, they all suffer from the same drawback: They are very expensive to use. A condition that may take only a few seconds to analyze on a workstation using linear lifting surface theory [9,10] will often take the better part of a day on a supercomputer to simulate using nonlinear aerodynamics. In addition, it is not always clear how the results of a nonlinear simulation (which usually consists of time history data or frequency/damping values for a single flight condition) should be used most effectively. While there is a tremendous amount of analysis and optimization software (and experience) available for designing airplanes using linear (or linearized) aerodynamics, there has been little progress in integrating the fully nonlinear techniques into the airplane aeroelastic analysis and design phases. This has left aeroelastic CFD tools to peform mostly research roles, with some forays into the "real" world to analyze isolated conditions.

The design of an airplane typically requires the steady and unsteady aeroelastic analysis of thousands of conditions. Due to the large number

of analyses required, the nonlinear techniques mentioned above are unlikely to significantly impact the aeroelastic design of future airplanes unless two goals can be met: The computational cost must be reduced by orders of magnitude, and the nonlinear aerodynamic data must be integrated into production quality aeroelastic analysis and design tools.

For many years, aeroelasticians have recognized the shortcomings of linear aerodynamics. In flight regimes where the accuracy of linear methods is insufficient, they have attempted to develop improved accuracy models. While there has been some recent work in developing reduced-order unsteady aerodynamic models based on nonlinear CFD codes [11,12,13,14,15, 16,17,18], the approach has historically been to apply weighting factors to the lift and moment distributions obtained from linear theory in order to match nonlinear data [19,20]. Typically, the available data has been experimental (i.e. wind tunnel) airplane lift and moment coefficients, and when available, the spanwise lift and moment distributions. The resulting weighting factors are typically functions of the flight condition, including Mach number, Reynolds number, angle of attack, etc.

While the weighting factor approach has been used with some success for analysis of high aspect ratio wings, there are several difficulties. Weighting factors are typically used to force the corrected lift (and sometimes moment) distributions to match nonlinear data. Since the number of available correction terms is much larger than the number of lift/moment constraints, this results in an underdetermined set of equations. In order to solve for the weighting factors, arbitrary shape functions (such as step/ramp functions) must be assumed, or a least squares approach [20] must be taken. This can lead to unreasonable (i.e. large or negative) weighting factors. Since the vast majority of wind tunnel tests are steady, and since unsteady aerodynamic data calculation using CFD codes is only now becoming affordable, most applications of aerodynamic correction techniques concentrate on steady aerodynamics. Some notable exceptions to this trend can be found in [19], where the authors have developed guidelines in applying steady correction factors (i.e. correction factors computed using steady test data) to unsteady aerodynamic matrices.

With recent advances in computer technology (and affordability!) and CFD codes, it has at last become possible to use the resulting "computational wind tunnel" to generate aerodynamic data that cannot be obtained economically from a conventional wind tunnel. Specifically, these codes make it possible to obtain a full description of the surface pressure distribution when the airplane is subjected to virtually any motion, including non-testable conditions such as a pure oscillation of a bending mode.

In this paper, an aerodynamic correction method is developed that specifically makes use of the distributed pressure data available from unsteady CFD solutions to develop improved linear (linearized) aerodynamics that can be used to predict the small-motion stability of the aeroelastic system. The new technique does not use weighting factors, and therefore does not require arbitrary weighting functions or least-squares solutions. In contrast to previous methods, which typically correct only the magnitudes of the aerodynamic coefficients, the current technique constructs corrected aerodynamic influence coefficient (AIC) matrices by directly using the unsteady data, which allows correction of both the magnitude and phase of the entire pressure distribution. Since the pressure distribution (rather than sectional lift and moment coefficients) is corrected, the present technique is more applicable to low aspect ratio configurations than previous approaches, and is more applicable to flutter mechanisms not dominated by classical bending/torsion interaction. It should be emphasized that the present technique requires linearization of the nonlinear aerodynamics, and is not intended to capture dynamically nonlinear behavior, such as limit cycle oscillation.

The Local Equivalence Concept

Consider an airplane undergoing a general aeroelastic deformation, including not only structural deflections, but also rigid body rotations and surface deflections as well. If we define a "representative" deflection shape function φ, then any arbitrary deformation of the airplane can be written in the form

$$u = \varphi \eta + \delta u \qquad (1)$$

Where u is the actual deflection of the airplane, η is a scalar coefficient determining the magnitude of the "representative" deflection φ, and δu is a residual. The pressure distribution on the airplane surface, which is of course dependent on the

airplane deflection u, can be expressed as a first order Taylor series

$$P^{NL}(u) \cong P^{NL}(\varphi\eta) + \frac{\partial P}{\partial u}\delta u \qquad (2)$$

where the superscript "NL" denotes a nonlinear quantity. If nonlinear aerodynamic data is available for deflections of the form $u = \eta\varphi$ for various values of η and a specified representative deflection shape φ, then the first term in the above equation can be taken directly from the available CFD solutions. Since φ is specified ahead of time, only the coefficient η can be chosen independently. The value of η is chosen in order to make the first term as dominant as possible, and to minimize the impact of the residual deflection on the pressures of interest. In general, the value of η will depend on the deflection u of the airplane.

For stability analysis, we are not so interested in the absolute values of the pressures, but in their derivatives with respect to deflection. These derivatives, or Aerodynamic Influence Coefficients (AIC's) are commonly used in aeroelastic analysis. The following derivation will not explicitly point out the unsteady nature of the AIC's, but each quantity is assumed to be complex-valued in general, and to depend implicitly on reduced frequency $k=\omega c/2V$. By simply differentiating equation (2) with respect to deflection, we can approximate the derivative of the nonlinear pressure with respect to deflection (in essence, a corrected AIC matrix) as

$$\frac{\partial P^{C}(u)}{\partial u} = \frac{\partial P^{NL}(\varphi\eta)}{\partial \eta}\frac{\partial \eta}{\partial u} + \frac{\partial P}{\partial u}\frac{\partial \delta u}{\partial u} \qquad (3)$$

If the partial derivative of pressure with respect to deflection ($\partial P/\partial u$) in the residual term of the above equation is approximated by the linear AIC matrix AIC^{L} (which has little effect on the solution if the residual term is small), then the corrected AIC matrix can be written as

$$AIC^{C} \cong \frac{\partial P^{NL}}{\partial \eta}\frac{\partial \eta}{\partial u} + AIC^{L}\frac{\partial(u-\varphi\eta)}{\partial u} \qquad (4)$$

where the definition of δu from Equation (1) has been substituted into the last term, the explicit dependence of P^{NL} on $\varphi\eta$ has been omitted for brevity, and the notation of the corrected AIC matrix AIC^{C} has been introduced. This can also be written as

$$AIC^{C} = AIC^{L} + \left(\frac{\partial P^{NL}}{\partial \eta} - AIC^{L}\varphi\right)\frac{\partial \eta}{\partial u} \quad (5)$$

Therefore, if the nonlinear aerodynamic pressure distribution is known for a given φ and various values of η, and if the (unsteady) derivatives of the nonlinear pressure with respect to η are known, then a corrected AIC matrix can be constructed that captures some of the effects of aerodynamic nonlinearities. It should be emphasized that this technique is not a "correction factor" in the traditional sense. Typically, correction factors are multiplicitave corrections applied to the linear AIC matrix in order to bring some selected derivative values into agreement with nonlinear data. In this technique, however, the linear pressures are not simply multiplied by a factor, but a component of the linear pressure distribution (the third term of equation 5) is *removed*, and it is *replaced* with a nonlinear pressure distribution (the second term of equation 5). For deflections u which are nearly collinear with the shape function φ, the part that is replaced is the dominant part, and the residual term is small.

It should be noted that the derivative $\partial P^{NL}/\partial \eta$ is, in general, a function of Mach number, Reynolds number, reduced frequency, and the steady-state incidence and deformation of the airplane. Although the example presented below is based on a symmetric wing at zero angle of attack (and therefore zero steady-state deflection), the procedure can be expanded to compute a corrected AIC matrix that depends on the steady-state trim and deformation state of the airplane.

The technique of Equations (2) and (5) is termed an equivalence technique, since the aerodynamic nonlinearities are introduced through an "equivalent" scalar variable η. The introduction of the equivalent variable η makes is possible to estimate the nonlinear pressure distribution (and its derivatives) due to various values of η, and to apply them to correct an entire AIC matrix. This is feasible, since the subspace of deflections for which nonlinear aerodynamic data is required is now one-dimensional, rather than the many-dimensional space of all possible deflections.

The problem now is to choose a value of η such that the "equivalence" concept makes sense. The choice of values for η can be thought of as a (potentially non-orthogonal) projection from the space of all possible deformation states of the airplane to the subspace of the deformations for which more accurate aerodynamic data is

available. If the projection is linear, then it can be written in matrix form as

$$\eta = Du \qquad (6)$$

In order to illustrate the possible correction techniques that can be built from the equivalence concept, we shall consider several methods of choosing the parameter η. In the first case, let us assume that η simply represents the angle of attack of the airplane, and δu contains all the aeroelastic deflection. The representative mode vector φ then is simply a vector representing a unit angle of attack, and the projection operator D in this case is simply

$$D = \begin{bmatrix} 0 & 0 & \cdots & \dfrac{1}{\varphi_i} & \cdots & 0 & 0 \end{bmatrix} \qquad (7)$$

where the non-zero entry corresponds to the pitch degree of freedom of some reference point on the airplane (such as the center of gravity). The value φ_i is the magnitude of the pitch rotation of that degree of freedom in the mode shape φ. This is certainly nothing new, since the method described above is essentially identical to the common practice of using experimental or CFD data for a rigid airplane, and appending a linear correction for aeroelastic effects.

This approach has the advantage of simplicity, but has several shortcomings. Perhaps most significant is the fact that the equivalent deflections depend only upon the position of a single reference point, and make no use of information about the deformation of the rest of the airplane. Another possible technique is to use a simple vector projection, such that

$$D = \frac{\varphi^T}{|\varphi|^2} \qquad (8)$$

In this case, the representative deflection of the airplane will be that of an equivalent "mean" angle of attack of the configuration. With this formulation, it might be expected that better results could be obtained, because the true shape of the airplane would be in some sense "balanced" around the representative shape, and the largest error would be smaller than that obtained with the first technique.

Each of the approaches described above makes use only of the vector definitions of the deformed shapes of the airplane, and therefore has no information pertaining to the aerodynamic interference that may be occurring. A third

method computes the equivalent deflection based on equivalence of some aerodynamic quantity such as lift. In this case, the projection operator D is given by

$$D = \left(H\ AIC^L \varphi \right)^{-1} H\ AIC^L \qquad (9)$$

where AIC^L is the linear aerodynamic influence coefficient matrix, and H is an integration matrix converting aerodynamic pressures into an integrated aerodynamic coefficient. If the φ vector again represents a unit angle of attack, the equivalent deflection η computed using this technique is the angle of attack that, assuming linear aerodynamics, gives the same overall lift coefficient as the deformed shape in question.

This is perhaps the best of the techniques presented so far. This concept, which is based on equivalence of some integrated aerodynamic quantity (such as lift) is an improvement over the others presented, but it still has the disadvantage that the aerodynamic nonlinearities are only applicable to a global "mean" deformation. Since the airplane will (presumably) encounter other deformations, this is a serious shortcoming, and must be overcome in a successful method.

One technique for accounting for some of the effects of unpredicted deformations is to apply the method of equations 2 and 5 to discrete areas, or "zones" of the airplane, each of which have their own distinct values of η. In this paper, for simplicity, the only type of zone that will be considered is a streamwise strip of the wing, but the technique allows for more general definitions. If the airplane is discretized into zones, then for a given deflection state, each zone has a given value of the integrated coefficients of interest, and therefore has its own equivalent deflection η. The pressure distribution on that zone can then be computed using a variation of that used in Equations (3-5):

$$\left[\frac{\partial P^C}{\partial u} \right]_i = \frac{P^{NL}}{\partial \eta} \left(H_i AIC^L \varphi \right)^{-1} H_i AIC^L + $$
$$AIC^L \left[I - \varphi \left(H_i AIC^L \varphi \right)^{-1} H_i AIC^L \right]$$
$$= AIC^L + \left(\frac{P^{NL}}{\partial \eta} - AIC^L \varphi \right)$$
$$\left(H_i AIC^L \varphi \right)^{-1} H_i AIC^L$$

$$\qquad (10)$$

where the subscript i indicates that the equation only applies to compute pressures on zone i, and the matrix H_i integrates the aerodynamic coefficients of zone i (such as the local sectional lift coefficient). The overall corrected AIC matrix is then formed by taking the appropriate rows from each of the $[\partial P^C/\partial u]_i$ matrices and assembling them into one full AIC matrix. This can be written in matrix notation as

$$AIC^C = \sum_{i=1}^{nzone} J_i \left[\frac{\partial P^C}{\partial u} \right]_i \qquad (11)$$

where the matrix J_i is a diagonal matrix with null entries for aerodynamic elements (boxes) that are not in zone i, and unit (1.0) entries for aerodynamic boxes that are included in zone i.

Conceptually, this approach is very simple if one considers the special case of a high aspect ratio wing where the equivalent deflection is a rigid airplane angle of attack and the local equivalence zones are wing strips. In general, any deflection of the wing affects the flow over the entire wing, and this effect is captured by the concept of a locally equivalent angle of attack. For example, if the wingtip pitches up, a lift will be induced over the entire wing. At a given span station (strip), the nonlinear pressure distribution due to the total (including induced) lift is assumed to be equivalent to that generated by an "equivalent" airplane angle of attack, for which the nonlinear pressures are known. Any residual effect is corrected using linear theory.

Results: The AGARD 445.6 Wing

The process described above has been applied to the transonic flutter analysis of the AGARD 445.6 wing. This configuration is well documented in the literature, and has been extensively analyzed using many codes, ranging from the simplest linear methods [21] to small disturbance solutions [2,3] to full Navier-Stokes simulations [6,22]. In this study, the AGARD 445.6 wing is analyzed using a linear lifting surface method, a transonic time-marching aeroelastic simulation method, and a linear analysis with corrected aerodynamics. While the transonic effects for this configuration are not extreme, the results indicate that the local equivalence correction factor technique can accurately predict the stability boundaries in the presence of a transonic flutter dip.

The baseline linear flutter analysis was performed using the pk-method of flutter solution with linear doublet lattice aerodynamics [10,23], while nonlinear aerodynamic and aeroelastic solutions were computed using the transonic small disturbance (TSD) equations [1,2,3]. While the TSD equation is one of the simplest models of transonic aerodynamics, it is expected that if the corrections can successfully capture the behavior of the TSD solutions, they should also capture the transonic effects of Euler or Navier-Stokes solutions.

The AGARD 445.6 wing configuration was actually a series of models tested in the NASA LaRC Transonic Dynamics Tunnel (TDT) in the 1970's, and the geometry and mode shapes are thoroughly documented in reference [21]. All solutions presented here correspond to the so-called "Weak3" model. The experimental flutter boundaries are also presented in [21], and correlation between nonlinear aeroelastic solutions and the experimental flutter boundaries are presented in [3,6,22].
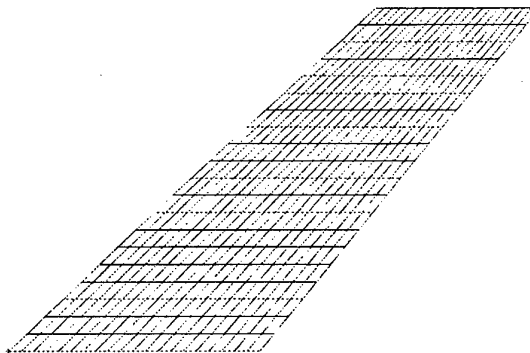
Figure 1: Planform Geometry and Aerodynamic Box Geometry of the 445.6 Wing.

The main focus of this paper is not to correlate with the experimental data, but to show correlation between an "expensive" nonlinear aeroelastic solutions and an "inexpensive" corrected linear solution. Therefore, there is no discussion of the experimental flutter results. However, a brief discussion of the model geometry and vibration characteristics is in order. The 445.6 wing is a semispan wing with the planform shown in Figure 1. The wing has a (full span) aspect ratio of 4.0, leading edge sweep of 45 degrees, and a taper ratio of 65%. The airfoil section is a symmetric NACA 65A004 section. The aeroelastic behavior of the 445.6 wing is a classical bending-torsion flutter, and is accurately captured using only the first two vibration modes. The first bending mode has a frequency of 9.6 Hz, and the torsion mode has a

frequency of 38.1 Hz. Since the flutter mechanism of interest is a classical bending/torsion interaction, the first bending and torsion modes of the wing are shown in Figure 2.
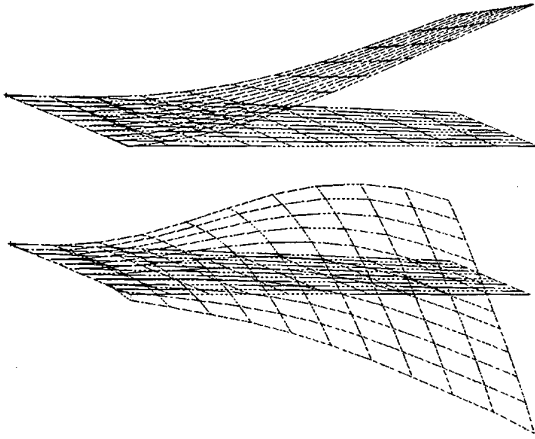
Figure 2: First Bending and First Torsion Mode Shapes. View from Inboard Trailing Edge

Choice of Unsteady Motion

The first step in applying the correction method described above is to decide on what type of unsteady motion (representative deflection φ) for which to obtain unsteady aerodynamic data. Ideally, the representative deflection should be chosen to be as similar to the target flutter mechanism as possible in order to improve the fidelity of the corrected aerodynamic matrices in predicting the flutter mechanism of interest. This implies that the value of η on all zones will be approximately equal, and that the residual term δu will be small.
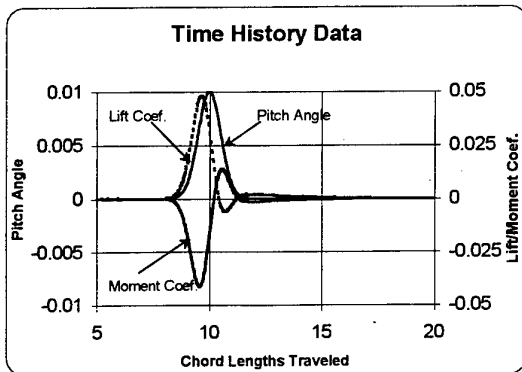
Figure 3: Time History of Pitch Angle and Wing Lift and Moment Coefficient.

Unfortunately, it is often impractical to choose a representative deflection shape in this manner, either because multiple flutter mechanisms are targeted, or because the mechanisms are not known accurately ahead of time. For reasons of simplicity and economy, it is also desirable for the corrected aerodynamics to be constructed using unsteady aerodynamic solutions due to simple rigid body motion of the airplane, rather than elastic motion. In this work, the "representative deflection" φ was chosen to be a rigid body pitching motion about the midchord of the wing root. While not the most accurate choice possible, the use of rigid body pitching as a representative deflection is a good test of the robustness of the proposed technique. Since the flutter mechanism of interest is primarily first wing bending, greater accuracy could probably be obtained if the "representative deflection" was selected to mimic the first bending mode.
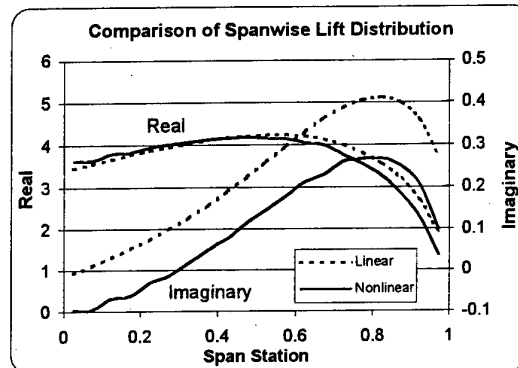
Figure 4: Spanwise Lift Distribution Due to Pitching Motion. Mach 0.95, k = 0.1.

Nonlinear unsteady data

The nonlinear unsteady aerodynamic data for generating correction factors was generated using the pulse transform method [24] with the transonic small disturbance aerodynamic method of [1]. In this technique, a forced motion analysis is performed, where a single generalized displacement is defined as a function of time as

$$u(t) = ae^{-c(t-t_c)^2}$$

where a is the pulse amplitude (chosen to be small enough that small perturbation assumptions are not violated), c is a constant determining the width of the pulse (chosen to be small enough that significant excitation is obtained in the reduced frequency of interest), and t_c is the "center"of the pulse, chosen such that the deflection when the

solution is started is essentially zero, avoiding discontinuities and the associated transients in the solution. For this analysis, the generalized displacement was wing pitch about the root midchord, the amplitude was 0.01 radians. The resulting time histories of the wing pitch and wing lift coefficient is shown in Figure 3. Note that since the airfoil is symmetric and the flutter solution is at zero angle of attack, the initial and final lift and moment coefficients are zero.
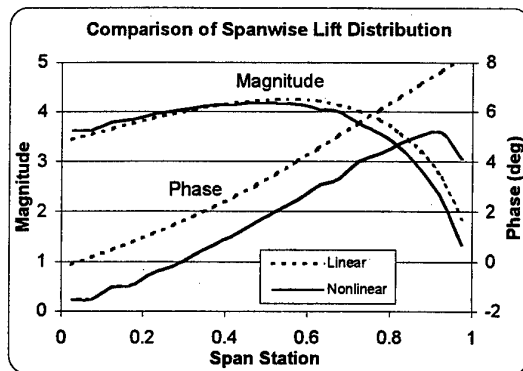
Figure 5: Spanwise Lift Distribution Due to Pitching Motion. Mach 0.95, k = 0.1.

From this time history data, and the associated time histories of the surface pressures, the Fourier transforms of the input (pitch) and the outputs (pressures) can be obtained, and by simple frequency-by-frequency division, the pressure distribution due to a harmonic pitching oscillation at various frequencies can be estimated. A comparison between the pulse transform technique and a direct harmonic oscillation of the wing was performed, and showed very close agreement. The spanwise distribution of lift coefficient is shown in Figures 4 and 5 at a reduced frequency of 0.1 (near the flutter reduced frequency). Figure 4 shows the lift distribution in terms of real and imaginary parts, while Figure 5 shows magnitude and phase. By definition, the corrected aerodynamics exactly match the nonlinear aerodynamics for pitching motion.

Since the flutter mechanism is primarily wing bending, let us consider what happens when the wing is vibrated in the first wing bending mode. Recall that the wing is divided into zones (strips), and that when the wing is excited in the first bending mode, each strip will have its own "equivalent" pitch angle determined by the local equivalence process described above. In order to illustrate the concept, Figure 6 shows the spanwise distribution of "equivalent" pitch angle (real and imaginary part) for the first bending mode (shown

in Figure 2). The equivalent pitch angle is shown for at a reduced frequency of 0.1, which is near the flutter frequency. For comparison, Figure 6 also shows the geometric pitch angle (real and imaginary parts) as a function of span. Note that the equivalent pitch angles include the induced effects of the entire wing deformation, so the equivalent pitch angle is a "smeared" version of the geometric pitch angle (i.e. the higher pitch angles at the tip induce upwash at the root, causing an induced angle of attack that is shown in the equivalent pitch).
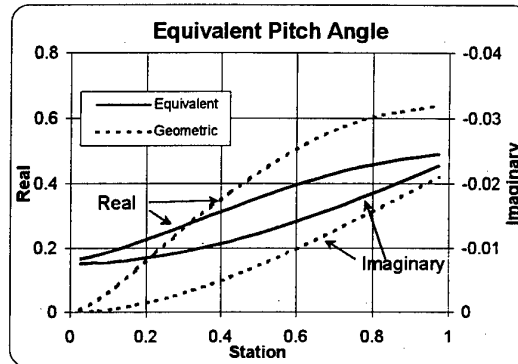
Figure 6: Equivalent Pitch Distribution for the First Wing Bending Mode.
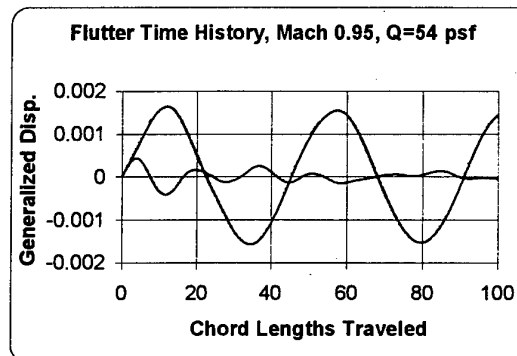
Figure 7: Time History of First Two Generalized Displacements for Direct Flutter Solution at Mach 0.95.

Flutter Results

The variation of frequency and damping with dynamic pressure as computed in the linear flutter solution at Mach 0.95 is shown in Figures 8 and 9. The linear flutter crossing is fairly mild, at a dynamic pressure of approximately 79 pounds per square foot (PSF). The corresponding nonlinear time-marching flutter solution is shown in Figure 7, showing the time histories of the first two
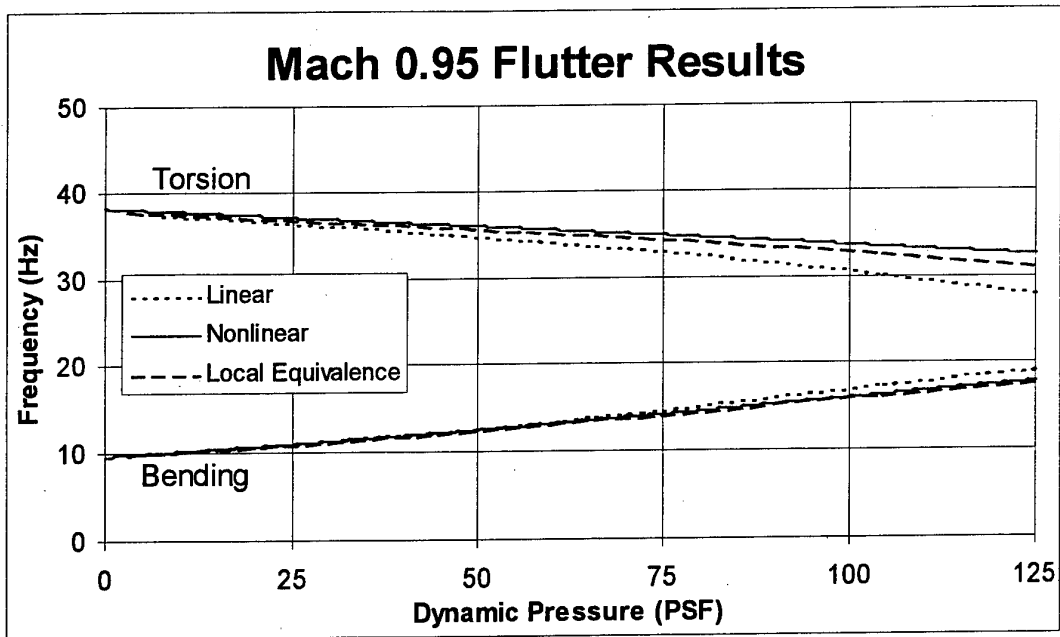
Figure 8: Frequency vs. Dynamic Pressure Comparison Between Linear, Full Nonlinear, and Corrected Solutions Using Local Equivalence Corrections.
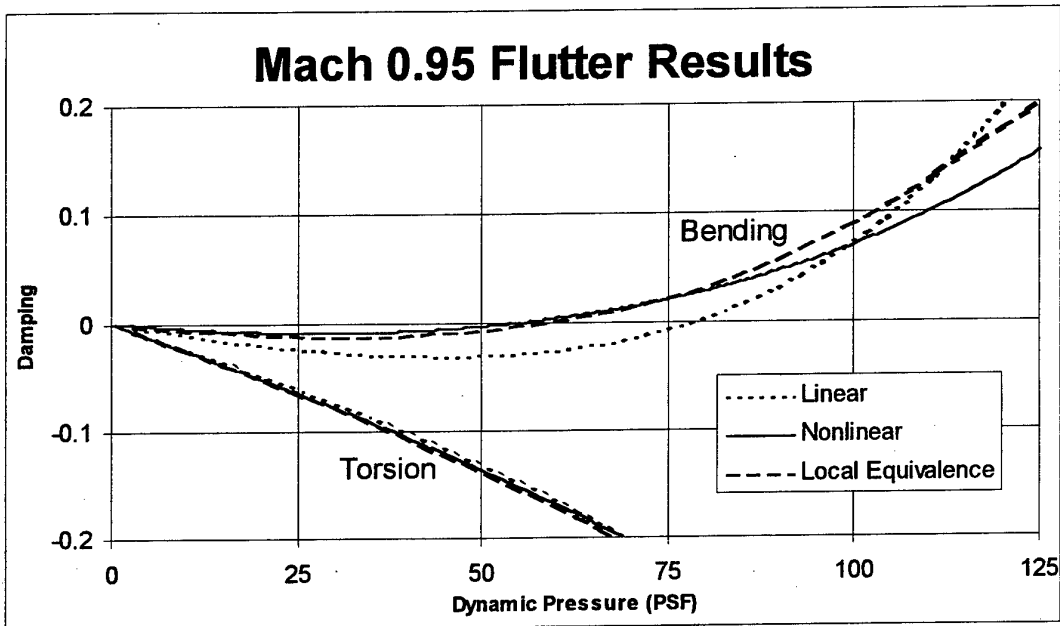
Figure 9: Damping vs. Dynamic Pressure Comparison Between Linear, Full Nonlinear, and Corrected Solutions Using Local Equivalence Corrections.
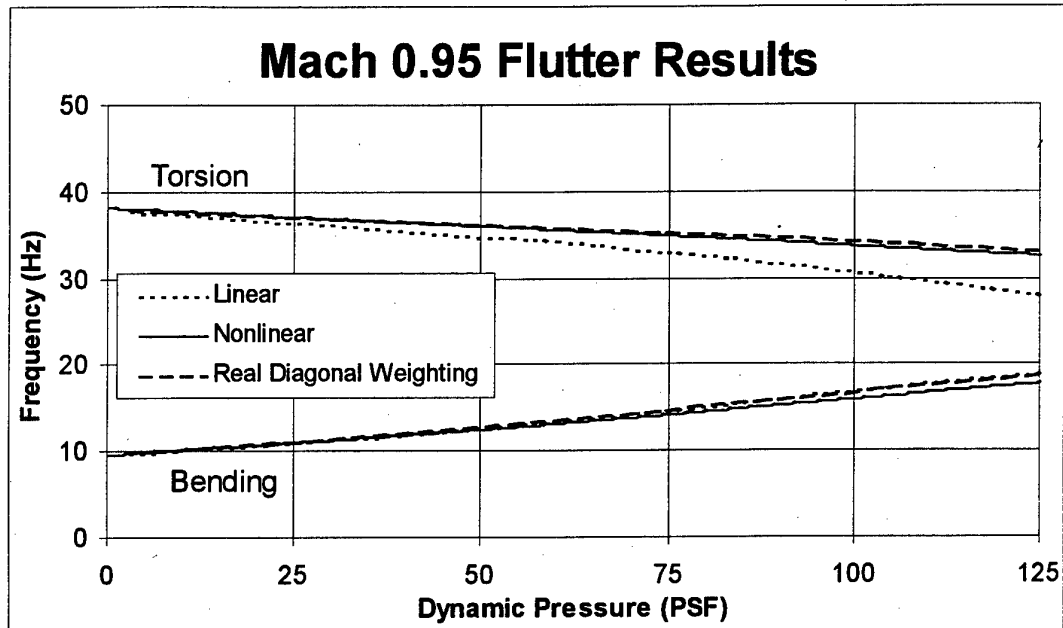
Figure 10: Frequency vs. Dynamic Pressure Comparison Between Linear, Full Nonlinear, and Corrected Solutions Using Conventional Real Multiplicative Correction Factors.
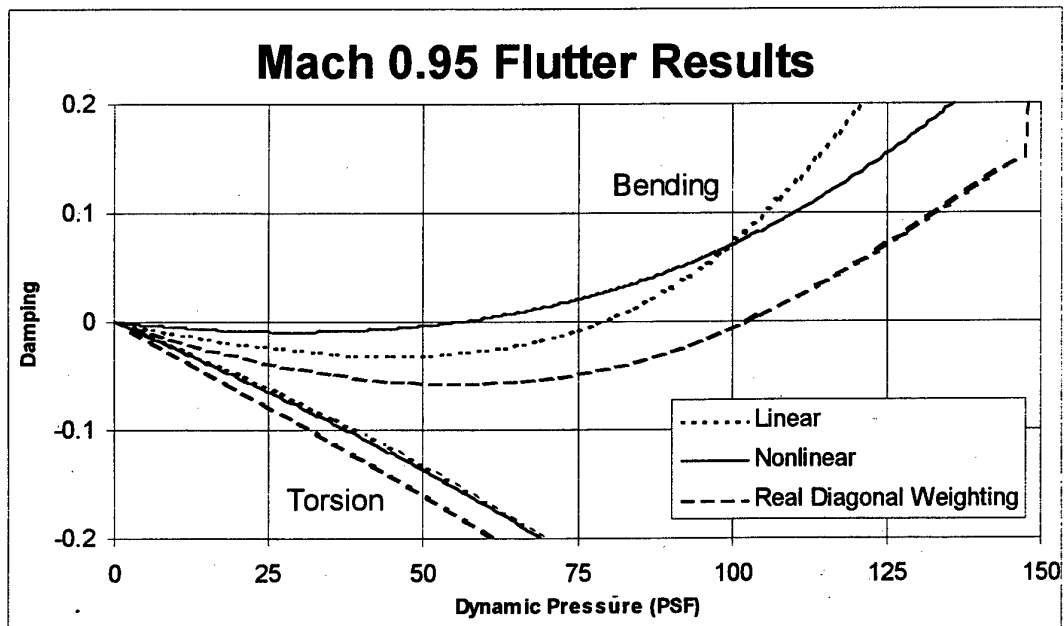
Figure 11: Damping vs. Dynamic Pressure Comparison Between Linear, Full Nonlinear, and Corrected Solutions Using Conventional Real Multiplicative Correction Factors.

generalized displacements, corresponding to the first bending and first torsion modes. This time history data is computed at a dynamic pressure of 54 PSF, which is very close to the neutral stability point (estimated at 56.2 PSF). Figures 8 and 9 also show the estimated variation of frequency and damping with dynamic pressure, based on the nonlinear aeroelastic time-marching solution. As in the linear case, the nonlinear flutter solution shows a coalescence between the bending and torsion frequencies, and a fairly mild flutter crossing. However, the flutter dynamic pressure and frequencies are much lower than those predicted by the linear analysis.

Finally, Figures 8 and 9 also show the variation of frequency and damping with dynamic pressure for the flutter analysis using corrected linear flutter analysis. The solution method is identical to that used to generate the linear solutions, but the aerodynamic influence coefficient (AIC) matrices have been corrected to match the nonlinear unsteady aerodynamic data due to pitching motion about the root midchord. Once again, the flutter crossing is fairly mild, but the dynamic pressure at instability is very close to the nonlinear stability boundary, at about 60 psf.

These figures indicate that the local equivalence correction technique can indeed be used to accurately estimate aeroelastic stability in the presence of transonic aerodynamics. The obvious question is: Can other, simpler correction methods do the same (or better) job? While a rigorous survey of all correction techniques that have been proposed over the years is beyond the scope of a single paper, one common technique was tested. In the transport aircraft industry, it is common to generate a real valued, diagonal pre-multiplier correction factor matrix W and apply it to the AIC matrix at each reduced frequency such that the corrected AIC matrix is given by

$$AIC^C = W\,AIC^L \qquad (12)$$

The values of the correction factors W are typically chosen such that some commonly measured quantities, such as the spanwise lift and moment distributions due to a unit angle of attack, are matched exactly at zero frequency. This technique was applied to the flutter analysis of the AGARD 445.6 wing at Mach 0.95, and the flutter results are compared to the linear and nonlinear solutions in Figures 11 and 12. In the steady aerodynamic solutions, the lift distribution predicted by linear theory was fairly accurate, but the aerodynamic center location was significantly forward of that

predicted by the nonlinear code. This results in a diagonal correction factor matrix that significantly amplifies the pressures on the aft portion of the wing, while depressing the leading edge pressure spike. This effect can clearly be seen in the behavior of the torsional mode frequency with increasing dynamic pressure, since the more aft aerodynamic center reduces the "softening" effect of the aerodynamics.

Overall, the real diagonal method reproduces the frequency variation with dynamic pressure fairly well. However, since the real correction factors do not correct the phase of the unsteady aerodynamic forces, this technique fails to accurately predict the stability boundary, in fact showing significantly more error than uncorrected linear theory.

Mach	0.90	0.95
Linear	93.8 PSF 16.4 Hz	79.0 PSF 15.0 Hz
Nonlinear (CAP-TSD)	86.5 PSF 15.5 Hz	56.2 PSF 12.9 Hz
Local Equivalence Correction	83.6 PSF 14.4 Hz	59.8 PSF 13.0 Hz
Sectional Lift & Moment Correction	N/A	102.5 PSF 17.0 Hz

Table 1: Summary of Linear, Nonlinear, and Corrected Flutter Results. Dynamic Pressure in PSF, followed by frequency in Hz.

Since the AGARD 445.6 wing has a moderate aspect ratio, and since the flutter mechanism is a pure interaction between bending and torsion flutter, it is somewhat surprising that this technique gives such poor results. It is conjectured that this is due to the failure of a real weighting factor to correct the phase of the unsteady forces, and improved results might be obtained with complex, frequency-dependent weighting factors for this configuration.

A similar set of linear, nonlinear, and corrected linear analyses using the local equivalence approach were performed at Mach 0.90, with comparable results. The aerodynamic corrections did not change the character of the flutter mechanism, but the dynamic pressure at the instability was significantly reduced due to the

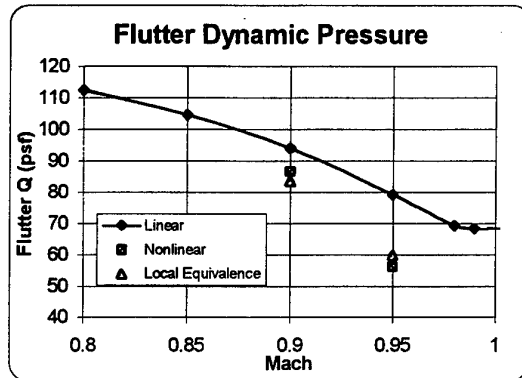nonlinear aerodynamics. The flutter results are summarized in Table 1, and in Figures 12 and 13.

Flutter Dynamic Pressure

Figure 12: Summary of Linear, Nonlinear, and Corrected Linear Flutter Boundaries.
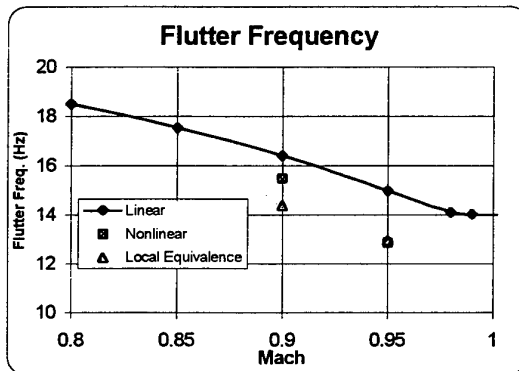
Flutter Frequency

Figure 13: Linear, Nonlinear, and Corrected Linear Flutter Frequencies.

Conclusions

A new technique has been presented that allows linear unsteady aerodynamic matrices to be corrected to improve agreement with nonlinear unsteady aerodynamic data, which can come from CFD codes or wind tunnel tests. The new technique is distinct from previous correction factor techniques in that the correction is not in the form of a multiplicative weighting factor, but is formed by directly replacing part of the linear aerodynamic pressures with data from a nonlinear analysis. Any residual is accounted for with linear theory. The corrections are applied to discrete zones on the aircraft such that for each zone, the nonlinear pressure distribution is based on that zone's "equivalent deflection." Since the corrections are computed and applied on a zone-by-zone basis, the technique is called local equivalence. Since the local equivalence

correction technique directly replaces a component of the linear pressure distribution with nonlinear values, there is no requirement for arbitrary weighting functions or least squares solutions. Since the technique corrects pressures, rather than spanwise lift/moment coefficients, the technique is more applicable to low aspect ratio configurations than previous methods, and would be expected to give better performance for non-bending/torsion flutter mechanisms.

The resulting corrected linear aerodynamics were applied to a dynamically linear stability analysis of the AGARD 445.6 wing, and good agreement was shown between a direct nonlinear stability calculation and the corrected linear solution. Several other flutter analyses were performed using linear aerodynamics with simple correction factors applied to correct the spanwise lift and moment distribution, and it was shown that the local equivalence corrections give significantly better correlation with the direct nonlinear solution.

While the emphasis of the current paper is unsteady applications, the local equivalence correction technique presented is also applicable to steady nonlinear aeroelastic analysis (i.e. loads), and provides a simple and elegant method for including the effects of nonlinear aerodynamics into production-level aeroelastic analysis and aeroelastic optimization.

Further validation of the local equivalence correction technique for steady and unsteady aerodelastic analysis, including applications to complex, low aspect ratio configurations using Euler and Navier-Stokes aerodynamics is ongoing.

Acknowledgements

References

1. J. T. Batina, "Efficient Algorithm for Solution of the Unsteady Transonic Small-Disturbance Equation," J. Aircraft, 25, 7, July, 1988, pp. 598-605.

2. H. J. Cunningham, J. T. Batina, and R. M. Bennett, "Modern Wing Flutter Analysis by

Computational Fluid Dynamics Methods," J. Aircraft, 25, 10, October, 1988, pp. 962-968.

3. J. W. Edwards, R. M. Bennett, W. Whitlow, Jr., and D. A. Seidel, "Time-Marching Transonic Flutter Solutions Including Angle-of-Attack Effects," J. Aircraft, 20, 11, November 1983, pp. 899-905.

4. B. K. Bharadvaj, "Computation of Steady and Unsteady Control Surface Loads in Transonic Flow," AIAA Paper 90-0935, April 1990.

5. J. T. Batina, "Unsteady Euler Algorithm with Unstructured Dynamic Mesh for Complex Aircraft Aeroelastic Analysis," AIAA Paper 89-1189-CP, 1989.

6. E. M. Lee-Rausch and J. T. Batina, "Wing Flutter Computations Using an Aerodynamic Model Based on the Navier-Stokes Equations," J. Aircraft, 33, 6, November-December 1996, pp. 1139-1147.

7. P. M. Hartwich and S. Agrawal, "Method for Perturbing Multiblock Patched Grids in Aeroelastic And Design Optimization Applications,""AIAA Paper 97-2038-CP, June/July 1997.

8. G. P. Guruswamy and C. Byun, "Fluid-Structural Interactions Using Navier-Stokes Flow Equations Coupled with Shell Finite Element Structures," 24th AIAA Fluid Dynamics Conference, Orlando, FL, 1993.

9. J. P. Giesing, T. P. Kalman, and W. P. Rodden, "Subsonic Unsteady Aerodynamics for General Configurations, Part I – Vol. I – Direct Application of the Nonplanar Doublet Lattice Method," AFFDL-TR-71-5, November 1971.

10. E. Albano and W. P. Rodden, "A Doublet Lattice Method for Calculating Lift Distributions on Oscillating Surfaces in Subsonic Flows," AIAA Journal, 7, 2, February 1969, pp. 279-285. Also, Errata published in 7, 11, November, 1969, pp. 2192.

11. E. H. Dowell, "Eigenmode Analysis in Unsteady Aerodynamics: Reduced Order Models," 36th AIAA/ASME/ASCE/AHS/ ASC Structures, Structural Dynamics, and Materials Conference, New Orleans, LA, 1995.

12. K. C. Hall, "Eigenanalysis of Unsteady Flows About Airfoils, Cascades, adn Wings," AIAA Journal, 32, 12, December 1994, pp. 2426-2432.

13. M. C. Romanowski and E. H. Dowell, "Using Eigenmodes to Form an Efficient Euler Based Unsteady Aerodynamics Analysis,""Aeroelasticity and Fluid Structure Interaction Problems, Vol. AD-44, ASME, 1994.

14. M. C. Romanowski and E. H. Dowell, "Aeroelastic Analysis of an Airfoil Using Eigenmode Based Reduced Order Unsteady Aerodynamics," AIAA Paper #95-1380-CP, 1995.

15. W. A. Silva, "Extension of a Nonlinear Systems Theory to General-Frequency Transonic Aerodynamic Responses," 34th AIAA/ASME/ASCE/AHS/ASC Structures, Structural Dynamics, and Materials Conference, La Jolla, CA, 1993.

16. W. A. Silva, "Application of Nonlinear Systems Theory to Transonic Aerodynamic Responses," J. Aircraft, 30, 5, September-October, 1993, pp. 660-668.

17. M. L. Baker, D. L. Mingori, and P. J. Goggin, "Approximate Subspace Iteration for Constructing Reduced Order Models of Unsteady Aerodynamic Systems," 37th AIAA/ASME/ASCE/AHS/ASC Structures, Structural Dynamics, and Materials Conference, Salt Lake City, Utah, April 1996.

18. M. L. Baker, "Model Reduction of Large, Sparse Dynamic Systems with Application to Unsteady Aerodynamics," Ph.D. Dissertation, University of California, Los Angeles, 1996.

19. J. P. Giesing, et. al., "Modifications to the VIBRA-6 Nuclear Blast Response Computer Program," USAF Report AFWL-TR-81-166, Part 1, August 1983.

20. J. P. Giesing, T. P. Kalman, and W. P. Rodden, "Correction Factor Techniques for Improving Aerodynamic Prediction Methods," NASA CR-144967, May 1976.

21. E. C. Yates, Jr., AGARD Standard Aeroelastic Configurations for Dynamic Response I – Wing 445.6, AGARD Report No. 765, 1988.

22. E. M. Lee-Rausch and J. T. Batina, "Wing Flutter Boundary Prediction Using Unsteady Euler Aerodynamic Method," J. Aircraft, 32, 2, March-April 1995, pp. 416-422.

23. W. P. Rodden and E. H. Johnson, MSC/NASTRAN Aeroelastic Analysis User's Guide, Version 68, The MacNeal-Schwendler Corporation, 1994.

24. S. R. Bland and J. W. Edwards, "Airfoil Shape and Thickness Effects on Transonic Airloads and Flutter," J. Aircraft, 21, 3, pp. 209-217, 1984.

INVESTIGATION OF BUFFET LOAD ALLEVIATION ON A SCALED F-15 TWIN TAIL MODEL

L. J. Huttsell
J. A. Tinapple
Air Force Research Laboratory
Wright-Patterson AFB OH 45433 USA

and

R. M. Weyer
Aeronautical System Center
Wright-Patterson AFB OH 45433 USA

SUMMARY

One of the common problems on twin tail fighters operating at high angles of attack is buffet. The Air Force Research Laboratory Unsteady Aerodynamics Integrated Product Team (IPT) performed an experimental buffet investigation on a scaled F-15 model. The model was tested in the Subsonic Aerodynamic Research Laboratory (SARL) located at Wright-Patterson AFB, Ohio. Phase I of this program characterized the buffet characteristics and investigated tangential blowing as a means of buffet suppression. Phase II will investigate the use of piezoelectric actuators on the flexible tail to suppress the structural response due to buffet. A numerical simulation of the rigid model was performed for a Mach number of 0.2, 24 degrees angle of attack, and -4 degrees of slideslip using an unstructured CFD (Computational Fluid Dynamics) code. A second computation was performed to evaluate engine mass flow effects. This paper will present the results of the buffet tests, the computational effort, and a comparison of the computational and test results.

LIST OF SYMBOLS

AOA	Angle of Attack
M	freestream Mach number
PSD	Power Spectral Density
psf	pounds per square foot
Q	dynamic pressure
α	angle of attack

1. INTRODUCTION

Current fighters are required to maneuver at high angles of attack and are experiencing structural problems due to buffet on aft components of the empenage, in particular vertical tails. The ability to accurately predict the buffet on a vertical tail is difficult due to the complexity of the interaction between the aircraft geometry, flow field, vortex trajectory and empenage structure. In the past, the dynamic buffet loads have been estimated from model tests by means of scaling procedures. References 1, 2, and 3 report buffet testing on the F-15, F/A-18, and F-111 TACT aircraft.

The buffet or aerodynamic excitation associated with separated flow is normally broad-band random fluctuations with predominant frequencies associated with the air flow properties of the aircraft (i.e., vortex flow from inlets and sharp corners, wakes behind pods or other components of the aircraft). The buffeting, or structural response to buffet, can result in large oscillatory responses at resonant frequencies of the aircraft. A good review of the general principles of the buffet problem is given by Jones (4). The effects of buffeting and other transonic phenomena on maneuvering aircraft were

the subject of a study conducted by an AGARD Working Group (5). Lamar (6) summarized this study and documented the comprehensive state-of-the-art review of buffet techniques and prediction methods by the Working Group. Another assessment of dynamic loads due to flow separation is reported by Mabey (7).

The vortical flow pattern on the F/A-18 aircraft at high angle of attack is shown in Figure 1. The burst vortex travels aft and
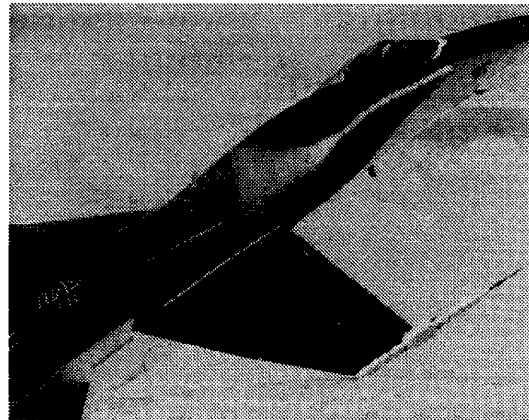
Figure 1. Vortical Flow on F/A-18 at High Angle of Attack

upward, impinges on the vertical tail and causes very high dynamic loads. A full-scale F/A-18 aircraft was tested in the National Full Scale Aerodynamic Complex 80 by 120 Foot wind tunnel at NASA Ames. Buffeting pressures and the resulting structural response of the vertical tails were obtained over a range of angle of attack and sideslip conditions (8 and 9). The tests were conducted with and without the Leading-Edge-Extension (LEX) fences (installed to reduce the buffet load). NASA Langley has also conducted buffet tests on a 16 percent scale F-18 model. Three different suppression concepts (existing rudder, oscillating cylinder, and piezoelectric actuators) were evaluated. A comparison of the pressure measurements from the 1/6 scale tests and the full-scale tests is presented in reference 10. Buffet tests on F/A-18 models have also been performed by others such as Lee and Tang (11). Under a Phase II SBIR (Small Business Innovative Research) contract, Active Control eXperts (ACX) is developing an active buffet suppression system for an F/A-18 (12). The suppression system uses distributed piezoelectric actuators and will be demonstrated by ground tests on a full scale vertical tail.

In 1981, buffeting pressure measurements were made on the vertical tail surfaces of a 13 percent F-15 model (1). The test variables included dynamic pressure, angle of attack, vertical tail incidence, and rudder deflection. The pressures and associated vibration response levels reached a maximum at approximately 22 degrees angle of attack. The flow field characteristics in the vicinity of the vertical tail were investigated and are shown in Figure 2. Other flow field
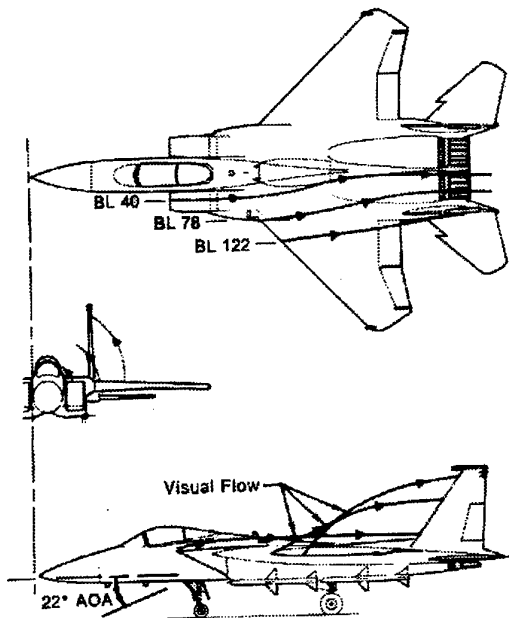

Figure 2. F-15 Vertical Tail Flowfield Characteristics

measurements on an F-15 model at high angles of attack have been performed by Komerath et al (13). An on-going SBIR contract with Rohini International and Georgia Tech is investigating the use of stacked piezoelectric actuators for buffet alleviation. Several structural fixes have been made to the F-15 aircraft to extend the fatigue life of the vertical tails. The most recent modification is the addition of a composite "exoskin" doubler (14).

Within the Air Force Research Laboratory, an Integrated Product Team (IPT) was formed for coordinating and integrating unsteady aerodynamic research. The IPT is a multidisciplinary team with members from the Aeromechanics, Flight Controls, and Structures Divisions. One of the on-going projects is buffet suppression. This paper will present the results of the buffet tests on a scaled F-15 model and the CFD computations.

2. EXPERIMENTAL PROGRAM

The wind tunnel testing was conducted in the Subsonic Aerodynamic Research Laboratory (SARL) located at Wright-Patterson Air Force Base, Ohio (USA). The SARL facility is a modern high contraction ratio open circuit wind tunnel with a maximum Mach number of approximately 0.55. The test section is 10 feet high by 7 feet wide and 15 feet in length with 2 foot flats on the corners to give the cross section an octangular shape. A honeycomb section sandwiched between two sets of screen arrangements dampen and condition the inlet flow to provide low turbulence in the test section. Fifty-

six percent of the test section walls are comprised of optical quality Plexiglas to allow any model view angle, and laser light sheet visualization techniques.

The SARL data system consist of a Micro VAX III programmable computer connected to a software controlled, 120 channel, 40 mV to 10 V, double ended multiplexer and a 13 bit 100,000 samples per second, auto ranging analog to digital converter. Balance channels, discrete pressure transducers, strain gages and accelerometer signals were fed through Dynamic brand amplifiers/bridge conditioners. Additionally for this test a Metrum dynamic data recorder was used to record the vertical tail surface pressure, bending and torsion strain gages, and tip pod accelerometers.

For these tests the tunnel was operated at Mach 0.2. An existing 4.7% scale model of an F-15C aircraft was modified for these tests. Figure 3 shows a photo of the sting mounted model in the SARL wind tunnel. The model was a standard
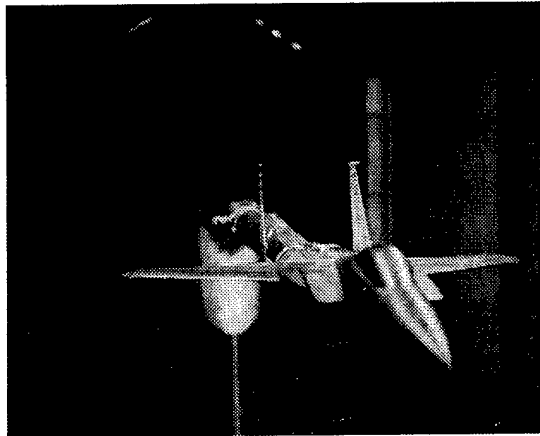
Figure 3. F-15 Model in SARL Wind Tunnel

aerodynamic model, essentially rigid at these low speeds and dynamic pressures. The model was modified by replacing the rigid vertical tail on the left hand side with a scaled flexible tail that emulated the first several vibration modes of the full size tail. The tail was constructed using a single aluminum spar with a thin aluminum web to form the profile of the tail. End grain balsa wood was used to form the airfoil shape. The flexible tail was equipped with bending and torsion strain gauge bridges located at the root to measure bending and torsion moments, both static and dynamic. Accelerometers were placed in the forward and aft areas of the tip pod. Six pressure transducers were mounted on each side of the rigid and flexible tails to measure static and oscillatory pressures. The locations of these transducers (Figure 4) were the same on both sides so that a pressure difference across the tail could be obtained.

The model was further modified to allow for blowing introduced tangentially at three locations (the nose, the gun bump, and the wing root leading edge). Figure 5 shows a sketch of these blowing locations. The six blowing locations (two laterally symmetric blowing slots at each location) were all achieved by designing and fabricating new model segments that replaced the existing solid segments. All six blowing locations featured a tangential blowing slot that was .010 inch wide by 0.75 inch long and was fed by a plenum built into the model. Before the test entry each of the six blowing slots was calibrated for mass flow verses plenum pressure (for choked flow) using a precision orifice plate flow meter. At the wind

tunnel test condition of 56 psf, blowing coefficients of up to 0.005 were obtained.
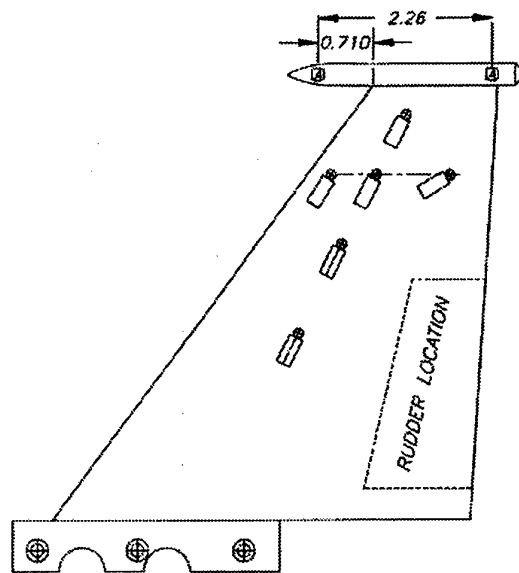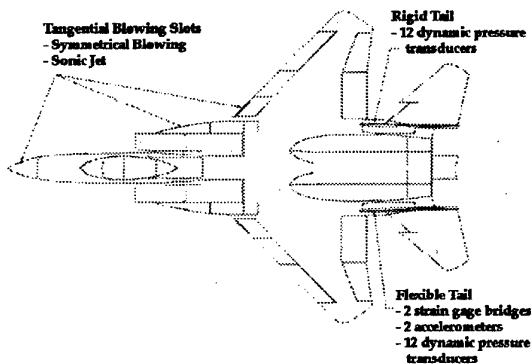

Figure 4. Location of Pressure Transducers

Figure 5. Location of Blowing Ports

3. CFD SIMULATIONS

The CFD simulations were performed at one tunnel test condition (M=0.2, 24 degrees angle of attack, and -4 degrees of sideslip) to aid in the determining the origin of the vortex and to describe the flowfield experienced by the vertical tails. Another goal of the CFD effort was to demonstrate the capabilities of a new unstructured grid method for complex configurations. The simulation used the inviscid (Euler) form of the equations of fluid flow, and globally marched in time until convergence was reached.

A clean F-15C aircraft was computationally modeled similar to the wind tunnel model, except for the aft end. The wind tunnel model was sting mounted through the centerline. Both models had flow through ducts, and the inlets and internal ramps were set for the subsonic high angle of attack condition. Computationally all surfaces were rigid and no tunnel wall effects were modeled.

The geometry used for this effort resided on a CAD system. An in-house utility converted the actual aircraft surfaces to 250 discretized structured surface panels. The Interactive Graphics for Geometry Generation & Visual Interactive Rapid Grid Generation (I3G/VIRGO) was used to clean the surface geometry. The unstructured gird generator TETMESH (15) was used to define the distribution of grid points along each of the surface panels received from I3G. The points were clustered in areas of highly curved geometry, corners, and small gaps. The density of points was also biased toward the upper surface of the aircraft to capture the vortical flow structure. Figure 6 shows the left side (forward half) of the aircraft with its surface triangles. Once the surface was completed, then the volume grid was generated with tetrahedrals using Delaunay method. The farfield for the grid was a sphere that was located ten times the wing semispan from the aircraft. The resulting volume grid had 578,000 tetrahedral cells.
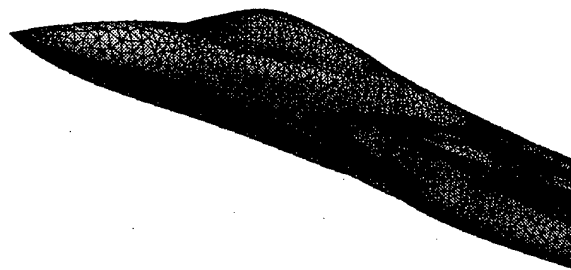
Figure 6. Surface Grid for CFD Computations

Cobalt (16) was the aerodynamic flow solver used. It can treat two-dimensional, axisymmetric, and three-dimensional problems with structured or unstructured grids. Cobalt solves the inviscid or viscous sets of fluid flow equations. It has the Spalart-Allmaras (17) and Baldwin-Barth (18) one-equation turbulence models. Cobalt uses the approximate Riemann solution method of Collela (19) in combination with the iterative method of Gottlieb-Groth (20) which is all based on the exact Riemann solver of Bodunov. The fundamental algorithm is finite-volume, cell-centered, first-order accurate in space and time. Second-order accuracy in space is patterned after van Leer's MUSCL scheme (21) and linear variations are constructed using a least squares method, second, third, and fourth-order temporal accuracy is achieved via the low storage Runge-Kutta methods of Williamson (22). For these simulations the code was run with an unstructured grid and used the inviscid flow equations. The solution was run with second order accuracy in space and time.

A second computation was performed at the same tunnel conditions to help bridge the step from a flow through inlet model to an aircraft in flight. For this engine-on case, the nozzle vanes were rotated and set to the correct exit area ratio. The grid for this case used a new design for the farfield and added more points on the vertical tail surfaces. This resulted in an inviscid single zone volume grid with 630,000 tetrahedrals.

4. RESULTS

First the test results with no blowing will be presented as PSD plots of bending and torsion responses as a function of angle of attack with sideslip variations. Figure 7 shows the root

bending response for angles of attack (AOA) up to 32 degrees for the three different angles of sideslip (-4, 0, & 4 degrees). Note that the bending responses for all three angles of sideslip increase with AOA and that the negative sideslip tends to increase the response compared to the other cases. This makes sense when considering that the vortex is outboard of the left tail (flexible tail) and negative sideslip moves the left wing forward which pushes the left hand vortex into the left tail. Higher AOA is needed to define the bending peak response. Figure 8 shows the root torsion response for the

same range of angle of attack and sideslip. The torsional response peaks within the AOA range, with the sideslip effects before peaking showing the same trend as in bending plot. After the torsional response peaks, the positive sideslip tends to increase the response.

Tangential blowing at the nose and gun bump had little effect on the vertical tail response. Blowing at the wing root was the most effective, but produced mixed results for the various test conditions. Figures 9 and 10 are a set of cross plots that shows
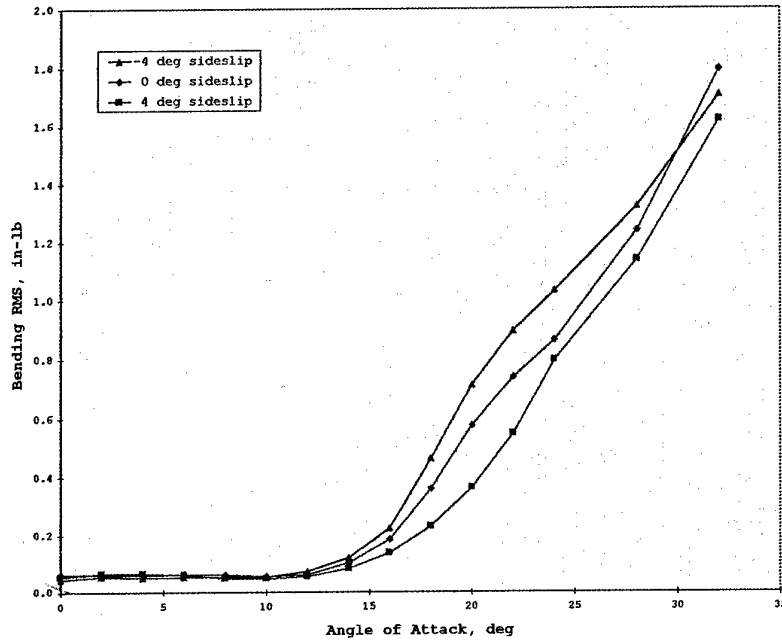
Figure 7. Bending Response, Q=56 psf, No Blowing
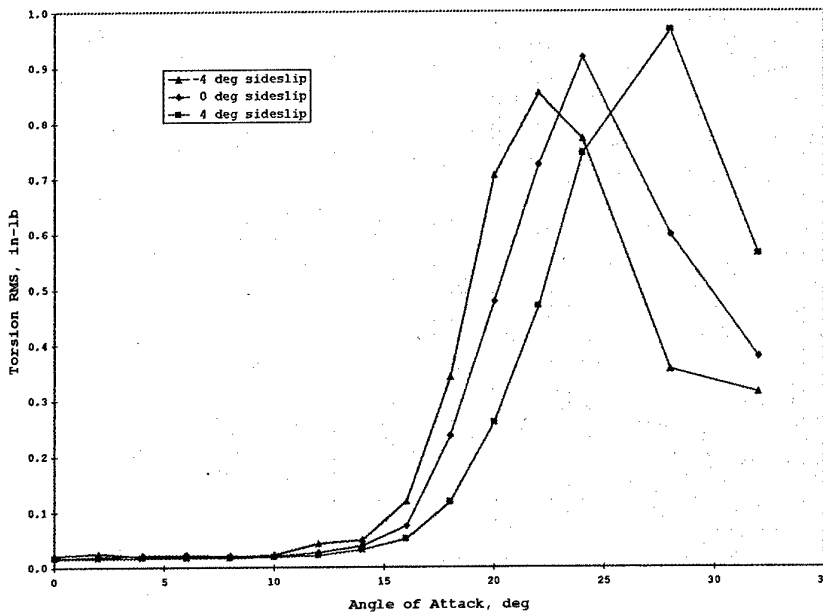
Figure 8. Torsion Response, Q=56 psf, No Blowing

Response of Bending Mode for Various Levels of Blowing
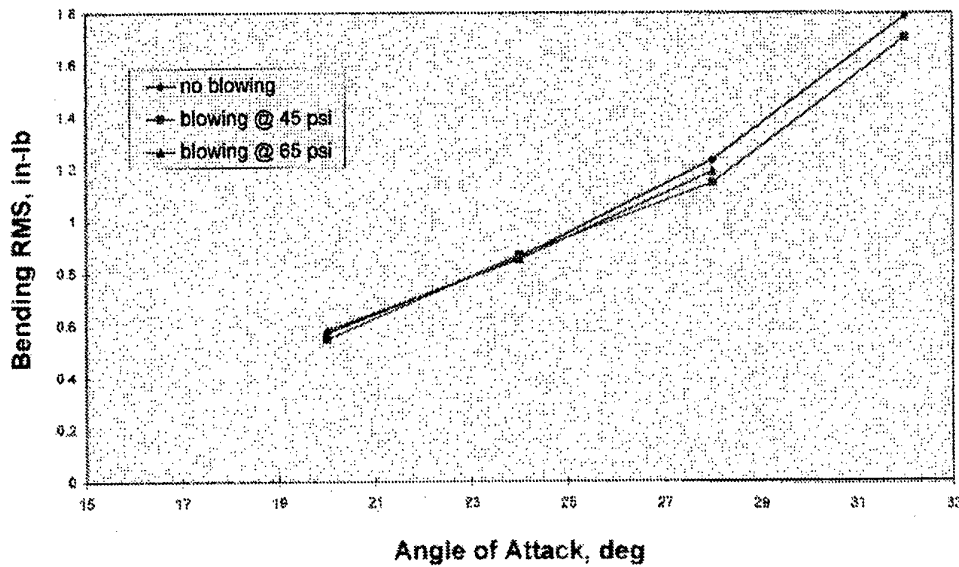
Figure 9. Bending Response with Blowing, Q= 56 psf

Response of Torsion Mode for Various Levels of Blowing
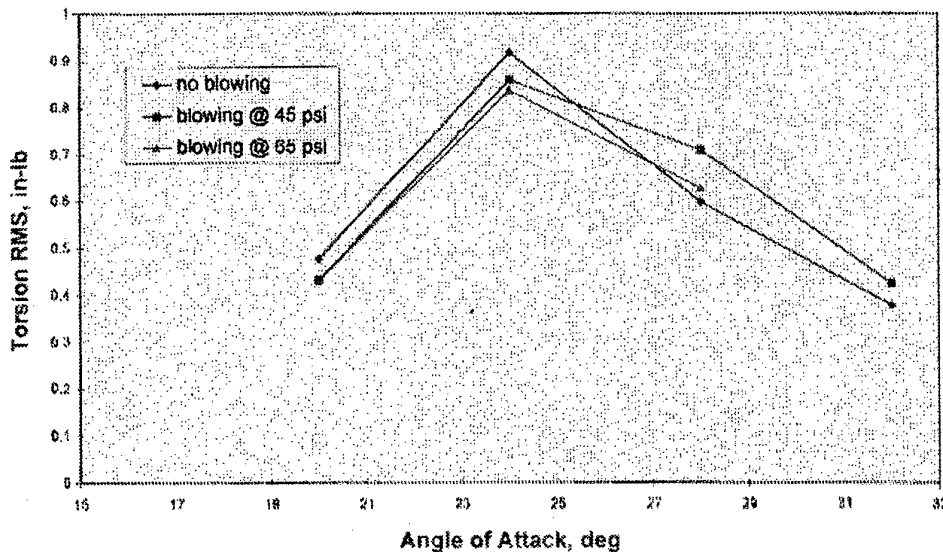
Figure 10. Torsion Response with Blowing, Q= 56 psf

the effect of blowing at the wing leading edge for zero sideslip. The tail response is plotted versus angle of attack for three values of blowing (0, 45, and 65 psf). Blowing tends to slightly increase the bending response at lower angles, while at the higher angles, blowing decreases the response. For negative sideslip where buffet is stronger, the effect of blowing tends to increase response up through larger angles of attack. For positive sideslip a 45 psf blowing tends to decrease response at lower angles of attack, but increases response at higher angles. The blowing pressure of 65 psf shows a reduction in response at higher angles. Torsional responses are different, peaking around angle of attacks of 24-28 degrees, with blowing showing reduction of the response below the peak and increases above the peak. Both bending and torsion responses suggest that the flow injection can move the vortex activity into or away from the tail as well as move the vortex spanwise along the tail.

The computations of forces and moments for the flow through inlet case are compared to the experimental data in Table 1. The lift coefficient is only 1 percent high compared to test data. The drag coefficient differs by 29 percent presumably due to the lack of viscosity in the computations. The pitching coefficient differs by 6 percent and the rolling coefficient differs by 27 percent. The side force and yawing moment coefficients are small making the percentage difference large.

Table I. Force and Moment Comparison (Wind Axis) for Flow Through Inlet Case

Coefficient	Test	Computations
Lift	1.2901	1.3032
Side Force	-.0055	-.0015
Drag	0.8257	0.5829
Pitching Moment	-.1834	-.1722
Yawing Moment	0.0026	0.0054
Rolling Moment	0.0158	-.0201

For the inviscid solution (flow through inlet case), the origin of the vortex was on top of the inlet at station 425 for the leeward side and station 427 on the windward side. The flow sweeping over the gun bump fairing to the top of the inlet initiates the vortical flow shown in Figure 11. From the top of the inlet, the vortex core flows aft and then turns out on the wing to about mid-span. It then lifts away from the surface and travels aft outside the vertical tail as shown in Figure 12. This same surface flow behavior was demonstrated during the wind tunnel test where a surface flow visualization run was done with the same freestream conditions. The wind tunnel test showed more separation at the wing tip. Also shown in Figure 11 is another vortex which forms from the nose of the aircraft on the leeward side at station 406. It tracks over the fuselage just right of the centerline, but loses its structure near the wing leading edge (approximately station 500).

Figure 11. Flowfield Around the Forward Section
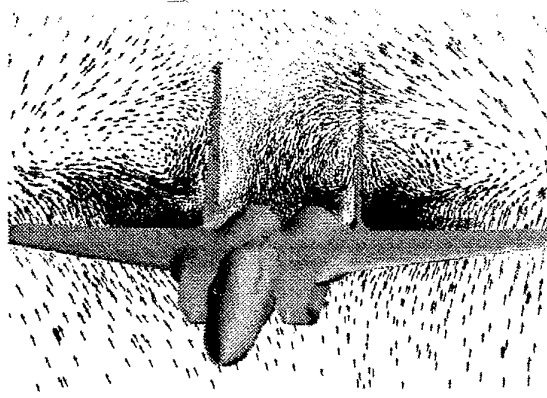
Figure 12. Flowfield Just Forward of Vertical Tails

A laser light sheet was also used in the test to highlight the vortex shape. Figure 13 is an enhancement of a frame showing the vortex shape at the vertical tail station. Figure 14 clearly indicates the impact of the vortical flow with the outer part of the vertical tail and tip pods. Also visible are the smaller vortices that form between the tails and at the root of the vertical tails. The path of the vortex is indicated from the streamline traces from the inlet area shown in Figure 15. Figure 16 shows that the flow from the inlet top remains close to the surface and travels out the wing and then lifts up, while the flow from the wing leading edges separates from the surface. Figure 17 takes a slice about mid-span of the left wing and shows the velocity vectors in the x-z plane. Note that the air above the wing is flowing inboard. The lengths of the velocity vectors are scaled differently for each figure to enhance the visualization.

Figure 13. Laser Light Sheet
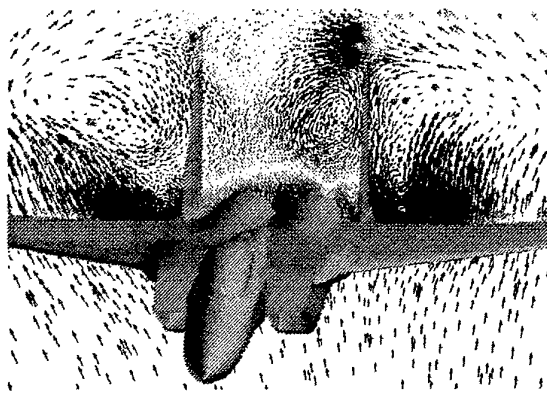
Figure 14. Vortical Flow Near Tip Pods

Figure 17. Vector Plot in X-Z Plane (Mid-Span of Left Wing)
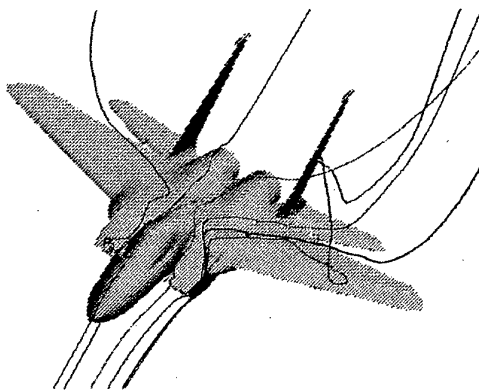
Figure 15. Streamlines Showing the Flow Over the Inlets

Table II. Force and Moment Comparison (Wind Axis) for Flow Through and Engine-on Case

Coefficient	Engine-on	Flow Through
Lift	1.3833	1.3032
Side Force	-.0023	-.0015
Drag	0.6453	0.5829
Pitching Moment	-.1841	-.1722
Yawing Moment	0.0001	0.0054
Rolling Moment	-.0192	-.0201

The influence of the engine suction on the location of the vortex origin is that it moved forward by three inches on the leeward side and three inches aft on the windward side. The vortex from the nose of the aircraft on the leeward side does not form until 12 inches farther aft (station 418). The vortical flowfield is similar, however, the engine-on case has main vortices that are tighter and closer to the vertical tails.

For the engine-on case, the mass flow rate through the inlet represented the engine running at this flight condition. Table 2 presents a comparison of the computed forces and moments with those for the flow through inlet case. In the engine-on case the lift is increased by 6 percent and the drag is increased by 10 percent. The pitching moment increased by 7 percent. For both tails, the inner surface has a larger side force than the outer surface. These differences were small.

5. CONCLUSIONS

The wind tunnel tests of the 4.7% scale F-15 model provided detailed buffet characteristics for a range of angle of attack (0 to 32 degrees) and three angles of sideslip. Buffet alleviation tests using tangential blowing provided alleviation in some cases but showed mixed results. A second buffet alleviation test is planned using an active control system with piezoelectric actuators on the vertical tail. This test is scheduled for March 1998.

The computation solution provided insight into the flowfield around the F-15 for M=0.2, alpha=24 degrees, and -4 degrees of sideslip. The origin of the vortex was determined to initially form on the top of the inlet for this inviscid solution. Flowtrace and vector plots were used to describe the path of the vortex and the entire flowfield of the aircraft. The forces and moments were calculated and compared reasonably well to the test results. This computational effort also demonstrated the ability of the grid code, TETMESH, to generate an inviscid unstructured grid around a complex configuration.

Under an on-going computational effort, a structured grid is being generated for the F-15 and an Euler simulation will be performed with one rigid and one flexible vertical tail. The Euler/Navier-Stokes 3-Dimensional Aeroelasticity (ENS3DAE) code (23) will be used for this computation.

Figure 16. Side View of Streamlines

6. ACKNOWLEDGEMENTS

7. REFERENCES

1. Triplett, W. E., "Pressure Measurements on Twin Vertical Tails in Buffeting Flows", AFWAL-TR-82-3015, April 1982.

2. Zimmerman, N. H., Ferman, M. A., Yurkovich, R. N., and Gerstenkorn, G., "Prediction of Tail Buffet Loads for Design Application", AIAA-89-1378, AIAA Structures Structural Dynamics and Material Conference, April 1989.

3. Coe, C. F. and Cunningham, A. M., Jr., "Predictions of F-111 TACT Aircraft Buffet Response and Correlation of Fluctuating Pressures Measured on Aluminum and Steel Models and the Aircraft", NASA CP 4069, May 1987.

4. Jones, J. G., "Dynamic Response of Aircraft with Fluctuating Flow Fields", Von Karmon Institute For Fluid Dynamics Lecture Series 1981-4 on Unsteady Airloads and Aeroelastic Problems in Separated and Transonic Flow, March 1981.

5. "Effects of Buffeting and Other Transonic Phenomena on Maneuvering Combat Aircraft", AGARD Advisory Report No. 82, July 1975.

6. Lamar, W. E., "Effects of Buffeting and Other Transonic Phenomena", AGARD Conference Proceedings No. 187 on Flight/Ground Testing Facilities Correlation, April 1976.

7. Mabey, D. G., "Some Aspects of Aircraft Dynamic Loads Due to Flow Separation", Royal Aircraft Establishment Tech Memo Aero 2110, July 1987.

8. Pettit, C., Banford, M., Brown, D., and Pendleton, E., "Pressure Measurements on an F/A-18 Twin Vertical Tail in Buffeting Flow", J. Aircraft, 33, 6, November-December 1996, pp 1148-1156.

9. Meyn, L. A. and James, K. D., "Full-Scale Wind-Tunnel Studies of F/A-18 Tail Buffet", J. Aircraft, 33, 3, May-June 1996, pp 589-595.

10. Moses, R. W. and Pendleton, E., "A Comparison of Pressure Measurements Between a Full-Scale and a 1/6 Scale F/A-18 Twin Tail During Buffet", Paper presented at the AGARD 83rd Structures and Materials Panel Meeting, September 1996.

11. Lee, B. H. K. and Tang, F. C., "Characteristics of the Surface Pressures on a F/A-18 Vertical Fin Due to Buffet", J. Aircraft, 31, 1, January-February 1994, pp 228-235.

12. Moore, J. W., Lazarus, K. B., and Henderson, D. A., "Buffet Load Alleviation Using Distributed Piezoelectric Actuators", Symposium on Adaptive Structures, ASME International Mechanical Engineering Congress and Exposition, 1996.

13. Komerath, N. M., McMahon, H. M., Schwanz, R. J., Liou, S. G., and Kim, J. M., "Flow Field Measurements Near a Fighter Model at High Angles of Attack", Paper presented at AIAA Aerodynamic Ground Test Conference, Seattle, WA, June 18-20, 1990.

14. Ferman, M. A., Liguore, S. L., Smith, C. M., and Colvin, B. J., "Composite "Exoskin" Doubler Extends F-15 Vertical Tail Fatigue Life", AIAA-93-1341-CP, Paper presented at the 34th Structures, Structural Dynamics and Materials Conference, April 1993.

15. Reddy, M. P., "STORESIM: An Integrated System for Multi-Body CFD Simulations Using Unstructured, Adaptive Grids", WL-TR-97-3003, December 1996.

16. Strang, W. Z. "Cobalt User's Manual", WL/FIMC, Wright-Patterson Air Force Base OH, March 1996.

17. Spalart, P. R. and Allmaras, S. R., "A One-Equation Turbulence Model for Aerodynamic Flows", AIAA-92-0439, January 1992.

18. Baldwin, B. S. and Barth, T. J., "A One-Equation Turbulence Transport Model for High Reynolds Number Wall-Bounded Flows", NASA TM 102847, August 1990.

19. Collela, P., "Glimm's Method for Gas Dynamics", SIAM J. Sci. Stat. Comp., Vol. 3, No. 1, pp 76-110, 1982.

20. Gottlieb, J. J. and Groth, C. P. T., "Assessment of Riemann Solvers for Unsteady One-Dimensional Inviscid Flows of Perfect Gasses", J. Comp. Phys., Vol. 78, pp 437-458, 1988.

21. van Leer, B., " Towards the Ultimate Conservative Difference Scheme, A Second-Order Sequel to Godunov's Method", J. Comp. Phys., Vol. 32, pp 101-136, 1979.

22. Williamson, J. H., "Low-Storage Runge-Kutta Schemes", J. Comp. Phys., Vol. 35, pp 48-56, 1980.

23. Schuster, D. S., Beran, P. S., and Huttsell, L. J., "Application of the ENS3DAE Euler/Navier-Stokes Aeroelastic Method", Paper presented at AGARD 85th Meeting of the Structures and Materials Panel, October 1997.

TRANSONIC AEROELASTIC SIMULATION OF A FLEXIBLE WING SECTION

Silvio Schulze

Deutsche Forschungsanstalt für Luft- und Raumfahrt e.V. (DLR)
Institute of Aeroelasticity
Bunsenstr. 10
37073 Göttingen, Germany

ABSTRACT

Flutter characteristics and results of aeroelastic time response analyses of NACA64010 airfoils oscillating in transonic flow are presented. These solutions were obtained by a newly developed two-dimensional aeroelastic simulation code which is designed in such a manner that the flow and the structure can be modelled independently by using the so-called domain decomposition approach. The coupled field problem is then effectively solved in the time domain by applying a partitioned solution procedure in which the fluid and the structural solvers are executed in an alternating fashion and exchange interface data only at certain time steps.

In this study the prediction of the flow field around airfoils in arbitrary motion is based on the solution of the unsteady Euler equations. The structure might either be modelled as a rigid body system or as a more realistic flexible configuration. In this context, the finite element method is used to model elastic effects in the chordwise direction of a typical wing section, thus accounting for more general motions of the airfoil including the fluid structure interaction boundary.

The underlying theory is briefly outlined and results are presented for several aeroelastic test cases of varying complexity in the structural model. Both cases with and without control surface are dealt with and the effect of flexibility on the transonic aeroelastic stability behavior is investigated.

1 INTRODUCTION

Although the field of aeroelasticity is well established, modern developments, e.g., the maturing adaptive structures technology combined with modern control system theory, continuously pose new problems to the aeroelastician. The general problem of meeting future air transport requirements challenges researchers, particularly when new concepts such as the new class of super transport aircraft are pursued. Among other problems introduced by the use of smart materials, control systems, etc., the increasing size and, hence, the structural flexibility of such aircraft result in a variety of severe static as well as dynamic aeroelastic and flight mechanic problems, particularly in the transonic flight regime, which is generally of primary concern.

The physical domain of aeroelasticity in the transonic region is richly varied due to nonlinear aerodynamics. Apart from flow separation, the physical manifestation of nonlinear aerodynamics lies in the development of strong pressure discontinuities, generally referred to as shocks. Indeed, the formation of shocks may be regarded as the definition of transonic (mixed subsonic supersonic) flow.

Some important aeroelastic problems caused by nonlinear aerodynamics are listed here:

- transonic dip (i.e., a significant decrease in flutter speed when the Mach number approaches unity)

- limit cycle oscillations (LCO) (i.e., flutter with finite amplitudes due to the dynamics of shock waves, sometimes with flow separation)

- aileron buzz (i.e., transonic control surface flutter where shock wave motions and flow separation in the vicinity of the control surface play an important role)

In general, one can say that undesired, yet not well understood aeroelastic phenomena impose constraints on advanced aircraft designs. New phenomena cannot be anticipated by simply extrapolating current experience, particularly when nonlinearities are present. In order to expand the design frontiers for high performance aircraft new methods must be developed and applied. This is of paramount importance since the usefulness of classical flutter and divergence prediction methods based on Fourier-type solution procedures in the frequency domain is limited in the transonic flight regime. This is because the aerodynamic nonlinearities mentioned earlier cannot be adequately represented by these methods and the airloads have to be calculated in the time domain.

In the past decade much progress has been made in the development of computational methods for the calculation of unsteady aerodynamics around airfoils, wings, and complete aircraft configurations in the time domain, typically referred to as Computational Fluid Dynamics (CFD). The favored formulation of fluid dynamic equations is generally Eulerian and finite difference methods have proven to be a powerful tool for their solution. On the other hand, in the field of structural and solid mechanics finite element methods using the Lagrangian formulation have taken over other alternatives, including finite difference methods, and are firmly established and widely used in practice today. It is unlikely that finite difference methods will experience a revival in solid mechanics, nor can it be expected that finite element methods will replace finite differences in fluid mechanics in the near future. Hence, in order to take full advantage of developments in the single domains, the coupling of fluid and structural solvers is widely practiced for the treatment of fluid structure interaction problems. As for the solution, partitioned analysis procedures provide an efficient and modular way to deal with such problems. Thus, in conjunction with recent advances in supercomputers, aeroelastic time domain calculations for the prediction of highly nonlinear aeroelastic phenomena have become feasible.

In order to do justice to the nonlinear aspects of transonic flow and the increased flexibility of future aircraft structures, a two-dimensional aeroelastic simulation code called SNAP2d (Simulation of Nonlinear Aeroelastic Phenomena) has been developed. It is designed in such a manner that the flow and the structure can be modelled separately by using the domain decomposition approach. Regarding the presented results, the prediction of the flow field around airfoils in arbitrary motion is based on the solution of the unsteady Euler equations. The structure might either be modelled as a rigid-body system or as a more realistic flexible configuration using the finite element method.

The purpose of this study is to present some preliminary results showing the effect of flexibility on transonic flutter and limit cy-

cle behavior. The first part gives an overview of the underlying theory while the second part is devoted to the presentation of the obtained results and their discussion.

2 AEROELASTIC MODEL AND METHOD OF SOLUTION

It is well-known that in order to study the motion of a continuous body essentially two approaches exist, namely the Lagrangian and the Eulerian description. In the Lagrangian description one observes the motion of all material particles of a continuum from the initial to the end condition. This formulation is particularly suited for structural dynamics because in this field small particle motions are generally of primary concern. In the Eulerian description one observes the material flux and, hence, the time variation of physical variables at a fixed geometrical point in space. This formulation is generally preferred in fluid dynamics where large particle motions are present and it usually suffices to know the change in flow variables at certain points in space. However, for many free-surface flows and problems of fluid structure interaction, a more versatile description of the fluid domain is needed. Accordingly, the demand to apply boundary conditions on moving surfaces and the desire to effectively control solution accuracy led to the idea of moving and adaptive meshes, respectively. These generalized descriptions, generally referred to as mixed or arbitrary Lagrangian-Eulerian formulations (ALE), were originally developed by Noh [30] and Hirt, Amsden and Cook [2], [23] in finite difference formats while Belytschko et al. [7] and Donea et al. [20] contributed to the development of the theoretical framework for mixed Lagrangian-Eulerian finite element formulations for compressible inviscid flows. An ALE finite element method for incompressible viscous flows had first been reported by Hughes [25]. Fairly recently, Bendiksen [9] introduced the arbitrary Lagrangian-Eulerian formulation to aeroelastic stability and response analysis and demonstrated the capabilities of the method in simulating transonic aeroelastic phenomena with emphasis on the nonlinear effects in a sequel of papers [10], [11], [12].

From the above, one can draw the conclusion that the arbitrary Lagrangian-Eulerian formulation is the most promising solution for treating future aeroelastic problems. Indeed, certain problems have been successfully solved with this method but it also has specific shortcomings. First, due to the inevitably distinct physical nature of the two media, fluid and structure, both domains in general have different natural time constants in the sense of their response characteristics, thus, accurate solutions by a monolithic time integration scheme can only be obtained by the use of very small time steps. Second, establishing a reliable computer program would be at least as much work as was necessary to develop the single domain codes and would run three risks: uncontrollable complexity, rigidity in formulation (and thus the inability to accommodate technology advances), and lack of flexibility to deal with new problems. Finally, insufficient experience is a disadvantage which should not be underestimated.

As a consequence, and keeping in mind the fact that the bulk of existing engineering software has been developed for the treatment of single-field problems, it appears that the coupling of available and reliable single-field solvers is the most practicable and efficient alternative. In so doing, different field solvers including its pre- and post-processing software can be used as „plug in" modules, thus offering the analyst flexibility to deal with the specific problem at hand. Also, maintaining simplicity in the single-field solver facilitates the adoption of new problem formulations. Rather than establishing large-scale comput-

er programs that do everything - and probably not too well - already existing software should be utilized to deal with multidisciplinary problems. This approach is favored by the majority of researchers in the field of aeroelasticity, as is here as well.

2.1 Aerodynamic Model

Since aeroelasticity is concerned with interactions between the elastic deformations of structures in an airstream and the resulting aerodynamic reactions, the accurate evaluation of the nonconservative forces acting on the structure is of vital importance. As long as flow separation does not occur, the Euler equations are a reasonable aerodynamic model for transonic flutter calculations. The development and motion of shock waves in particular can be adequately described.

2.1.1 Governing Equations

The two-dimensional conservation form of the Euler equations, derived from the fundamental physical principles:

- conservation of mass,
- conservation of momentum, and
- conservation of energy

in an inviscid compressible fluid and applied to a finite control volume V with the surface S fixed in space in Cartesian coordinates (x, z), can be written in integral form as follows

$$\iiint_{(V)} \frac{\partial Q}{\partial t}\, dV = -\iint_{(S)} (F dS_x + H dS_z) \qquad (1)$$

$$Q = \begin{bmatrix} \rho_{Fl} \\ \rho_{Fl} u \\ \rho_{Fl} w \\ \rho_{Fl} E \end{bmatrix},\ F = \begin{bmatrix} \rho_{Fl} u \\ \rho_{Fl} u^2 + p \\ \rho_{Fl} uw \\ \rho_{Fl} u H_T \end{bmatrix},\ H = \begin{bmatrix} \rho_{Fl} w \\ \rho_{Fl} uw \\ \rho_{Fl} w^2 + p \\ \rho_{Fl} w H_T \end{bmatrix},$$

with Q, the vector of independent solution variables, and F and H, the two flux vectors in the x and z direction, respectively. The variables ρ_{Fl}, p, u, w are the fluid density, pressure, Cartesian velocity components and E, H are the specific total energy and enthalpy. Under the condition of an ideal gas the pressure p can be eliminated from Eq. (1) using the relations

$$p = (\kappa - 1)\rho_{Fl} e = \frac{\rho_{Fl} a^2}{\kappa}, \qquad (2)$$

$$E = \frac{a^2}{\kappa(\kappa - 1)} + \frac{1}{2}(u^2 + w^2), \qquad (3)$$

$$H_T = \frac{a^2}{\kappa - 1} + \frac{1}{2}(u^2 + w^2), \qquad (4)$$

where a is the local speed of sound and $\kappa = c_p/c_v$ the ratio of specific heats.

In view of a numerical solution of the Euler equations by means of finite difference methods the partial differential form of equation (1)
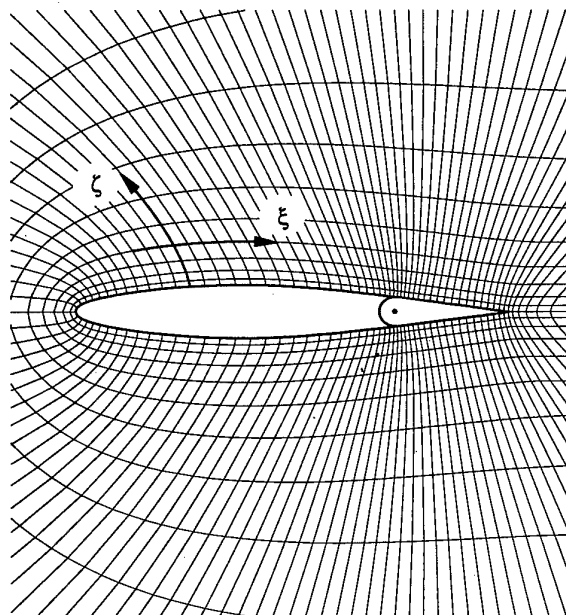
$$\frac{\partial Q}{\partial t} + \frac{\partial F}{\partial x} + \frac{\partial H}{\partial z} = 0 \qquad (5)$$

is preferred and can be directly obtained by applying the fundamental physical principles to an infinitesimal fluid element or indirectly by manipulating the integral form.

Equation (5) was derived in Cartesian coordinates and for a control volume fixed in space. For the aeroelastic problems to be solved here, however, a transformation to a boundary-fitted moving coordinate system (ξ, ζ) which allows for general deformations of the control volume is needed.
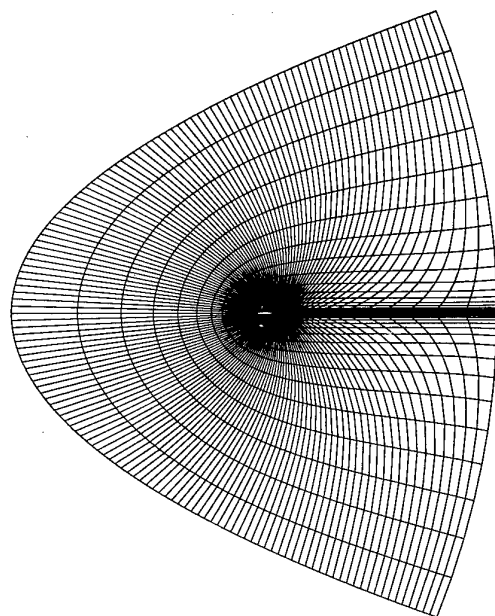
a) C-mesh around profile including far-field b) C-mesh near profile including coordinate definition

Fig. 1 Spatial discretization around profile

On condition that the relation

$$x = x(\xi, \zeta, \tau) \qquad \xi = \xi(x, z, t)$$
$$z = z(\xi, \zeta, \tau) \quad \Leftrightarrow \quad \zeta = \zeta(x, z, t) \qquad (6)$$
$$t = \tau \qquad \tau = t$$

between the Cartesian and boundary-fitted coordinate systems are known at any time t, the Euler equations (5) are now given in the new coordinate system still in conservative form by

$$\frac{\partial \hat{Q}}{\partial \tau} + \frac{\partial \hat{F}}{\partial \xi} + \frac{\partial \hat{H}}{\partial \zeta} = 0 \qquad (7)$$

with the transformed vectors

$$\hat{Q} = \hat{J} Q ,$$
$$\hat{F} = \hat{J}(\xi_t Q + \xi_x F + \xi_z H) , \qquad (8)$$
$$\hat{H} = \hat{J}(\zeta_t Q + \zeta_x F + \zeta_z H) .$$

The subscripts in equation (8) denote derivatives of the considered coordinate with respect to its subscript, e.g. $\xi_x = \partial \xi / \partial x$, the so-called metric terms, while

$$\hat{J} = \frac{\partial(x, z)}{\partial(\xi, \zeta)} = \begin{vmatrix} x_\xi & x_\zeta \\ z_\xi & z_\zeta \end{vmatrix} = x_\xi z_\zeta - x_\zeta z_\xi \qquad (9)$$

is the Jacobian or functional determinant of the transformation.

2.1.2 Mesh Generation

In order to make the application of kinematic boundary conditions easier, the Euler equations have been transformed to contour adaptive coordinates. In the present study, as is depicted in Fig. 1, a C-mesh is used where $\zeta = $ const. -lines map the inner and outer boundary. Thereby, the influence of the gap between the wing and the control surface on the fluid flow is assumed to be negligible, thus not included in the spatial descretization of the fluid domain. The mesh consists of 149 points in the ξ and

21 in the ζ direction with 105 mesh points coinciding with the airfoil's surface. Since stronger gradients in the flow were expected in the vicinity of the control surface hinge, the mesh lines were contracted in this region. The necessary mesh deformations are computed by the elliptic mesh generation method described in [17]. This procedure is based on a set of Poisson equations, so that the mesh generation itself becomes a boundary value problem. Although this is computationally more expensive than algebraic methods, it appears superior with respect to the smoothness of the mesh and the capability of treating complicated boundary conditions. During the computation the mesh is smoothly deformed from zero at the outer boundary (far-field boundary) to the values prescribed by the motion of the profile's surface (fluid structure boundary). Orthogonality constraints are imposed at the inner boundary to reduce the computational effort in determining the pressure acting at the deformed surface.

2.1.3 Boundary Conditions

The governing equations above are valid for inviscid fluid flow in general. They are the same equations whether the flow is through a cascade, a wind tunnel, or around an airfoil. The difference enters through the boundary conditions. Since the fluid flow is very sensitive to changes in the boundary conditions and the exchange of information between the structure and the fluid only takes place via the fluid structure boundary, it is of utmost importance to be very careful in their numerical implementation.

In case of a stationary surface with the flow passing over it, the physical boundary condition for an inviscid fluid demands that the flow slips over the surface since there is no friction. Hence, the flow must be tangent at the surface. This condition of tangent flow along the airfoil's surface is satisfied by setting the velocity components normal to the surface to zero $\vec{v} \cdot \vec{n} = 0$,

where $\vec{v}$ is the velocity vector and $\vec{n}$ the normal vector, positive outward. In case of a moving boundary the relative normal velocity vector $\vec{v}_{rel}$ has to be considered

$$\vec{v}_{rel} \cdot \vec{n} = (\vec{v} - \vec{v}_\tau) \cdot \vec{n} = 0 , \qquad (10)$$

where $\vec{v}_\tau$ is the vector containing the surface mesh speeds.

The pressure on the body's surface is determined from the normal momentum equation following the proposal of Rizzi [32]. This method is more accurate than the simple extrapolation of the pressure from interior field values.

Non-reflecting boundary conditions are applied in the far-field, which ensure that disturbances can leave the interior field across the outer boundary without being reflected into the computational domain.

2.2 Structural Model

For the theoretical investigation of the probably most dangerous, though not the most frequently encountered type of aircraft flutter, which results from the coupling of fundamental bending and torsional motions of relatively large aspect-ratio wings, the two-dimensional representative wing section introduced by Theodorsen and Garrick [33], [34] has been extensively used and a great deal of qualitative information can be obtained about the influence of various system parameters on the above-mentioned type of aeroelastic instability.

In order to do justice to the increased flexibility of modern lightweight aircraft the finite element method is used in this study to account for more general motions of a typical wing section. With the introduction of additional degrees of freedom it is possible to describe the motion of the airfoil more accurately. In particular, local changes of the profile's surface leading to local changes in the angle of attack, thus changing the pressure distribution, are captured.

2.2.1 Governing Equations

The governing finite element equations are usually generated via variational principles, e.g. the principle of virtual work or displacement and stationarity of the total potential. Hamilton's principle or the principle of virtual work in combination with d'Alembert's principle can be applied for dynamic problems. Both formulations are equivalent to each other and lead to the same differential equations of motion. While Hamilton's principle uses energy expressions, the virtual work principle directly considers the actual loads acting on the structure.

Since the main idea of the finite element method is the approximation of a continuous body by a finite number of discrete elements interconnected at the nodal points at the element boundaries, it is expedient to establish general relations on the element level using a local coordinate system in which the local degrees of freedom at the nodes are measured. The system matrices of the total element assemblage are then obtained by identifying the global degrees of freedom which correspond to the local element degrees of freedom using some kind of connectivity array. If the local coordinates are not aligned with the global coordinate system, an additional transformation is necessary prior to the assemblage.

Applied on the element level denoted by the superscript (e), Hamilton's principle in its extended form, taking into account non-conservative external loads can be written as [16]

$$\int_{t_1}^{t_2} (\delta L^{(e)} + \delta W_{ext}^{(e)}) \, dt = 0 , \qquad (11)$$

where δ is the variational operator, $\delta L^{(e)} = \delta T^{(e)} - \delta U^{(e)}$ is the variation of Lagrange's function with $T^{(e)}$ and $U^{(e)}$ as the element specific kinetic and potential energy, and δW_{ext} is the virtual work of all external loads acting on the element no matter whether they can be derived from a scalar potential or not.

Assuming a linear elastic continuum where the stress-strain relationship is given by Hook's law

$$s^{(e)} = H^{(e)} e^{(e)} , \qquad (12)$$

with $H^{(e)}$ as the symmetric, positive definite matrix of material constants, and the vectors $s^{(e)}$ and $e^{(e)}$ representing the stresses and strains, the element specific potential energy including discrete linear springs of stiffness c_i at the points i can be expressed as

$$U^{(e)} = \frac{1}{2} \int_{(V^{(e)})} e^{(e)T} H^{(e)} e^{(e)} \, dV^{(e)} + \frac{1}{2} \sum_{(i)} v_i^{(e)2} c_i , \qquad (13)$$

where $v_i^{(e)}$ are the displacements at the points i, and $V^{(e)}$ is the element volume. The element strains $e^{(e)}$ depend on the element displacements $v^{(e)}$ and can be evaluated by differentiation using an element specific differential operator $D^{(e)}$

$$e^{(e)} = D^{(e)} v^{(e)} . \qquad (14)$$

It should be noted that the displacement vector $v^{(e)}$ is related to all particles i of the continuum and represents a continuous displacement field. Following the original ideas of Lagrange, however, it is generally assumed that the motion of the body can be described by a carefully chosen set of generalized (or Lagrange) coordinates $u^{(e)}$, which, in case of the finite element method, are identical with the nodal displacements. The interior displacement field, necessary for calculating the strains and stresses, is then approximated by interpolation (shape) functions (Ritz method). Introducing the element displacement interpolation matrix $G^{(e)}$, it follows for the displacement field, the strains, and the stresses, respectively:

$$v^{(e)} = G^{(e)} u^{(e)} , \qquad (15)$$

$$e^{(e)} = D^{(e)} G^{(e)} u^{(e)} = D_G^{(e)} u^{(e)} , \qquad (16)$$

$$s^{(e)} = H^{(e)} D^{(e)} G^{(e)} u^{(e)} = H^{(e)} D_G^{(e)} u^{(e)} , \qquad (17)$$

where $D_G^{(e)}$ stands for the application of the differential operator $D^{(e)}$ to $G^{(e)}$.

It is now possible to rewrite the potential energy as a function of the generalized nodal displacements $u^{(e)}$ only

$$U^{(e)} = \frac{1}{2} \int_{(V^{(e)})} u^{(e)T} D_G^{(e)T} H^{(e)} D_G^{(e)} u^{(e)} \, dV^{(e)} + \frac{1}{2} \sum_{(j)} u_j^{(e)2} c_j \qquad (18)$$

Similarly, the element specific kinetic energy can be found as

$$T^{(e)} = \frac{1}{2} \int_{(V^{(e)})} \rho^{(e)} \dot{u}^{(e)T} G^{(e)T} G^{(e)} \dot{u}^{(e)} dV^{(e)} , \qquad (19)$$

where $\rho^{(e)}$ is the element material density and $\dot{u}^{(e)}$ are the element nodal velocities (i.e., the first time derivative of $u^{(e)}$).

The variation of Lagrange's function in generalized coordinates results in

$$\delta L^{(e)} = \delta \dot{u}^{(e)T} \frac{\partial L^{(e)}}{\partial \dot{u}^{(e)}} + \delta u^{(e)T} \frac{\partial L^{(e)}}{\partial u^{(e)}}$$

$$\delta L^{(e)} = \int_{(V^{(e)})} \rho^{(e)} \delta u^{(e)T} G^{(e)T} G^{(e)} \ddot{u}^{(e)} dV^{(e)} -$$

$$\int_{(V^{(e)})} \delta u^{(e)T} D_G^{(e)T} H^{(e)} D_G^{(e)} u^{(e)} dV^{(e)} - \tag{20}$$

$$\sum_{(j)} \delta u_j^{(e)} c_j .$$

Considering only the distributed surface loads $p^{(e)}$, the virtual work in generalized coordinates reads as

$$\delta W_{ext}^{(e)} = - \int_{(S^{(e)})} \delta u^{(e)T} G_S^{(e)T} p^{(e)} dS^{(e)} , \tag{21}$$

where $G_S^{(e)}$ is the surface displacement interpolation matrix analog to $G^{(e)}$, and $S^{(e)}$ the element surface.

Introducing equations (20) and (21) into (11), the solution of equation (11) as variational problem leads to the well-known Lagrange equations of second kind

$$\frac{d}{dt}\left(\frac{\partial L^{(e)}}{\partial \dot{u}_j^{(e)}} \right) - \frac{\partial L^{(e)}}{\partial u_j^{(e)}} = f_j^{(e)}(t) , \quad j = 1,2,...,N . \tag{22}$$

Neglecting structural damping effects, the equations of motion of the element (e) in local coordinates follow as

$$M^{(e)} \ddot{u}^{(e)} + K^{(e)} u^{(e)} = f^{(e)} \tag{23}$$

with the element mass matrix, the element stiffness matrix, and the applied loads, respectively

$$M^{(e)} = \int_{(V^{(e)})} \rho^{(e)} G^{(e)T} G^{(e)} dV^{(e)} , \tag{24}$$

$$K^{(e)} = \int_{(V^{(e)})} D_G^{(e)T} H^{(e)} D_G^{(e)} dV^{(e)} , \tag{25}$$

$$f^{(e)} = \int_{(S^{(e)})} G_S^{(e)T} p^{(e)} dS^{(e)} . \tag{26}$$

The assumption of small strains in general permits the evaluation of the integrals over the undeformed geometry of the element without significant error.

The assembly process might be written symbolically as

$$\sum_{(e)} (M^{(e)} \ddot{u}^{(e)} + K^{(e)} u^{(e)}) = \sum_{(e)} f^{(e)} \tag{27}$$

and, after introducing boundary constraints, leads to the equations of motion of the entire system in global coordinates

$$M\ddot{u} + Ku = f , \tag{28}$$

where M and K are the constant global mass and stiffness matrices, and f is the global vector of applied loads.

2.2.2 Application to Typical Wing Section

Following the ideas of Theodorsen and Garrick, a typical wing section of unit width in the spanwise direction is considered, as illustrated in Fig. 2. It is assumed that the inertial and elastic properties of the system can be represented by a finite element

assemblage of beams or plates which do not necessarily model the aerodynamic surface of the system. In addition, the spatial discretization of the structure is independent of that of the fluid (and vice versa) and is accomplished by structural constraints like material discontinuities, the need to implement hinges, elastic supports, and the specification of nodal displacement conditions only. Every node k might be supported by a translational and/or rotational spring, and adjoining elements e might be interconnected by a stiffness coupling matrix to establish a hinge for the purpose of modelling one or several control surfaces, as indicated in the figure. The local element degrees of freedom are measured in the local coordinate system $(x^{(e)}, z^{(e)})$, while the global degrees of freedom refer to the global coordinate system (x, z), both of which are Cartesian. The surface of the profile in the global coordinate system is given by $\eta(x)$ and coincides with the inner $\zeta = $ const. line of the aerodynamic mesh. During the temporal integration of the coupled field problem the pressure p is computed in each mesh cell and assumed to be constant throughout each cell.

finite elements $\quad e = 1, 2, ..., n$
finite element nodes $\quad k = 1, 2, ..., n + 1$
aerodynamic points $\quad i = 1, 2, ..., m$
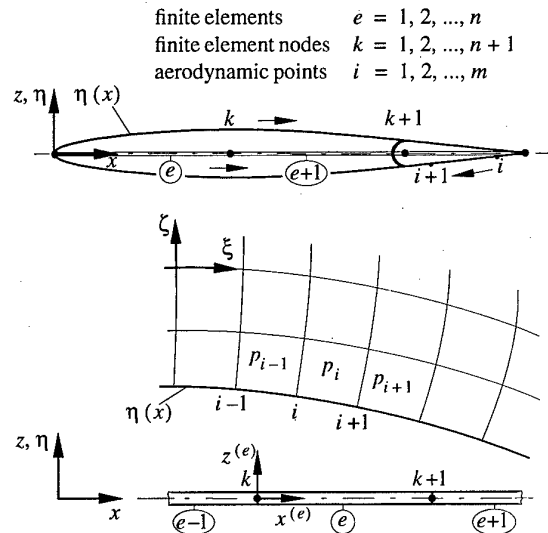
Fig. 2 Typical wing section and relation between the spatial discretization of the fluid and the structural domain
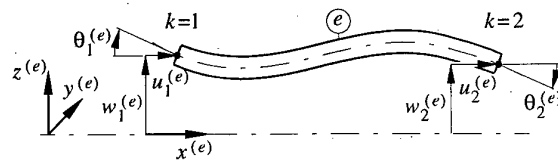
Fig. 3 Definition of local nodal displacements

Since in the decomposition approach favored here the only way to communicate between the structure and the fluid is via the surface (fluid structure boundary), it is of utmost importance to describe the motion of the surface as accurately as possible. The importance is twofold. Firstly, the time-varying surface specifies the kinematic boundary for the fluid, and secondly, some assumptions about the kinematic of the surface have to be made in order to be able to determine the generalized forces (i.e., the evaluation of the integral (26)) transmitted from the fluid to the structure in a consistent manner with the mechanical

principles already applied (kinetic or natural boundary condition for the structure). This leads us to the matter of shape functions for the elements.

For the sake of simplicity, a beam element of unit width with the nodal degrees of freedom

$$u^{(e)} = \begin{bmatrix} u_1^{(e)} & w_1^{(e)} & \theta_1^{(e)} & u_2^{(e)} & w_2^{(e)} & \theta_2^{(e)} \end{bmatrix}^T \quad (29)$$

measured in the local coordinate system $(x^{(e)}, z^{(e)})$ is considered, as illustrated in Fig. 3.

Based on the well-known differential equations of equilibrium of a prismatic beam for bending and axial behavior the interior continuous displacement field

$$v^{(e)}(x^{(e)}) = \begin{bmatrix} u^{(e)} & w^{(e)} & \theta^{(e)} \end{bmatrix}^T \quad (30)$$

can be exactly expressed (within the classical beam theory) as function of the nodal displacements according to equation (15), where the element displacement interpolation matrix can be written as

$$G^{(e)}(x^{(e)}) = \begin{bmatrix} g_u^{(e)T} \\ g_w^{(e)T} \\ g_\theta^{(e)T} \end{bmatrix}. \quad (31)$$

The vectors $g_u^{(e)}$, $g_w^{(e)}$ and $g_\theta^{(e)}$ contain the so-called Hermitian polynomials [5] corresponding to the degrees of freedom $u^{(e)}$, $w^{(e)}$ and $\theta^{(e)}$, so that, e.g. $u^{(e)} = g_u^{(e)T} u^{(e)}$.

Finally, the surface displacements $v_S^{(e)}$ as functions of the nodal degrees of freedom $u^{(e)}$ remain to be specified. For this purpose, an element including its corresponding surface (fluid structure boundary) in local coordinates is shown in Fig. 4, where, for matters of simplicity, only the upper side is considered. The shape of the surface given by $\eta^{(e)}(x^{(e)})$ in the undeformed state (its slope is $\eta'^{(e)} = \partial\eta^{(e)}/\partial x^{(e)}$) can be arbitrary with the only exception that it should be not too far away from the element, and, of course, continuous at the element boundaries. In so doing, a linear relation between the displacements of the elastic center line and the surface displacements of the element can be obtained.

The following model for the deformation of the surface is applied. In the undeformed state the surface is measured perpendicular to the elastic center line of the element, i.e., perpendicular to the $x^{(e)}$ axis. While the deformation the surface point P moves to $\tilde{P}$, assuming that the distance between the center line of the element and the surface does not change and that it is still measured perpendicular to the now deformed elastic center line. The continuous surface displacements are identified by the subscript S. According to this procedure, a bending moment assumed to be positive in the clockwise direction about the $y^{(e)}$ axis causes tension in the top fibers of the element and the upper surface is stretched while the bottom fibers of the element and the lower surface are subjected to compression. This is simply the transfer of the well-known hypothesis of Bernoulli for bending deformations of prismatic beams, which, without emphasizing it explicitly, has already been assumed to be valid in the construction of the shape functions for the beam element.

It is important to note that the elastic and inertial properties of the system are solely represented by the finite element and that

no resistance comes from the tension and compression of the surface. From a mechanical point of view one can imagine the following: Along the bearing element aligned with the $x^{(e)}$ axis, several massless and infinitely rigid beams, allowing the transmission of axial forces and bending moments, are perpendicularly and rigidly connected to this element. The lengths of these beams are prescribed in a way that they model the aerodynamic surface, i.e., their outer ends coincide with the surface.
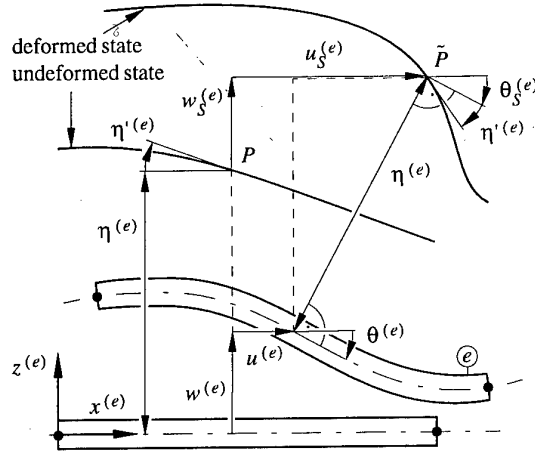
Fig. 4 Definition of local element surface displacements

From the geometrical interpretation of Fig. 4 one can derive the following relation

$$v_S^{(e)}(x^{(e)}) = \begin{bmatrix} u_S^{(e)} \\ w_S^{(e)} \\ \theta_S^{(e)} \end{bmatrix} = \begin{bmatrix} u^{(e)} + \eta^{(e)}\sin\theta^{(e)} \\ w^{(e)} - \eta^{(e)}(1-\cos\theta^{(e)}) \\ \theta^{(e)} \end{bmatrix}, \quad (32)$$

which gives linearized

$$v_S^{(e)}(x^{(e)}) = \begin{bmatrix} u^{(e)} + \eta^{(e)}\theta^{(e)} \\ w^{(e)} \\ \theta^{(e)} \end{bmatrix}. \quad (33)$$

Applying Eq. (15) in conjunction with (31) to (33) finally yields

$$v_S^{(e)}(x^{(e)}) = \begin{bmatrix} g_u^{(e)T} + \eta^{(e)}g_\theta^{(e)T} \\ g_w^{(e)T} \\ g_\theta^{(e)T} \end{bmatrix} u^{(e)} \quad (34)$$

$$= G_S^{(e)}(x^{(e)}) u^{(e)},$$

where $G_S^{(e)}$ is the searched element surface displacement interpolation matrix.

With the help of $G_S^{(e)}$ the surface's motion can be automatically determined if the nodal displacements $u^{(e)}$, and thus, the interior element displacement field $v^{(e)}$ are known. In addition, the knowledge of $G_S^{(e)}$ allows for the calculation of the integral (26) to obtain the generalized element forces.

2.2.3 Boundary Conditions

As already mentioned above, every node might be supported by a translational and/or rotational spring and adjacent elements might be interconnected by joints. In the following example cal-

culations the system is similarly supported by discrete linear springs like the classical wing section model and has an optional control surface. Under this condition, the fundamental degrees of freedom responsible for classical flutter are retained while still allowing for elastic deformations in the chordwise direction.

All nodal degrees of freedom can be constrained or prescribed with the additional feature of having the possibility to impose dynamic displacement conditions. This is useful in order to initialize an unsteady aeroelastic calculation or for the determination of unsteady aerodynamic coefficients. In this study the axial displacements $u^{(e)}$ of all elements are constrained since their contribution to the overall solution is negligible and leads only to increased computational effort.

The kinetic boundary condition is fulfilled with the evaluation of the integral (26).

2.3 Method of Solution

The coupled field problem can be effectively solved in the time domain by applying a partitioned solution procedure in which the fluid and the structural solvers are executed in an alternating fashion and exchange interface data such as pressure, displacements, and velocities at certain time steps. Theoretically, a large number of available finite difference expressions can be employed. However, with effectiveness considerations in mind, only a few methods need to be considered.

2.3.1 Fluid Domain

The Euler code used in this study was written and adopted to the requirements of the partitioned solution procedure by the author of [18], where it is described in detail and applied to two-dimensional transonic cascade flow. Results of computations of unsteady transonic flow around oscillating airfoils are given and compared with solutions of a Full Potential method and experimental data in [37]. The agreement is generally good in the whole frequency range important for flutter prediction.

The Euler code makes use of the flux vector splitting method developed by van Leer [36] for Cartesian coordinate systems. Anderson et al. [3], [4] paved the way to enable the application of this naturally dissipative upwind method also to boundary-fitted moving coordinates while retaining the advantages of the original splitting, in particular the shock capturing capabilities. The solution in the time domain is based on the approximately factored Beam/Warming implicit single-step algorithm [6] using a cell-centered finite volume formulation with a MUSCL-type extrapolation (Monotonic Upstream Centered Scheme for Conservation Laws) [35] for the spatial discretization. The condition for numerical stability of the fluid solver depends on the spatial and temporal discretization and can be expressed by means of a linear stability analyses by the CFL number (Courant-Friedrichs-Lewy).

2.3.2 Structural Domain

For the time integration of the structural equations of motion, Newmark's method [29] is employed, which can be cast in explicit and implicit form by the variation of two method-specific parameters. It also has the advantage of being a single-step algorithm, thus, the whole procedure is easily extended to varying time step sizes. The critical time step required for stability and accuracy has to be calculated from the mass and stiffness properties of the complete finite element model. More specifically, the highest frequency obtained by an eigenanalysis of the free vibration equilibrium equations determines the time step. Comprehensive discussions of this important subject can be found, e.g., in [5], [39].

Since the required number of operations to solve equation (28) is directly proportional to the order and bandwidth of the system matrices, the computational effort can be considerably reduced by transforming the basis to modal (normal) generalized coordinates using the eigensolutions of the free vibration equilibrium equations with neglected damping. In so doing, the system matrices can be diagonalized, hence, the system of differential equations (28) decoupled. Also, only a fraction of the total number of decoupled equations needs to be considered to obtain a good approximate solution, which is generated by the mode superposition principle. The contributions of higher frequencies and mode shapes are usually negligible and the solution is dominated by the low frequency content of the system. As a result, much larger time steps can be used. Once a decision has been made on the modal approach, and the reduction of the system to the normal generalized degrees of freedom which significantly contribute to the expected response has been performed, the question whether to employ the implicit or explicit formulation of Newmark's method does not arise. The admissible time step has to be almost the same for both methods due to accuracy requirements. For simplicity, the explicit scheme, which is spectrally equal to the well-known central difference method [5], is used.

2.3.3 Solution of Coupled Field Problem

The coupled time integration procedure can be conceptionally described as follows employing the same time step Δt for the fluid and the structure (Fig. 5).

1. Obtain starting values from the actual state of the entire system, i.e., generalized displacements u_i, velocities $\dot{u}_i$, accelerations $\ddot{u}_i$, and aerodynamic loads f_i at time level t_i. If the system is not already in motion, the generalized aerodynamic load vector is determined from the free-stream condition corresponding to the fixed initial wing-surface boundary.

2. Compute generalized displacements u_{i+1}, velocities $\dot{u}_{i+1}$, and accelerations $\ddot{u}_{i+1}$ at time level $t_{i+1} = t_i + \Delta t$ using the aerodynamic forces at time level t_i.

3. Update the aerodynamic mesh, advance the fluid domain, and calculate the generalized aerodynamic load vector f_{i+1} according to u_{i+1}, $\dot{u}_{i+1}$, and $\ddot{u}_{i+1}$ at time level t_{i+1}.
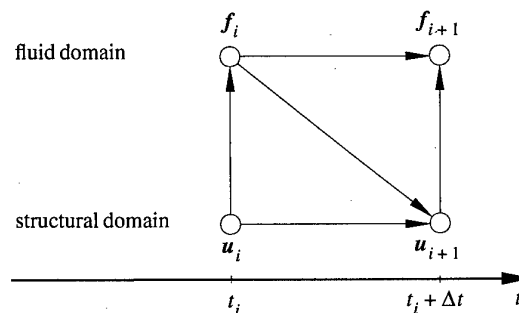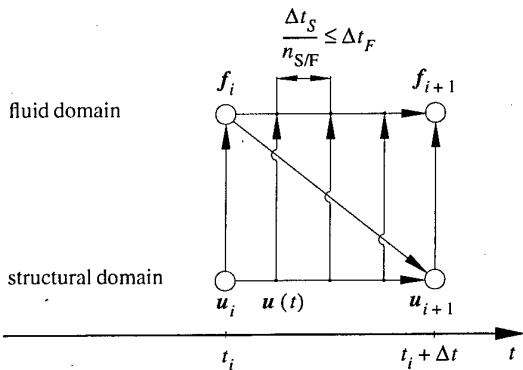
Fig. 5 Temporal flow diagram illustrating the coupled field integration scheme assuming the same time step for the fluid and the structural domain

This cycle is repeated until the desired response is obtained. The mutual time step for stability of the coupled field integration procedure is determined from the condition

$$\Delta t = \min \{\Delta t_F (\text{CFL}), \Delta t_S (\omega_{max})\} , \quad (35)$$

where Δt_F and Δt_S are the admissible time steps for the fluid and the structure, respectively, which are restricted by the requirements discussed above.

Of course, in the case of making use of the modal approach, the computed normal generalized displacements, velocities, and accelerations have to be transformed into the physical plane at each time step since the fluid structure boundary is described in physical coordinates, while on the other hand, the aerodynamic loads acting on the surface have to be transformed into the computational plane of generalized forces corresponding to the normal coordinates.

Assuming a judicious choice of the mathematical model representing the structure, in aeroelastic response and stability analyses a greater time step for the integration of the structural equations of motion can generally be chosen as compared to that of the fluid. However, when considering that the computation of the aerodynamic data by modern CFD methods makes up the lion's share of the total computational costs, it is usually not worth applying a different scheme. Only when working in heterogeneous hardware environments, where the single-field solvers are executed on different platforms, it might be desirable to reduce the time needed to exchange data by employing different time steps in each domain. With these considerations in mind, the coupled time integration procedure described above has been extended as follows.

Fig. 6 Temporal flow diagram illustrating the coupled field integration scheme assuming different time steps for the fluid and the structural domain

If $\Delta t_F < \Delta t_S$, the global time step $\Delta t = \Delta t_S$ is divided into $n_{S/F}$ equally spaced intervals so that

$$\frac{\Delta t_S}{\Delta t_F} \le n_{S/F} \quad (36)$$

holds, where Δt_F is determined by the CFL condition and Δt_S by the highest frequency of the structural system. The structural domain is time-marched from t_i to t_{i+1} in a single time step $\Delta t = \Delta t_S$, as described above, while the fluid domain is advanced from t_i to t_{i+1} in $n_{S/F}$ time steps. Since data exchange is only permitted at the time steps t_i and t_{i+1}, the necessary

generalized displacements, velocities, and accelerations to advance the fluid domain within the open time interval $t_i < t < t_{i+1}$ have to be approximated, e.g. by linear interpolation.

$$u(t) = u_i + \frac{t - t_i}{\Delta t}(u_{i+1} - u_i), \quad t_i \le t \le t_{i+1} \quad (37)$$

It should be noted that u_{i+1} is already known within the full accuracy of the employed structural integration scheme and that only the values inside the open interval $t_i < t < t_{i+1}$ are approximated. However, experience has shown that the use of higher order interpolation functions has no significant, if any effect on the overall solution. The procedure is illustrated in Fig. 6.

2.3.4 Energy Considerations

Newmark originally proposed the constant average acceleration method, also well-known as the trapezoidal rule, which today is considered a special case within the Newmark family of algorithms [5], [39]. It is probably not exaggerated to say that it is the most popular and most often applied time-step algorithm in structural dynamic analysis. This is because for this class of problems it possesses a unique property that it shares with the exact continuum equations of motion for undamped systems subjected to a conservative force field. It exactly conserves the total energy of the structural system

$$E_{tot} = T(\dot{u}, t) + U(u, t) = E_0 = \text{const.} , \quad (38)$$

i.e., the sum of kinetic T and potential energy U remains constant during the evolution in time and is equal to the initial energy E_0. This means that no amplitude decay is introduced and that also the higher frequency components, although not accurately evaluated, are not damped out and still retained in the response, which is in sharp contrast to the behavior of other implicit time integration schemes.

On the other hand, the fundamental conservation law (38) does not hold for non-conservative loadings, but the more general energy identity

$$E_{tot} = T(\dot{u}, t) + U(u, t) = E_0 + \int_0^t \dot{u}^T(\tau) f_{nc}(\tau)\, d\tau, \quad (39)$$

readily derivable from Lagrange's equations, can be employed, where the integral comprises the effects of all non-conservative generalized forces f_{nc}. In this case the total energy E_{tot} is not a constant equal to the initial energy E_0, it is in- or decreased by the value of the integral in the time t.

Since damping and other dissipative effects have been neglected in the derivation of the structural equations of motion, the following energy identity

$$E_{tot} - W_{ext} = T(\dot{u}, t) + U(u, t) - \int_0^t \dot{u}^T(\tau) f(\tau)\, d\tau = E_0, \quad (40)$$

must be satisfied by the solutions of the initial-value problem (28), where W_{ext} is the external work done by the generalized aerodynamic forces f.

Such energy relations are commonly valid in physical problems and have long been used in the theory of differential equations to prove existence and uniqueness of solutions. However, beginning with the work of Courant, Friedrichs, and Lewy [19], they also have a long tradition to attest numerical stability and accuracy of finite difference approximations [31].

As discussed further below, the energy identity (40) can be used to check the accuracy of the proposed partitioned time integration procedure, which is why it is included here.

3 RESULTS OF AEROELASTIC COMPUTATIONS

Based on the progress in computational fluid dynamics, many aeroelastic applications have followed. For matters of simplicity and the reasons given above, the two-dimensional typical wing section introduced by Theodorsen and Garrick [33], [34] was often used as structural model in these studies. In particular, extensive efforts to predict transonic aeroelastic phenomena have resulted in a sequel of papers, e.g., [8], [21], [22], [26], [38]. It is, however, clear that the assumption of two-dimensionality of the flow at transonic speeds is only valid for some portions of large aspect-ratio wings.

More recently, Blom and Leyland [15] presented related work concerning the partitioned solution procedure, while Bendiksen [9] also accounted for camber bending in the stability analysis of a typical wing section using a newly proposed ALE method for aeroelastic applications.

In order to be able to compare the results of the suggested method with previous flutter calculations and also to show the effect of chordwise flexibility of a wing segment in two-dimensional transonic flow on aeroelastic stability, the classical rigid wing section was used as reference model. Since the general formulation of the finite element method allows for the lumping of structure properties and loads, the exact rigid case can readily be treated in a very effective manner. Another alternative offers the application of the modal decomposition technique. Either procedure leads to a reduced order structural model resulting in larger admissible time steps for the integration of the structural equations of motion in time. This is an advantage of the present method in contrast to Bendiksen's ALE formulation of the problem [9], where the rigid case is achieved by letting the stiffness of the elements approach infinity. Further considering that in reference [9] the five-stage Runge-Kutta scheme was used for the entire fluid structure domain, which is only conditionally stable and thus demanding very small time steps not only for accuracy but above all for numerical stability, considerable computing time can be saved by using the domain decomposition approach. Personal experience has shown that by stiffening the elements to a degree where no significant camber bending occurs, the admissible time step for the structure using an unconditionally stable scheme is decreased well below that acceptable for the fluid domain.

In this section, transonic time response solutions are presented for five test cases, two of which were previously studied using the well-known transonic codes LTRAN2-NLR [24] and USTS [26], which solve the two-dimensional transonic small disturbance equations. More specifically, a two-degree-of-freedom (2 d.o.f.) system investigated by Isogai [26] and a three-degree-of-freedom (3 d.o.f.) system examined by Yang and Batina [38] were used as basis configurations. The aeroelastic parameter values for both cases are listed below using the definition of parameters and sign conventions of reference [38].

Isogai [26]:

$$a_h = -0.3, x_\alpha = 0.5, r_\alpha = 0.7, \omega_h/\omega_\alpha = 0.2, \mu = 60$$

Yang/Batina [38]:

$$a_h = -0.2, x_\alpha = 0.2, r_\alpha = 0.5, \omega_h/\omega_\alpha = 0.3, \mu = 23.48$$

$$x_\beta = 0.008, r_\beta = 0.06, c_\beta = 0.5, \omega_\beta/\omega_\alpha = 1.5$$

The remaining test cases are modifications of the latter model utilizing the same parameters. First, a 2 d.o.f. system was established by merely locking the control surface to the wing, and second, this 2 d.o.f. system and the original 3 d.o.f. system were allowed to have chordwise flexibility. For the sake of clarity, the test cases are listed in Table 1, where the sequence of cases is chosen according to the complexity of the structural model.

Table 1 Aeroelastic test cases

Case A	Case B	Case C	Case D	Case E
Isogai [26], 2 d.o.f, rigid	same as Case C, but with 2 d.o.f	Yang/Batina [38], 3 d.o.f, rigid	same as Case B, but chordwise flexible	same as Case C, but chordwise flexible

It should be noted that originally Cases C and E were the main objectives of this investigation, where the flutter boundaries surprisingly exhibited two transonic dips in flutter speed. This phenomenon was initially attributed to the presence of the control surface, which is why the control surface was locked in a second attempt resulting in Cases B and D. Perhaps not surprisingly, these cases also showed a second dip, since the relatively high stiffness in the control surface hinge of Cases C and E ($\omega_\beta/\omega_\alpha = 1.5$) effectively diminishes possible flutter for the bending-aileron and torsion-aileron branches. Due to the fact that in reference [38] results for the considered case are only presented for a single Mach number, and therefore a sound basis of comparison was still lacking, an additional example, taken from reference [26], was considered (Case A) with the advantage of having comprehensive information on the behavior of critical flutter parameters vs. Mach number for a typical 2 d.o.f. system. As is discussed further below, a second dip was also detected for this case.

Regarding the finite element modelling, the continuous mass and stiffness parameters were obtained by formulating and solving nonlinear constrained optimization problems, so that the global system parameters exactly match the prescribed discrete values. In this context, some assumptions were necessary about the way in which the structural properties should be distributed. Accordingly, the mass and stiffness coefficients were approximately scaled to the square and cube of the profile's thickness, respectively. In so doing, it turned out that in order to retain the global structural parameters, especially the location of the center of gravity of the wing and the mass-balanced control surface, the introduction of two small eccentric tuning masses was necessary. Except where noted, nine beam elements were used in the chordwise direction in the present study. The rigid body Cases A to C were exactly obtained by lumping the distributed system properties. Also note that for Cases B to E the same finite element model was used since only the boundary conditions needed to be changed.

All results of aeroelastic computations presented here were performed for zero mean angle of attack and using a NACA64A010 airfoil, where the airfoil coordinates were taken from reference [14]. In order to extract the frequency, damping, amplitude, and phase information from the simulation data, the time-history series were fitted in a least square sense with complex exponential functions [13]. The problem of finding the critical flutter solution, which by definition is an oscillation with steady amplitude, so with zero damping, was iteratively solved by employing the Newton-Raphson method [5], which is qua-

dratic in convergence. The iteration cycle: (1) prescribe (in- or decrease) flight speed, (2) compute aeroelastic time response, and (3) determine vibration parameters, was continued until a predefined tolerance for the damping coefficients was achieved.

3.1 Results for Rigid Wing Section (Cases A to C)

The results for the three typical rigid wing segments presented in this section serve as a basis for comparison with previously published results and as reference solutions for the Cases D and E. Although not shown here, it should be noted that additional flutter computations in the low subsonic Mach number range were successfully carried out during the checkout phase of the program, including comparisons with results obtained from classical frequency domain flutter computations.

3.1.1 Results for Case A

Case A is the same as Case B in reference [26] studied by Isogai and simulates the vibrational characteristics of an unswept wing. A relatively mild transonic dip was observed, as shown in Fig. 7, where the non-dimensional flutter velocity coefficient $U_F^* = U_F / (b\omega_\alpha \sqrt{\mu})$ vs. Mach number M is plotted. Also shown in the figure is a result predicted by Bendiksen for the same case at a Mach number of $M = 0.8$, taken from reference [8]. The results are compared to the predictions obtained by the present code for the ideal rigid wing segment. As can be seen, the agreement is generally good, but a second dip was detected in the Mach number range $0.85 < M < 0.9$ with the present code. It is interesting to note that Isogai did not present any results for this very range. The two neighboring points were merely connected with a dashed line. Fig. 8 shows the corresponding flutter frequencies ω_F, non-dimensionalized by the torsion natural frequency ω_α, vs. Mach number, which also compare very well with the previously obtained results except for the Mach numbers $0.85 < M < 0.9$.

In order to impart an idea of the response behavior of the system, typical time-domain solutions for Case A are presented at $M = 0.8$ for four different flight speeds. These examples correspond to the neutrally stable, stable, unstable, and LCO solutions depicted in Fig. 7. Fig. 9 shows the displacement response and the evolution of the energy quantities with time for the critical flutter velocity coefficient $U_F^* = 0.453$. The system was forced to oscillate according to the previously determined flutter mode

$$\frac{h(t)}{b} = \frac{h_0}{b} \sin(\omega_F t + \varphi_h),$$

$$\alpha(t) = \alpha_0 \sin(\omega_F t + \varphi_\alpha),$$

$$\frac{\alpha_0}{(h_0/b)} = 0.155, \quad \frac{h_0}{b} = 0.01, \quad \varphi_\alpha - \varphi_h = 6.1594 \text{ [rad]}$$

for four cycles $8\pi/\omega_F$ of the flutter frequency ω_F given by the frequency ratio $\omega_F / \omega_\alpha = 0.349$. After its release, additional 25 cycles of free motion were computed in order to obtain the aeroelastic time response. As can be seen, no disturbances occur at the transition from forced to free motion, indicating that the exact flutter conditions were used to initiate the time response calculation. Also, the values of the displacement amplitudes were chosen within the range where the unsteady aerodynamic coefficients depend linearly on the displacement amplitudes, as has been investigated in [26].

The energy quantities were only computed for the free motion of the system according to equation (40) and non-dimensionalized by the initial energy E_0, so that the difference between the total energy and the external work should be equal to one in the whole simulation period $(E_{tot} - W_{ext})/E_0 = \text{const.} = 1$.

This means that neither energy is introduced nor dissipated by the numerical integration scheme. In so doing, the energy identity (40) provides an autonomous check on the numerical accuracy and stability of the finite difference approximation of the coupled field problem. However, it should be noted that the satisfaction of (40) does not guarantee a „healthy" solution of the entire aeroelastic problem, since it does not account for mistakes in the calculation of the generalized forces from aerodynamic pressure data. For example, any arbitrary constant (in reasonable bounds) can be added to the generalized force vector without violating the energy identity (40).
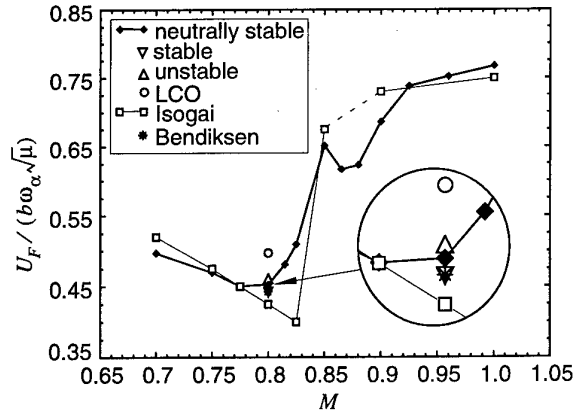
Fig. 7 Flutter velocity coefficient vs. Mach number for Case A
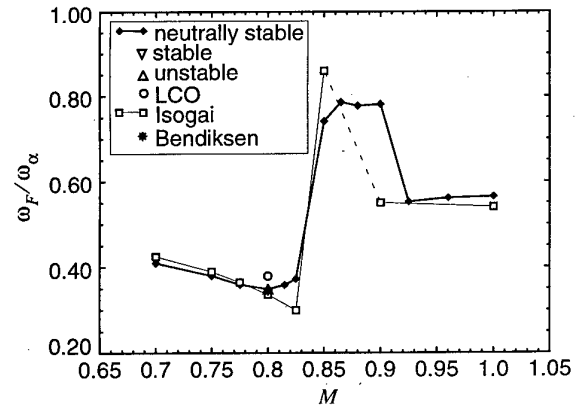
Fig. 8 Flutter frequency vs. Mach number for Case A

As can be seen in Fig. 9, the difference $E_{tot} - W_{ext}$ remains constant and equal to the initial energy E_0, thus attesting the quality of the proposed partitioned integration procedure. No systematic divergence of $E_{tot} - W_{ext}$ away from the initial energy could be detected, as was repeatedly observed by Bendiksen [9], [11] using the domain decomposition approach. Even for long-term calculations up to 100 cycles, covering more than 60.000 time steps, the energy identity (40) was satisfied and the aeroelastic response remained neutrally stable as if the first 25 cycles in Fig. 9 had been copied to the end of the simulation period.

Fig. 10 shows the displacement response and energy evolution for Case A at $M = 0.8$ for a subcritical velocity coefficient, while Fig. 11 shows the same for a supercritical velocity coeffi-
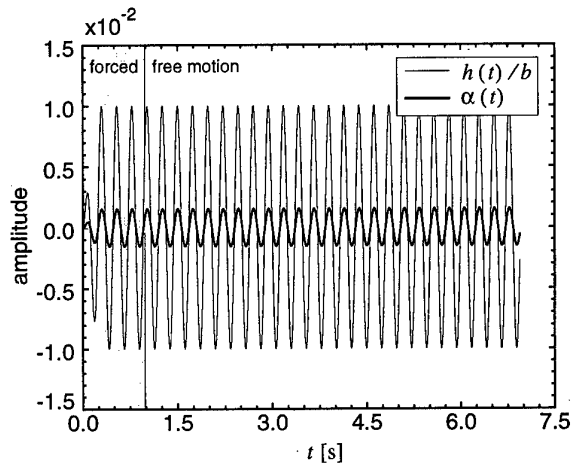
Fig. 9 Displacement response and energy
evolution for Case A at $M = 0.8$ for
critical flutter velocity coefficient
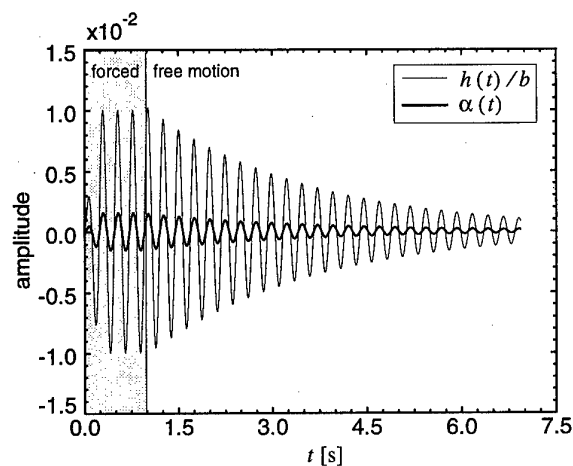$U_F^* = 0.453$ (neutrally stable solution)

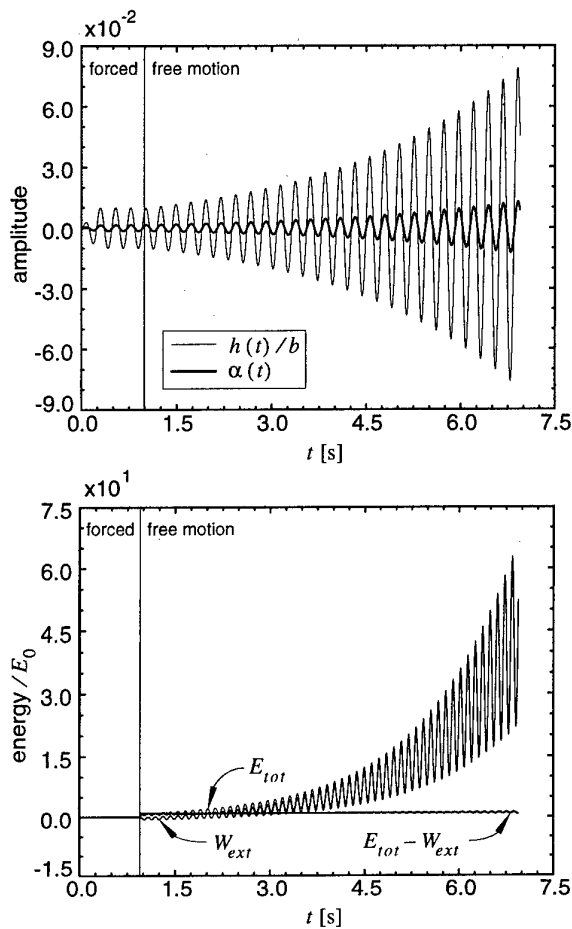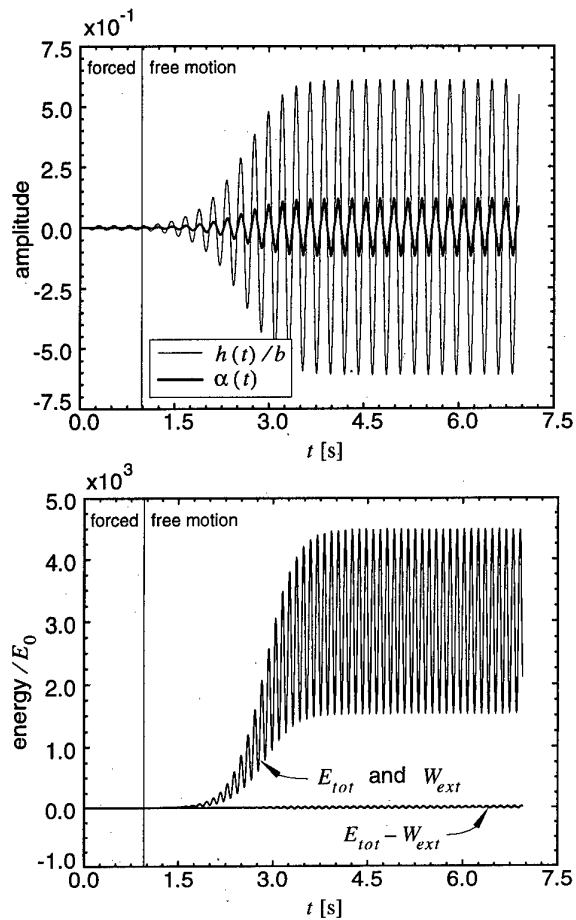**Fig. 10** Displacement response and energy
evolution for Case A at $M = 0.8$ for
subcritical velocity coefficient
$U^* = 0.443$ (stable solution)

cient. More specifically, the stable solution was obtained by decreasing, and the unstable solution by increasing the critical flutter speed by about two percent.

Again, the calculation was initiated by forcing the system to oscillate according to the flutter mode as described above. Then the airfoil was left free in order to obtain the aeroelastic response. As compared with the neutrally stable response, the frequency for the stable solution (Fig. 10) was found to be slightly lower and for the unstable solution (Fig. 11) to be slightly higher than that for the critical flutter solution.

When the flight speed was increased by about 10%, the solution entered a steady limit cycle oscillation (LCO) after 12 cycles of free motion, as can be seen in Fig. 12. The reason for this bounded amplitude oscillation lies in the dynamics of the strong shocks present at this Mach number for the considered airfoil. The vibrations are characterized by an increased amplitude and frequency ratio. Also, the torsional response is no longer a simple harmonic oscillation but shows the presence of higher harmonics resulting from the shock wave motions.

In this context, it should be noted that whether or not LCO is found depends to a certain degree on the length of the chosen simulation period, since the approach of the system to a steady LCO depends on the magnitude of the flow velocity. The higher the flow velocity for a given (sufficiently high) Mach number

the faster the system reaches its steady LCO amplitude and vice versa. It is therefore anticipated that the unstable solution depicted in Fig. 11 might have entered a LCO solution for an extended simulation period.

As can be seen in Fig. 12, the difference in energy $E_{tot} - W_{ext}$ starts oscillating slightly about the mean value E_0 as the amplitudes increase. However, the spurious growth and decay of energy tend to compensate each other over one cycle of oscillation, thus no systematic divergence occurs. The same behavior was observed for even higher torsional amplitudes, where the applicability of the method is open to question since the assumption of small displacements, thus the justification of linearity in deriving the governing structural equations of motion is violated. Although very interesting limit cycle solutions were repeatedly computed during this study, it is beyond the scope of this paper to discuss their origin and mechanism in detail. Numerical investigations on this fascinating nonlinear aeroelastic phenomena have been published by Kousen and Bendiksen [27], where the interested reader is referred to.

3.1.2 Results for Case B

Case B is a modification of the 3 d.o.f. system previously studied by Yang and Batina [38], which is the object of investigation in the next section. As for the results presented in this section, the system was modified in so far as the control surface

Fig. 11 Displacement response and energy evolution for Case A at $M = 0.8$ for supercritical velocity coefficient $U^* = 0.461$ (unstable solution)

Fig. 12 Displacement response and energy evolution for Case A at $M = 0.8$ for supercritical velocity coefficient $U^* = 0.497$ (LCO solution)

was locked to the wing, while keeping the values for the aeroelastic parameters as used for Case C. The computed flutter boundary for Case B is depicted in Fig. 13, while the corresponding flutter frequency, amplitude ratio, and phase difference of the displacement response vs. Mach number are depicted in Fig. 14.

In Fig. 13 also shown by specific symbols are some additional representative results, which were obtained during the search and trail of the expected flutter boundary. Whereas most symbols in context with the legend descriptions are self-explanatory, the cross 'x' symbolizes explosive flutter, which is accompanied by the failure of the numerical scheme within a few cycles in so far as the amplitudes grow without bound.

For Mach numbers lower than 0.70 no shocks are present and the solution rapidly grows (unstable solution) when the critical value of the flutter speed is exceeded. Decaying (stable) solutions are obtained for subcritical speeds. The flutter modes at the critical values of flight speed are characterized by typical bending-torsion motions at a frequency between those of the uncoupled natural frequencies of the binary system. Also, for this range of Mach numbers, no significant change in the phase difference between the torsional and bending motions exists, as can be recognized from Fig. 14.

With increasing Mach number attended by the development of weak shocks, a mild drop in critical flutter speed and a broadening of the region where exponentially growing solutions were computed is found. The minimum value of the critical flutter speed coefficient is predicted at $M = 0.78$ when the shock wave is located at about 55 to 60 percent of the profile's chord. The presence of the shocks is well reflected by the unsteady load distribution, as has been shown in great detail in the excellent work of Isogai [26]. In order to impart an idea on the behavior of the unsteady lift and moment coefficients at a relevant reduced frequency $k = \omega b/U$ (b - semichord) for Case B, the variations of the in-phase (real part) and out-of-phase (imaginary part) components of the first harmonic of the lift coefficient $c_{l1,\alpha}$ and the torsional moment coefficient $c_{m1,\alpha}$ for small torsional oscillations about the elastic axis $x = a_h b$ (40% chord position) versus Mach number are plotted in Fig. 15 and Fig. 16, respectively. The coefficients are defined as in reference [26]. As is obvious from these figures, the large negative value of the out-of-phase component of the torsional moment coefficient at about $M = 0.78$ (which means that there is a considerable phase lag between the torsional motion of the profile and the unsteady aerodynamic response) has a damping effect on the torsional degree of freedom of the system, while at the same time the drop in the out-of-phase component of the lift
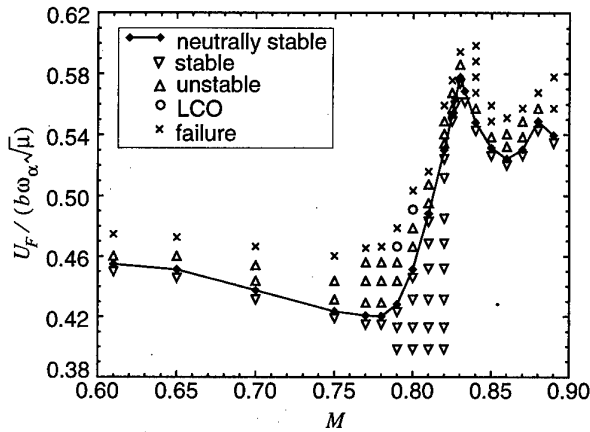
Fig. 13 Flutter velocity coefficient vs. Mach number for Case B
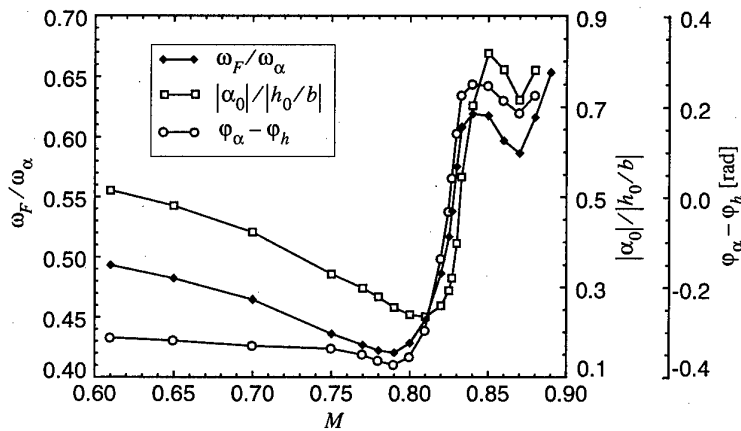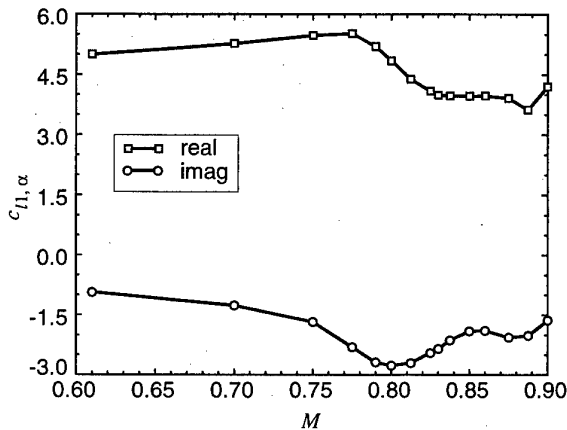
coefficient (bearing the sign convention in mind) indicates less aerodynamic damping in the bending degree of freedom. This is also mirrored by the displacement responses (Fig. 14), where at the bottom of the first dip in flutter speed the flutter frequency approaches a minimum close to the first natural frequency (bending), involving an increase in the bending amplitude. This implies a bending-dominated flutter mode at the bottom of the first transonic dip. With increasing Mach number the shocks strengthen and migrate further aft towards the trailing edge, which is accompanied by a significant decrease in the magnitude of the in-phase component of the torsional moment coefficient, since the center of pressure shifts also aft towards the elastic axis. This, and the decrease in the in-phase component of $c_{m1,\alpha}$, have a stabilizing effect on the flutter boundary (Fig. 13).

In addition, the out-of-phase component of the torsional moment coefficient rapidly rises, thus resulting in less aerodynamic damping in the torsional degree of freedom. This enables the transition from bending-dominated flutter to torsion-dominated flutter for Mach numbers beyond where the first dip in flutter speed occurs, as is well reflected in the displacement responses (Fig. 14). The flutter frequency approaches the torsion natural frequency, the torsional amplitude increases, and the phase difference between the bending and torsional motions reverses.

Within the considered range of free-stream Mach numbers the flutter boundary reaches a maximum at $M = 0.83$. With a further increase, a second drop in flutter speed occurs which might be interpreted in a similar fashion as just discussed, since the aerodynamic coefficients as well as the displacement responses change anew, though at different absolute values. More specifically, the notable point in Fig. 16 is

Fig. 14 Flutter frequency, amplitude ratio and phase difference of displacement response vs. Mach number for Case B

Fig. 15 Unsteady lift coefficient vs. Mach number for torsional oscillations about elastic axis at $k = 0.22$ for Case B
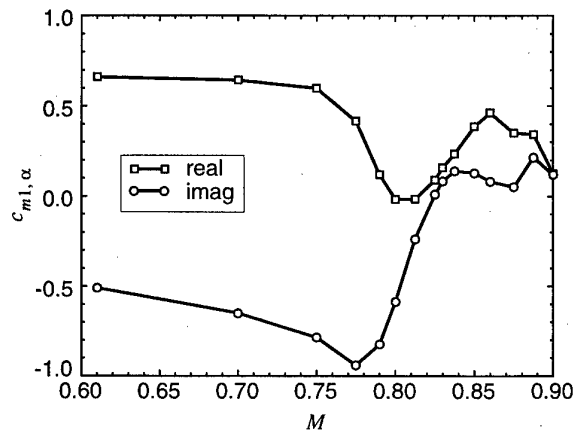
Fig. 16 Unsteady torsional moment coefficient vs. Mach number for torsional oscillations about elastic axis at $k = 0.22$ for Case B

that the out-of-phase component of the torsional moment coefficient is actually positive, thus producing negative aerodynamic damping in the torsional degree of freedom. This might also be the reason that explosive flutter and no limit cycle behavior is predicted in this Mach number range for slightly higher flight speeds than the critical speed.

It is interesting to note that such behavior of the flutter boundary at transonic speeds has been observed only for three-dimensional transport-type wing configurations so far. For example, two transonic dips have been found experimentally for a supercritical wing model tested at NLR [40] while numerically predicted flutter boundaries exhibiting two dips are reported on in reference [28]. The observations made in these studies that the first (,,usual") transonic dip involves bending-dominated flutter while the second dip is characterized by an almost single degree-of-freedom torsional type of flutter are also striking in the present study using a strictly two-dimensional model. It is recognized, however, that viscous effects might play an important role at these Mach numbers, as was observed in the experiment at NLR [40], where the single degree-of-freedom torsional type of flutter was found under separated flow conditions for higher angles of attack.

Finally, it should be noted that extensive attempts to find multiple solutions of the flutter boundary near the first dip were unsuccessful and, apart from explosive flutter, resulted in either decaying, exponentially growing, or LCO solutions, as is indicated in Fig. 13. Such multiple solutions have been reported for binary systems simulating the vibrational characteristics of an swept wing, see e.g. [8].

3.1.3 Results for Case C

Case C is identical to the 3 d.o.f. system studied by Yang and Batina [38] using the NACA64A010 airfoil. In reference [38] results of time response and classical flutter analyses are presented at $M = 0.825$, applying unsteady aerodynamic coefficients computed by the codes LTRAN2-NLR [24] and USTS [26]. For the given parameters the flutter speed and mass ratio were found to be $U_F^* = 0.539$ at $\mu = 20.86$ using LTRAN2-NLR coefficients and $U_F^* = 0.518$ at $\mu = 27.60$ using USTS coefficients. Based on the flutter solution using LTRAN2-NLR aerodynamics, with $h_0/b = 0.001$, $\alpha_0 / (h_0/b) = 0.748$, $\beta_0 / (h_0/b) = 0.638$, and $\omega_F / \omega_\alpha = 0.616$ (no phase information given), diverging responses were obtained with the present code. However, neutrally stable responses resulted at $U_F^* = 0.509$ and $\mu = 23.48$.
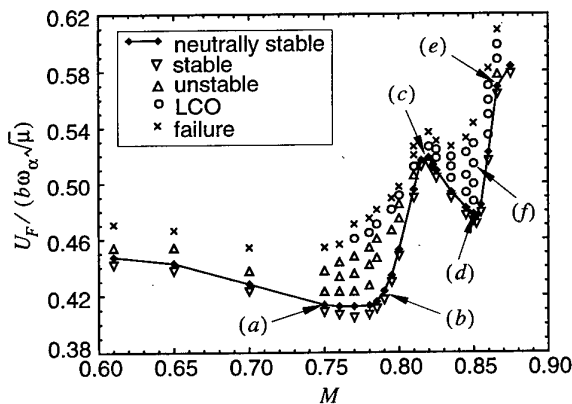
Estimates of the vibrational parameters of the critical aeroelastic response were determined to $\alpha_0 / (h_0/b) = 0.817$, $\beta_0 / (h_0/b) = 0.565$, $\omega_F / \omega_\alpha = 0.617$, $\varphi_\alpha - \varphi_h = 0.679$, and $\varphi_\beta - \varphi_h = 5.413$ [rad].

The flutter boundary for Case C as a function of Mach number as predicted by the present code is shown in Fig. 17, while the corresponding flutter frequencies are depicted in Fig. 18. The amplitude and phase information of the critical displacement responses vs. Mach number are plotted in Fig. 19.

Fig. 18 Flutter frequency vs. Mach number for Case C
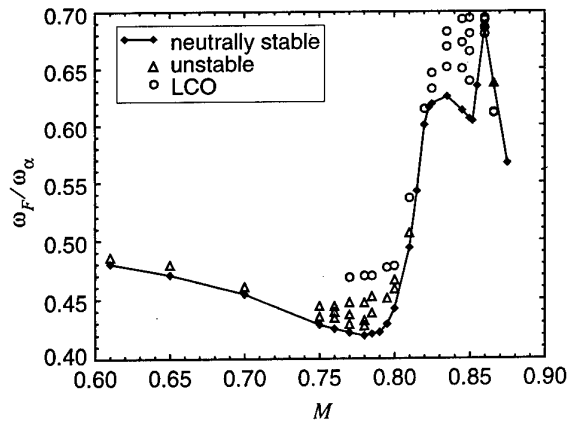
Fig. 17 Flutter velocity coefficient vs. Mach number for Case C
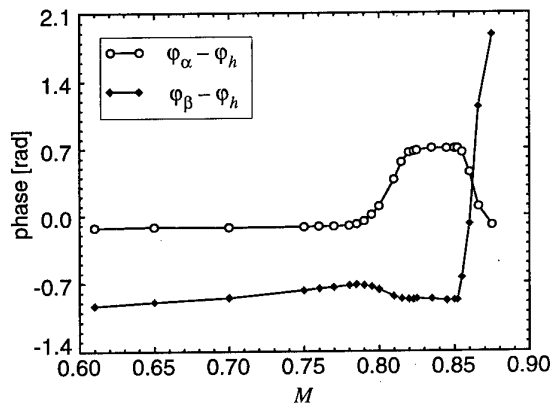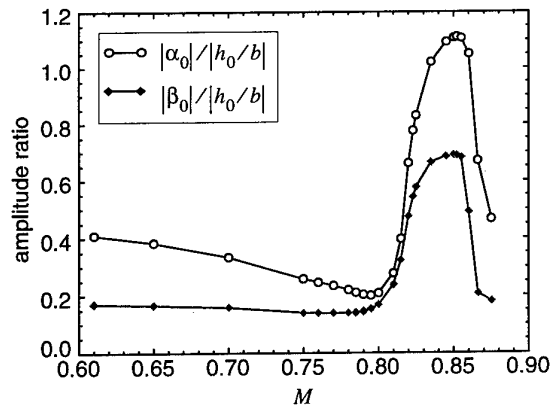
Fig. 19 Amplitude and phase information of displacement response vs. Mach number for Case C
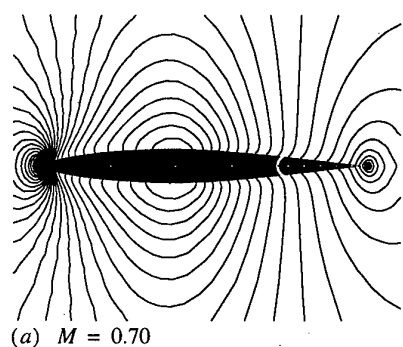
(a) $M = 0.70$
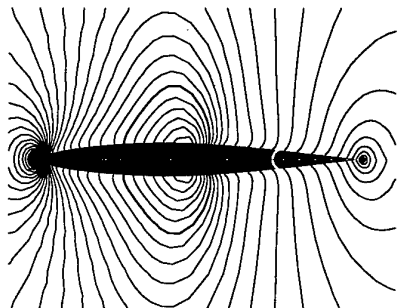
(b) $M = 0.79$
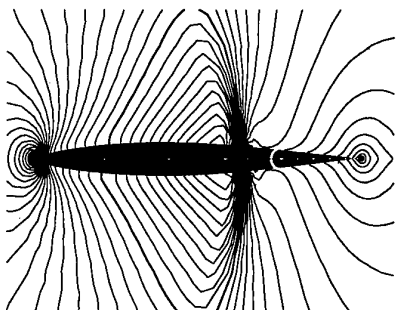
(c) $M = 0.82$
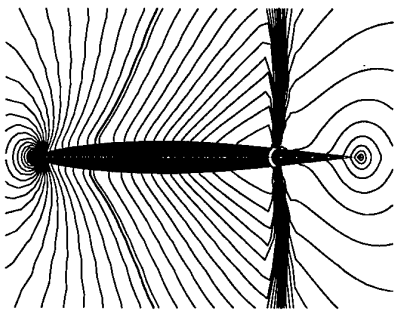
(d) $M = 0.85$
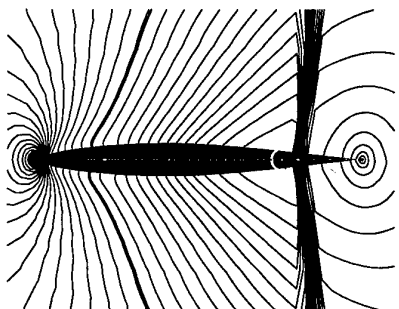
(e) $M = 0.866$

- continued
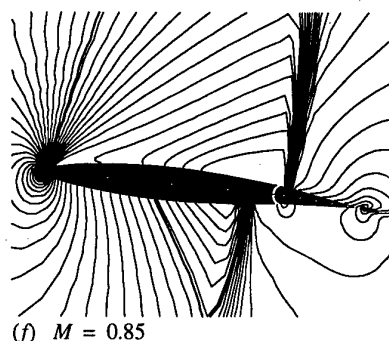
(f) $M = 0.85$

Fig. 20 Iso-Mach contour lines at various Mach numbers for Case C

Also, in order to impart insight into the distinct flow patterns, the instantaneous contour lines at various Mach numbers are shown in Fig. 20. The animation snapshots correspond to the points in Fig. 17 which are labeled (a) through (f).

For Mach numbers lower than 0.80 the flutter behavior differs only little from that of Case B. This is not surprising, since the system can approximately regarded as a 2 d.o.f. system because of the high stiffness in the control hinge. The high frequency ratio of $\omega_\beta / \omega_\alpha = 1.5$ totally avoids flutter for the bending-aileron branch. However, as will become apparent in the following, it still allows for torsion-aileron torsion associated aeroelastic instabilities.

As the Mach number increases a steep upward rise of the flutter boundary and an increase in flutter frequency is predicted, as was observed in the 2 d.o.f. system. However, as compared to Case B the second drop in flutter speed appears somewhat earlier at about $M = 0.82$. This behavior has a close relation to the presence of the control surface and the strong shock waves in its vicinity at these Mach numbers. As is clear from the amplitude and phase information depicted in Fig. 19, the flutter mode changes and becomes primarily torsion flutter, where it is evident that the control surface degree of freedom contributes appreciably to the flutter mode in the range of Mach numbers $0.82 < M < 0.855$. In addition, the flutter frequency rises and reaches a maximum value shortly after the bottom of the second dip at $M = 0.86$, reflecting the dominance of the torsion natural mode.

For Mach numbers higher than 0.86, when the shocks move towards the trailing edge, the flutter mode changes and the flutter boundary increases anew. At $M = 0.875$ the amplitude and phase parameters of the bending-torsion branch, $|\alpha_0|/|h_0/b|$ and $\varphi_\alpha - \varphi_h$, approach almost the same order of magnitude as they exhibit at Mach numbers lower than 0.70.

3.2 Results for Flexible Wing Section (Cases D and E)

Based on sample calculations using the arbitrary Lagrangian-Eulerian formulation, Bendiksen concluded that camber bending might play an important role in the transonic flutter problem. This conclusion reached in reference [9] is more definitely confirmed in the present study and may have particular implications for the application of adaptive structures in wing technology. In this section, the effect of chordwise flexibility on the aeroelastic response behavior of two typical wing segments, namely those of Case B and C, is investigated.

In order to gain insight into the possible dynamic behavior of the studied cases and also to provide a meaningful measure for the flexibility taken into account, the eigensolutions of the re-

spective free vibration equilibrium equations of motion were computed first. In addition, since there is usually little justification for including the dynamic responses of the higher frequency modes, the computational effort was significantly reduced by transforming the basis to modal (normal) generalized coordinates and considering only a few modes. This implies that all results presented in this section were computed using the modal approach. It should, however, be noted that during the checkout phase of the program also computations for the rigid wing segments (Cases B and C) were performed using either discrete or modal (normal) generalized coordinates, which led to exactly the same results within the accuracy of the output routine (8 digits).

The influence of the flexibility on the dynamic behavior was assessed by comparing the fundamental mode shapes ϕ_b of Cases D and E with the corresponding sets of mode shapes ϕ_a obtained for the rigid body Cases B and C. On condition that the considered eigenvectors ϕ_a, ϕ_b consist of the same number of components representing the same coordinates (sign convention) in a common basis, this can be achieved by employing the Modal Assurance Criterion (MAC) [1]

$$MAC = \frac{(\phi_a^T \phi_b)^2}{(\phi_a^T \phi_a)(\phi_b^T \phi_b)} \cdot 100\%,$$

which is independent from the possibly different normalization of the eigenvectors. Maximum conformity is given by a MAC value of 100%, while at least a MAC value of 70% is required in order to speak of related mode shapes.

For the purpose of enabling direct comparison between the Cases B and D as well as Cases C and E by applying the Modal Assurance Criterion, the eigenvectors of Cases B and C were exactly expanded to the required size.

3.2.1 Results for Case D

Case D is the same as Case B except that the dynamic behavior of the system is now described by 20 degrees of freedom. More precisely, 9 beam elements are used in the chordwise direction of the typical wing segment, each of which has two degrees of freedom at each node, i.e., one translational and one rotational degree of freedom. The entire finite element assemblage then has 20 degrees of freedom, thus accounting for more general deformations, or in other words for chordwise flexibility, of the typical wing segment. From inspection of the eigensolutions of the system it was concluded that the first four mode shapes are sufficient to represent the global dynamic behavior of the system including camber bending effects. As a result, the frequency content of the system is reduced from initially $\omega_{max}/\omega_\alpha = 1.34 \cdot 10^3$ to $\omega_{max}/\omega_\alpha = 7.81$ accompanied by a reduction in the admissable time step for the structural domain from $\Delta t_S/T_\alpha = 4.97 \cdot 10^{-6}$ to $\Delta t_S/T_\alpha = 6.39 \cdot 10^{-3}$ (where $T_\alpha = 2\pi/\omega_\alpha$), assuming that one period of the highest frequency of the system is resolved by 150 time steps, i.e., $\Delta t_S = 1/(150 f_{max})$. Typical admissible time steps $\Delta t_F/T_\alpha$ for the temporal integration of the fluid domain are of a order of magnitude of about 10^{-4} for the explicit and 10^{-3} for the implicit time integration scheme. This attests more precisely the statement given above that the admissible structural time step can decrease well below that acceptable for the fluid domain.

The MAC values with respect to the first and second natural mode shapes of Case D are 99.85% and 98.61%, respectively, while the corresponding frequencies exhibit relative errors of - 0.33% and - 3.5%. As is clear from these values, the fundamental modes of the rigid body system (Case B) are well reproduced by the finite element model. Even more surprising are the remarkable changes in the flutter boundary and the flutter frequency, which are plotted vs. Mach number in Fig. 21 and Fig. 22. Also depicted in these figures are the solutions obtained for the corresponding rigid system in order to make comparison easier and also to contrast the effects of flexibility.
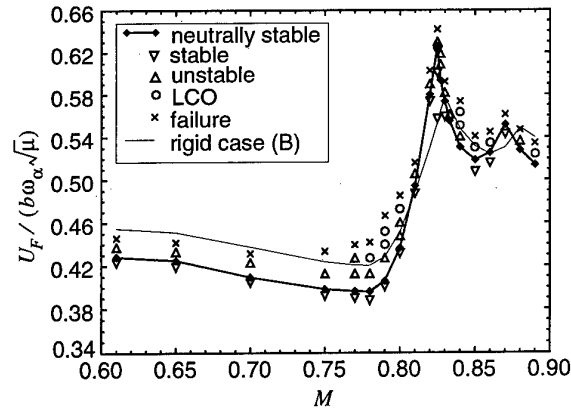

Fig. 21 Flutter velocity coefficient vs. Mach number for Case D
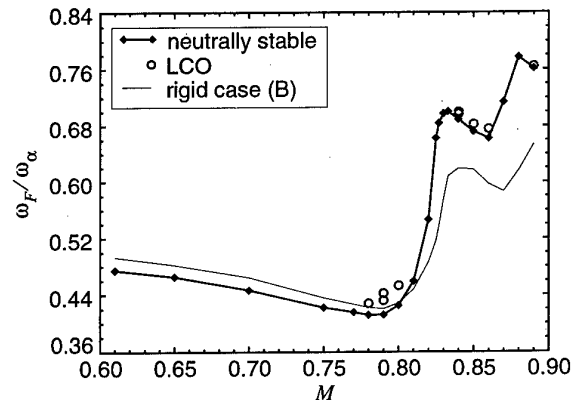

Fig. 22 Flutter frequency vs. Mach number for Case D

As can be seen, for Mach numbers lower than 0.79 the flutter boundary as well as the flutter frequency are shifted towards lower values. This means that the minimum of the first transonic dip is also shifted towards lower critical flight speeds. The reason for this might lie in the effect that camber bending motions of the profile increase the in-phase components of the unsteady aerodynamic coefficients, thus increasing the impact of the aerodynamic forces on the structure. The minimum value in flight speed is predicted at the same Mach number as for Case B, indicating that the out-of-phase components of the unsteady aerodynamic coefficients remain relatively unchanged. For Mach numbers slightly higher than 0.79 a steep upward rise of the flutter boundary is predicted, and reaches a maximum at a significantly higher level than was observed for Case B.

Another notable point is that the flexibility seems to have a stabilizing effect on the limit cycle behavior of the system. For example, in the region where the second dip occurs no LCO was found for the rigid wing section, while stable LCO solutions were predicted for the flexible wing segment.
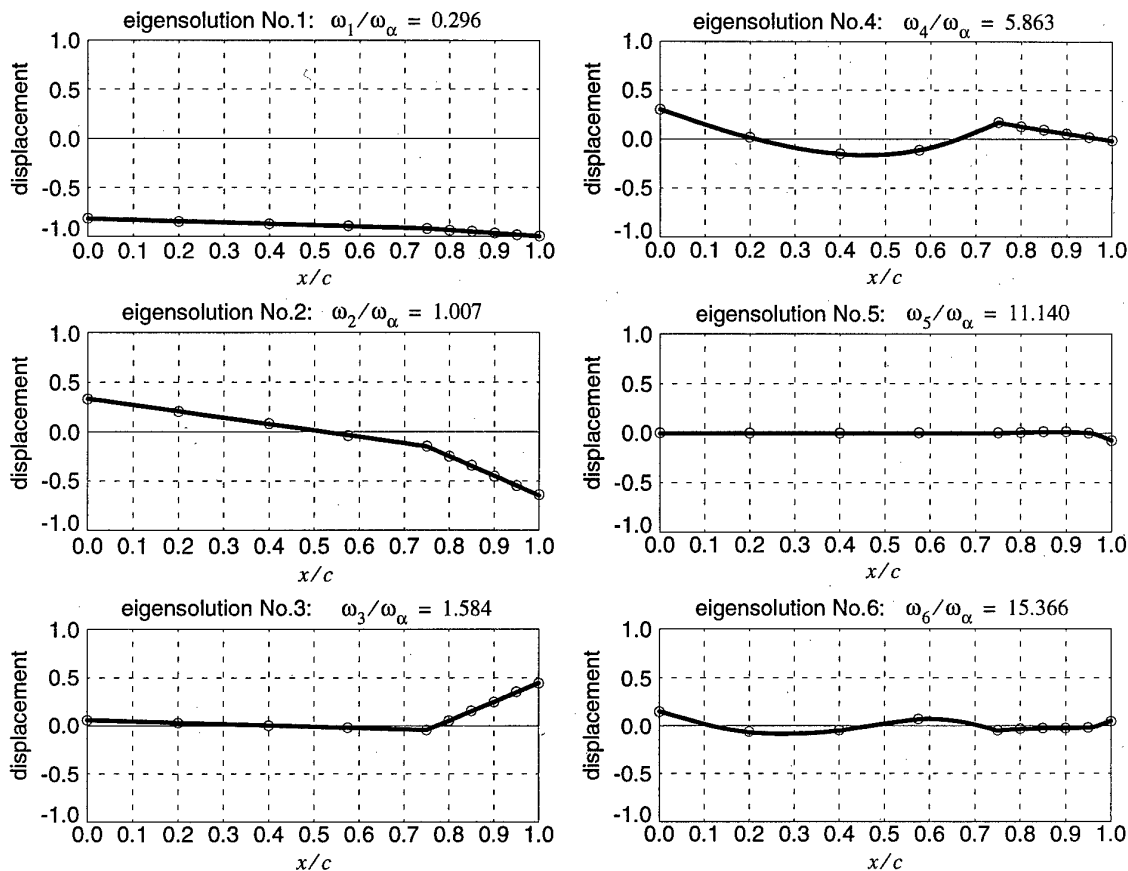
Fig. 23 Considered eigensolutions for Case E

However, as already mentioned above, whether or not LCO is found depends on the length of the considered simulation period. It is therefore expected that some of the unstable solutions depicted in Fig. 13 for Mach numbers where firm shocks are present might have resulted in LCO solutions for extended simulation periods. In addition, the higher the flow velocity the faster the system reaches its steady LCO amplitude and vice versa. In so far the rapid approach of the flexible system to its steady LCO solution might also be viewed as an effect of the increased impact of the airloads due to camber bending.

The second drop in flutter speed is predicted at slightly lower Mach numbers compared to Case B, which, from the discussion in section 3.1.2, implies that camber bending affects the precise position of the shocks, therefore producing a phase shift in the unsteady aerodynamic coefficients.

3.2.2 Results for Case E

By analogy with the comparison of the results for Case D with those of Case B, the results for Case E are now compared to the results obtained for the 3 d.o.f. system studied in section 3.1.3 (Case C). The finite element assemblage used for Case E has 21 degrees of freedom. However, again the dynamic behavior of the system was found to be sufficiently accurately described by mode superposition using only the first six mode shapes of the system. The respective eigensolutions are depicted in Fig. 23. Also, in order to impart an idea on the possible deformations of the typical wing section including its surface (fluid structure interaction boundary), Fig. 24 shows a sketch of the 6th mode as an example.

Fig. 24 Example of deformed typical wing section using the 6th mode shape of Case E

The MAC values with respect to the first three natural mode shapes were computed as discussed in the previous section and are 99.81%, 99.73%, and 99.35%, respectively. The relative errors in the corresponding frequencies are -0.40%, -5.42%, and -3.07%. Again a high level of conformity between the mode shapes of the two systems is obvious, though the relative error in the frequency of the second mode (torsion) is noteworthy.

In Fig. 25 and Fig. 26, the predicted flutter boundaries and variations in flutter frequencies for the Cases C and E are plotted vs. Mach number in the same figures. Again, the flutter boundary as well as the corresponding flutter frequencies are shifted towards lower values for Mach numbers smaller than those where the minimum in flutter speed was predicted for Case C. In contrast to the phenomenon found in Case D, where compared to the rigid case the flutter boundary reached a even more pronounced maximum for slightly higher Mach numbers beyond the first transonic dip, the flutter boundary for Case E

reaches almost the same value before it starts to drop anew with increasing Mach number. As with the first drop in flutter speed, the minimum of the second transonic dip is also found to be smaller than that of the rigid wing segment.
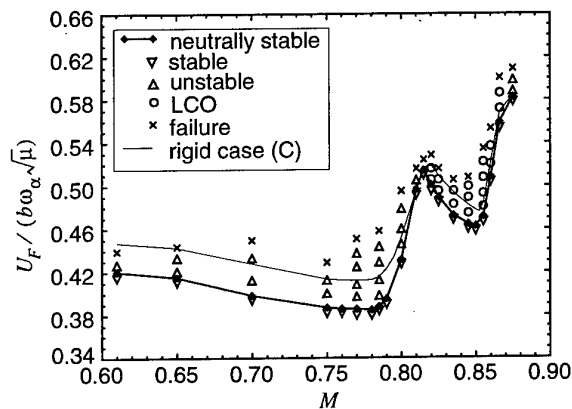
Fig. 25 Flutter velocity coefficient vs. Mach number for Case E
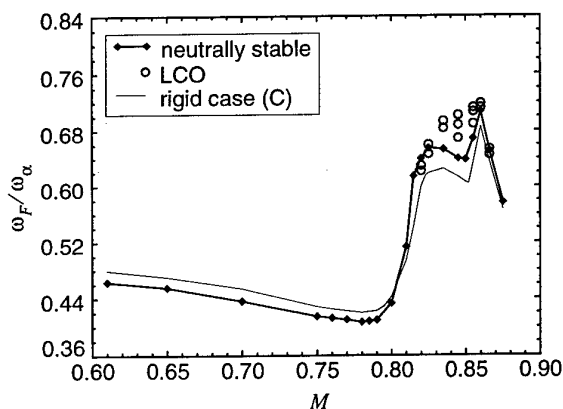
Fig. 26 Flutter frequency vs. Mach number for Case E

Another notable point in comparing Cases C and E with each other is that the consideration of chordwise flexibility seems to have a destabilizing effect on the limit cycle behavior, as can be seen from the obtained LCO solutions for both cases (Fig. 17 and Fig. 25). This is in contrast to the observed behavior for Cases B and D, where for the flexible Case D (Fig. 21) more stable LCO solutions were predicted than for the corresponding rigid Case B (Fig. 13). This effect, however, was not further investigated in this study.

4 CONCLUDING REMARKS

An aeroelastic simulation code has been developed to analyze the response behavior and stability characteristics of typical airfoil sections in two-dimensional transonic flow by using the domain decomposition approach. The prime features of the proposed method are viewed in its capability to implement aerodynamic models of varying complexity and in the general formulation of the structural model by means of the finite element method, while different spatial discretizations in the fluid and structural domain are permitted. Elastic effects in the chordwise direction of a typical wing section are taken into account, thus allowing for more general motions of the airfoil including the fluid structure interaction boundary. The exact rigid case is readily treated in a very effective manner by lumping the structural properties and distributed loads. In addition, the proposed method allows for the application of the widely used modal decomposition technique to the structural equations of motion, which was shown to lead to a significant decrease in computational costs.

In this study transonic aeroelastic time response calculations were carried out for several test cases and the effect of chordwise flexibility on the aeroelasitc stability behavior was investigated. More specifically, the flutter characteristic of a two degree-of-freedom airfoil oscillating in pitch and plunge was first calculated and compared with previously published results. The agreement was generally good, though for a narrow range of free-stream Mach numbers a second drop in flutter speed was predicted with the present code, which did not show up in the previous analysis. The same phenomenon was found in all considered cases and was shown to be closely related to the shock dynamics.

An energy identity was implemented to obtain an independent check on the accuracy of the proposed partitioned time integration procedure. This was mainly done to verify the conclusion reached in references [9] and [11] that the „classical" domain decomposition approach overestimates the energy flux from the fluid to the structure, thus leading to a systematic divergence of the difference between the total energy of the structural system and the work done by the aerodynamic loads. As is clear from the present analyses, a well-posed partitioned time integration procedure is capable of correctly reproducing the energy exchange between the fluid and the structure.

Based on sample calculations using the arbitrary Lagrangian-Eulerian formulation, it was also concluded in reference [9] that camber bending might play an important role in the transonic flutter problem. This conclusion was more definitely confirmed in the present analyses and may have particular implications for the application of adaptive structures in wing technology. The investigations in this study revealed that for the considered cases the minimum of the flutter boundary is shifted towards lower critical flight speeds if camber bending motions are included in the analysis. In addition, the minimum of the second drop in flutter speed is predicted at slightly lower Mach numbers as compared to the corresponding rigid case, which implies that camber bending affects the precise position of the shocks, therefore producing a phase shift in the unsteady aerodynamic coefficients.

5 REFERENCES

[1] Allemang, R. J.; Brown, D. L.: A Correlation Coefficient for Modal Vector Analysis; Proceedings of the 1st International Modal Analysis Conference; Orlando, FL., USA; 1982; pp. 110-116

[2] Amsden, A. A.; Hirt, C.W.: An Arbitrary Lagrangian-Eulerian computer program for fluid flow at all speeds; Report LA-5100; Los Alamos Scientific Laboratory; Los Alamos; NM; March 1973

[3] Anderson, W. K.; Thomas, J. L.; van Leer, B.: A Comparison of Finite Volume Flux Vector Splittings for the Euler Equations; AIAA Paper; No. 85-0122; 1985

[4] Anderson, W. K.; Thomas, J. L.; Rumsey, C. L.: Flux-Vector Splitting for Unsteady Calculations on Dynamic Meshes; NASA CP 3022; Part 1; 1989; pp. 193-214

[5]   Bathe, K.-J.: Finite Element Procedures in Engineering Analyses; Prentice-Hall, Inc.; Englewood Cliffs; New Jersey 07632; 1986/1996

[6]   Beam, R. M.; Warming, R. F.: An Implicit Finite-Difference Algorithm for Hyperbolic Systems in Conservation-Law Form; Journ. Comp. Phys.; Vol. 22; 1976; pp. 87-110

[7]   Belytschko, T.; Kennedy, J. M.; Schoeberle, D. F.: Quasi-Eulerian Finite Element Formulation for Fluid Structure Interaction; paper 78-PVP-60; Joint ASME/CSME Pressure Vessel and Piping Conference; Montreal; Canada; 1978

[8]   Bendiksen, O. O.; Kousen, K. A.: Transonic Flutter Calculations Using the Euler Equations; NASA CP 3022; Part 2; 1989; pp. 477-491

[9]   Bendiksen, O. O.: A New Approach to Computational Aeroelasticity; AIAA 32nd Structures, Structural Dynamics, and Material Conference; Baltimore; Md.; April 1991; pp. 1712-1727

[10]   Bendiksen, O. O.: Role of Shock Dynamics in Transonic Flutter; AIAA Dynamics Specialist Conference; AIAA-92-2121; Dallas; TX; April 16-17, 1992

[11]   Bendiksen, O. O.: Eulerian-Lagrangian Simulation of Transonic Flutter Instabilities; Symposium on Fluid-Structure Interaction and Aeroelasticity, ASMA Winter Annual Meeting; Chicago; IL; November 11; 1994

[12]   Bendiksen, O. O.; Davis, G. A.: Nonlinear Traveling Wave Flutter of Panels in Transonic Flow; 36th AIAA/ASME/ASCE/AHS/ASC Structures, Structural Dynamics, and Material Conference; AIAA-95-1496; New Orleans; LA; April 10-12, 1995

[13]   Bennett, R. M.; Desmarais, R. M.: Curve Fitting of Aeroelastic Transient Response Data with Exponential Functions; Flutter Testing Techniques NASA SP-415; Conference at Dryden Flight Research Center; Edwards; CA; October9-10; 1975; pp. 43-58

[14]   Bland, S. R.: AGARD Two-Dimensional Aeroelastic Configurations; AGARD-AR-156; August 1979

[15]   Blom, F.; Leyland, P.: Analysis of Fluid-Structure Interaction on Moving Airfoils by means of an Improved ALE-method; AIAA 97-1770; 28th Fluid Dynamics Conference; Snowmass Village, CO; June 29-July 2, 1997

[16]   Budo, A.: Theoretisch Mechanik; VEB Deutscher Verlag der Wissenschaften; Berlin; 1956

[17]   Carstens, V.: Two-Dimensional Elliptic Grid Generation for Airfoils and Cascades; DFVLR-FB 88-52; Göttingen 1988

[18]   Carstens, V.: Computation of the Unsteady Transonic 2D Cascade Flow by an Euler Algorithm with Interactive Grid Generation; AGARD CP 507; AGARD Specialist's Meeting on Transonic Unsteady Aerodynamics and Aeroelasticity; San Diego, USA; Oct. 7-11, 1990

[19]   Courant, R.; Friedrichs, K. O.; Lewy, H.: Über die partiellen Differentialgleichungen der mathematischen Physik; Math. Ann.; Vol. 100; 1928; pp. 32

[20]   Donea, J. et al.: An Arbitrary Lagrangian-Eulerian Finite Element Procedure for Transient Dynamic Fluid-Structure Interaction Problems; paper B1/3; Trans. 5th International Conference on Structural Mechanics in Reactor Technology; Berlin; Germany; 1979

[21]   Guruswamy, G. P.; Yang, T. Y.: Aeroelastic Time Response Analysis of Thin Airfoils by Transonic Code LTRAN2; Journal of Computer and Fluids; Vol. 9; No. 4; Dec. 1981; pp. 409-425; see also AFFDL-TR-79-3077; June 1979

[22]   Edwards, J. W.; Bennett, R. M.; Whitlow, W., Jr.; Seidel, D. A.: Time-Marching Transonic Flutter Solutions Including Angel-of-Attack Effects, J. Aircraft, Vol. 20, No. 11, Nov. 1983, pp. 899-906

[23]   Hirt, C. W.; Amsden, A. A.; Cook, J. L.: An Arbitrary Lagrangian-Eulerian computing method for all flow speeds; J. Comput. Phys.; No. 14; 1974; pp. 227-253

[24]   Houwink, R.; van der Vooren, J.: Results of an Improved Version of LTRAN2 for Computing Unsteady Airloads on Airfoils Oscillating in Transonic Flow; AIAA Paper 79-1553; AIAA 12th Fluid and Plasma Dynamics Conference; Williamsburg, VA; July 23-25, 1979

[25]   Hughes, J. R.; Liu, W. K.; Zimmermann, T. K.: Lagrangian-Eulerian Finite Element Formulation for Incompressible Viscous Flows; Computer Methods in Applied Mechanics and Engineering; Vol. 29; 1981; pp. 329-249

[26]   Isogai, K.: Numerical Study of Transonic Flutter of a Two-Dimensional Airfoil; NAL TR-617T; National Aerospace Laboratory; Tokyo; Japan; July 1980

[27]   Kousen, K. A.; Bendiksen, O. O.: Nonlinear Aspects of the Transonic Aeroelastic Stability Problem; Proceedings of the AIAA/ASME/ASCE/AHS 29th Structures, Structural Dynamics, and Material Conference; Williamsburg; Virginia; April 18-20; 1988; pp. 760-769

[28]   Mohr, R. W.; Batina, J. T.; Yang, T. Y.: Mach Number Effects on Transonic Aeroelastic Forces and Flutter Characteristics; Proceedings of AIAA/ASME/ASCE/AHS 29th Structures, Structural Dynamics, and Materials Conference; Williamsburg; Va.; April 18-20; 1988; pp. 749-759

[29]   Newmark, N. M.: A Method of Computation for Structural Dynamics; Proceedings of the American Society of Civil Engineers; Vol. 85; No. EM3; 1959; pp. 67-94

[30]   Noh, W. F.: A time-dependent, two-space dimensional, coupled Eulerian-Lagrangian code; in Adler, B. et al, eds.: Methods in Computational Physics; Academic Press; New York; 1964; pp. 117

[31]   Richtmyer, R. D.; Morton, K. W.: Difference Methods for Initial-Value Problems; Second Edition; Interscience Publishers a division of John Wiley & Sons, Inc.; 1967

[32]   Rizzi, A.: Numerical Implementation of Solid-Body
        Boundary Conditions for the Euler-Equations; ZAMM;
        Vol. 58; 1978; pp. 301-304

[33]   Theodorsen, T.; Garrick, I. E.: Mechanism of Flutter, A
        Theoretical and Experimental Investigation of the Flut-
        ter Problem; NACA Report 685; 1940

[34]   Theodorsen, T.; Garrick, I. E.: Flutter Calculations in
        Three Degrees of Freedom; NACA Report 741; 1942

[35]   van Leer, B.: Towards the Ultimate Conservative Differ-
        ence Scheme V. A Second Order Sequel to Godunov's
        Method; Journ. Comp. Phys.; Vol. 32; 1979; pp. 101-136

[36]   van Leer, B.: Flux Vector Splitting for the Euler Equa-
        tions; ICASE Report No. 82-30; 1982

[37]   Voß, R.; Carstens, V.: Computation of Unsteady Transon-
        ic Flows around Oscillating Airfoils Using Full Potential
        and Euler Equations; Proceedings of the European Fo-
        rum on Aeroelasticity and Structural Dynamics; Aachen,
        Germany; April 17-19, 1989

[38]   Yang, T. Y.; Batina, J. T.: Transonic Time-Response
        Analysis of Three D.O.F. Conventional and Supercritical
        Airfoils; Proceedings of AIAA/ASME/ASCE/AHS 23rd
        Structures, Structural Dynamics, and Material Confer-
        ence; New Orleans; La.; May 1982; pp. 256-266

[39]   Zienkiewicz, O. C.; Taylor, R. L.: The Finite Element
        Method; Vol. II: Solid and Fluid Mechanics - Dynamics
        and Non-Linearities; McGraw-Hill Book Company;
        1989/1991

[40]   Zwaan, R. J.: Verification of Calculation Methods for
        Unsteady Airloads in the Prediction of Transonic Flutter;
        AIAA-84-0871; AIAA/ASME/ASCE/AHS 25th Struc-
        tures, Structural Dynamics, and Material Conference;
        Palm Springs, CA; May 14-16, 1984;

NLR-TUDelft Experience in Unsteady Aerodynamics and Aeroelastic Simulation Applications

J.J. Meijer   M.H.L. Hounjet   B.J.G. Eussen
meijer@nlr.nl   hounjet@nlr.nl   eussen@nlr.nl
National Aerospace Laboratory, NLR
Amsterdam, The Netherlands

B.B. Prananta
b.b.prananta@lr.tudelft.nl
Delft University of Technology
Delft, The Netherlands

SUMMARY

The development of computational aerodynamic and aeroelastic simulation codes is steadily making progress. Nevertheless these codes are only modestly being accepted by the end-users in industry and other agencies in charge of flutter clearance or aeroelastic responses, in general.
Various shortcomings of the current codes can be named which cause the reserve of the end-users. One of them is often unacceptable amount of manpower required for pre- and postprocessing.
NLR is developing a numerical aeroelastic simulation environment for applications to civil and fighter-type aircraft, of which a pilot version is in operation. Special attention has been given to the design of userfriendly pre- and postprocessing.
The paper will discuss the motivation of an aeroelastic simulation environment, the status of the NLR AEroelastic SIMulation system, the current research activities, the pre- and postprocessing and future research activities. Several applications will be shown, demonstrating the use to both civil and fighter-type aircraft.

ABBREVIATIONS

CUA	Computational Unsteady Aerodynamics
CAS	Computational Aeroelastic Simulations
CFD	Computational Fluid Dynamics
DL	Doublet Lattice Method
EE	Euler Equations
FEM	Finite Element Method
FP	Full Potential
LCO	Limit Cycle Oscillation
MIMO	Multiple Input/Multiple Output
(TL)NS	(Thin Layer) Navier Stokes

1. INTRODUCTION

The objective of the present paper is a review of the current status and ongoing research at NLR of

- the technological readiness of both Computational Unsteady Aerodynamics (CUA) and Computational Aeroelastic Simulations (CAS),
- the industrial readiness of these methods in pratical applications.

Since the last meeting in this subject area [1, 2, 3] many advances were made at NLR in refining mathematical models, applications to more complex aircraft configurations and computational efficiency.

However, a gradually increasing gap exists between the technological and industrial readiness, manifested e.g. by an overpresentation of contributions in this research area from the side of research institutes and universities in comparison with industry. A preparatory step to diminish this gap was presented in [4], which describes the industrial needs and expectations of CUA/CAS.

The subject here is being addressed because of these industrial needs for an efficient aeroelastic simulation system able to improve aircraft design with adequate and efficient assessment of aeroelastic behaviour (flutter and/or dynamic responses) for transonic flight or other nonlinear conditions.

Today's industrial aeroelastic studies are performed mainly with a set of classical methods restricted to linear assumptions due to their efficiency in assessing the critical state cases for a large state space. For transonic flow these results are questionable and the aforementioned methods are often matched with data obtained from experiment and or other CFD methods.

The NLR AESIM method is developed with the objective to assist in the design of future aircraft which are subjected to increases in flexibility, aerodynamic loading and nonlinearity and might be of value in the early design and development phase for assessing flight stability and control, safety and risk valuation and ride qualities. The method focuses primarily on aeroelasticity at transonic and mildy separated flows where aerodynamic nonlinearities are a non-negligible factor which cannot be estimated with extrapolating current methodology which is suited for flight at subsonic and low angle-of-attack supersonic speeds.

The system was developed primarily for flutter certification of transport-type aircraft, with the aim to become an affordable tool for industry. Recently activities have been started to extend the AESIM method in the direction of flows and geometries which are encountered in fighter-type aircraft. Then the code will

be ready to prove its value in applications with mild flow separation which is primarily responsible for inducing strong Limit Cycle Oscillation (LCO) structural responses, which might restrict the flight envelope of the aircraft.

In the next section an outline is presented of the current status and ongoing research activities of the CUA/CAS method AESIM, which will be discussed and illuminated with applications in the subsequent sections.
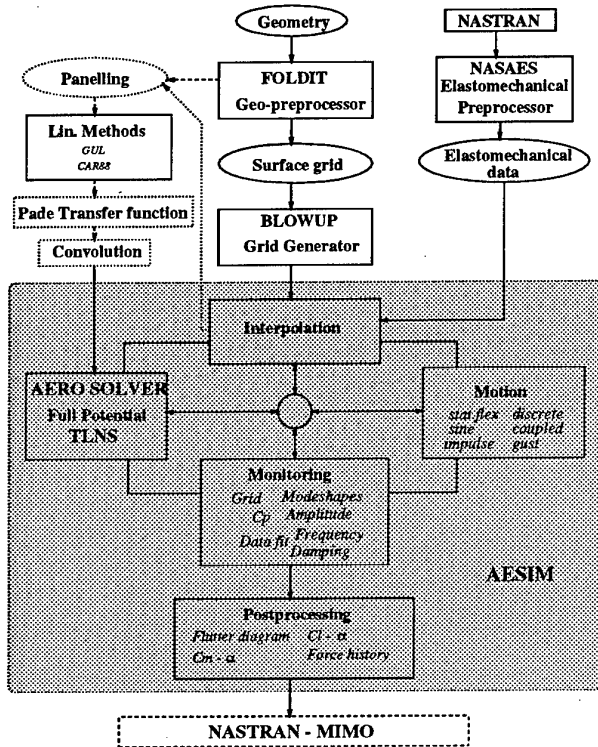

Figure 1: AEroelastic SIMulation system.

2. OUTLINE

In order to identify the current status of the AEroelastic SIMulation system and the current research activities a list of the main and sub items have been given below. The aim of these activities are to obtain a realistic and affordable aeroelastic simulation system for both transport- and fighter-type aircraft.

- **Motivation**

    * **Realistic and Affordable aeroelastic simulation**

- **AEroelastic SIMulation system status [5, 6]**

    * **Realism**

        ★ Application of flow solver for off-design conditions

        ★ Application of aeroelastic simulation beyond the envelope usually demonstrated by design codes
            · Solver downgrading in difficult areas to incompressible flow
        ★ Aeroelastic Accuracy
            · Arbitrary grid reduction in I-, K-direction

    * **Affordability**

        ★ Tailoring of Surface and Field grid generation
        ★ Volume Spline Interpolation [7]
        ★ Efficient flow solvers linear DL, FP, EE, TLNS [8, 9]
        ★ Efficient aero-structural coupling methods [10]
        ★ Direct visualization and on-line analysis
        ★ Analysis from single point towards multi-point prediction [11]
        ★ No ad-hoc implementations

- **Current research activities**

    * **MIMO research**

        ★ CEAS Rome 1997 paper Hounjet/ Eussen/Soijer [11]
        ★ Cooperation Delft University of Technology
        ★ Points of attention:
            · Multi-point strategy
            · Signal processing

    * **TLNS+ research**

        ★ CEAS Rome 1997 paper Prananta/ Hounjet [10]
        ★ Cooperation Delft University of Technology
        ★ Superiority TLNS for LANN wing
        ★ Points of attention:
            · Time-step reduction/Extrapolation methods
            · Prognostics using TAM
            · Turbulence models

    * **Linear aero research**

        ★ CEAS Rome 1997 paper Hounjet/ Eussen/Soijer [11]
        ★ Points of attention:
            · Complex curve fitting
            · Transfer functions for control system design
            · Most straightforward approach

    * **LCO simulation system [12]-[15]**

        ★ CEAS Rome 1997 paper Meijer [15]
        ★ LCO database experience

- **Future research activities**

3. AEROELASTIC SIMULATION SYSTEM

At NLR much effort has been spent to create a complete
AEroelastic SIMulation system, to be used primarily
for the flutter certification of transport-type aircraft in
the transonic speed regime. Time-accurate simulation
of fluid and airframe structure interaction is empha-
sized. The AEroelastic SIMulation system is referred
to as AESIM, after the name of the core program.
The AEroelastic SIMulation system is built around the
AESIM core and consists of six independent main pro-
gram modules, (Fig. 1):

* **FOLDIT**: surface grid generation.
* **BLOWUP**: grid generation.
* **NASAES**: elastomechanical data manipulation.
* **AESIM** core.
* Output interfacing e.g. to NASTRAN or MIMO.
* Linear methods library.

The AESIM core program is divided into 5 individual
modules and contains those subroutines which are CPU
intensive and make it possible to run the core in stand
alone mode:

* **Interpolation**: Interpolation of elastomechanical
  and aerodynamic data (Volume Spline Method [5, 7]).
* **Aero solver**: Time-accurate solving of aerodynamic
  equations (FP and TLNS [1]).
* **Motion**: Either description of motions, seeded flows,
  or solving of elastomechanical equations with or with-
  out external loadings.
* **Monitoring**: Visualization of simulated data.
* **Postprocessing**: Recollection and assimilation of
  facts and figures of past simulation(s).

The various aspects of this environment will now be
discussed in some detail.

3.1 Surface grid generation

Consistent with aeroelastic requirements and discussed
in [5] only the sub-structures of aircraft which are slen-
der and have surfaces with low curvature (wing, tail
and fin) need to be modelled quite well in obtaining the
aerodynamic force in normal direction. Consequently
the quality and density of the surface grids can be re-
laxed in the other areas. While the aeroelastician is not
expected to be an expert surface modeller who creates a
surface grid from scratch, the assumption is made that
an initial surface grid is available which can be tuned to
his needs in routine applications by the geometry pre-
processor.

The geometry preprocessor FOLDIT generates a mono-
block structured surface description and/or paneling of
the complete aircraft with embedded upwind slits and
downwind slits (wake surfaces) by assembling and inter-
polating separate parent surface grids (provided by the
user by means of CAD/CAM programs). Instrumental
in assisting the user in specifying the required spacing of
each component in order to obtain smooth transitions is

---

[1]Recently the TLNS methodology as reported in [8, 9] has
been embedded.
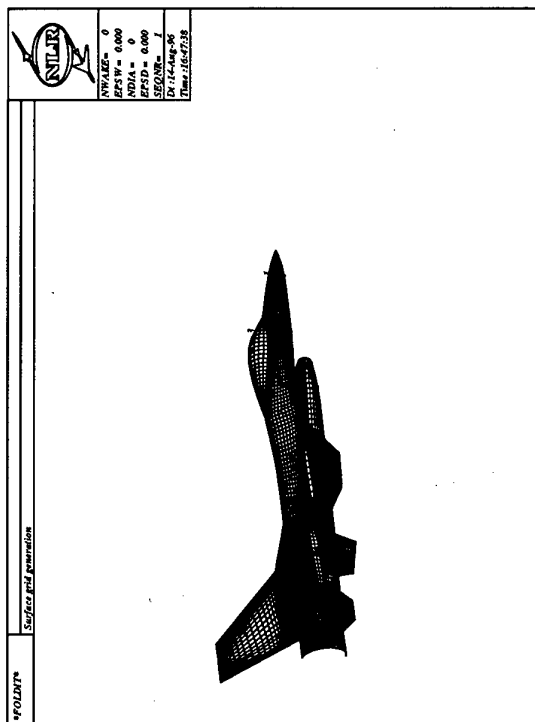
Figure 2: Fighter-type aircraft geometry input for
FOLDIT.

the so-called **domino** approach. This approach requires
the input of the spacings and the number of patches for
a few of the parent surface grids which are interpolated
(extrapolated) by the volume spline method [7] to the
other surface grids. On the floor this means that the
user only has to specify the leading and trailing edge
resolution of the lifting parts.

FOLDIT also constructs the slits, allows for redistri-
butions, data editing, data smoothing and stripping
and tailors the configuration to aeroelastic needs. By
this, considerable flexibility is offered to the aeroelasti-
cian who is not directed to other programs when minor
changes have to be made for parametric studies. Also
identification tags are generated which may be required
by the interpolation of the elastomechanical data to the
surface grid.

3.2 Grid generation

The grid generation is performed by the hyperbolic grid
generation method BLOWUP described in [16]. The
effort to generate mono-block **HO** grids about the sur-
face description of the complete aircraft with embed-
ded upwind slits and downwind slits (wake surfaces)
with mild concavities is low enough to be applied by
'non-grid expert applicators'. The grids have accept-
able quality about concave areas such as airfoil noses
and wing-fuselage junctions. The consequence of some
limitations in accuracy of the mono-block grid approach
to more complex configurations is considered acceptable
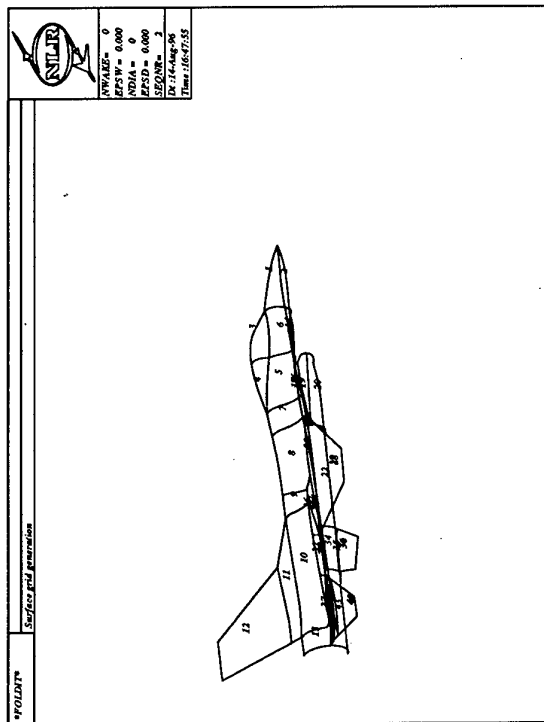
Figure 3: Outline of support surfaces of a fighter-type aircraft.
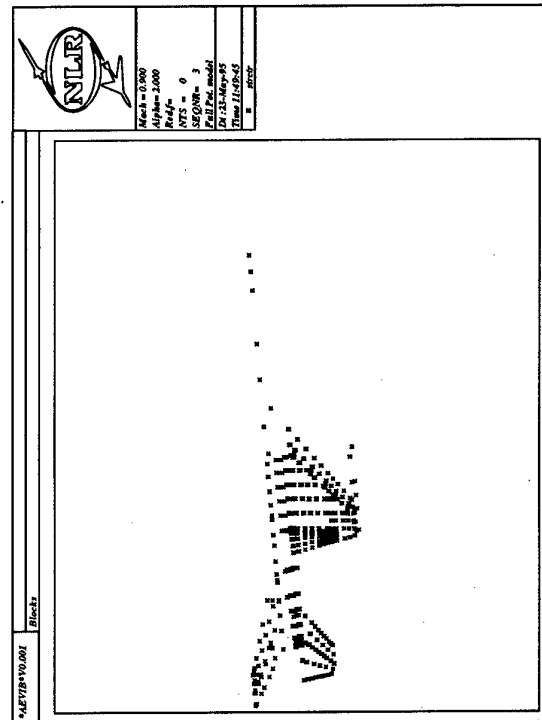
Figure 4: Location of structural points of a fighter-type aircraft.

for aeroelastic applications rather than for performance design.

In the solution of the aforementioned modelling, additional in-plane dissipation terms are applied which are well described in [17]. In addition, metric regularization terms have been developed to guarantee a proper behavior at axis, slit tips, strongly swept surfaces and non-smooth surface grids at wing-body junctions, tip regions, etc.

Also it has turned out that the constant implicitness parameters which are applied nowadays in most hyperbolic grid generators and control the out-of-plane dissipation required for preventing grid lines from crossing in the marching direction should be enhanced to prevent impairing the grid in convex zones. Therefore NLR has introduced a flexible implicitness parameter which can be applied more selective (small in convex zones and large in concave zones) and has worked well in all cases treated so far.

Many configurations can be gridded without angle control terms. In this case one relies on the dissipation terms for rendering concave domains. However, for some cases experiencing very strong concavities it might be necessary to use one of the following angle control options:

- The terms are automatically derived from previously generated planes.
- The terms are built from directions of the far field.

- The terms are evaluated by a 2-D aerodynamic panel method.
- The terms are provided by the surface(volume) spline method.
- The terms are provided from a feedback procedure to prevent grid folding.

In addition BLOWUP has been equipped with the possibilities:

- Starting with an orthogonal grid.
- Post-elliptic smoothing with control functions to smooth the grid. The smoothing is primarily meant for smoothing the transition zone between the hyperbolic and the algebraic generated grid contours and in strong concave zones.
- Algebraic grid generation of grid surfaces in the far field (far front, far rear and far radial surfaces) can be applied when outer boundaries are to be prescribed.
- A hyperbolic shooting method is embedded to generate a grid with a fixed far field boundary distribution.
- Finally existing grids can be refined, enlarged and/or smoothed.

Also **CH,CO** topologies of the grid are provided for single wing applications of the AESIM system. Other topologies that are provided include **HH**, **XH** and **OC**. A complete description of the BLOWUP grid generator is presented in [18].
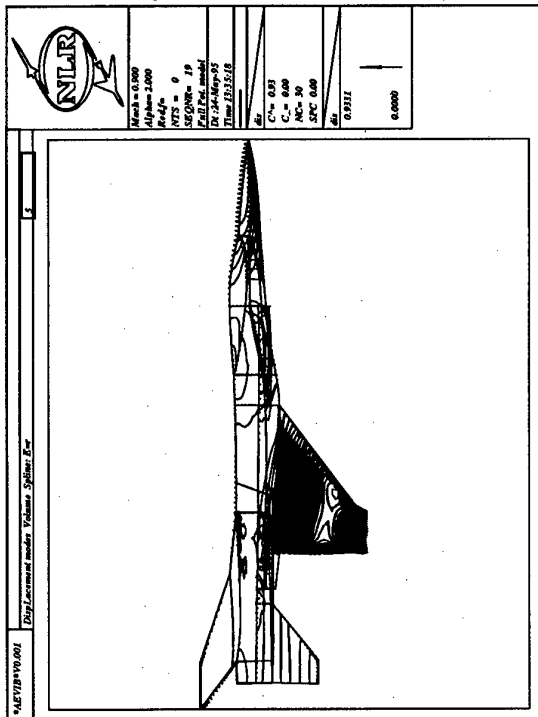
Figure 5: 3-D view of vector plot and contour plot of normal displacements of an arbitrary symmetric vibration mode of a fighter-type aircraft.

Figure 6: 3-D projections of vector plot and contour plot of normal displacements of an arbitrary symmetric vibration mode of a fighter-type aircraft.

3.3 Aerodynamic models

The aeroelastic solver is able to carry out the nonlinear aeroelastic analysis in the subsonic, transonic and supersonic speed range.

At present the time-accurate flow is modelled by:

- FP, completed by the Clebsch potential model for flows with strong shock waves which takes into account entropy and vorticity corrections [19].

  The choice for this model, mainly motivated by operational requirements with respect to turn-around time and computational costs, is discussed in [5].

- Recently the EE/TLNS methodology as described in [8, 9] has been embedded because there is enough evidence that with the TLNS complemented with a simple turbulence modelling the needs of the industry can be met for many realistic configurations. The latter extension is motivated by the type of flows and geometries which are encountered with fighter-type aircraft.

3.4 Simulations

The present version of the method enables the following types of simulation around 2-D and 3-D configurations:

- Steady aerodynamic simulation at given M_∞ and angle-of-attack for rigid configuration;

- Steady aeroelastic simulation with static deformations at given M_∞, angle-of-attack and dynamic pressure;

- Unsteady aerodynamic simulation for forced motion, deformation or gust at given M_∞, angle-of-attack, vibration mode and type of the motion (gust) (sinusoidal, impulse, jump, polynomial, etc.);

- Unsteady aeroelastic simulation due to elastomechanical motion or deformation at given M_∞, angle-of-attack, dynamic pressure and vibration modes. Also an external force due to exciters (flutter vane, gusts) can be included.

Simulations can be performed about symmetric configurations with symmetric and/or anti-symmetric vibration modes with respect to the xy (horizontal) and xz (vertical) planes. Also simulations are possible for wing-tail configurations and for complete bodies which require circumferential periodicity conditions to be applied.

On slit surfaces emanating from apices or non-trailing edge body parts the imposing of a hard wall, a free jet or a undisturbed pressure condition can be imposed.

3.5 Elastomechanical model

The elastomechanical model is split into a static part and a dynamic part which are explained in the following sections. The static deformation of the aircraft configuration is obtained by means of the 'free-free' flexibility
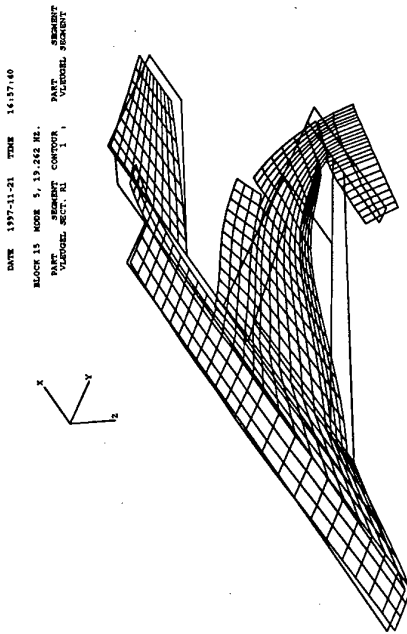
Figure 7: Normal displacements of an arbitrary symmetric vibration mode (5th) of a fighter-type aircraft, from flutter computational chain (surface-spline).

matrix. The dynamic structural behavior of the aircraft is based on the generalized modal deflection approach. The dynamic deformations are expressed in generalized coordinates q_i and their associated modal mass M, damping D, stiffness K and vibration modes $\bar{h}_i$. For a description see [5].

3.6 A(ero)E(lasto) Transfer

The information transfer at the fluid/structure interface is performed by the interpolation models which are well described in [7].

From the implemented interpolation models [5] it has turned out in applications that the Least Squares Polynomial approximation of the data and Hounjet's volume spline interpolation method are attractive to select because they do not require any user preparation or intervention. The well-known planar surface spline interpolation and its curvilinear application are hardly used in applications.

In general it is assumed that the elastomechanical data are obtained through e.g. NASTRAN so that for this case the interface NASAES has been created.

3.7 Others

Besides the vibration modes, other sets of geometric disturbance fields (control modes, pseudo vibration modes) which are interpolated by the volume spline or polynomial spline method might be specified by the user. These modes are also described in [5].

In order to facilitate the comparison with other reference pressure data during the simulation, the volume
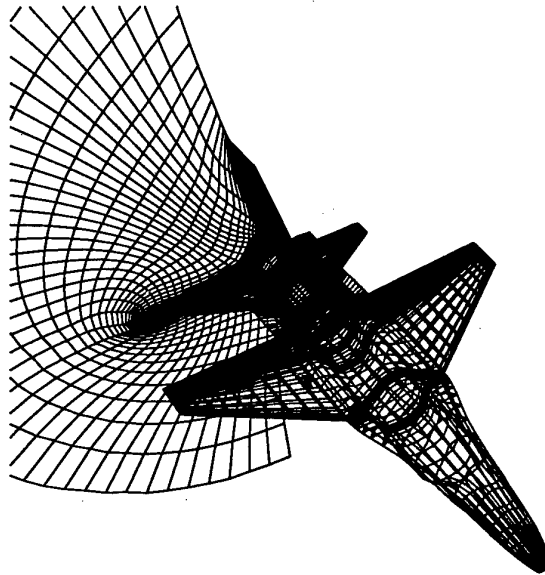
Figure 8: Mesh around wing-body-tail fighter-type configuration, number of points $\sim$ 200,000.

spline method is also used to interpolate arbitrary data to the aerodynamic surface grid.

3.8 Time signal analysis

One of the fundamental tasks in an aeroelastic analysis is the determination of the frequency and damping of aeroelastic modes (e.g. to detect if one of the generalized displacements becomes unstable and flutter will occur). As many different time response signals may have to be analyzed several methods for curve-fitting should be available. In general each time response signal exists of contributions of various modal modes, of which the frequency and damping of each one have to be determined.

Therefore, during an unsteady simulation the data must be analyzed on-line in the time domain in order to determine the behavior of a coupled system. The main purpose of this analysis is to determine the frequency and damping characteristics of the discrete time signal. To fulfil that task the following methods have been embedded [11]:

- The exponential sine fit,
- Prony's method,
- Fast Fourier Transform analysis,
- Curve-fitting of transfer functions.

Since a wide array of time response signals is available several ways exist to make use of the above-mentioned time-fitting tools. The most common time response signals which can be used to determine the frequency and damping characteristics of the discrete time signal consist of:

- For every modal mode separately:
  - the generalized coordinate,
  - the velocity of the generalized coordinate,
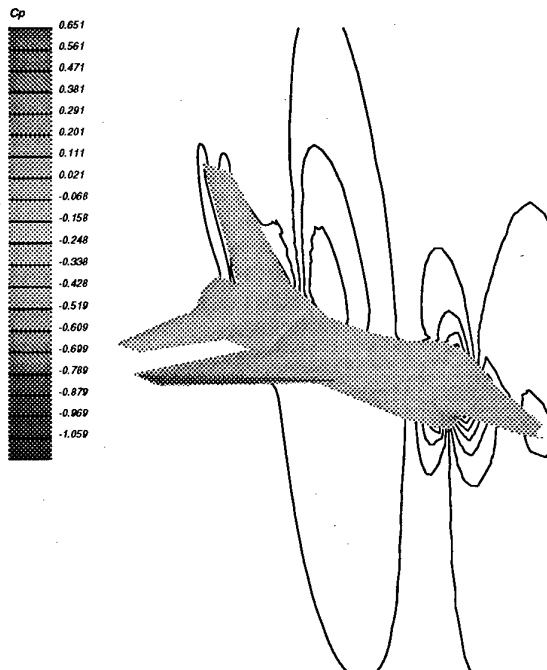
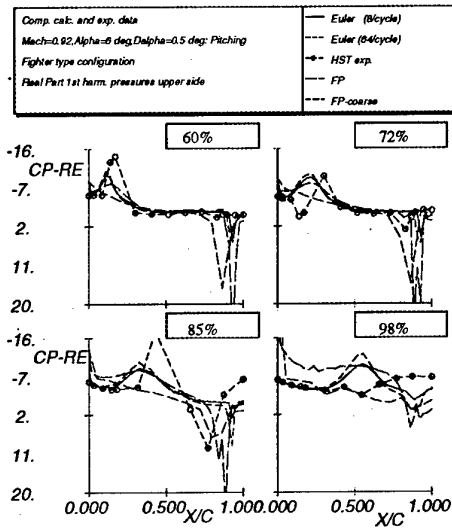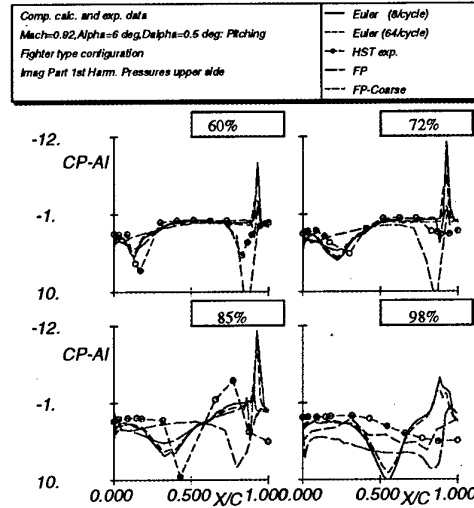Figure 9: Mean pressure contours (EE) on fighter-type configuration at $M_\infty = 0.92, \alpha_m = 6.0$ deg.

Figure 10: Comparison of experimental and calculated mean pressure distributions on the wing of fighter-type configuration at $M_\infty = 0.92, \alpha_m = 6.0$ deg.

- the generalized force.
- Also a combination of modal modes and/or the pressure or deformation data at selected points can be analyzed.

3.9 Monitoring and Postprocessing

Direct monitoring and analysis of all aeroelastic quantities of interest are of major importance to the user. The monitoring of the system is able to provide a graphical presentation of the deformations and pressure distribution on the configuration at selected time samples as well as the mean steady pressure distribution and its first harmonics over a selected time interval. Furthermore, the monitoring is able to provide the dynamic response of integrated loads as lift and moment coefficients for complete configurations as well as individual components. Also the pressure coefficients might be compared with:

- Pressure coefficients generated at a different time or iteration index which is important for checking convergence.
- Pressure coefficients generated in a different session which is important for checking different modellings (e.g. FP against EE).
- Arbitrary reference pressure (experimental) coefficients during the simulation which is important for identification. The volume spline method is used to interpolate the arbitrary data to the aerodynamic surface grid.

When the aeroelastic equations are solved for several flow conditions (variable Mach numbers, angles-of-attack, amplitudes and frequencies of oscillation) facilities are available to monitor and predict the derivatives of the unsteady airloads in that range and to estimate the critical flutter speed.

Attention has been paid to provide the user with 2-D and 3-D plot and analysis facilities to inspect and analyze all aeroelastic quantities of interest during the simulation. At any time the user may interrupt the program for the analyses and inspection of the data. Again this strongly reduces the workload of the aeroelastician who is not directed to other programs for visualization. The visual output includes screen output and off-plot PostScript output.

Except for the mean and first harmonic components of the aforementioned data which is only available after finishing a complete period of a harmonic motion, the data may be required by the user at any time or iteration step.

3.10 Inspection: Screen and PostScript plots

Two kinds of visualization tools are available:

- A 2-D facility for plotting collections of 2-D abscissa-ordinate plots gathered on one screen or on multiple screens.
- A 3-D facility for plotting collections of 3-D surfaces with contour plots and/or vector plots on one screen or on multiple screens.

The facilities may be used to plot the aforementioned quantities depending on the type of simulation. The plots can be stored in color PostScript format (using the special options in the interactive plot facility or using screen dump techniques in combination with other plot facilities.

Figure 11: Comparison of experimental and calculated first harmonic pressure distributions (real part) on the wing of fighter-type configuration at $M_\infty = 0.92, \alpha_m = 6.0$ deg, $\alpha_{amp} = 0.5$ deg and $k = 0.16$.

Figure 12: Comparison of experimental and calculated first harmonic pressure distributions (imag. part) on the wing of fighter-type configuration at $M_\infty = 0.92, \alpha_m = 6.0$ deg, $\alpha_{amp} = 0.5$ deg and $k = 0.16$.

3.11 Applications

The applicability of the method is directed to 2-D airfoils, 3-D wings, 3-D wing-bodies, T-tail, etc. Many applications of the simulation method were already presented in references [5, 6, 19]. The examples here will focus on current ongoing activities in 3-D to demonstrate the status of the aeroelastic environment. Two applications will be considered. The first one deals with a fighter-type configuration and the second one with a transport-type T-tail fuselage configuration.

3.11.1 Fighter-type aircraft

In view of the development of time-accurate aerodynamic solvers the ability of the aeroelastic simulation system to deal with fighter-type aircraft (Fig. 2,3) is considered. The complete geometry from ICEM-CFD was processed by **FOLDIT**, in order to obtain a surface grid. The surface grid initiates then the volume grid (Fig. 8). The surface grid should fulfil the requirements to investigate the requested aeroelastic phenomena. This means that tailoring of surface and field grid generation may play an important role.

Running the process to manipulate or tailor the geometry the volume spline interpolation technique [7] has shown to be of invaluable value. This interpolation technique, which may be applied for both structured and unstructered data in general, is demonstrated here for the elastomechanical data transfer between the structural grid and the aerodynamic surface grid.

A NASTRAN finite element model is available from which the symmetric vibration modes and structural grid for a typical fighter-type configuration of the con-

sidered aircraft were obtained. In total 679 structural points were applied (Fig. 4). An existing surface grid containing 43 support surface patches (Fig. 3) was used to perform the interpolation.

Results are shown in figures 5,6 of an arbitrary symmetric vibration mode (5th). The figures show the outlines of the patches, the displacement vectors at the outlines and contour values of the absolute displacement vector normal to the surfaces. The result of the same symmetric vibration mode obtained with the "standard chain" of computational flutter tools has also been presented in figure 7, which was calculated with a 2-D surface spline technique. It appears that the results shown in figures 5,6 agree well with the result represented in figure 7. Interpolations for other vibration modes demonstrate comparable results as well. More details of interpolation applications are discussed in [7].

Recently the TLNS methodology has been embedded as mentioned in section 3.3. The applicability of the time-accurate TLNS method is demonstrated by comparing calculated data with experimental data for a realistic fighter-type configuration oscillating in pitch at 56.8 % of the root chord with an amplitude of 0.5 deg. The case considered is a transonic flow condition at $M_\infty = 0.92$ and $\alpha_{mean} = 6.0$deg. The reduced frequency $k = 0.16$ based on the semi-mean aerodynamic chord corresponding with a frequency of $f = 4.5$Hz for the real aircraft. Because the robustness of the code for small and large time steps will be shown, only EE results are considered, since from accuracy reasons these allow the largest time steps to be taken. Experimental data are obtained from [3, 20].

Figure 8 shows a mesh with about 200,000 points
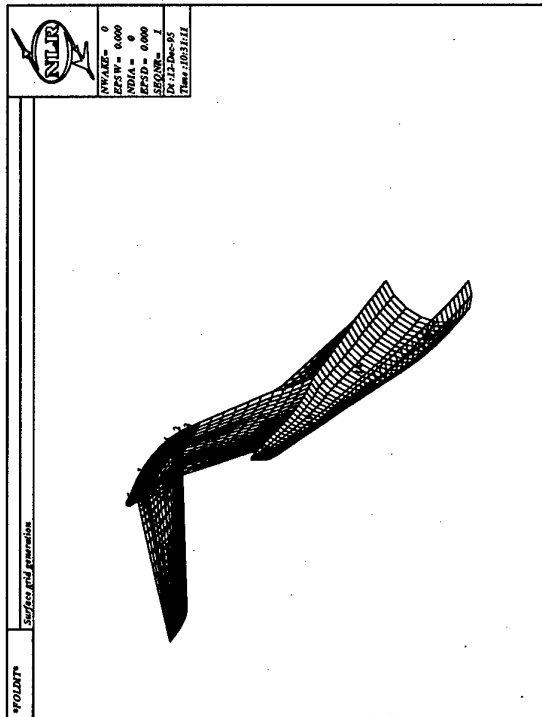
Figure 13: T-tail configuration.

Figure 14: Steady pressure distribution (FP) on horizontal tail.

around the configuration. The inlet of the engine has been smoothed. All results were obtained using FP (fine and coarse grid) and EE equations. Figure 9 shows the mean pressure contours (EE) on the surface of the aircraft. The comparison of the pressure on the upper surface of the wing between the present results (EE,FP) and the experimental data is presented in figure 10. The overall agreement is good except at the shock and tip region. The latter may be explained by the fact that the experimental result was obtained using a wind tunnel model having a tip-launcher, while the present calculation was carried out without one. The shock which is too strong may be improved by using the NS equations. Note that the FP calculations both on a fine and on a coarse grid show fairly well results, espacially those on the coarse grid perform well except near the tip span station.

Figures 11,12 show the real and imaginary part of the first harmonic pressures (EE,FP) on the upper surface of the wing compared to the experimental results. Two runs were made for the EE calculations employing small time steps (64/cycle) and large time steps (8/cycle). Except for peak values the small time step results as well as the large time step results show a good agreement with the experimental data. Details of the EE calculations are further discussed in [10].

Again the FP calculations both on a fine and on a coarse grid present fairly well results, except for the peak values. In general it can be concluded that the coarse grid does not have sufficient resolution for a detailed descrip-

tion of the unsteady flow, but if one is only interested in a global impression of the flow field and an estimate of hysteresis effects then a coarse grid can be sufficient for a first impression.

3.11.2   T-tail-fuselage

In order to demonstrate the ability of the system to deal with existing aircraft structures the transport-type T-tail fuselage configuration has been chosen (Fig. 13), as discusses in [6]. It should be noted that no parts of the geometry were omitted. The complete geometry from ICEM-CFD was processed by FOLDIT, in order to obtain a surface grid. The surface grid initiates the volume grid of which characteristic grid planes are shown in reference [6], which shows also the ability of the grid generator to deal with strongly swept wings and non-uniform distributions.

For the grid 67x30x33 nodes were applied. Figure 14 shows the steady pressure distribution (FP, $M_\infty = 0.84$) on the horizontal tail. From top left to bottom right pressure distributions at different spanwise stations from root to tip are depicted. A considerable transonic flow effect is apparent.

As an example the second mode shape of the T-tail configuration is shown in figure 15. Unsteady calculations (FP aerodynamics) were performed at $M_\infty = 0.84$ and zero altitude in Standard Atmosphere. The elasto-mechanical model consisted of the first ten vibration modes, obtained with MSC/NASTRAN FEM method.
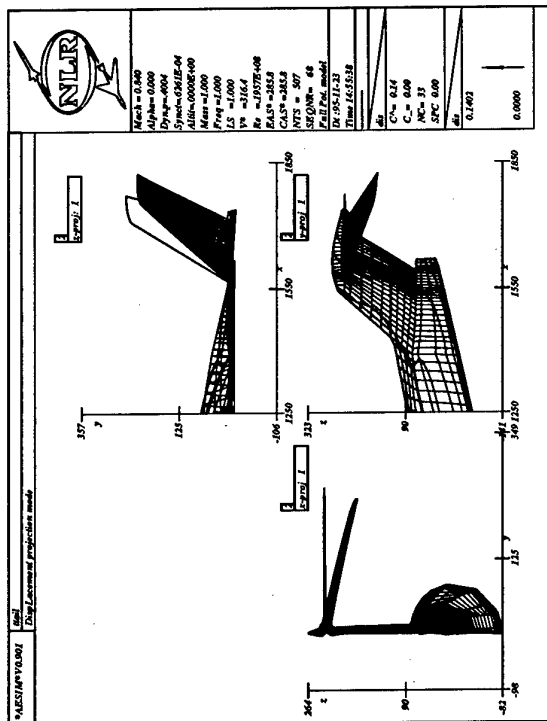
Figure 15: Second mode shape of T-tail configuration.

Figure 16: Result of a T-tail configuration of dynamic response of generalized coordinates at $M_\infty = 0.84$ and altitude 0.0 ft in Standard Atmosphere.

The generalized coordinates of each individual mode were calculated in time as a result of a non-zero initial value for the acceleration of the generalized ccoordinate. The result of the simulation is shown in figure 16. In figure 17 the time response data is evaluated through exponential sine fit signal processing [11] to get damping and frequency information. The exponential sine fit results compare well with the simulated data.

The results of these simulations confirm that the T-tail has a stable dynamic behavior for the flight condition under consideration. This is in accordance with the MSC/NASTRAN flutter diagram [6].

4. CURRENT RESEARCH ACTIVITIES

In this section a number of current research activities are discussed, viz. the subjects:

- MIMO class research
- TLNS+ research
- Linear aero research
- LCO simulation system

4.1 MIMO research

To analyze the many time response signals a number of methods have been embedded (see section 3.8). Very recently a feasibility study has been started to apply the promising MIMO-class techniques [21] for that purpose too. They will enhance the analysis capability as depicted in figure 18.

Experience has learned that for a fail safe analysis of an

elasto-mechanical system the mentioned fitting routines are applied first to the non-aerodynamically loaded system and next to the system loaded using linear aerodynamics [22], through convolution of transfer functions, [23]. The data from these analyses might act as a guideline for the analysis of the non-linear time signal, originating from the coupled non-linear fluid structure simulation. The analysis process has been fully automated through use of scripts. This facility allows the analysis process to be repeatible and to be documented.

It should be noted that also the analysis might provide a prognostic way to speed up the simulation by allowing for larger time steps [10].

The adoption of **MIMO** technology [21] permits a black box [2] evaluation of the aeroelastic system in such a way that after a single fully-coupled simulation for one flight condition the system state for other flight conditions (e.g. q_{dyn}) might be predicted and to extract useful data (e.g. Generalized Forces) from the coupled simulation which can be used for other purposes.

The main purpose is to extend the single point application of coupled simulation methods to multiple points and wayhead is given to perform postprocessing activities, pk-, k-method etc, with extracted data from an application of a fully-coupled simulation. This multi-point strategy is explained in the figures 19,20 and further

---

[2]No knowledge is assumed of coefficients of the structural and aerodynamic system.
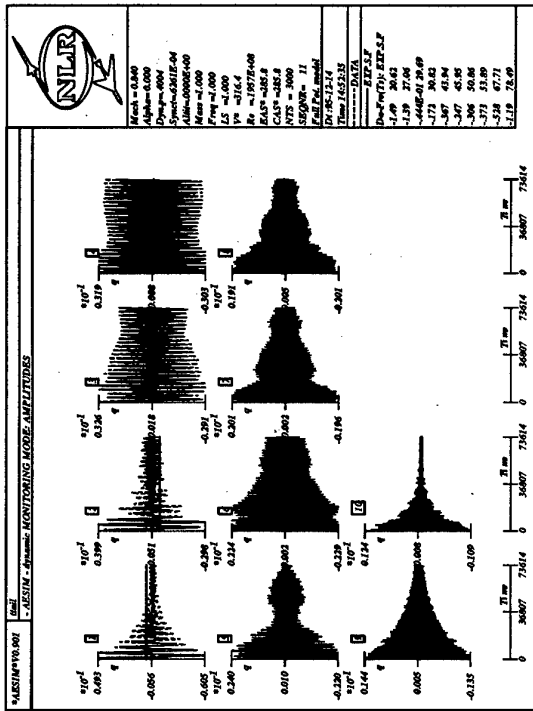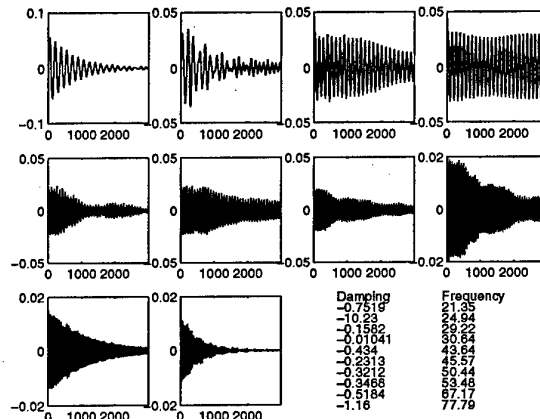
Figure 17: Result of a T-tail configuration after exponential sine fit signal processing of dynamic response of generalized coordinates at $M_\infty = 0.84$ and altitude 0.0 ft in SA.

described in [21]. A slightly different model structure MIMO* includes auto regressive terms on the outputs. Two examples here focus on current ongoing MIMO activities [11] with respect to the time-analysis and demonstrate the status of the aeroelastic environment too.

4.1.1 AGARD I-wing 445.6

The first example of the applicability of the MIMO-class techniques, in this case the modified MIMO* method, in flutter analysis is presented for an aeroelastic investigation which was conducted for one of the 3-D AGARD standard aeroelastic configurations in subsonic, transonic and supersonic flow. This configuration is described in [24]. The configuration for dynamic response I-wing 445.6 model "weakened no. 3" was selected at Mach=0.901. The data were obtained from [10].

The data (generalized forces) as obtained from simulation with the identified MIMO* model, together with the original data for subcritical flight condition are presented in figure 21. The data has been plotted for time points after the transition has damped out. An excellent agreement is shown between both data sets (they conincide entirely!).

The main purpose of the excercise will be a simulation, at an increased airspeed to a supercritical value, applying the MIMO* results obtained from the subcritical
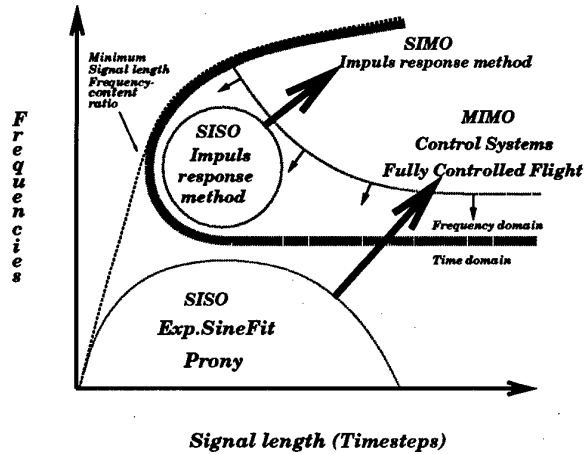
Figure 18: Deployment time-analysis methods with respect to aeroelastic systems.
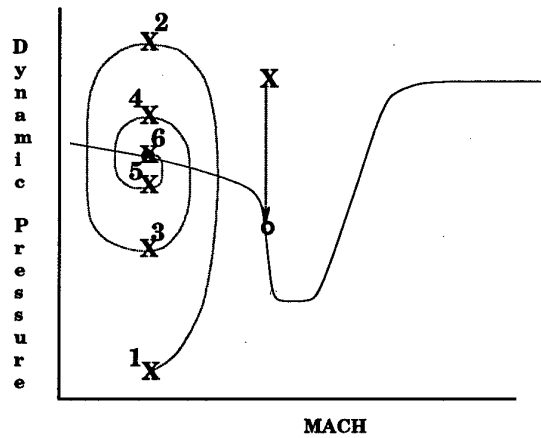
Figure 19: Multi-point strategy.

condition and make the comparison with results of the aeroelastic simulation at the higher airspeed. Figure 22 depicts the comparison which shows that the system at the supercritical airspeed is unstable and that the linear MIMO* model prediction performs very well for the lower 3 modes. Mode 4 is overpredicted.

Slightly larger errors were found with the MIMO model, i.e. without the auto regressive terms [11]. Which model set results in the best estimates for aerodynamic modelling in aeroelastical closed-loop systems is yet to be investigated.

4.1.2 T-tail-fuselage

The second example to demonstrate the ability of the MIMO-class techniques deals with the transport-type T-tail fuselage combination, which was already considered in section 3.11.2. The conclusion was that the exponential sine fit results (Fig. 17) of the time signals compare reasonably well with the simulated data (Fig. 16). Results with the MIMO-class procedure are depicted in figure 23. The MIMO-class fit results are
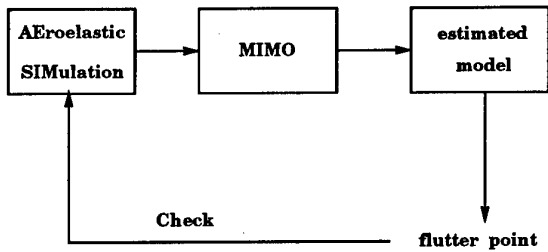
Figure 20: Flowdiagram multi-point strategy.
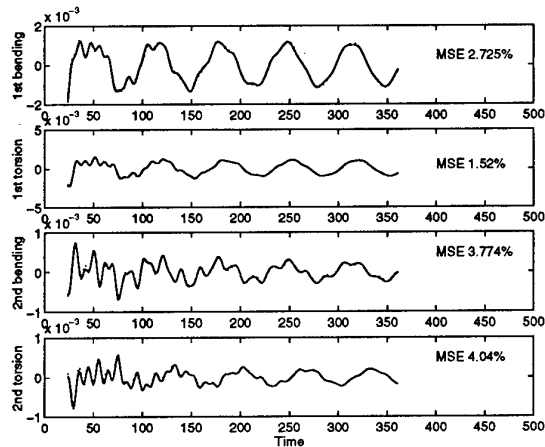
Figure 21: Comparison of MIMO* fitted (...) with auto regressive terms on outputs and original (-) generalized forces data for AGARD I-wing 445.6 at subcritical flight condition.

astonishingly good. Both methods revealed about the same damping and frequencies. The results of these simulations show again that the T-tail has a stable dynamic behavior for the flight condition under consideration.

4.2 TLNS+ research

Transonic aeroelastic investigations of modern aircraft put increasingly higher demands on the accuracy of predicting unsteady aerodynamic loads and aeroelastic characteristics. Methods for numerical aeroelastic simulations have joined, in which the aerodynamics and structural dynamics are considered simultaneously and so provide an integrated approach for the multidisciplinary aeroelastic problems. A central question is the affordability of of these methods at various levels of pratical applications. It is evident that opinions about affordability depend on local needs conditions and appreciations. It is also clear, however. that answering this question should be based on a thorough insight into potential gains in efficiency and robustness of these methods. The exploration of these gains is a research topic in which Delft university of Technology (DUT) and the National Aerospace Laboratory (NLR) in Amsterdam cooperate.

The outcome of that research so far has been presented
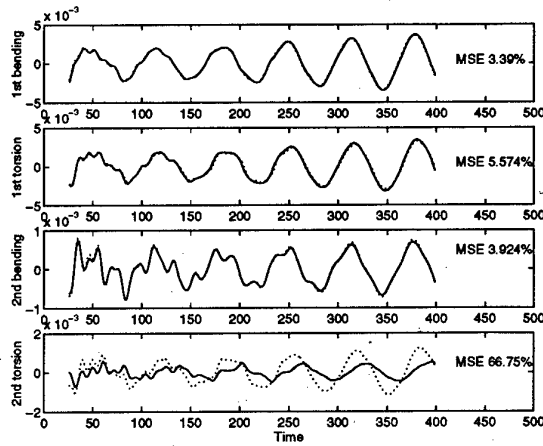
Figure 22: Comparison of MIMO* predicted (...) and reference (-) generalized forces data for AGARD I-wing 445.6 at supercritical flight condition.

Figure 23: Result of T-tail configuration after MIMO signal processing of dynamic response of generalized coordinates at $M_\infty = 0.84$ and altitude 0.0 ft in SA.

in [8, 9, 10] for 2-D and 3-D CUA and CAS methods using EE and TLNS solvers. One of the main features of these solvers is the development of a robust efficient upwind implicit time-marching algorithm for time-accurate TLNS equations, employing subiterations, espaciallly directed to the aeroelastic analysis in viscous transonic flow. The purpose of using subiterations is to accelerate steady-state convergence and to permit a large time step in time-accurate simulations, thereby reducing the computational cost, while maintaining adequate accuracy. Further details are discussed in [8, 9]. The ability of the method was demonstrated for many cases, including cases of inherently unsteady flow due to shock-induced separation. Considered 3-D cases were: 1) ONERA M6 wing, 2) Fighter-type wings and 3) LANN wing.

Important observations related to pratical aeroelastic

simulations concluded in [9] were:

- Accurate results have been generated applying not more than 24 and 48 time steps per period for the EE and the TLNS applications, respectively. In that perspective again attention is devoted to the calculation results with EE equations employing small time steps (**64/cycle**) and large time steps (**8/cycle**) for a fighter-type configuration (see section 3.11.1 and [9]).
- The methods turned out to be very robust and the only principal user-supplied numerical parameter for an unsteady calculation is the time step.
- The comparison with experiments demonstrated the superiority of the TLNS method over the inviscid methods for cases involving thick wings.
- The 3-D methods have turned out to be about a factor $\mathcal{O}(5)$ to $\mathcal{O}(15)$ slower as compared ta a time-accurate FP method for the inviscid and the TLNS applications, respectively. This makes them affordable for embedding in an aeroelastic simulation environment.
- *Since the stability restriction to the time step of the components of the aeroelastic simulation have been strongly relaxed, the next goal is to improve the coupling of the aerodynamic and structural equations.*
- Also it seems to be appropriate now to improve on the turbulence modelling.

Related to the above-mentioned observations a number of current research subjects and/or subjects, which need continously attention, are discussed and illuminated with some applications. These subjects are:

- Applications of the current TLNS method
- Time-step reduction in CUA applications
- Time-step reduction in CAS applications by:
  - Higher order extrapolation methods
  - Prognostics using Time Analysis Methods (TAM)
- Turbulence models:
  - Baldwin-Lomax
  - Sparlat-Allmaras

4.2.1. Semi-span straked delta wing

To investigate the efficiency and robustness of the current TLNS code the applicability is further demonstrated by comparing calculated data with experimental data of the NLR wind tunnel test described in [25] for the semi-span straked delta wing. The geometry of the outer wing panel is the same as that of the fighter-type configuration discussed in section 3.11.1. The flow condition is $M_\infty = 0.90, \alpha_m = 6.0$ deg. Steady calculations have been performed with the EE mode of the TLNS code [9] on a mesh of 97×125×30 grid points.

Figure 24 shows the planform and steady isobar contours at the upper side of the wing with total pressure contours behind the wing. Clearly visible are the vortices initiated by the simple strake and the tip of the outer wing panel. Measured mean pressure contours at the same flow conditions are presented in figure 25.

A qualitative comparison of the pressure contours (Figs. 24,25) on the upper surface at the indicated wing stations of the outer wing panel shows a fairly well agree-

ment, in particular the presence of the lambda shock waves near the tip [3].
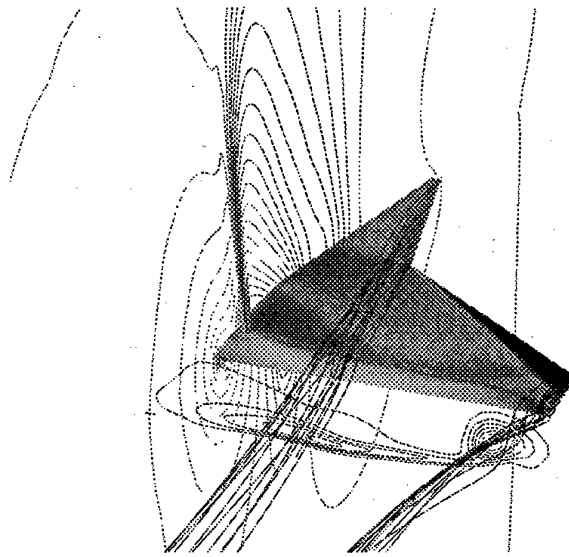
Figure 24: Steady pressure contours (EE) on a semi-span straked delta wing configuration with total pressure contours behind the wing at $M_\infty = 0.90, \alpha_m = 6.0$ deg.
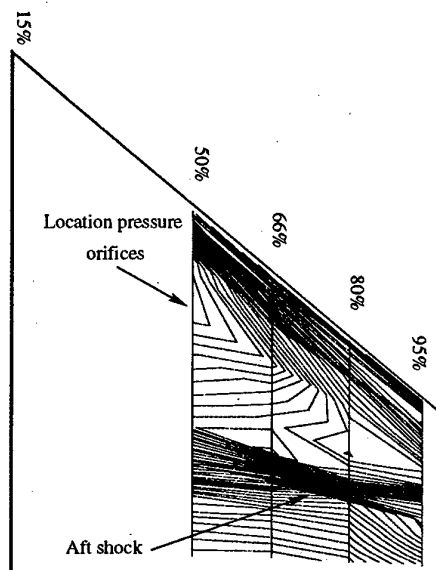
Figure 25: Measured mean pressure contours on a semi-span straked delta wing configuration at $M_\infty = 0.90, \alpha_m = 6.0$ deg.

---

[3]Quantitative comparisons and results for oscillating conditions in pitch will be presented in a forthcoming publication.

4.2.2 LANN wing

To verify the current TLNS method for 3-D steady and unsteady applications with moderate viscous and transonic effects for cases involving thick wings the LANN wing was selected in [9]. The superioty of the TLNS method over the inviscid methods for the LANN wing was clearly demonstrated. Because of the superioty of the TLNS method and future applications for fighter-type aircraft the results are presented again.

The geometry of the wing has been taken from [26]. The experimantal data is obtained from [27]. Extensive comparison of calculated FP data with experimental data was already performed in [28].

Calculations and comparisons were made for pitching oscillation about 62.1% root chord at $M_{infty} = 0.822, \alpha_m = 0.6$deg and $Re_\infty = 7.3 \times 10^6$ based on root chord. The amplitude of oscillation was 0.25 deg, with a reduced frequency $k = 0.102$ based on root semi-chord. The dimension of the grid was 128×32×24 for the inviscid case and 128×32×36 for the viscous case. The same surface grid was used in both cases. For the turbulence modelling the simple Baldwin-Lomax algebraic model was applied.

Comparison of the mean pressure distributions is shown in figure 26 at selected span stattions. The Euler results show already a substantial offset to the experimental data, even at the lower side. The TLNS data are in fairly good agreement with the experimental data for the whole wing at both sides for both shock positions and peak suction levels at the leading edge. Note that the FP results approximate good the Euler data.

Unsteady first harmonic pressure coefficients are compared in figures 27, 28. The EE results were generated with 24(12) time steps per cycle and TLNS results were obtained using 48(16) time steps per cycle.

The lower side shows, except at the root, a subsonic distribution. The upper side shows clearly the effect of the lamda shock waves. Except for peak values the real part of the data is predicted fairly well by the TLNS method. The Euler data show too much differences.

The agreement for the imaginay part of the data is less adequate at both sides. Aft of the shock wave the TLNS method performs better. In front of the shock wave the Euler data seem to compare better.

In general, is has to be concluded that a fairly good agreement has been achieved. Part of the differences between calculated and experimental data should be attributed to the deformation of the wind tunnel model during wind-on conditions and the added complication of peak measurements and integration in the experiment.

4.2.3 Time-step reduction in CUA

In view of the development of a robust and an efficient algorithm for time-accurate TLNS equations to obtain a realistic and affordable simulation system an earlier application discussed in [8], will be reconsidered, viz. the 2-D AGARD standard test case for transonic viscous
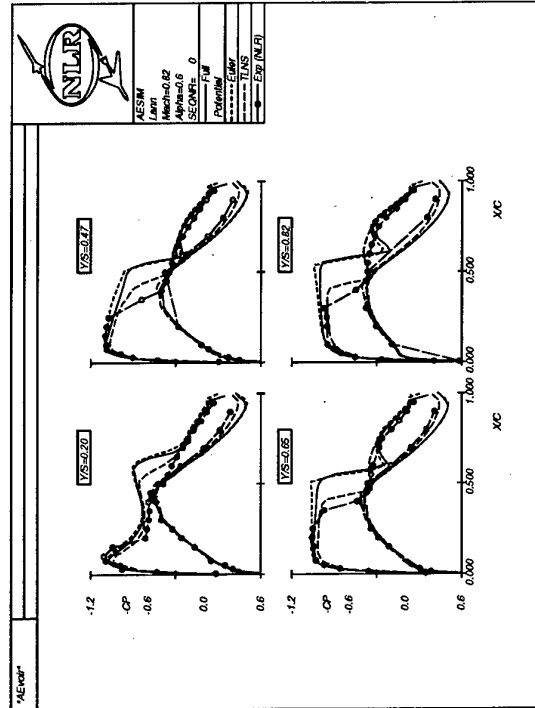
Figure 26: Comparison of experimental with FP, EE and TLNS calculated mean pressure coefficients on LANN transport-type wing, $M_\infty = 0.82, \alpha_m = 0.6$ deg and $Re_\infty = 7.3 \times 10^6$.

flow (case 3 of Landon [27]). The flow conditions are $M_\infty = 0.60, \alpha_m = 4.86$ deg , $Re_\infty = 4.8 \times 10^6$ and the boundary layer is fully turbulent. The mode of vibration is a pitching oscillation of the NACA 0012 profile about quarter-chord with an amplitude of 2.44 deg and a reduced frequency $k = 0.081$ based on semi-chord.

In [8] the computational efficiency of the code for the current case was demonstrated for several variations of the iteration parameters, i.e. time steps/period, subiterations and Jacobian recalculations, thereby applying 2nd order extrapolation.

Comparison of calculated sectional coefficients, C_l and C_m (Fig. 29) for variety of time step simulations reveals that larger time steps/period for 3rd order extrapolation could be obtained, thereby reducing the computational cost, while maintaining adequate accuracy. Four cases of calculated results have been presented for high (400) to very low number (16) of time steps/period in combination with 4 and 12 subiterations, respectively. The lift coefficient shows a very good agreement. The moment coefficient shows a more sensitive behavior. Some differences are apparent, but the extremities appear to be captured well enough by all the cases. For this particular viscous test case it seems that 16 time steps with 12 subiterations is sufficient.
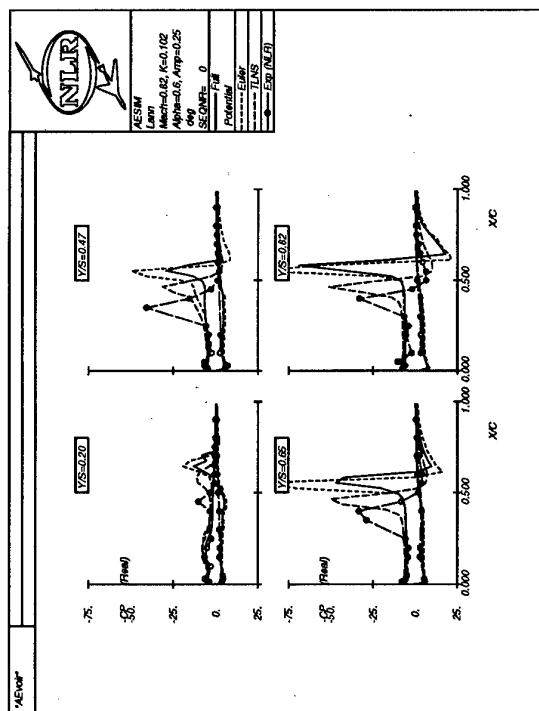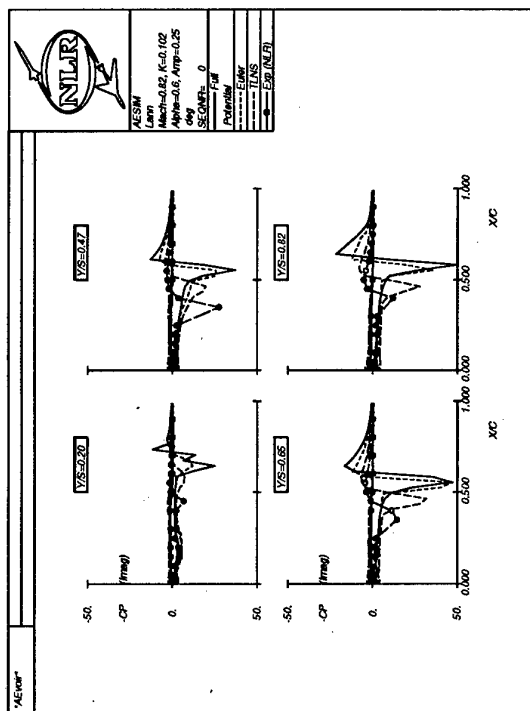
Figure 27: Comparison of real part of experimental with FP, EE and TLNS calculated first-harmonic pressure coefficients on LANN wing at $M_\infty = 0.82, \alpha_m = 0.6$ deg, $\alpha_{amp} = 0.25$ deg and $k = 0.102$.

Figure 28: Comparison of imag. part of experimental with FP, EE and TLNS calculated first-harmonic pressure coefficients on LANN wing at $M_\infty = 0.82, \alpha_m = 0.6$ deg, $\alpha_{amp} = 0.25$ deg and $k = 0.102$.

4.2.4 Extrapolation methods in CAS

Driven by the requirement of realistic aeroelastic simulations, special attention is devoted not only to a proper modeling of the physics but also to their efficiency and robustness. Consequently, an important practical aspect is the capability to march accurately at a large time step, thereby reducing the overall turn-around time. However, this implies that all components of the simulation methodology should possess a **large time step** capability.

Therefore, an improvement of the aero-structural coupling procedures is necessary to benefit from the large time step allowed by the current aerodynamic methods, shown earlier. In [10] two coupling methods have been studied: an improved aerodynamic extrapolation method and a structural extrapolation method. Also a third one is introduced: the prognostic method. The latter is an extension of the structural extrapolation method and uses results of the time analysis to guess the new states. The three coupling approaches have been presented in detail in [10], therefore the main features will be discussed briefly and exemplified with a few applications.

In general the equations of motion for the aeroelastic system can be written into a standard state-space form as:

$$\dot{X} = AX + BU \tag{1}$$

A standard method [10] can be used to solve Eq.1:

$$\begin{aligned} X^{n+1} &= \Phi X^0 + \int_0^{t(n+1)} \Phi(t - \tau)BU(\tau)d\tau \\ &\approx \Phi(\Delta t)X^n + \Theta(\Delta t)\bar{U}, \end{aligned} \tag{2}$$

where $\bar{U}$ is a representative value of the aerodynamic force $U(t)$ between time levels (n) and $(n + 1)$. Calculation of Φ and Θ are described in [10]. This commonly used loosely coupled method was originally suggested in [29], where the aerodynamic force $U\langle t\rangle$ is assumed to vary linearly between time steps (n) and $(n + 1)$. The aerodynamic force at time level $(n + \frac{1}{2})$ is then extrapolated as:

$$U^{n+\frac{1}{2}} \approx \frac{3}{2}U^n - \frac{1}{2}U^{n-1}. \tag{3}$$

This value is used to represent the value of U between time step (n) and $(n+1)$. This method fails, however, to give good results for large time steps simulations. Two approaches are studied to improve the method:

Aerodynamic extrapolation

The aerodynamic force is expressed as:
$U = U(Q, X)$ and the extrapolation to time level $(n + \frac{1}{2})$ is:

$$U^{n+\frac{1}{2}} \approx U^n + \left(\frac{\partial U}{\partial Q}\frac{\partial Q}{\partial t} + \frac{\partial U}{\partial X}\frac{\partial X}{\partial t}\right)\frac{\Delta t}{2}. \tag{4}$$
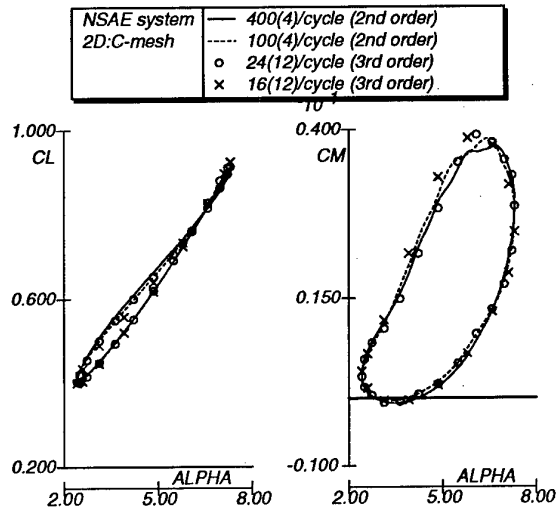
Figure 29: Comparison of sectional coefficients, C_l and C_m for variety of time step simulations, during oscillatory pitching motion of NACA 0012 profile at $M_\infty = 0.60, \alpha_m = 4.86$ deg , $Re_\infty = 4.8 \times 10^6, \alpha_{amp} = 2.44$ deg and $k = 0.081$.

where Q is defined by the TLNS equations [10]. The $\partial Q/\partial t$ and $\partial X/\partial t$ are readily available data while $\partial U/\partial Q$ and $\partial U/\partial X$ have to be calculated.

Structural extrapolation

The reason for this method is the fact that the structural part behaves smoother than the aerodynamic forces. Thus a better result may be expected from extrapolating the structural state. To obtain the aerodynamic force at time level $(n + \frac{1}{2})$, the state of the mesh is first approximated as:

$$X^{n+\frac{1}{2}} \approx X^n + \dot{X}^n \frac{\Delta t}{2}. \qquad (5)$$

The $\dot{x}$ in the second term is readily available while the $\ddot{x}$ is approximated simply as $(\dot{x}^n - \dot{x}^{n-1})/\Delta t$. Using this data a mesh is generated and the surface velocity is used to enforce the boundary condition. Thus the aerodynamic part of the method marches at a time level between the structural states. This method is more efficient than the first one since all quantities needed for extrapolation are readily available or can be easily calculated.

To show the applicability of the improved extrapolation methods for large time step simulations a forced vibration case [10] of the 3-D configuration for dynamic response I-wing 445.6 model *weakened no.3* is presented. Only calculation results with EE are shown. The applied grid consists of $121 \times 29 \times 24$ mesh points. The case at $M_\infty = 0.96$ is considered. The second mode of the wing is excited in a sinusoidal motion with reduced frequency $k = 0.10$, based on root semi-chord, and an amplitude of 0.005. Figure 30 shows the response of the first two vibration modes using a small time step (48
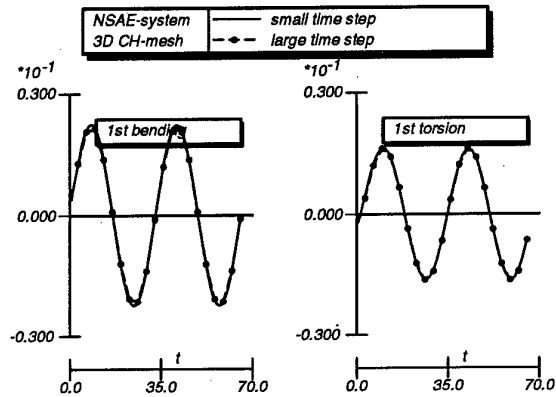
Figure 30: Comparison of time responses between small (48/period) and large (10/period) time step simulations for improved aerodynamic extrapolation method, for AGARD I-wing 445.6 at $M_\infty = 0.96, \alpha_m = 0.0$ deg, $amp = 0.005$ (2nd mode) and $k = 0.10$, during forced vibration.
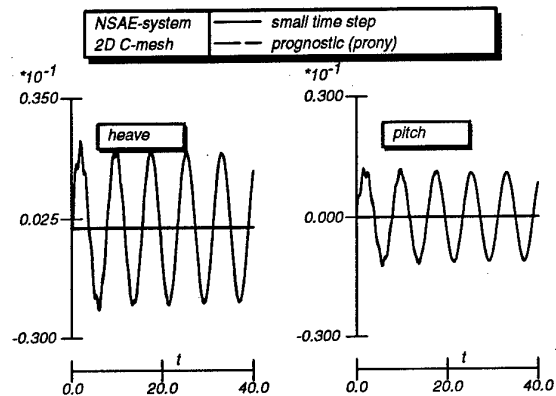
Figure 31: Comparison of time responses between small (32/period) and large (8/period) time step simulations for the prognostic method, employing Prony's method, on Isogai case A at $M_\infty = 0.85$.

steps/period) and a large time step (10 steps/period). The conclusion is that no significant differences are observed. Other applications have been demonstrated in [10].

Finally a prognostic method is proposed, which is discussed in the next section.

4.2.5 Prognostics using TAM in CAS

The prognostic method proposed in [10] which is a refinement/generalization of the previous extrapolation methods and mightbe regarded as a higher-order extrapolation using transfer functions. In each time step the structural or aerodynamic part is extrapolated to the next time level by:

$$X^{(n+\frac{1}{2})} \approx P\left(X, U, n + \frac{1}{2}\right) \text{ or}$$

$$U^{(n+\frac{1}{2})} \approx P\left(X, U, n + \frac{1}{2}\right)$$

Here $P(\#, t)$ denotes the approximation of time trace $\{\#_n, \#_{n-1}, \ldots \ldots, \#_{n-m}\}$ at t which should be obtained by performing one of time analysis methods (**TAM**) presented in [10], m denotes the number of retarded time steps in the time domain. It will be obvious that as soon as the function P is not changing anymore the simulation can be finished since the following time steps will not present any new additional information. In fact this means the time step is virtually infinite.

A 2-D aeroelastic application of the prognostic extrapolation method, discussed in [10], is presented for the NACA 64A010 airfoil using structural data from the Isogai case A [30]. The structural parameters are $a=-2.00$, $x_\alpha=1.80$, $r_\alpha^2=3.48$, $\mu=60.00$ and the ratio of the uncoupled frequency $\omega_h/\omega_\alpha=1.00$. The flutter boundaries of this case, compared to some other methods, have already been shown in [8]. The result presented here will concentrate on the large time step aspect of the method. A mesh consisting of 140×32 points was applied. Only application with EE equations will be presented. The simulation is started from a steady condition with an initial $\dot{x}$. The small time step simulation uses **32** time steps/period of the uncoupled mode while the large time step simulation applies **8** time steps/period.

The case considered is a subcritical condition at $M_\infty = 0.85$ with $V^\star = U_\infty/(\omega_\alpha b\sqrt{\mu}) = 0.53$. Comparison of simulation using small time steps and large time steps for the prognostic method, employing Prony's [11] analysis for the time traces is shown in figure 31. The results of both simulations show an excellent agreement, no differences are observed. The inadequacy of the common method [29] for large time step simulations of this case have been shown in [10].

4.3 Linear Aero Research

To ease applications and to build confidence a coupled aeroelastic simulation should also be run based on linear aerodynamics. This requires the generalized aerodynamic forces (transfer functions) which are in general available in the frequency domain to be fitted [23, 31] and transformed to the time-domain.

Figure 32 shows a number of possibilities to calculate the generalized aerodynamic forces together with the transformation tools to obtain transfer function representations of the loads for ease formulation in the time domain. The blocks in the four outer corners of the diagram are sources to calculated the aerodynamic forces. The three inner blocks around the kernel of the diagram, **transfer function**, are fitting procedures for the aerodynamic forces. These fitting procedures include: 1) Complex curve fit in s-domain, 2) Real fit curve in s-domain, and 3) MIMO-class techniques and Prony's method, which have been described in [11].

A feasibility study with 2-D airloads and 3-D airloads has been performed [11] to investigate the most efficient way to embed linear aerodynamics in the AESIM

method. Without the analytical details the procedure was as follows [11].

The assumption is made that the behavior of any unsteady parameter of interest such as an aerodynamic load or a pressure coefficient can be described by a appropriate form for the transfer function which is a ratio of two s dependent polynomials which is known as the Padé approximation. The complex fitting procedure has been assumed to obtain the approximation. The rational polynomial has been transformed to the state-space form. Subsequently, this system has been solved using the Newmark scheme embedded in the AESIM system. Two applications of the study will be presented, a 2-D case for a flat plate and a 3-D case of the AGARD I-wing 445.6.

2-D application Calculations of unsteady airloads have been performed with DOULAT for a flat plate heaving (mode 1) and pitching about an axis $0.5c$ in front of the leading edge (mode 2) at $M_\infty = 0.5$ and a reduced frequency range up to $\mid s \mid = 1.0$. (Note: The reduced frequency is defined here as $k = Im(s)$, based on the semi-chord.) The generalized forces data generated by DOULAT were fitted with the afore-mentioned procedure. Thereafter the Newmark scheme was applied to oscillatory motions in the same frequency range and the time traces were transformed to the frequency domain. Figure 33 shows the comparison in the frequency domain between the original data (circle) and the fitted data (line-cross) which show a good agreement. Figure 34 shows the comparison in the frequency domain between the original data (circle) and the data (cross) obtained by analysing the time traces which again show a good agreement. From this the conclusion might be drawn that the aforementioned procedure is applicable in 2-D.

3-D application Calculations have also been performed with GUL for the 3-D AGARD I-wing 445.6 at $M_\infty = 0.901$. This configuration is described in [26]. Again two modes were selected, modes 2 and 4. A similar procedure was applied as outlined above.

Figure 35 shows the comparison in the frequency domain between the original data (circle) and the fitted data (line-cross) which show a good agreement. Figure 36 shows a comparison in the frequency domain between the original data (circle) and the data (cross) obtained by analysing the time traces which shows again a good agreement.

From this the conclusion might be drawn that the aforementioned procedure shows good promise for embedding in the AESIM system.

4.4 LCO simulation system

Modern fighter-type aircraft operating in the high subsonic, transonic and low supersonic speed regime may experience under certain conditions transonic nonlinear flutter, known as limit cycle oscillations (LCO). The
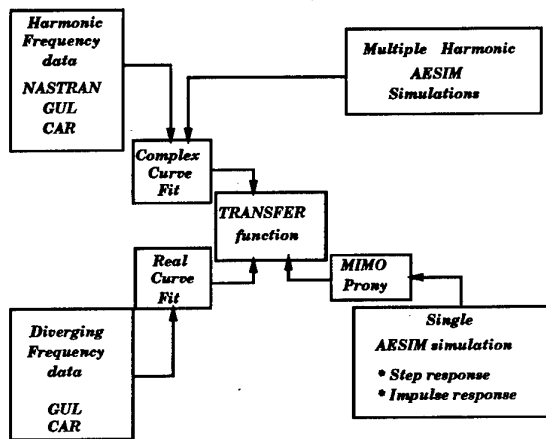
Figure 32: Flowchart of techniques for transforming linear aerodynamics between frequency and time domain.

Figure 33: Comparison of directly calculated and fitted unsteady coefficients of a harmonically heaving and pitching flat plate at $M_\infty = 0.5$.
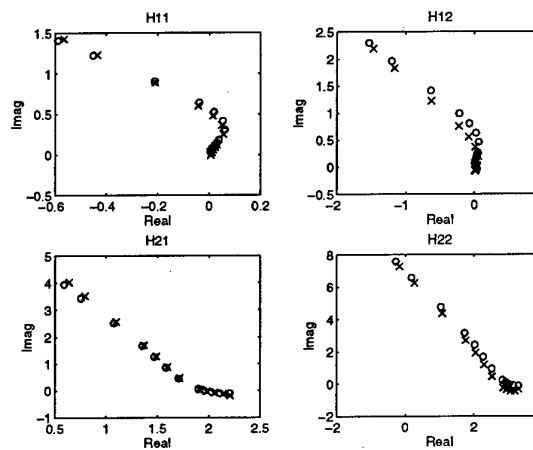

Figure 34: Comparison in the frequency domain of directly calculated and to and fro transformed unsteady coefficients of a harmonically heaving and pitching flat plate at $M_\infty = 0.5$.
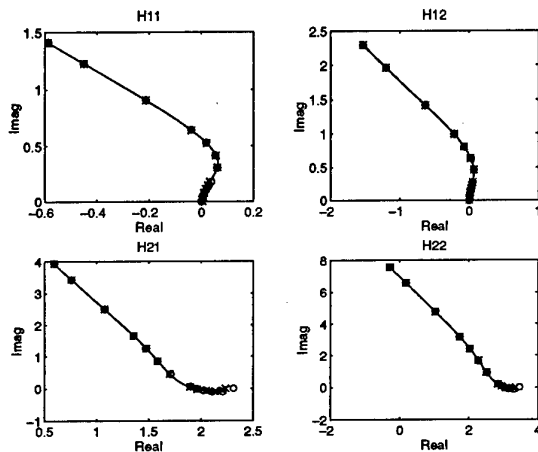
phenomenon is related to flutter but affects aircraft performance in a manner similar to buffet. Conditions of transonic LCO instabilities are moderate angle-of-attack, usually smaller than 10 deg and transonic Mach numbers ranging from ~ 0.9 to ~ 1.1. The flow conditions during this type of LCO are characterized by **mixed attached/separated flow**. Lowly damped vibration modes tend to respond provided they have the proper characteristics to couple with this type of flow. The coupling frequently occurs near flutter boundaries obtained with linear theory [14], i.e. with panel methods for attached flow.

To determine accurately this kind of nonlinear aeroelastic instabilities, an investigation was started at NLR in the early nineties to understand the nature of LCO experienced by fighter-type aircraft maneuvering at transonic speeds. In addition to conducting an extensive wind tunnel investigation on oscillating fighter type wings [3, 20, 32], a major objective was to develop a semi-empirical method for predicting LCO [12, 13, 15] characteristics of full scale aircraft.

As part of the method, a model for determining aerodynamic loads from steady and unsteady data bases was developed that is suitable for predicting LCO of fighter-type aircraft at transonic speeds. Based on previous studies using steady pressure data [32], it was shown that time lags in the aerodynamic flow field are essential to obtain realistic LCO amplitudes. Analysis of unsteady wind tunnel data obtained from [3, 20] showed that these aerodynamic time lags are affected by the various types of flow field involved. Further, on the basis of the knowledge of these flow field types and the results of the unsteady wind tunnel measurements, an aerodynamic (pressure) state-space model was developed by NLR, for transforming the unsteady highly nonlinear aerodynamic loads into a form appropriate for use in time simulation methods. This pressure model is similar to the nonlinear "ONERA" aerodynamic model initially developed by Tran & Petot [33]. The development of the NLR unsteady pressure model and capability of producing nonlinear transonic aerodynamics that are typical of transonic LCO were presented in [12, 13, 15]. It was also demonstrated for a number of aircraft configurations [12, 13, 15] that the current status of the semi-empirical LCO prediction method with implementation of the NLR unsteady pressure model produced results which correlate correctly with flight test data.

The above description of the NLR pressure model shows that extensive use is made of steady and unsteady wind tunnel test data. It is clear that the effectiveness and reliability of the model strongly depends on the completeness of the experimental data base and the thoroughness of the evaluation of the model. These, however, have been obtained on a limited scale in the present re-
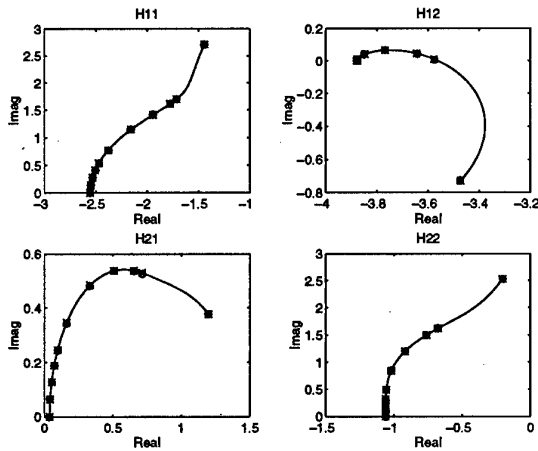
Figure 35: Comparison of directly calculated and fitted unsteady coefficients of the harmonically oscillating AGARD I-wing 445.6 at $M_\infty = 0.901$, (modes 2 and 4).
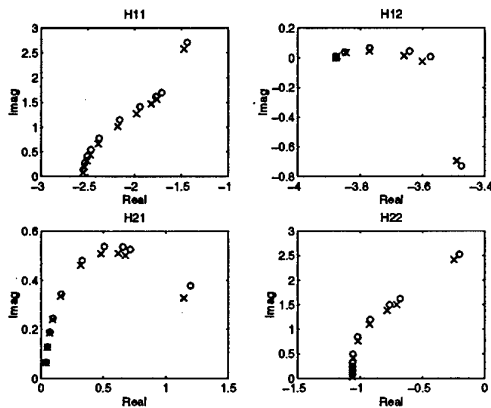
Figure 36: Comparison in the frequency domain of directly calculated and to and fro transformed unsteady coefficients of the harmonically oscillating AGARD I-wing 445.6 at $M_\infty = 0.901$, (modes 2 and 4).

search program. Continued research is therefore needed to enhance the confidence in the model and to establish its applicability for wide ranges of model and flow parameters. Such research may be defined in one or more of the following directions.

• Continued pressure and load measurements in the wind tunnel.

The aim of this test is to extend the unsteady part of the data base, which currently corresponds to a limited number of model and flow parameter values, and so to bring it in balance with the steady part [32] of the data base, which corresponds to an extensive set of parameter values. Particularly, interest exists in collecting data for more leading-edge and trailing-edge flap deflections and denser frequency ranges (e.g. frequency sweeps). In the

test use can be made of the existing wind tunnel model.

• Application of CUA/CAS.

CUA For model configurations and flow conditions which have not or can not be represented in a wind tunnel test program the required aerodynamic information may be obtained from CUA-techniques, steady and unsteady. The current development of these techniques shows that they are very promising, even for the complicated types of flow including flow separation (see sections 3 and 4), but that they have matured more sufficiently. It is to be expected that in the near future these CUA-techniques may play a complementary role. Measured steady and unsteady pressure and loads data [3, 20, 32] may be used to validate those techniques.

CAS Extensions for typical fighter-type aircraft applications of the discussed **AESIM** system to perform realistic computational aeroelastic simulations. Because of the modular design of the system, such extensions should be carried out relative easy. Measured flight test data may be used to validate the updated AESIM system. Further, calculated aeroelastic responses may be compared with results of the semi-empirical prediction method, or vice-versa.

Realisation of the suggested extension of the AESIM system will enhance the aeroelastic analysis capability for fighter-type aircraft as depicted in figure 37.
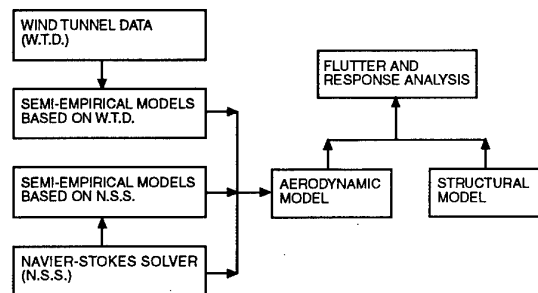
Figure 37: Classification of prediction methods.

5. FUTURE RESEARCH ACTIVITIES

Future aeroelastic research activities will be focused on realistic and affordable aeroelastic simulations depicted in In figure 38. The aim is to extend the current AESIM system to an aeroelastic simulation environment for fighter-type aircraft application.
Starting with the basic ingredients of the aircraft:
• Structural modelling,
• Aerodynamic modelling and

Aero-elastic Simulation Method
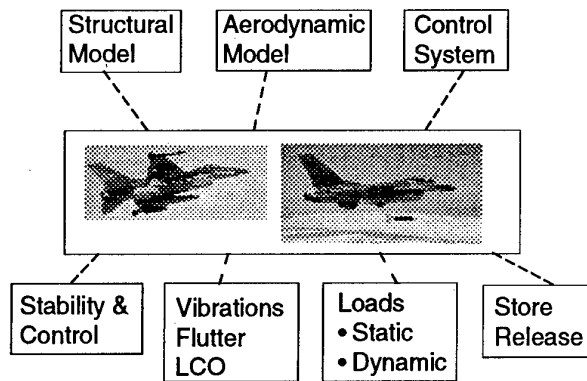
Figure 38: Future developments of AEroelastic SIMulation method.

- Control system modelling

the following analyses should be performed in more or less detail:

- Vibrations, flutter, non-linear flutter (LCO),
- Loads: static and dynamic, inclusive deformations,
- Aeroelastic responses due to store release and
- Impact of control system on aeroelastic responses.

6. CONCLUSIONS

In this paper the status of the NLR system for aeroelastic simulations has been presented and demonstrated with an up to date account of applicability. Experiences with recent applications and ongoing developments led to the following observations:

- The most critical part in the AEroelastic SIMulation is the geometry handling.
- The interpolation at the fluid/structure interface can be carried out satisfactory with the available models.
- The volume spline method has proven its value as interpolation tool for structured as well as unstructured data.
- The analysis of time-signals can be carried out satisfactory with the available models.
- The availability of direct graphical monitoring of all relevant data is crucial.
- The effort to obtain consistency between the geometrical and elastomechanical input data sets is often overlooked in interdisciplinary use.
- Accurate results: EE/TLNS at 8/48 time steps per period.
- Adequate coupled EE results are obtained using 8 time steps per cycle.
- Present 3D EE/TLNS aerodynamic computations are about 5/15 times slower compared to FP.
- Increased affordability.

REFERENCES

1 Hounjet, M.H.L., "NLR Inviscid Transonic Unsteady Loads Prediction Methods in Aeroelasticity", AGARD SMP Specialist Meeting on Transonic Unsteady Aerodynamics and Aeroelasticity, San Diego, California, 9-11 October 1991, AGARD CP 507.

2 Meijer, J.J., Cunningham, Jr., A.M., "Development of a Method to Predict Transonic Limit Cycle Oscillation Characteristics of Fighter Aircraft", AGARD SMP Specialist Meeting on Transonic Unsteady Aerodynamics and Aeroelasticity, San Diego, California, 9-11 October 1991, AGARD CP 507.

3 Cunninghamg, Jr., A.M., Boer, R.G. den, "Transonic Wind Tunnel Investigation of Limit Cycle Oscillations on Fighter Type Wings", AGARD SMP Specialist Meeting on Transonic Unsteady Aerodynamics and Aeroelasticity, San Diego, California, 9-11 October 1991, AGARD CP 507.

4 Burt, M., "The Impact of Computational Unsteady Aerodynmaics in Aerospace Engineering – Past, Present and Future", European Forum: Recent Developments and Applications in Aeronautical CFD, 1-3 September 1993, Bristol, UK (paper 12).

5 Hounjet, M.H.L., and Eussen, B.J.G., "Outline and Application of the NLR Aeroelastic Simulation Method", 19th ICAS Congress, Anaheim, California, September 18-23, 1994.

6 Eussen, B.J.G., Hounjet, M.H.L., Zwaan, R.J., "Experiences in Aeroelastic Simulation Practices", Euromech-colloquium 349: Simulation of fluid-structure interaction in aeronautics, Göttingen, Germany, September 16-18, 1996.

7 Hounjet, M.H.L., Meijer, J.J. "Evaluation of Elastomechanical and Aerodynamic Data Transfer Methods for Non-Planar Configurations in Computational Aeroelastic Analysis", International Forum on Aeroelasticity and Structural Dynamics 1995, Manchester, UK, 26-28 June 1995.

8 Prananta, B., Hounjet, M.H.L., Zwaan, R.J., "A Thin Layer Navier-Stokes Solver and its Application for Aeroelastic Analysis of an Airfoil in Transonic Flow", International Forum on Aeroelasticity and Structural Dynamics 1995, Manchester, UK, 26-28 June 1995.

9 Prananta, B.B., Hounjet, M.H.L., "Aeroelastic Simulation with Advanced CFD Methods in 2-D

and 3-D Transonic Flow", Symposium Unsteady Aerodynamics 1996, RAeS, London, UK, July 17-18, 1996.

10 Prananta, B.B., Hounjet, M.H.L., "Large Time Step Aero-Structural Coupling Procedures for Aeroelastic Simulation", International Forum on Aerelasticity and Structural Dynamics, Rome, Italy, 17-20 June 1997.

11 Hounjet, M.H.L., Eussen, B.J.G., Soijer, M.W., "Analysis of Computational Aeroelastic Simulations by Fitting Time Signals", International Forum on Aerelasticity and Structural Dynamics, Rome, Italy, 17-20 June 1997.

12 Meijer, J.J., Cunningham, Jr., A.M., "Outline and Applications of a Semi-Empirical Method for Predicting Transonic Limit Cycle Oscillation Characteristics of Fighter Aircraft", International Forum on Aeroelasticity and Structural Dynamics 1995, Manchester, UK, June 26-28, 1995.

13 Meijer, J.J., "Modeling of Semi-Empirical Transonic Unsteady Aerodynamics for Predicting Limit Cycle Oscillation Characteristics of Fighter Aircraft", 20th ICAS Congress, Sorrento, Italy, September 8-13, 1996.

14 Meijer, J.J., Hounjet, M.H.L., "Evaluation of Aeroelastic Methods to Predict Wing/Store Flutter at Subsonic, Transonic and Supersonic Speeds", Euromech-colloquium 349: Simulation of fluid-structure interaction in aeronautics, Göttingen, Germany, September 10-12, 1996.

15 Meijer, J.J., "Determination of Transonic Unsteady Aerodynamic Loads to Predict the Aeroelastic Stability of Fighter Aircraft", International Forum on Aeroelasticity and Structural Dynamics 1997, Rome, Italy, June 17-20, 1997.

16 Hounjet, M.H.L., "Hyperbolic grid generation control by panel methods", NLR TP 91061 U, June 1991.

17 Chan, W.M. and Steger, J.L., "A generalised scheme for three-dimensional hyperbolic grid generation", AIAA-91-1588-CP, July 1991.

18 Hounjet, M.H.L. and Eussen, B.J.G., "AESIM: An Aeroelastic simulation method for transport aircraft in transonic flow", NLR CR 96009 C, January 1996

19 Westland, J., and Hounjet, M.H.L., "Clebsch variable model for unsteady, inviscid, transonic flow with strong shock waves", AIAA 93-3025, July 1993.

20 Cunningham, Jr., A.M., Boer, R.G. den, "Transonic Wind Tunnel Investigation of Limit Cycle Oscillations on Fighter Type Wings – Update", 33rd AIAA, ASME, ASCE, AHS, ASC, SDM Conference, Dallas, Texas, April 13-17, 1992.

21 Soijer, M.W., "Frequency Domain Identification of Rotorcraft State Space Models and Applications to a BO105 Rigid Body Model", Master's thesis, Delft University of Technology, Faculty of Aerospace Engineering, December 1996

22 Hounjet, M.H.L., "Calculation of unsteady subsonic and supersonic flow about oscillating wings and bodies by new panel methods", NLR TP89119 U, April 1989.

23 Hounjet, M.H.L., Eussen, B.J.G. "Prospects of time-linearized Unsteady Calculation Methods for Exponentially Diverging Motions in Aeroelasticity", 33rd AIAA, ASME, ASCE, AHS, ASC, SDM Conference/Dyn. Spec. Conference, Dallas, Texas, April 13-17, 1992.

24 Yates, C., "AGARD Standard Aeroelastic Configurations for Dynamic Response I-Wing 445.6", AGARD Report No. 765, 1988.

25 Cunningham, Jr., A.M., den Boer, R.G., Dogger, C.S.G., Geurts, E.G.M., Retèl, A.P., Zwaan, R.J. "Unsteady Transonic Wind Tunnel Test on a Semi-Span Straked Delta Wing Model Oscillating in Pitch", NLR CR 93570 L (parts I through III) 1993.

26 Bland, S.R., "AGARD Three dimensional aeroelastic configurations", AGARD Report AR-167, June 1979.

27 AGARD, "Compendium of unsteady aerodynamic measurements", AGARD Report R-702, Neully-sur-Aeine, August 1982.

28 Hounjet, M.L.H., Meijer, J.J., "Application of Time-Linearized Methods to Oscillating Wings in Transonic Flow and Flutter", AGARD CP-374, September 1984.

29 Edwards, J.W., Bennett, R.M., Whitlow, Jr., W., Seidel, D.A., "Time-marching Transonic Flutter Solutions including Angle-of-attack Effects", J. Aircraft, Vol.20, No.11, Nov.1983, pp. 899-906.

30 Isogai, K., "On the transonic dip mechanism of flutter of sweptback wing", AIAA Journal vol7, July 1979, pp 793-795.

31 Hounjet, M.H.L., Eussen, B.J.G., "Beyond the Frequency Limits of Time-Linearized Methods", International Forum on Aerelasticity and Structural Dynamics, Aachen, Germany, June 1991. 132

32 Elbers, W.K., "Wind Tunnel Data Report 1/9-Scale F-16A Pressure Model Investigation of Shock-Induced Separation for Limit Cycle Oscillation Studies (AEDC PWT-16T Test TF-695)", General Dynamics, Fort Worth Division Report 16PR4694, September 1985, (Contract No. F33657-84-C-2034).

33 Tran, C.T., Petot, D., "Semi-Empirical Model for the Dynamic Stall of Airfoils in View of the Application to the Calculation of Responses of a Helicopter Blade in Forward Flight", Vertica, Vol.5, 1981.

Flutter Prediction for Complex Configurations

M. J. de C. Henshaw,
British Aerospace Defence Ltd,
Military Aircraft and Aerostructures,
Skillings Lane, Brough,
East Riding of Yorkshire,
HU15 1EQ, UK.

D.D. McKiernan and C. Mairs,
British Aerospace Defence Ltd,
Military Aircraft and Aerostructures,
Warton Aerodrome, Warton, Preston,
Lancashire,
PR4 1AX, UK.

1. SUMMARY

Flutter analysis requires the linking of structural deformation modelling with unsteady fluid dynamics; at British Aerospace, Aerospace Military Aircraft and Aerostructures (MA&A) a series of computational methods are used to model the various aspects of flutter to provide clearance data for aircraft. The various methodologies will be briefly described and the manner in which the parts of the process interface outlined.

Future aircraft require the tools to be capable of modelling complex configurations including novel planforms and aircraft with stores; these must also include the difficult transonic flow regime. The requirements of the unsteady methods needed to provide this capability and the manner in which they must be inserted into the existing process will be discussed.

Initial results obtained using an unsteady Multiblock Euler method will be presented and the development of this method within the overall process will be detailed. These results will be used to illustrate the ways that sophisticated unsteady CFD methods must be developed, in terms of interface with structural components of the process, to meet project requirements for complex configurations. The post-processing requirements will also be presented.

2. INTRODUCTION

Development of tools to predict fluid-structure interaction requires a good deal of interaction between fluid and structural dynamicists. Probably because of the difficulty in economically calculating unsteady flows, for all but the most simple cases, Flutter Engineers have hitherto tended to lean more towards structural expertise, and the methods for calculating unsteady fluid flow have been somewhat limited in terms of the geometries and physical flows to which they are applicable. With improvements in computer power, and the development of more sophisticated CFD (Computational Fluid Dynamics) methods, greater degrees of complexity are now possible. At British Aerospace (MA&A) the developing process for flutter prediction is based on a modular approach, which allows new (more sophisticated) methods, as well as the most effective simple methods, to be easily inserted as they become available.

A key aspect of the flutter prediction philosophy is the application of the simplest, least expensive, method consistent with the particular stage of the design cycle being addressed. Thus, simple unsteady aerodynamic methods with empirical corrections may be favoured over more sophisticated methods, where these can provide adequate results more quickly. However, more sophisticated methods (e.g. Euler and Navier-Stokes) are being developed as a means of supplementing simple methods and studying new configurations. Use of more sophisticated methods will increase as they mature, but they are viewed as complementary to the simple methods, not as replacements for them. The benefits of improved fluid modelling are associated with extending the capability to more complex flows and geometries.

This paper begins with a description of the modular process for the design and qualification of military aircraft to prevent aeroelastic and aeroservoelastic instabilities, including flutter. The focus of the paper will be primarily on the CUA (Computational Unsteady Aerodynamic) application within the modelling and analysis phases of the process. The physical and geometric capabilities required for future designs will be discussed and the desired process improvements highlighted; this is intended to identify to academia the tools which industry requires to continue a pragmatic approach to application of theoretical modelling of flutter phenomena. Some initial results from studies comparing a simple lifting surface method, UTSP (Unsteady Transonic Small Perturbation) and Euler unsteady codes will be presented, and the next development stages, concerned with coupling these methods into the overall process will be discussed.

3. FLUTTER DESIGN & QUALIFICATION PROCESS

Figure 1 shows, in broad terms, the modular process that is developing for the design and qualification of military aircraft to prevent aeroelastic and aeroservoelastic instabilities, including flutter. The overall process can be divided into major phases of modelling, analysis, validation, qualification and certification.

The process is illustrated (figure 1) in terms of the analysis modules and the activities with which they would generally link. Thus, the geometry is transformed appropriately so that panels, or grids, may be constructed for input to one of the choice of CFD solvers. The solvers are grouped to show increasing sophistication (and cost) from left to right. The NASTRAN MSC structural modelling is standard for all and, as such, there is a high degree of commonality in the interpolation between structure and fluid models. Fluid models are validated using experimental unsteady data, and test data matching (ground and flight) is used to develop common structural models for each configuration. The interpolation procedure facilitates the use of coupled solutions, currently effort is directed principally at weakly coupled solution, however, a strongly coupled method could also be used, but must be developed in such a way as to be compatible with data input and output currently used.

Figure 1 Modular Flutter Design & Qualification Process
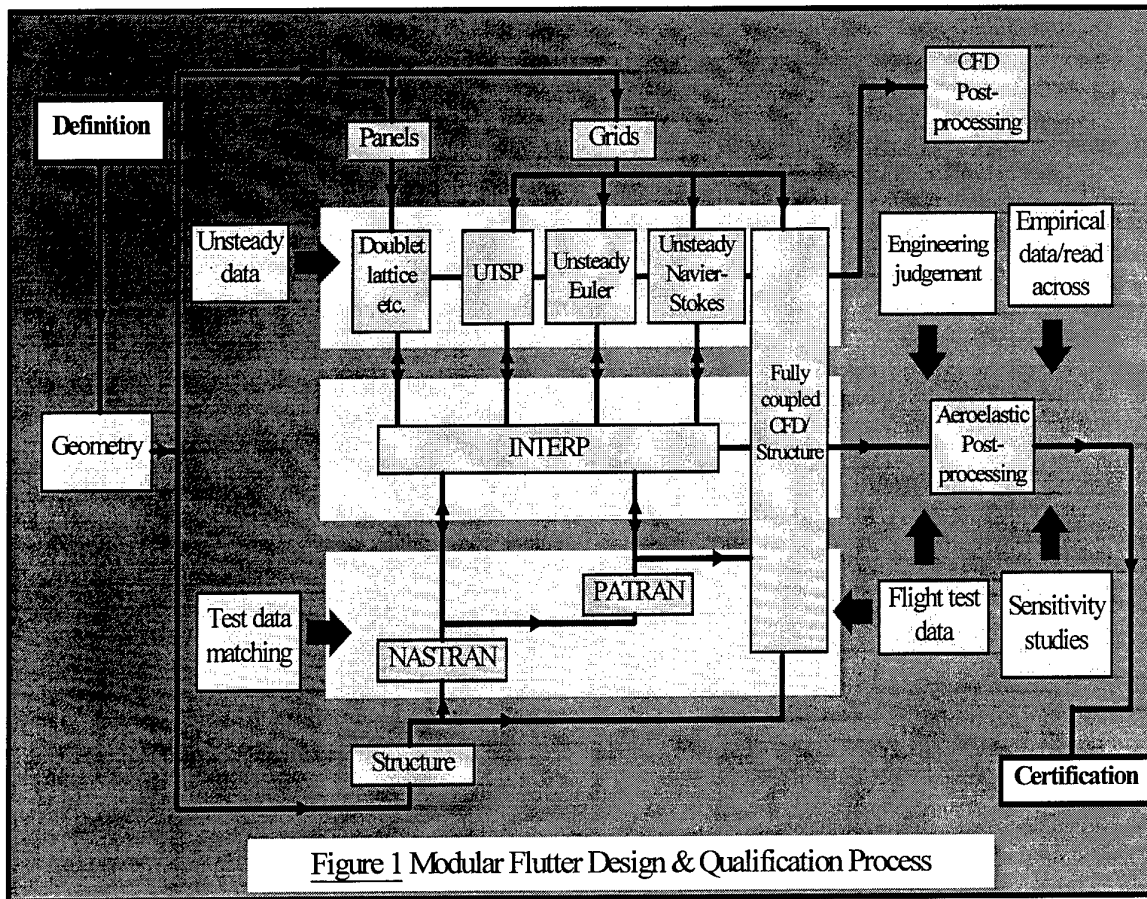
With existing tools and processes at MA&A, approximately 75% of the *effort* required to qualify flutter aspects is associated with the modelling and analysis phases. The bulk of this currently involves accurately modelling the structure; relatively little effort is required to use the linearised unsteady aerodynamic tools which are now established as the workhorse of the flutter engineer. The remaining 25% of the flutter *effort* involves validation, qualification and certification, which is predominately ground and flight testing.

It should be noted that *effort* (in terms of man years, say) expended on a given phase does not equate to the *cost* of that phase. Indeed, since flight flutter testing is expensive, around 75% of the overall flutter *cost* is associated with the validation and qualification phases.

Experience has shown that there is a high gearing between the modelling effort and the cost savings made through reduced flight testing. The risk of subsequent redesign is greatly reduced through the increased knowledge gained by high quality modelling and analysis.

The greatest potential for further reductions in both cost and risk lies with the use of advanced CUA codes to underpin the qualification of flutter in the transonic regime, particularly for complex configurations. This will inevitably lead to an increase in the modelling and analysis effort (and cost), but this is clearly justified if greater cost savings are made during testing and qualification. It is essential that the development and application of advanced CUA codes is managed effectively through close co-operation and mutual understanding on the part of code developers and end users.

4. PRESENT CUA CAPABILITY

The CUA methods currently available fall into one of two categories: those which are considered as being 'production standard' tools (and used on existing aircraft); and those which fall under the heading of 'advanced methods' which are yet to mature.

4.1 Production Standard CUA Tools

The CUA modelling techniques predominantly used by MA&A flutter groups are a combination of Doublet Lattice, Kernel Function, Characteristic Box and Finite Difference methods. The toolsets built around these methods are relatively quick, robust and easy to use in comparison with more advanced CUA tools. User confidence has been established in these methods through application to a range of aircraft projects, but a number of shortcomings are recognised, namely:

- Only subcritical / supersonic Mach numbers can be modelled, due to inviscid linearised flow prediction.

- Linearity requirement allows only small perturbations to be considered of attached flow (e.g. small deflections, low incidences).

- Limited capability to model complex configurations.

Within the calculation process the structural and aerodynamic models have different time step constraints and the grids each have a different geometric optimum, implying the need for interpolation. A significant challenge associated with interfacing the structural model with the aerodynamic

prediction method stems from the need to interpolate structural deflections onto an aerodynamic grid, and aerodynamic forces onto a structural grid. The mainstream tool used for structural modelling, MSC NASTRAN, now contains aerodynamic modelling capabilities comparable to traditional MA&A in-house linearised CUA tools. The interpolation burden is eased through the use of NASTRAN as an integrated structural and unsteady aerodynamic modelling tool.

The shortcomings of simple linearised CUA methods (and those provided by NASTRAN) in terms of flow physics tend to give a pessimistic prediction of flutter speeds due, for instance, to the over-prediction of unsteady trailing edge control effects. The strength of these methods lies in the rapid prediction of the fundamental unsteady aerodynamic trends for simple flutter mechanisms rather than quantitative accuracy. However, the use of these methods leads to a relatively conservative approach to flight qualification and testing, particularly in the transonic flight regime. The attractiveness of the speed of use of these methods within the design process is, therefore, offset by a more rigorous flight test programme.

Simple linearised CUA methods can model total aircraft unsteady aerodynamics assuming small perturbations and attached flow, and treating all components as flat plates or simple bodies. The unsteady aerodynamics generated by complex shapes requires more sophisticated methods.

4.2 Advanced CUA Methods
The UTSP (Unsteady Transonic Small Perturbation) code provides the means of calculating the flow where the freestream Mach number is close to unity, although the geometric capability is somewhat limited. UTSP is confined to modelling wings only, which it does through a flat plate representation with the sectional geometry introduced into the surface boundary conditions as functional terms. Three linearity options are available: non-linear harmonic, linear harmonic and linear indicial, and full-coupled solutions of the structural equations of motion with the non-linear TSP aerodynamic equation can be performed.

An unsteady Euler Multiblock code (UEMB) has been developed from a steady Euler solver, by introducing a global time step strategy, and effecting geometric motion through transpiration velocity boundary conditions. This code provides considerable enhancement to the geometric capability, and the well established grid generation tools, used in steady flow analyses, allow a fast turnaround in terms of model generation, even for complex shapes. The use of transpiration boundary conditions obviates the need for re-gridding within the scheme.

Development of an unsteady Navier-Stokes code (RANSMB) is currently underway. This has a high degree of compatibility with UEMB, and will extend the range of flow conditions (in particular to highly separated conditions). Moving grid technology is being developed within the RANSMB programme.

Although the solutions from UTSP or Euler calculations may be used for non-linear analysis, system identification algorithms may be used to provide accurate values of the frequency and damping for the air-on modes, together with the mode shapes. From these aerodynamic stiffness and damping matrices can be extracted and used as input to the (more familiar) linear flutter solvers to predict approximate flutter speeds The alternative analysis routes are shown in figure 2, which represents an end-users perspective of the flutter analysis process.

5. TARGET CUA CAPABILITY
CUA models, in conjunction with the structural mathematical model, perform two distinct functions in the flutter design and qualification process.

The first of these functions is the prediction of flutter characteristics, primarily on individual components, during the earlier phases of design. Quick turnaround of flutter analyses and sensitivity studies is essential to influence the design and minimise later modification. Hence the use of existing methods is best in terms of cost and time scale. However, future aircraft configurations may be dominated by design drivers other than aerodynamic considerations, which will need investigation with respect to the applicability of these methods.

The second function is the complete aircraft flutter prediction leading to clearances prior to flutter envelope expansion flying.
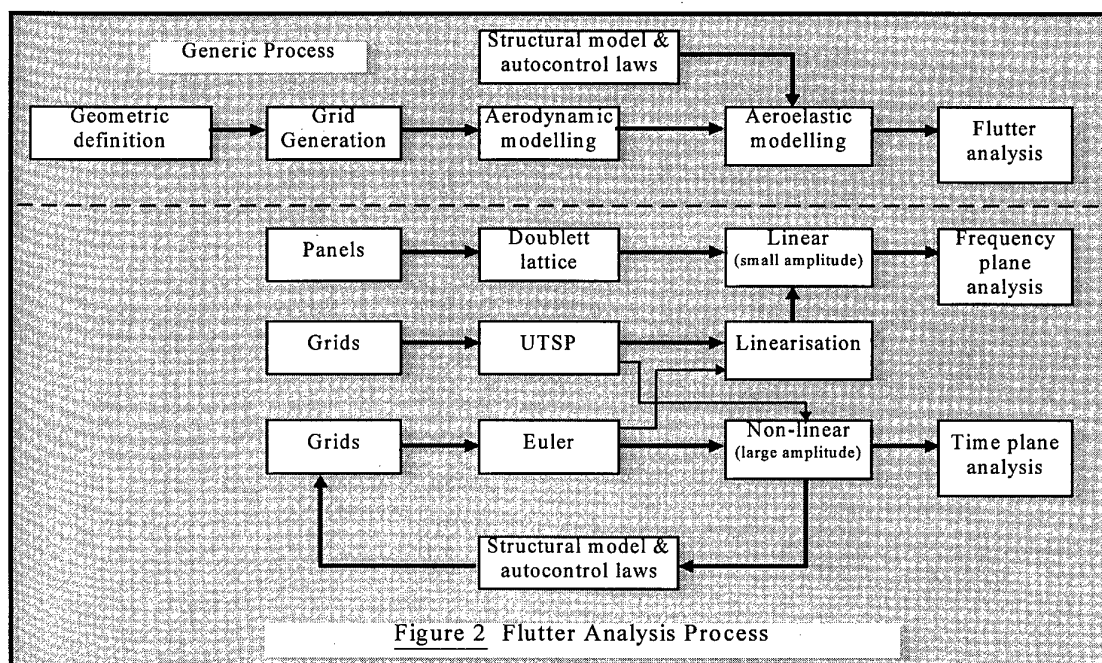
Figure 2 Flutter Analysis Process

This impacts directly on the flight qualification philosophy adopted, in that the known inaccuracy of linearised CUA methods leads to a relatively conservative approach to flight flutter testing. Flight testing within the transonic regime, and especially with external stores, requires particular caution. It is here that advanced CUA methods will have an impact on cost, time scales and adherence to specification.

In the short to medium term the use of advanced CUA methods will involve high turnaround times and computing costs, limiting their use within the early part of the design process. However, later in the design process (where accurate structural models are available) these disadvantages will be offset by a reduction in the necessary flight testing due to the increased accuracy of predictions. This approach will also capture, later than ideal in the process, but very early in the development flight testing, any previously unpredicted flutter problems not captured by the simpler methods.

6. CUA DEVELOPMENT ISSUES
Various issues within the CUA development programme are addressed below:

Configurations being proposed for future projects have a degree of novelty. The extent to which simple linearised CUA codes can cope with novel features is uncertain. Rules for usage of such codes, established by lessons learned on previous projects, are likely to be stretched and therefore further validation is required.

User requirements for advanced CUA methods need clear definition, as does the way the methods are to be validated and used in the design process.

It is anticipated that advanced CUA methods will require much greater run times and greater user expertise than existing methods. The effect of using these methods on costs and time scales must therefore be offset by a greater level of accuracy and user confidence which allows a more confident approach to be taken to flight testing with resulting reduced costs.

Experience of UTSP tool development has shown that user confidence must be gained in a new method if it is to become a production tool. Central to this is the user friendliness of the method, the validating evidence of its accuracy and the quality of the pre- and post processing. These latter two requirements need specifying in detail by the users to the code developers. Assessments of code developments should be carried out in a feedback loop between code developer and code user. A suitable link between developer and end-user is required for this purpose.

Performance of flutter solutions using non-linear aerodynamics (as offered by advanced CUA methods) will require the coupling of structural and aerodynamic models and time domain analysis of the structural response (including the FCS - flight control system - as appropriate). Consideration of non-linear structural models will also be possible. This will lead to the requirement for extensive post-processing software to derive frequency and damping information from response time history data. To a large extent the type of post-processing analysis required is similar to that used for flutter flight data analysis. Developments of such tools should therefore be geared to satisfying the requirements of both CUA and flight flutter analysis.

Aircraft time scale constraints inevitably come to bear as design freeze and flight dates approach. The academic community should be encouraged and supported in proposing and implementing cost efficient methods for the analysis of coupled solutions. In particular the aim should be to provide the flutter engineer with a means of minimising the number of time domain flutter simulations through the use of advanced post-processing techniques.

The level of modelling complexity determines the applicable type of flutter analysis. For the simple linearised methods frequency plane analysis is appropriate. The introduction of non-linear effects through use of UTSP, Euler and Navier-Stokes methods generally dictate the use of time plane analysis. System identification algorithms could offer an alternative approach to obtain frequency, damping and mode shapes. This effectively linearises the problem for subsequent frequency plane analysis. The two analysis routes are shown in figure 2. In many cases the more simple and familiar frequency plane analysis is sufficient.

7. DELIVERY OF PROJECT READY CAPABILITY
At MA&A the various components of the flutter design and qualification process (figure 1) are largely developed, the improvements being sought now are mostly concerned with the process as a whole, i.e. developing the links between the various components and improving the performance of combinations of modules rather than individual modules.

The methods themselves have significantly different model definition requirements, and so commonality is not strictly possible, although commonality of geometry definition is possible. The interpolation procedure is largely independent of the fluid model, and different interfaces to the fluid dataset make the addition of new capabilities a straightforward matter.

Doublet lattice and similar methods have been in use for many years and, although their direct applicability is very limited, used with empirical data, read across and engineering judgement they may be applied to a wide range of conditions. For existing aircraft a large body of knowledge has been built up which allow these methods to provide a fast turnaround capability. UTSP provides a refinement in terms of predictive capability in the transonic flow region, it should be noted that results indicate that the UTSP method provides a good match in terms of shock position (see section 8), however, this is entirely serendipitous and a degree of caution should be observed in using the method. UEMB, and in due course RANSMB, provide the geometric complexity that UTSP lacks, and these methods are required for the design of novel planforms, and for geometric detail such as wing, pylon, store or wing + tip missile type configurations. For instance, a wing with a tip missile might be modelled by first performing spot calculations using UEMB, but then intermediate points can be filled in by using UTSP. The missile can be modelled by applying twist to the wing tip through the boundary conditions to give a representative flow. Future developments require new methods to be inserted into the current process in such a way that the benefits of existing methods are not lost. As new configurations are approached, validation of existing techniques using the developing sophisticated methods will be an important aspect of the technology insertion. At MA&A this is conducted using link personnel between developer and end-user.

8. CASE STUDY - AGARD SMP TAILPLANE

The need to develop processes whereby simple methods are used to provide the bulk of the data, validated using more complex methods at a limited number of conditions is illustrated by comparing the processing time of the options available within the design and qualification process. It is instructive to compare the relative times for using the various methods on a standard simple test case; the AGARD SMP tailplane [ref. 1] (figure 3) has been chosen with the following condition:

M = 0.86 (Mach number)
α = 0.4° (angle of attack)
V = 0.9294 (frequency parameter)
Amplitude = 0.4°
Pitch axis = 0. 6819c_0 (c_0 = root chord)

8.1 Simple Method - Richardson Kernel Function

The simple model used was a Richardson Kernel function (lifting surface) theory, with a 7(x) X 8(y) grid, as shown in figure 4. This code uses a four 'kink-point' planform definition, and provides real and imaginary pressure coefficients for the bending, torsion and yaw modes. For the simple planform chosen for this case study the pre-processing time is extremely short (a few minutes), but for more complex planforms this increases depending on the level of complexity. The most time-consuming activity with this method is the post-processing.

8.2 UTSP

The volume grid used for this code consisted of 120(x) X 20(y) X 40(z) points, the surface distribution is shown in figure 5. Pre- and post-processing time are the most time consuming aspects of this calculation method, although currently a higher degree of user skill and understanding is required to obtain the most satisfactory results and interpretation from the method.

8.3 Unsteady Euler Multiblock (UEMB)

For this simple configuration a fully automatic grid generator may be used, but for general (complex) configurations a higher degree of user interaction is required, leading to a more substantial pre-processing effort, however, the solver CPU time is by far the most limiting factor with the Euler Multiblock code. The surface grid used consisted of 40(x) X 28(y) points (figure 6) giving a comparatively small (89964) number of nodes in the volume.

8.4 Results

8.4.1 Pressures

The real and imaginary pressures are shown at five spanwise stations for the three different methods and compared with experimental measurements in figure 7. There is a clear improvement in match to experiment as the level of modelling sophistication increases, and still further improvement might be expected from the inclusion of viscous effects either within Euler or as a Navier-Stokes solution.

8.4.2 Solution times

Table 1 shows the relative number of jobs it is possible to run using a simple method (such as the Richardson kernel function method) and UTSP compared with the Euler Multiblock code. The relative number of jobs based on CPU demonstrate that it is essentially the computational effort which is the most

limiting factor with regard to Euler methods (note that the CPU times were scaled to take varying platforms into account).

Method	Relative number of runs based on total time	Relative number of runs based on CPU	Relative number of runs based on turn around
UEMB	1	1	1
UTSP	46	1485	80
Simple method	165	89100	209

Table 1
Relative timings for obtaining solutions based on the AGARD SMP Tailplane test case.

The relative number of jobs based on total time includes the pre- and post-processing times for a single configuration, and the turn around time is based on the time required for an existing configuration (i.e. minimal pre-processing).

9. CONCLUSION

The comparative times indicate the desirability of a pragmatic approach, whereby an initial calculation with UEMB is used to guide subsequent runs using UTSP, which in turn may guide a large number of simple method runs with corrections applied.

This paper has reviewed the role of unsteady aerodynamics within the flutter design and qualification process used by MA&A; a process begun very much as discrete units is being developed into a fully integrated process, and future developments of specific methods (particularly with reference to more sophisticated CFD) must accommodate this requirement. The objective is to provide the flutter engineer with a toolbox which allows a choice of methods at various stages of the design process based on the imposed time scales, a clearly defined confidence level is required for each method used at each design stage. CPU time is the major limiting factor for methods such as Euler (and Navier-Stokes). Although performance of these methods is expected to substantially increase over the next few years, nevertheless these will complement, not replace, existing techniques.

10. REFERENCE

1. Mabey, D.G., Welsh, B.L. and Cripps, B.E., "Measurements of steady and oscillating pressures on a low aspect ratio model at subsonic and supersonic speeds", Royal Aircraft Establishment report TR84095, September 1984.
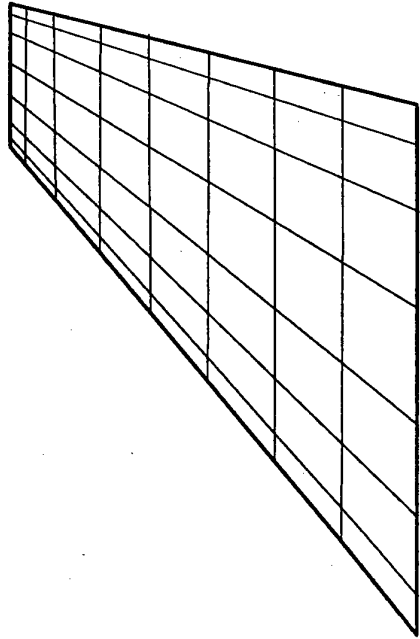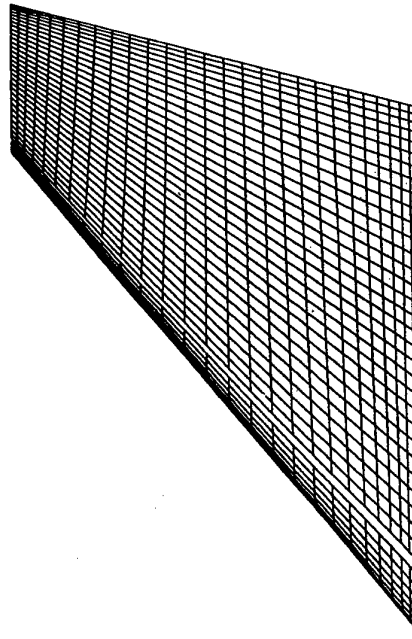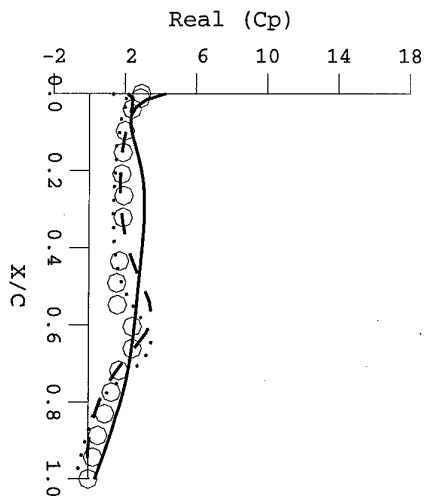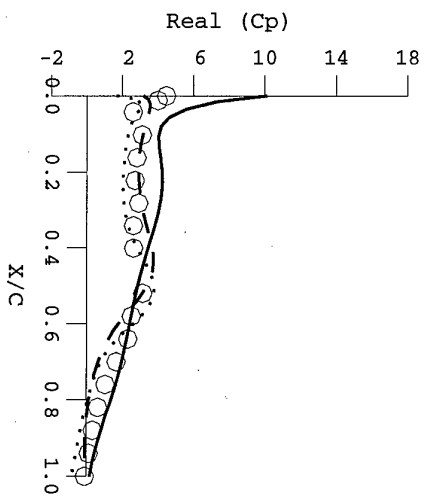
11. ACKNOWLEDGEMENT

Figure 4. Richardson Grid (sketch).
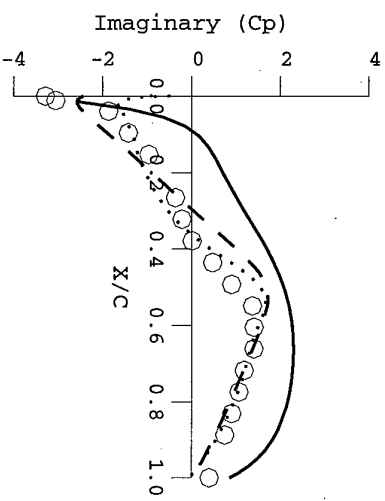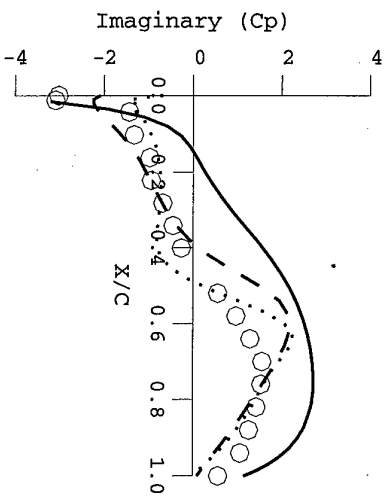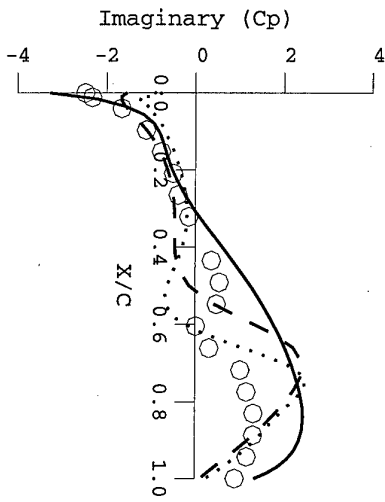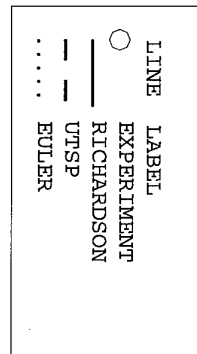

Figure 6. Euler Multiblock Surface Grid.

Streamwise section NACA 64 A 010

Aspect ratio 2.42

Taper ratio 0.27

$C(\eta)/s = 130 - 0.95\,|\eta|$

$S = 0.825 s^2$

$= 0.161 m^2$

$\Lambda_L = 50.2°$

$\Lambda_T = 14°$

Pitching axis

Pressure plotting stations

$\eta = 0.96$

$\eta = 0.84$

$\eta = 0.65$

$\eta = 0.42$

$\eta = 0.14$

$s = 1\ (442\,mm)$

0.35

0.31

0.41

0.89

Figure 3. AGARD SMP Tailplane Planform.

Figure 5. UTSP Surface Grid.
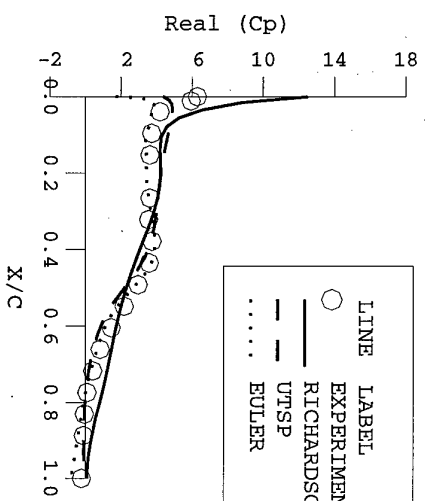
Figures 7a-c. AGARD SMP Tailplane Unsteady Lower Surface Pressures.

(d) y/S=0.841

(e) y/S=0.959
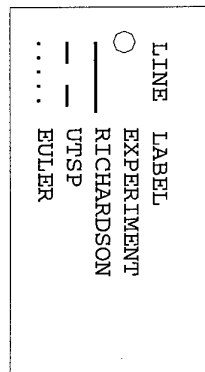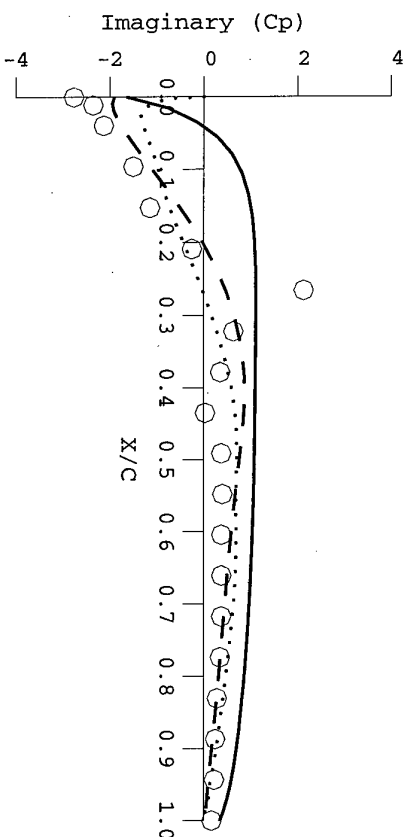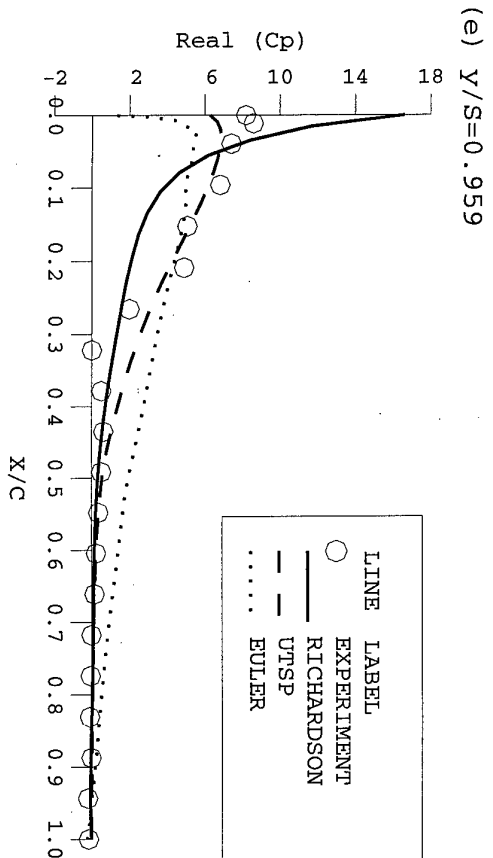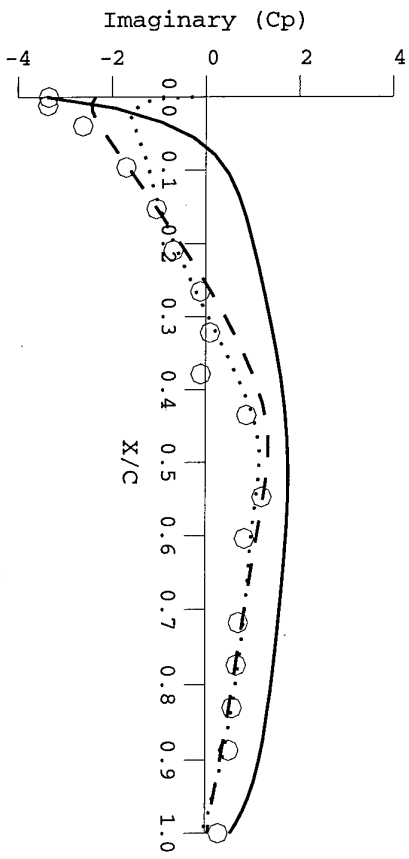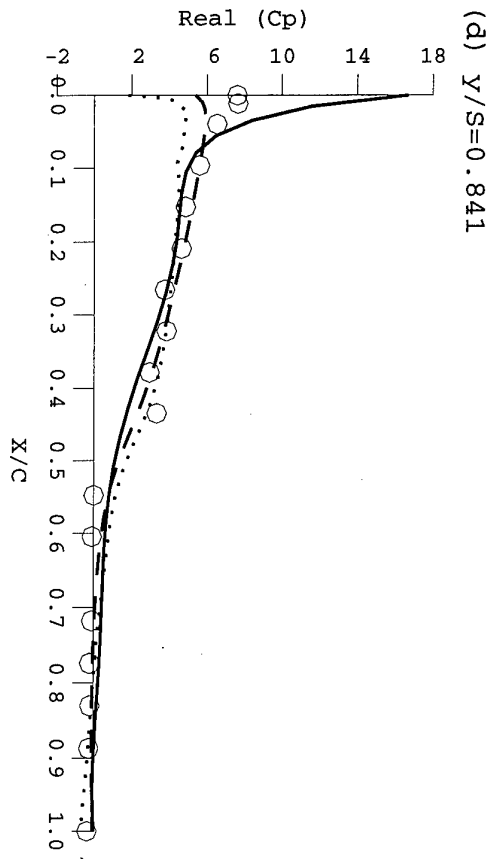
Figures 7d and 7e. AGARD SMP Tailplane Unsteady Lower Surface Pressure

High Incidence Unsteady Aerodynamic for Aeroservoelastic Predictions

W. Luber, J. Becker
Daimler-Benz Aerospace AG
Military Aircraft, MT24
P. O. Box 80 11 60
81663 Munich, Germany
Phone: +49-89-607-26996
Fax : +49-89-607-28707
E-mail: lu26996@dbmail.dasa.de

Summary

The aeroservoelastic stability of a fighter type aircraft is investigated at high angle of attack. The effects of non-linear, incidence dependent unsteady aerodynamic forces of elastic modes and of control surface deflections on the structural coupling are demonstrated for low and high subsonic speeds for different incidences. The difference of open loop frequency response functions calculated with linear and with high angle of attack unsteady aerodynamics documents the necessity of introduction of high incidence effects for aeroservoelastic stability calculations. Non-linear effects are introduced using unsteady pressures of windtunnel experiments on an oscillation model by correcting of theoretical pressures.

List of Symbols

V_L	Limit Airspeed
V_{0max}	Minimum Operational Airspeed
V_{0max}	Maximum Operational Airspeed
GM	Gain Margin> Minimum change in loop gain, at nominal phase, which results in an instability beyond that allowed as a residual oscillation
PM	Phase Margin ==> The minimum change, at nominal loop gain, which results in an instability
f_M	Mode frequency in Hz
q_r	generalised co-ordinate
ω_r	mode frequency
M_r	generalised mass
K_r	generalised stiffness
$A_{rj}(\alpha_o,Ma)$	generalised unsteady aerodynamic forces of the modes
$A_{r,IB}(\alpha_o,Ma)$	generalised unsteady aerodynamic efficiency of inboard flap
$A_{r,OB}(\alpha_o,Ma)$	generalised unsteady aerodynamic efficiency of outboard flap
$A_{r,FP}(\alpha_o,Ma)$	generalised unsteady aerodynamic efficiency of foreplane
$M_{r,IB}$	generalised inertia coupling term for inboard flap
$M_{r,OB}$	generalised inertia coupling term for outboard flap
$M_{r,FP}$	generalised inertia coupling term for foreplane deflection
$F_{ACT}(i\omega)$	Actuator impedance function
$F_{GYRO}(i\omega)$	Sensor transfer function
$F_{PHASE-ADV}(i\omega)$	Advance filter characteristic
K_{IB}	Inboard flap control loop gain
K_{OB}	Outboard flap control loop gain
K_{FP}	Foreplane control loop gain
$\Delta c_p(i\omega)_j$	pure theoretical pressure of the not measured mode j
$\Delta c_p(i\omega)_i$	pure theoretical pressure of the measured mode i
$\Delta c_p(i\omega)_{i-exp}$	experimental pressure of the measured mode i
$\alpha_j(x,y,i\omega)$	incidence distribution of the not measured mode j
$\alpha_i(x,y,i\omega)$	incidence distribution of the measured mode i
$\Delta c_p(i\omega)_j$	corrected pressure distribution of the not measured mode j

1. Introduction

This contribution describes a possible way to predict the aeroservoelastic stability of an aircraft at high incidence including non-linear aerodynamic effects. The design of flight control laws for modern aircraft is very much influenced by aeroservoelastic means to alleviate structural coupling effects. Notch filters or active feedback's of local elastic acceleration or rates have to be optimised in order

to give minimum structural coupling together with minimum acceptable effects on aircraft handling and on flutter phase and gain margins without violating required stability margins. The design of the notch filters or of the active feedback control laws is general based on an analytical dynamic model which includes the description of flight and structural dynamics together with unsteady aerodynamic forces of the elastic vibration modes and of control surface deflections. A specific problem area concerning layout of filters or control loops arises especially at high incidence, high altitude flight conditions, since the unsteady aerodynamic forces, especially in case of unstable aircraft configurations play an important role for the stability margins of elastic modes compared to the margins for on ground conditions.
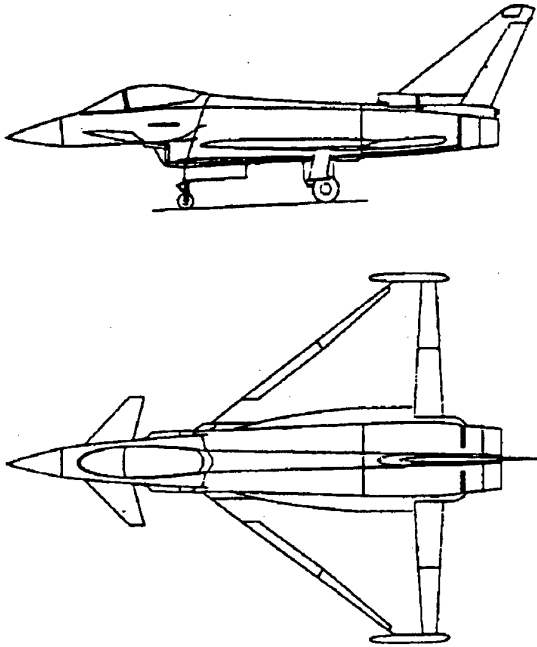
Fig. 1: Aircraft Two Side View

Usually theoretical unsteady aerodynamics from linear theory are applied which do not include high incidence aerodynamic effects, effects of flow separation or related non-linear aerodynamic behaviour. In general the high α unsteady aerodynamics of rigid and elastic aircraft modes cannot be predicted by existing theoretical methods. Numerical simulation of high α aerodynamics is not applicable for flexible aircraft aeroservoelastic design and clearance work. Much effort has to be invested into unsteady windtunnel experiments, and design and clearance tasks have still to be based on in-flight measurements. Unsteady windtunnel experiments of unsteady pressures for a rigid roll

mode as applied in this investigation have to be extrapolated for arbitrary mode shapes and carefully analysed and validated by comparisons to windtunnel and in-flight response calculations for measured accelerations before full application to the aircraft structure. Many effects like model support interference, freestream turbulence, Reynolds number, tunnel wall interference have to be considered. The investigation is performed for a typical delta canard fighter aircraft shown in Fig. 1.

2. Stability Criteria

For aeroservoelastic stability assessments of an aircraft with Flight Control System (FCS) criteria from the following MIL Specifications have to be applied:

- Flight Control System MIL-F-9490D

- Airplane Strength and Rigidity, Vibration, Flutter and Divergence MIL-A-8870

The military specifications for aircraft with FCS contain gain and phase margin requirements for the open loop frequency responses. For the rigid dynamics in the frequency range of the modes M from $0.06 < f_M <$ first aeroelastic mode which are in the range of minimum to maximum operational speed 6 dB gain and 45 degree phase margin and at limit airspeed V_L 4.5 dB gain and 30 degree phase margin. MIL-F-9490D requires for the mode frequencies $f_M >$ first elastic mode 8 dB and 60 degrees phase margin in the operational range and 6 dB and 45 degrees phase margin for V_L.
The requirements are summarized in Table 1.

Airspeed Mode Frequ.	Below V_{0min}	V_{0min} to V_{0max}	At limit speed V_L	Above $1.15V_L$
$f_M < 0.06$	GM=6.0 No PM below V_{0min}	GM=±4.5 PM=±30	GM=±3.0 PM=±20	GM=0. PM=0.
$.06 \leq f_M < 1$ st ASEM		GM=±6.0 PM=±45	GM=±4.5 PM=±30	stable nominal phase and gain
$f_M > 1$st ASEM		GM=±8.0 PM=±60	GM=±6.0 PM=±45	

Table 1: MIL-F-9490D minimum gain and phase margin requirements

Special requirements for mode frequencies $f_M >$ first elastic mode may be formulated which take into account uncertainties in the prediction of unsteady aerodynamic forces at extreme flight

conditions. Especially if actively controlled configurations are concerned, which are unstable. For these configurations the flight clearance has to be based upon prediction for open loop response functions.

The aeroservoelastic stability requirements defined for flutter in MIL-A-8870B shall be met as well. A minimum required flutter margin boundary of 15% in V_D at constant altitudes and Mach numbers is defined there. The damping coefficient g for any flutter mode shall be at least three percent.

The damping requirements are demonstrated in Figure 2.
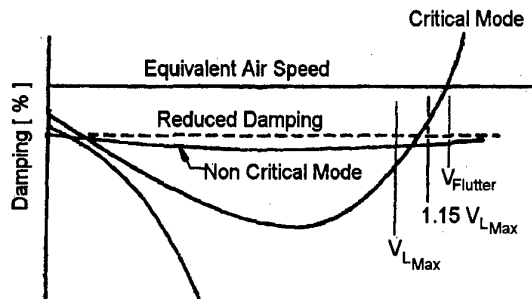
Fig. 2: Minimum Required Damping Margin

3. Description of the structural coupling problem

The structural coupling problem described here is specific for military aircraft with heavy underwing tanks and stores with low frequencies down to about 4 Hz tank/stores and wing bending modes are present due to the high mass condition. These low frequency wing bending elastic modes, shown for the configuration analysed in Figure 3, produce counteracting fuselage modes which are mainly rigid fuselage pitch oscillations.

Tank Yaw Mode f = 3.5 Hz

Wing Bending / Tank Roll f = 4.5 Hz

Wing Bending / Tank Pitch f = 5.4 Hz

Fuselage Bending / Engine Pitch f = 10.8 Hz

Fuselage Bending / Tip Pod Pitch f = 14.0 Hz
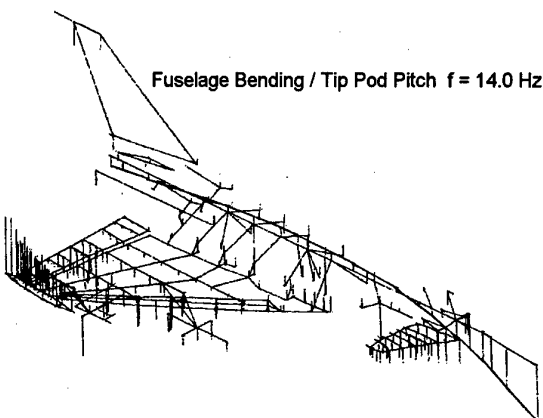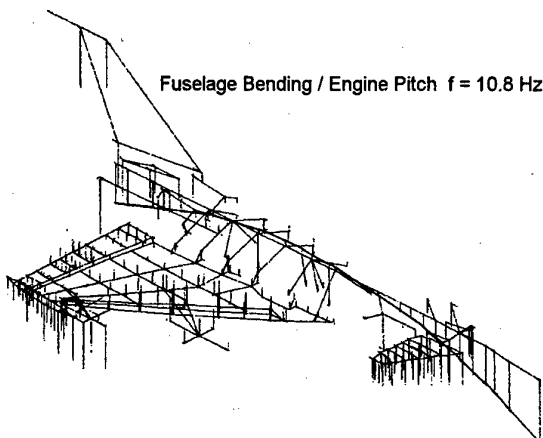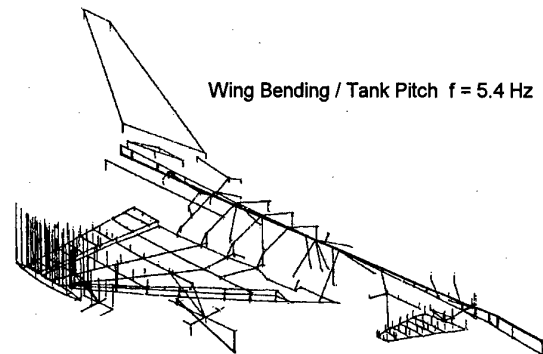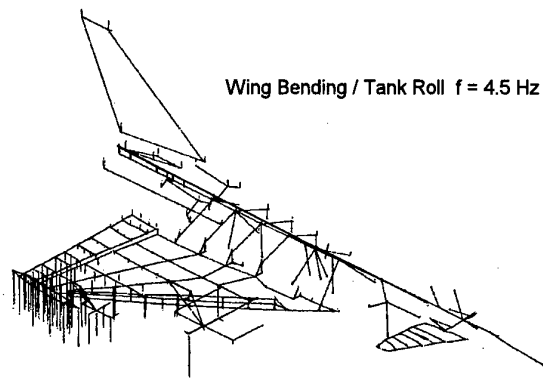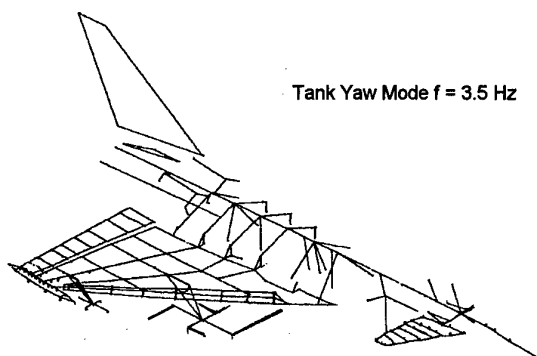
Fig. 3: Normal Mode Shape, A/C with Tank

The rigid fuselage modes caused by the wing bending mode creates a coupling problem which is in contract to the general well known structural coupling problem caused by the first elastic bending mode of the fuselage and the feedback of its elastic fuselage pitch rate signal through the gyros to the control surfaces, see Figure 3 fifth mode. The structural coupling effects caused by the first fuselage bending mode can easily be reduced by putting the gyros in a position of zero elastic mode pitch angle or rate. Strong notch filtering can be introduced in the feedback loop to avoid the structural coupling of the 1 st fuselage bending mode.

The feedback signal of the gyro in the frequency of the low frequency wing bending modes however cannot be influenced and alleviated by gyro positioning. In addition the frequency of the first elastic mode is so low that the normally used notch filter technique to reduce structural coupling cannot be applied fully. The stability criteria for handling would be affected by lose of phase at around the short period mode frequency due to effects of the notch filtering. Therefore the low frequency mode shall be shown as a phase stable mode, if this mode cannot be phase stabilised, configuration changes or active control means would be helpful. A typical behaviour of the structural coupling effect in the low frequency mode is the increase of the frequency response in flight due to unsteady aerodynamic excitation by the control surfaces. (This effect was not experienced in the structural coupling signal of the first fuselage bending mode of other fighter aircraft where the problem was always found critical for on ground conditions, in flight aerodynamic mode damping caused lower coupling.)

Therefore the aerodynamic excitation forces of the low frequency mode and its aerodynamic damping is of prime interest for the stability of heavy tank/stores aircraft configurations. The effects of unsteady aerodynamic forces at high angle of attack have to be considered carefully.

4.   Analytical Modelling

The calculation of open loop frequency response functions has to be based on an analytical model which represents the rigid aircraft dynamic and contains the dynamic equations of the control laws, the sensor, computer and actuators transfer functions. This rigid aircraft dynamic model is coupled to the structural dynamic aircraft model which represent to the dynamic behaviour of the

elastic aircraft including unsteady aerodynamic forces of the elastic modes and of the control surfaces (generalised aerodynamic force of elastic modes and generalised efficiencies of inboard, outboard and foreplane rotations). The structural dynamic equations are formulated for unsteady aerodynamic forces which are functions of the angle of attack.

$$-\omega^2 M_r q_r + K_r (1 + ig_r) q_r + \sum_i^j A_{rj} \cdot q_j(\omega) +$$

$$+\left\{ \left(A_{r,IB} \cdot \delta_{IB} \cdot K_{IB} + A_{r,OB} \cdot \delta_{OB} \cdot K_{OB} + A_{r,FP} \cdot \delta_{FP} \cdot K_{FP} \right) + \right.$$

$$\left. +\left(M_{r,IB} \cdot \delta_{IB} \cdot K_{IB} + M_{r,OB} \cdot \delta_{OB} \cdot K_{OB} + M_{r,FP} \cdot \delta_{FP} \cdot K_{FP} \right) \right\} \cdot$$

$$F_{ACT}(i\omega) \cdot F_{GYRO}(i\omega) \cdot F_{PHASE-ADV}(i\omega)$$

The unsteady aerodynamic forces A_{rj}, $A_{r,IB}$, $A_{r,OB}$, $A_{r,FP}$ be calculated by computer programs for the derivation of linear unsteady aerodynamic forces for the case of small angles of attack and for high angle of attack with the procedure as described in the following chapter.

5.   Prediction of unsteady aerodynamic forces at high incidence

Aeroservoelastic and flutter calculations with the inclusions of flight control effects are normally performed for level flight conditions using linear unsteady aerodynamic theory. The results of these calculations could be in error for manoeuvring conditions of military aircraft from medium up to high incidence, since the applied linear theories do not account for effects of leading edge vortices at higher incidences and effects of locally separated flow are not included in the calculation of motion induced unsteady aerodynamic forces. These effects may be introduced into the aeroservoelastic analysis using a correction method as described in ref. 1 to 3 and using measured unsteady pressure distributions on a windtunnel model for only one rigid mode.

5.1   Description of the correction method

The correction method as developed in ref. 1 is applied for the update of generalised forces used in the analytical model for aeroservoelastic calculations.

The calculation of the generalised aerodynamic motion dependent forces $A_{rj}(\alpha_0, Ma, k)$ is performed by a modification of linear unsteady aerodynamic theory, the 3D Doublet lattice method, or the collocation method using both measured steady pressure distributions and the measured unsteady

pressure distribution of a wing oscillation. The problem consists here mainly in the prediction of the diagonal terms A_{rr} and of the coupling terms A_{rj}, at separated flow condition if only one measured mode is available.

The corrected generalised aerodynamic motion dependent forces $A_{rj}(\alpha_0, Ma, k)$ are calculated as follows for given Machnumber Ma and reduced frequency k.

$$A_{rj} = \iint_S \left(\Delta c_{pr}^*(\alpha_0, k) + \left(\Delta \bar{c}_{pic}(\alpha_0, k) - \Delta c_{pi}^*(\alpha_0, k) \right) \right) u_j \, ds$$

The corrected unsteady pressure distribution Δc_{pi}^* of the measured vibration mode $u_i(x, y)$ is calculated by using a modified cinematic boundary condition.

$$\Delta c_{pi}^* = (D' + iD'')^{-1} \cdot \alpha^*$$

where:

$(D' + iD'')$ is the matrix of aerodynamic influence coefficients

$$\alpha^* = \frac{U_\infty + \bar{u}_0}{U_\infty} \cdot \frac{\partial u_i}{\partial x} + i \cdot k \cdot \bar{u}_i$$

The local velocity $U_\infty + \bar{u}_0$ is calculated from local Machnumber and speed of sound.

$$U_\infty + \bar{u}_0(x, y) = a(x, y) \cdot Ma(x, y)$$

$$Ma(x, y) = \left\{ \frac{2}{\kappa - 1} \left[\frac{1 + \frac{\kappa - 1}{2} \cdot Ma_\infty^2}{\left(1 + \frac{\kappa \cdot Ma_\infty^2}{2} \cdot c_p\right)^{\frac{\kappa - 1}{\kappa}}} - 1 \right] \right\}^{\frac{1}{2}}$$

The local speed of sound $a(x, y) = \sqrt{\kappa R T}$ is derived from adiabatic compression.

From the difference between measured and corrected unsteady pressure distribution of the measured vibration mode an additive correction term

$$\left[\Delta c_{pi} - \Delta c_{pi}^* \right]$$

is known, which for the formulation of arbitrary vibration modes is assumed to be independent of the mode.

The corrected pressure distribution for arbitrary mode shapes u_j are then calculated by

$$\Delta c_{pj} = [D' + iD'']^{-1} \cdot \alpha_j^* + \left[\Delta \bar{c}_{pic} - \Delta c_{pi}^* \right]$$

In general the measured motion induced pressure contains a contribution of the fluctuating pressure at the reduced frequency of the harmonic oscillation k. The contribution $\Delta \tilde{c}_{po}(k)$ may be approximately extracted from the static measurement.

Therefore the measured unsteady pressure can be corrected.

$$\Delta \bar{c}_{pic}(k) = \left[\Delta \bar{c}_{pi}(k) + \Delta \tilde{c}_{pi}(k) \right] - \Delta \tilde{c}_{po}(k)$$

5.2   Windtunnel model description

5.2.1   Unsteady pressure plotting model

Windtunnel tests were performed on a 1/7 scaled half model of a tactical fighter type aircraft. The model configuration included a delta wing, a foreplane and half a fuselage installed at the windtunnel wall. The wing and foreplane were very stiff, machined out of steel, see Figure 4.
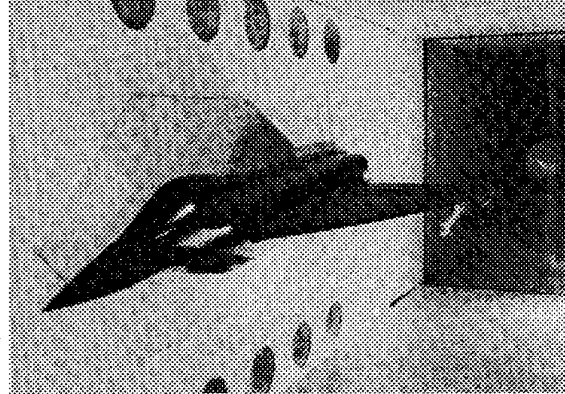
Fig. 4: Wind Tunnel Model

The fuselage was fixed to the turn table by means of a large rigid cylindrical part locked when incidence was reached by a set of hydraulic brakes, Fig. 5. The fuselage contained two hydraulic rotating actuators. The first one aligned with the foreplane axis, allowed to give static foreplane deflections while the second one aligned with the fuselage centre line provided roll excitation of the wing.

The different measurements performed were steady and unsteady pressure fields, steady and unsteady roll moment, accelerations on the wing. The model was equipped with 67 pressure pickups, 67 steady pressure tapping, 7 accelerometers, 3 strain gauge bridges. The steady and unsteady pressure pick-ups pairs were distributed along four wing sections on the upper surface and, in a smaller number, along three wing sections on the lower surface.
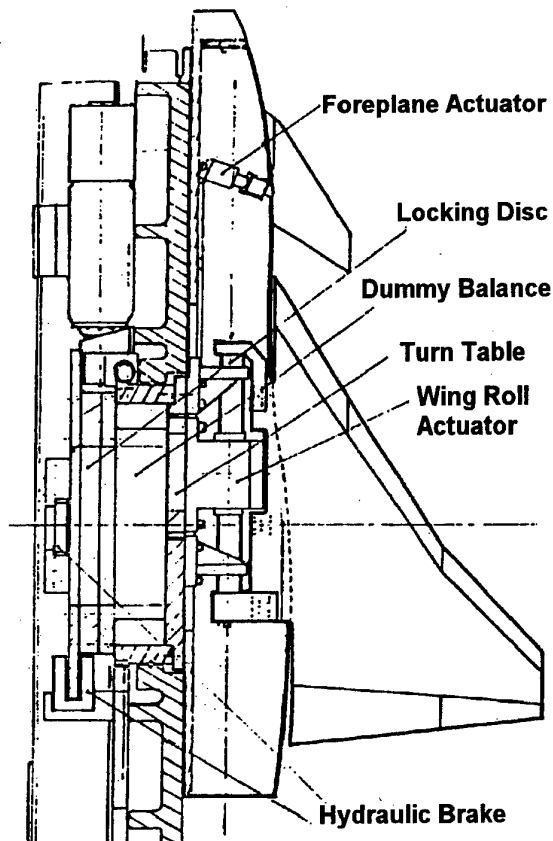

Fig. 5: Windtunnel Model Set Up

Tests were performed using sinusoidal wing roll excitation. After conditioning and switching, amplifying and filtering at a cut-off frequency chosen between once and twice the excitation frequency, the signals were digitalized at a sampling rate of eight times the excitation frequency. Fourier analysis was performed, modulus and phase of each signal, normalised to the amplitude of the roll oscillation were computed at the excitation frequency, giving unsteady pressure coefficients.

Tests were performed for different Mach numbers and angles of attack including buffeting situations. The Mach number ranged from 0.3 to 0.95, incidence ranged from 0 to 40 degrees, decreasing as Mach number increased: 40 degrees at M = 0.3, 10 degree at M = 0.85 and 0.9, 8 degrees at Ma = 0.95.

5.2.2 Steady pressure plotting model

In addition to the unsteady pressure model which included steady/quasisteady pressure measurement, a full series of quasisteady measurement have been performed on a steady pressure plotting windtunnel model. Especially steady pressures have been measured for different flap deflections at different high incidence to derived the derivatives due to flaps $\partial \Delta c_p / \partial \alpha_{Flap} (\alpha, Ma)$.

5.3 Measured quasisteady pressures distributions ($\alpha \pm \Delta \alpha$ conditions)

The quasisteady pressure distributions $\partial \Delta c_p / \partial \alpha$ are demonstrated for some characteristic conditions in Figures 6 to 8 for the upper and lower wing surface separately. There are 7 spanwise section shown for upper and lower side, 5 are corresponding to real measurement sections. The values at $y/s = 0.3$ and 0.15 are interpolated.

Mach 0.8, zero incidence
The pressure distribution at upper and lower side shown in Fig. 6 above is typical for subsonic flow, upper and lower side pressures are similar in amplitude, no transonic effect are apparent. The applicability of linear subsonic theory may be reasonable for this condition.
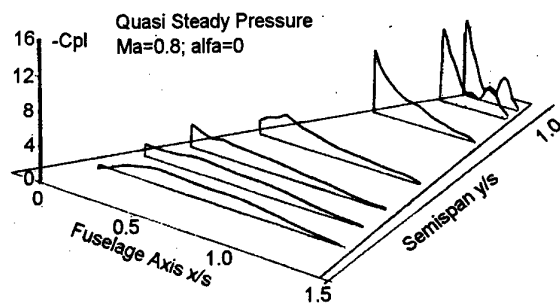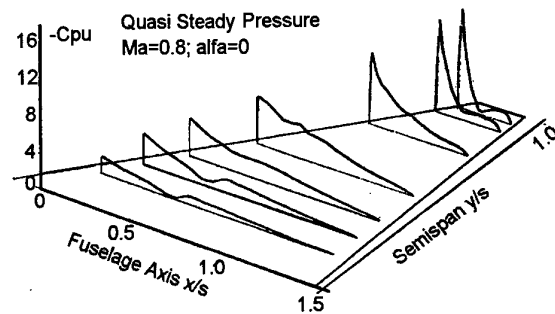
Fig. 6: Quasisteady Pressures at upper and lower side, Ma = 0.8, α = 0°

Mach 0.9, zero incidence

The pressure distribution at the wing upper side is characterised by transonic effects, visible in the spanwise sections y/s = 0.5, 0.75, 0.9, 0.95, possibly due to a shock located at about midchord is shown in Fig. 7.

The lower side shows less effects and is similar to the Ma = 0.8 results.

Quasi Steady Pressure
Ma=0.9; alfa=0
-Cpu

Quasi Steady Pressure
Ma=0.9; alfa=0
-Cpl
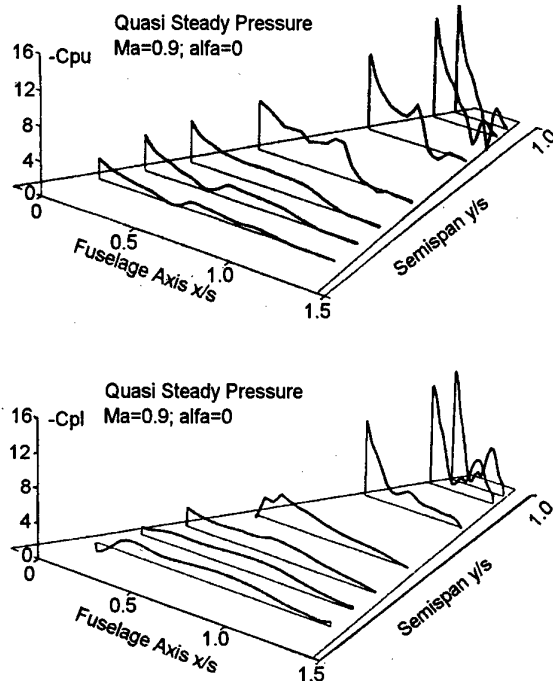
Fig. 7: Quasisteady Pressures at upper and lower side, Mach = 0.9, α = 0°

Mach 0.8, α = 8.0 degree

Strong changes can be observed in the upper side pressure distribution if the static incidence is increased from 0 to 8.0 degrees indicating a strong nonlinear behaviour of the quasisteady forces with incidence, Fig. 8. High effects due to a leading edge vortex are present for the inner wing resulting in high pressure peak's, even changes in pressure sign are observed at y/s = 0.5.

The lower side pressures are less effected, especially for inner wing sections, however outer wing sections show a decrease in amplitude compared to zero incidence results.

Similar strong leading edge vortex effects are observed also at Mach 0.9 at inner wing sections in the upper side pressure distribution.

The strong increase of the outer wing trailing edge pressures compared to zero incidence results observed at α = 8.0 deg. upper side gives an indication of the changes in mode excitation if the behaviour is extrapolated to pressure for outboard flap rotation.

Quasi Steady Pressure
Ma=0.8; alfa=8.
-Cpu

Quasi Steady Pressure
Ma=0.8; alfa=8.
-Cpl
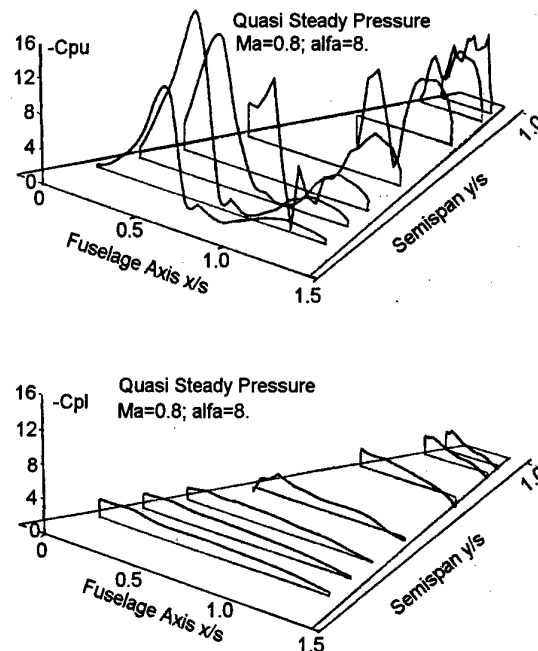
Fig. 8: Quasisteady Pressures at upper and lower side, Mach = 0.8, α = 8°

Conclusion from quasisteady pressures $\partial \Delta c_p / \partial \alpha$:

Mach 0.8, α = 8.0 deg.

- A very strong non-linear behaviour of quasisteady pressure distributions at wing upper side with static incidence observed both for Ma = 0.8 and Ma = 0.9. The lower side pressures are less affected by static incidence and remain almost unaffected from 6.5 degree onwards.

- Outer wing trailing edge pressures show an increase compared to zero incidence results, indication higher excitation forces if extrapolated for instance to outboard flap rotation both for Ma = 0.8 and Ma = 0.9 and incidences greater than zero.

Quasisteady pressure distributions for flap deflections $\partial \Delta c_p / \partial \delta_{Flap} \left(\delta_{Flap} \pm \Delta \delta_{Flap} \right)$

Normal force derivative versus incidence due to flap deflection. Fig. 9 demonstrates the trend of the normal force derivative due to inboard $\partial c_N / \partial \delta_{IB}$ and outboard flap $\partial c_N / \partial \delta_{OB}$ versus incidence. As shown above by quasisteady pressures the normal force derivative decreases strongly from 10 deg onwards both for inboard and outboard flap deflection.
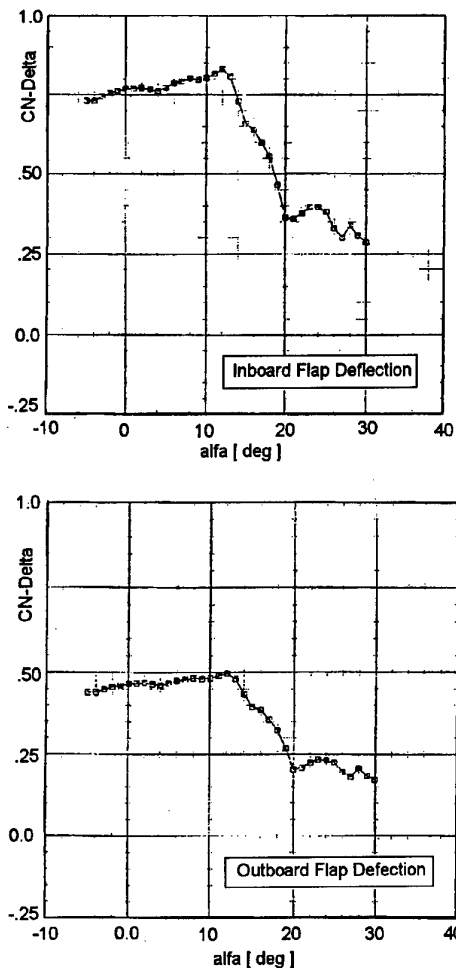
Fig. 9: Ma=0.8, Normal Force Derivative
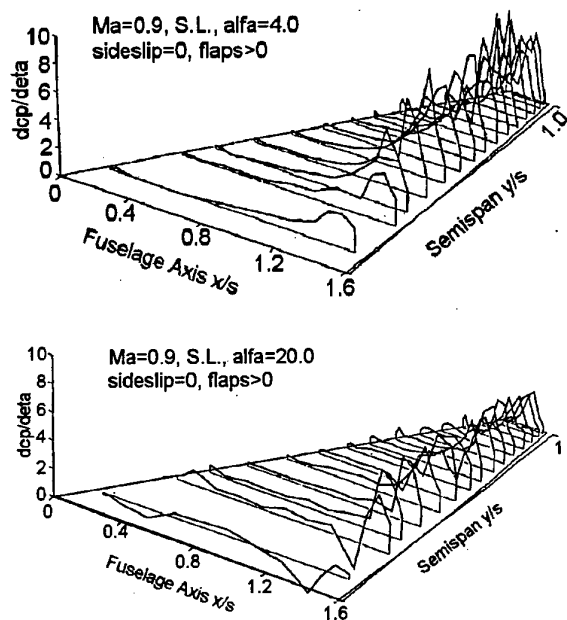Versus Incidence due to I/B and O/B Deflection

5. 4 Description of measured unsteady pressure distribution due to harmonic wing roll oscillations

Quasisteady pressure distributions for α = 4 deg and α = 20 deg due to fullspan flap deflection are demonstrated in Fig. 10 for Mach = 0.9 .
The comparison shows the decrease of $\Delta c_p \delta$ with incidence. Especially the outer wing experiences a strong decrease at 20 deg compared to α = 4 deg.

5.4.1 Mach 0.8 results

The pressure distributions due to harmonic wing roll are demonstrated for the upper and lower side of the wing in real and imaginary part of the unsteady pressure upper side in Figure 11.

$$c_{pu}(x,y,z) = c_{pu}(x,y,z) + i \cdot c_{pu}(x,y,z)$$

for real and imaginary part k = $2\pi fs/V$ reduced frequency f = 10 Hz.

Static incidence 8.0 degrees
Strong non-linear affects with incidence are found in general for the inner upper wing leading edge corresponding to leading edge vortex effects and also for the outer wing sections strong α dependent effects occur in the real and imaginary part of the unsteady pressure. The lower side pressure distributions are less influenced. Only one example is demonstrated here for 8.0 degrees and Mach 0.8.

Fig. 10: Quasisteady Pressure Distribution due to Flap Deflection: Comparison of high α
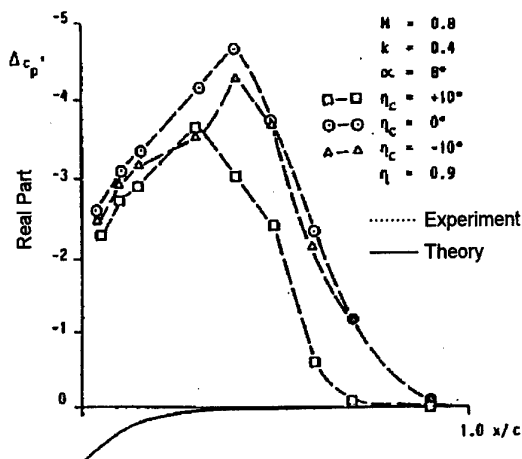
Fig. 11: Unsteady Pressures Distribution due to Wing Roll Motion, Ma = 0.8; α = 8°
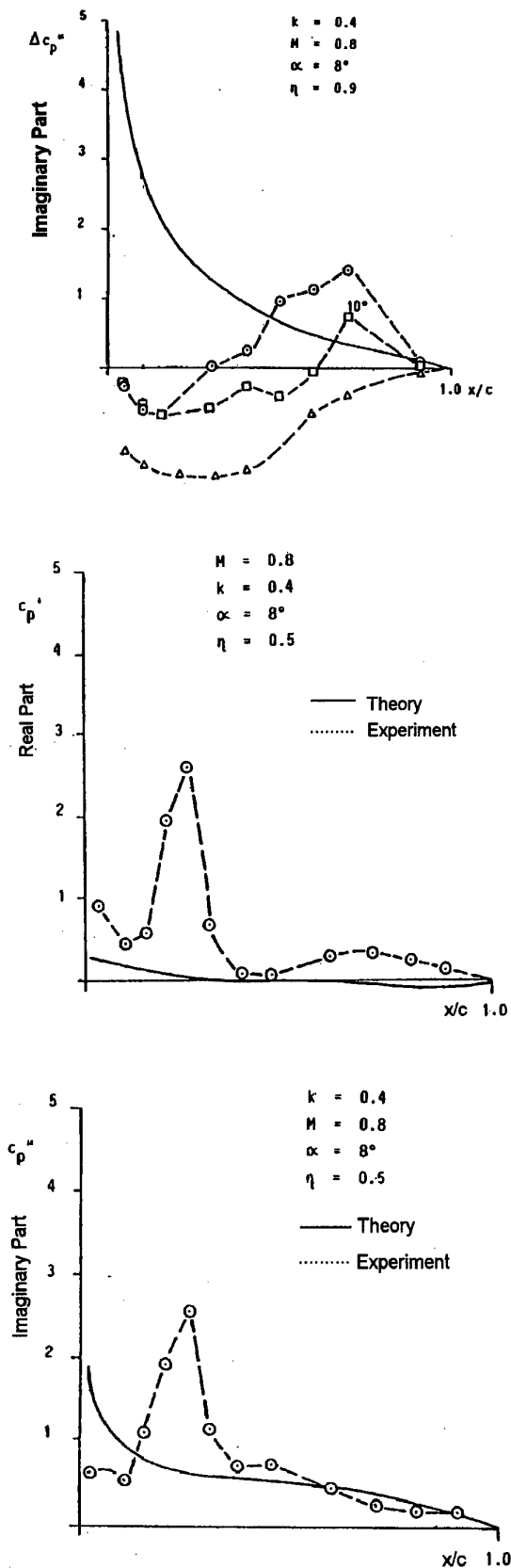
Fig. 11: Unsteady Pressures Distribution due to Wing Roll Motion, Ma = 0.8; $\alpha = 8°$

Conclusions of the unsteady results

Similar strong non-linear effects with static incidence as observed for quasisteady pressures are present in unsteady upper side pressures due to harmonic wing roll oscillations. The modulus of the unsteady pressures is increased at incidences 3.5 to 9.0 degrees at the inner wing loading edge region and at the trailing edge outer wing region in real and imaginary part. The lower side unsteady pressures are less affected by static incidence.

5.4.2 Mach 0.3 results

The unsteady pressure distributions due to the wing roll oscillations were evaluated for different static incidences from $\alpha = 12.5$ up to 40 degrees and roll motion frequencies 6, 12 and 18 Hz for the clean wing configuration for wing upper and lower side. Some results are shown in Figure 12 for 25 degrees.

Influence of frequency

The imaginary part of the upper side pressure distribution changes almost linearly with frequency in the measured frequency range 6 - 18 Hz. All typical leading edge vortex effects are repeated with different frequency for different high static incidences. A quasisteady behaviour is found at high incidence.

Influence of static incidences

The increase in the amplitude of the upper side outer wing imaginary parts of the pressure distribution at high incidence compared to zero incidence or linear theory gives indication of an increase in elastic mode damping at least for the first wing elastic bending mode.

There is also the indication that the aerodynamic damping of elastic modes will be present up to 40 degrees of incidence, since all imaginary parts of the pressure distribution for all high α conditions up to 40 degree are of significant amplitude and increase linearly with frequency. Therefore no loss of damping may be expected also for other modes than the rigid wing roll mode.

Lower mode excitation due to an inboard/outboard flap rotation might be expected due to the decrease ($\alpha > 13$ deg) of trailing edge real and imaginary pressures found at all high incidences as also found in quasisteady measurements. It might be concluded that quasisteady measurements are sufficient to predict the magnitude of unsteady aerodynamics.

-Cpu Unsteady Pressure Real Part upper side
4   Ma = 0.3, alfa = 25°, f = 6Hz

-Cpu Unsteady Pressure Imag. Part upper side
4   Ma = 0.3, alfa = 25°, f = 6 Hz

Cpl   Unsteady Pressure Real Part lower side
4   Ma = 0.3, alfa = 25°, f = 6 Hz

Cpl   Unsteady Pressure Imag. Part lower side
4   Ma = 0.3, alfa = 25 °, f = 6 Hz
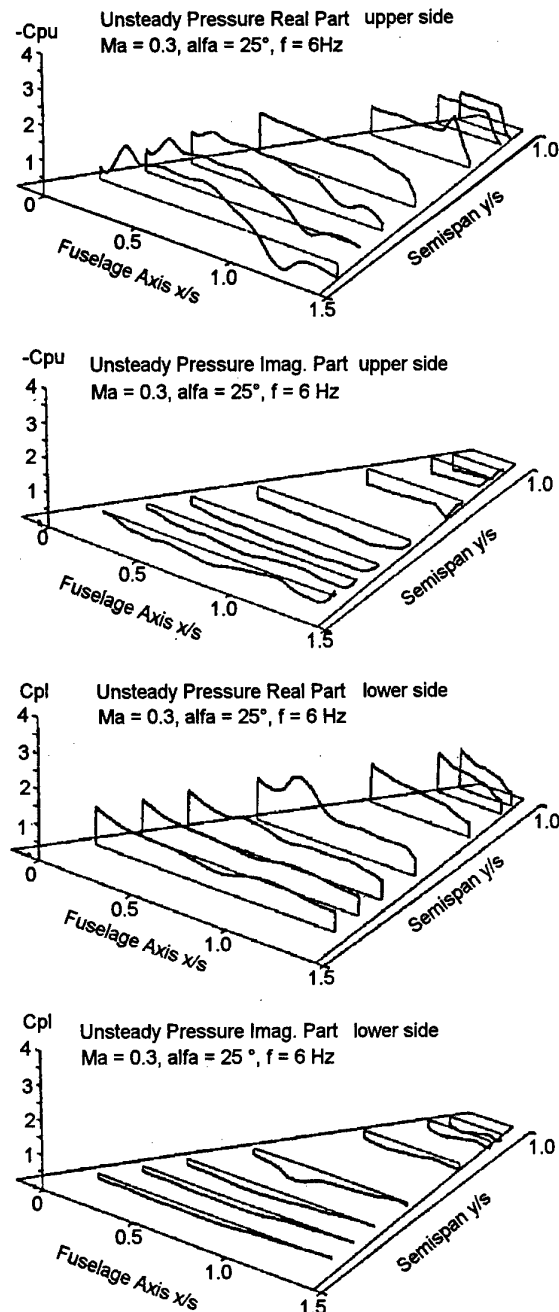
Fig. 12: Unsteady Pressure Distribution due to Wing Roll, Ma = 0.3, α = 25°, f = 25 Hz

5.5 Generalised aerodynamic forces at high incidence

Two aerodynamic magnitudes are essential for the aeroservoelastic stability namely:

- The generalised control surface efficiencies
- The aerodynamic mode damping

For the structural configuration treated the generalised aerodynamic damping of the low frequency elastic total aircraft modes and the generalised inboard and outboard flaperon unsteady efficiencies will cause the most interesting coupling effects in flight.

Generalised control surface efficiencies
α > 13 deg
For Mach 0.4 both for the inboard and outboard flap the correction causes in general a decrease in the magnitude of the real part of the generalised control surface efficiencies of about 10% - 48% of the theoretical value depending on the normal mode. The unsteady hinge moments of outboard flap is strongly decreased. The imaginary parts of the efficiencies are also strongly changed.

α < 10 deg.
The effects on unsteady outboard efficiencies are different at Ma = 0.8, α = 6.5 and 8 degrees. Factors up to 1.7 are present depending on the mode. The effects are smaller at Ma = 0.9 α = 7.5 deg, factors up to 1.35 are found compared to linear theory. The increase for α < 10, decrease for α > 13 degree was also found in the steady normal force derivative.

Aerodynamic mode damping

Comparison of corrected and theoretical generalised forces for the second elastic mode are shown in table 2 for Mach 0.4, and in table 3 for Mach 0.8.

- At Mach 0.4, 25 deg the imaginary part of the second elastic mode is increased by a factor of 1.25.

- At Mach 0.8, 6.5 degrees the imaginary part of the second elastic mode is increased by a factor of 1.7, at Mach 0.8, 9 degrees the factor is also 1.7.

- At Mach 0.9, 7.5 degrees the imaginary part of the second elastic mode is increased by a factor of 1.3.

It is noted that the aerodynamic mode damping is proportional to the imaginary part of the generalised force.

6. Proof of the prediction method

The validation of the prediction method has been performed earlier in ref. 2 and 3 using windtunnel measurements on a trapezoidal wing.

The corrected pressure distribution A_{cpj} of a not measured mode j is predicted from a measured mode i according to chapter 5.1

$$\Delta \overline{c}_p(i\omega)_j = \Delta c_p(i\omega)_{j-th} + \left(\Delta c_{pi}(i\omega)_{exp} - \Delta c_{pi}(i\omega)\right) \cdot \frac{\alpha_j(i\omega)}{\alpha_i(i\omega)}$$

The windtunnel measurements on the trapezoidal wing have been performed for a pitch and roll motion, see Figure 13.
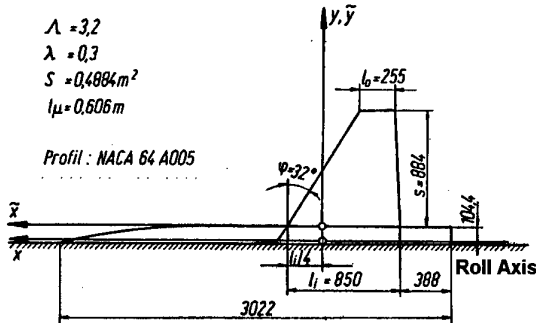
Fig. 13: Trapezoidal Wing Windtunnel Model for unsteady pressure measurement

For instance the corrected (predicted) pressure distribution of a pitch oscillation from a roll oscillation is

$$\Delta \overline{c}_{p,Pitch}(i\omega) = \Delta c_{p,Pitch}(i\omega) + \Delta c_{pD1}(i\omega) \frac{1 + ik(x - x_D)}{iky}$$

$$\Delta c_{pD1} = \Delta c_{p,Roll-exp.} - \Delta c_{p-Roll}$$

or the corrected pressure distribution of a roll oscillation from a pitch oscillation is

$$\Delta \overline{c}_{p,Roll}(i\omega) = \Delta c_{p,Roll}(i\omega) + \Delta c_{pD2}(i\omega) \frac{iky}{iky1 + ik(x - x_D)}$$

$$\Delta c_{pD2} = \Delta c_{p,Pitch-exp.} - \Delta c_{p-Pitch}$$

Figure 14 demonstrates the comparison between theoretical and measured results of a wing roll motion with predicted pressures from wing pitch motion pressures. The result fully validates the correction method for subsonic speeds.

$$\overline{\Delta c}_{pj} = [D' + iD'']^{-1} \cdot \alpha_j^* - \Delta c_{pi} - \Delta c_{pi}^*$$

$$\alpha_j^* = \frac{U_\infty + u}{U_\infty} \cdot \frac{f_j}{x} + ikf_j + \frac{v_o}{U_\infty} \cdot \frac{f_j}{Y}$$

is simplified because the influences of local velocity components were shown to be of minor influence for low subsonic flow.
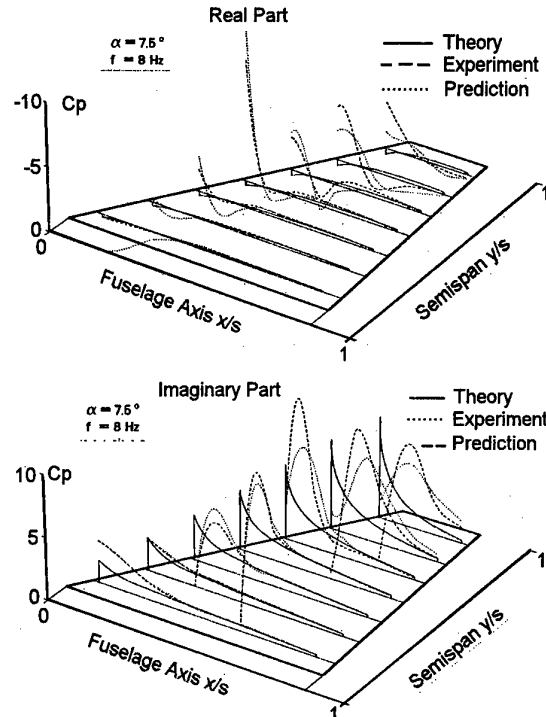
Fig. 14: Validation of the correction Method for High Incidence Aerodynamic

The validation of the method using transonic model results could not be performed in a consistent manner for high subsonic speeds since only one vibration mode, wing roll was tested.

In order to check the prediction at high Machnumber quasisteady results have been applied in order to predict unsteady pressures from wing roll measurements.

Using quasisteady pressures for the prediction of transonic model unsteady wing roll results was based on a reduced formula

$$\Delta c_{p-Roll}(\alpha, k) = \Delta c_{p-Roll_1}^{Theory} + \left[\Delta c_{p-\alpha}^{Exp}(\alpha, k = 0) - \Delta c_\alpha^{Theory}(k = 0)\right] \cdot iky$$

where

$\Delta c_{p-\alpha}^{Exp}(\alpha, k = 0)$ measured quasisteady

pressure distribution

$\Delta c_\alpha^{Theory}(k = 0)$ theoretical pressure distribution

The comparison of measured unsteady pressures of the transonic model wing roll motion with this prediction at Mach 0.8 and Mach 0.9 also demonstrated an improvement especially at the wing tip region.

7. Open loop frequency response functions

The effects of high incidence unsteady aerodynamic forces on gain and phase margins are illustrated in Figure 15 for the open loop response function of the longitudinal controller of the Delta Canard fighter aircraft for Mach 0.4, 25 degrees and sea level.

Figure 15 shows the Nicholas diagram with and without corrected aerodynamics in the frequency range up to the third elastic mode. The first wing bending mode with corrected unsteady aerodynamics shows a decrease in dB's and an additional phase shift compared to the not corrected frequency response.

The first elastic mode is shown to be phase stable, where as the second mode at 4.5 Hz does not meat the stability requirements indicated by the shaded area (notch filter effects are needed).

Fig. 15: Open Loop Frequency Response Function, Comparison high incidence aerodyn.
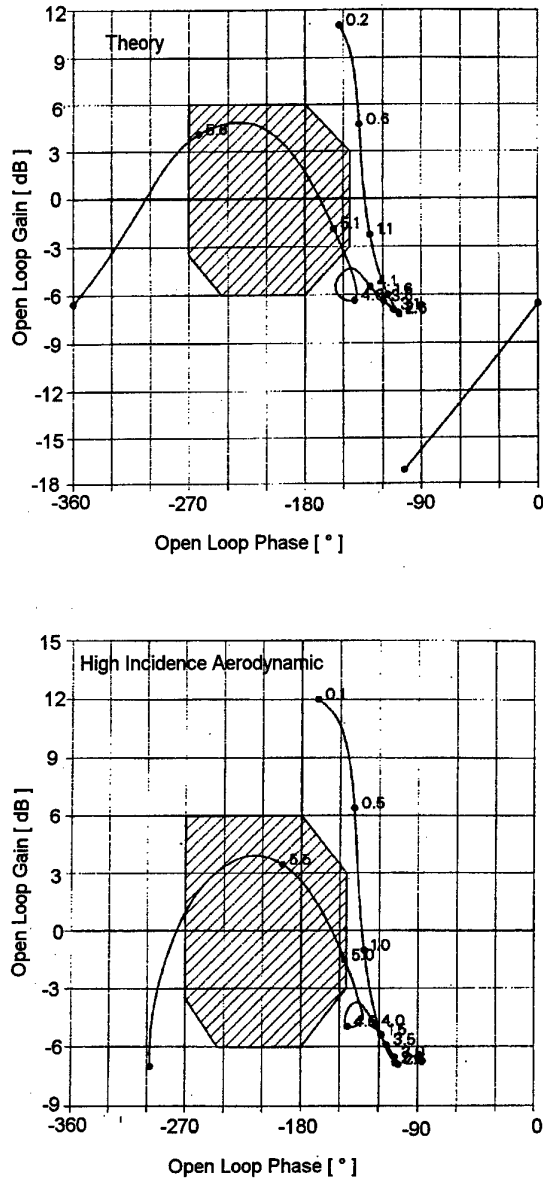
Fig. 16: Nichols Diagram open loop frequency Response, Comparison of High Incidence Aerodynamic Effects

In Figure 16 the results for Mach 0.8 and 8 degrees of incidence are illustrated without and with corrected unsteady aerodynamic forces in the Nicholas diagram. For corrected and pure theoretical unsteady aerodynamic forces the results show a phase stable first and second elastic mode.

The third mode at 5.5 Hz does not meet the requirements with and without the effect of high incidence aerodynamics, but with incidence correction a reduction of the positive dB`s is present. For higher elastic modes at 9 and 12 Hz the effect is about a 4 dB increase as demonstrated in the Bode diagram in Figure 17. In general the high α unsteady aerodynamic forces lead to alleviation of the dB level in the 1st wing bending mode and give raise to the phase shift.
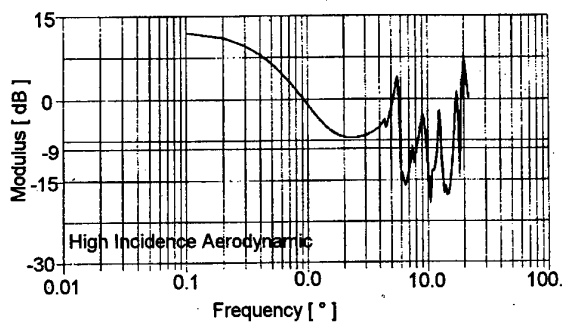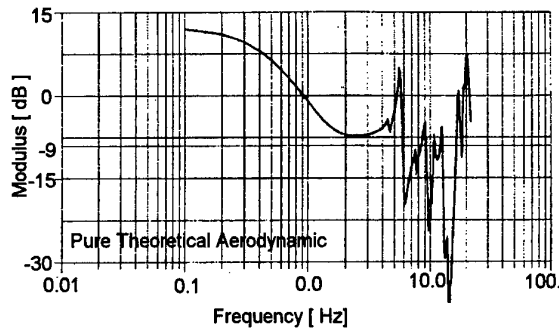
Fig. 17: Bode Diagram of Open Loop Frequency Response, Comparison of High Incidence Aerodynamic, Ma = 0.8, α = 8°

8. Conclusions

From the investigation of the aeroservoelaetic behaviour of a Delta Canard configuration at high incidence the following conclusion can be drawn:

- The structural coupling effects of low frequency elastic wing bending modes distribution caused by pitch rate feedback can not be influenced by

sensor positioning. The low frequency modes must be phase stabilised using filters.

- At incidences below about 6 to 13 degrees the unsteady aerodynamic damping of elastic modes is smaller than the damping at small incidence.

- At incidences above 13 degrees the elastic mode damping is higher than the values at small incidence.

- The control surface unsteady aerodynamic forces above about 13 deg of incidence are decreasing and their phase shift increases leading to dB reductions in open loop frequency response functions and additional phase shift.

- The prediction method for high incidence unsteady aerodynamics is validated by windtunnel tests.

- The prediction method has to be validated through flight test.

- In general high incidence aerodynamic effects have to be considered in aeroservoelaetic stability predictions.

9. References

1   Becker J.
Bewegungsinduzierte Luftkräfte bei abgelöster Strömung und ihre Übertragung auf die Ermittlung der Strukturresponce. 1983
Dissertation Technische Universität Braunschweig,

2   Becker J.; Weiss F.; Weitz U.
Prediction of unsteady aerodynamic forces at Static incidence
MBB/LKE292/S/R/1570 March 1986

3   Zingel H.
Experimental Investigation and Semiempirical Prediction of a low Aspect Ratio Trapezoidal Wing Due to Flow Separation.
AGARD-Specialists Meeting on Aircraft Dynamic Loads due to Flow Separation Sorrento, Italy, 1990

4   Becker J.; Gravelle A.
Some results of experimental and analytical buffeting investigations o a Delta wing. Second International Symposium on Aeroelasticity and Structural Dynamics,
April 1-3. 1985, Aachen

5   Luber W.; Schmid H.
Flutter Investigation in the Transonic Flow Regime
for a Fighter Type Aircraft
AGARD 55th SMP meeting, Toronto Canada,
1982

6   Becker J.; Luber W.
Unsteady Aerodynamic Forces at High Incidence
and Their Application in Structural- and Flight
Control System Design
International Forum on Aeroelasicity and Structural
Dynamics
26-28. June 1995, Manchester, UK

Generalised Forces of **First** Elastic Mode		
Mode	Ma = 0.4, k = 0.5, α = 0 °	
N0	Real Part	Imaginary Part
1	- 0.00001433	0.000002274
2	- 0.0001537	0.00001882
3	0.0001892	- 0.00000388
4	- 0.0002493	0.00003429
5	- 0.00009616	0.000003141
6	0.0001343	- 0.00005503
7	0.0002158	- 0.0000204
8	0.0000945	0.00001851
9	- 0.0002496	0.00001810
10	0.00004518	0.00008549

**Table 2a: Pure Theoretical Generalized
Aerodynamic Forces of 1st Elastic Mode
Ma=0.4, k=0.5, α=0°**

Generalised Forces of **First** Elastic Mode		
Mode	Ma = 0.4, k = 0.5, α = 25 °	
N0	Real Part	Imaginary Part
1	- 0.00001568	0.00000550
2	- 0.0001716	0.00006041
3	0.0002474	- 0.00007965
4	- 0.0002744	0.0001062
5	0.0001289	0.00003640
6	0.00007601	- 0.00002757
7	0.0002546	- 0.00004711
8	0.0001989	- 0.00002882
9	- 0.0003587	0.00007063
10	0.0001635	- 0.0005685

**Table 2b: Corrected Generalized Aerodynamic
Forces of 1st Elastic Mode
Ma=0.4, k=0.5, α=25°**

Generalised Forces of **Second** Elastic Mode		
Mode	Ma = 0.4, k = 0.5, α = 0 °	
No	Real Part	Imaginary Part
1	0.00003953	0.00005300
2	0.0005247	0.0006567
3	0.0008979	-.10211
4	0.0008267	0.001117
5	- 0.0004031	-0.0004026
6	0.0001672	-0.0003934
7	0.0007172	-0.0004710
8	0.0005312	-0.0003275
9	- 0.0007978	0.0006582
10	- 0.0005874	-0.0002293

**Table 3a: Pure Theoretical Generalized
Aerodynamic Forces of 2nd Elastic Mode
Ma=0.4, k=0.5, α=0°**

Generalised Forces of **Second** Elastic Mode		
Mode	Ma = 0.4, k = 0.5, α = 25 °	
No	Real Part	Imaginary Part
1	0.00003172	0.00006188
2	0.0004805	0.0008194
3	0.00096190	- 0.0014671
4	0.0006923	0.001403
5	0.0004330	0.0005823
6	0.0001387	0.0000602
7	0.0008705	- 0.000451
8	0.0007595	- 0.000673
9	- 0.0009688	0.000836
10	- 0.001742	0.000218

**Table 3b: Corrected Generalized Aerodynamic
Forces of 2nd Elastic Mode
Ma=0.4, k=0.5, α=25°**

Generalised Forces of First Elastic Mode		
Mode	Ma = 0.8, k = 0.5, α = 0 °	
No	Real Part	Imaginary Part
1	- 0.00001568	0.000003261
2	- 0.0001703	0.00002626
3	0.0002131	0.000000468
4	- 0.0002758	0.00004727
5	- 0.0001079	0.000004113
6	0.0001450	- 0.00008669
7	0.0002390	- 0.00004396
8	0.0001117	0.00002989
9	- 0.0002826	0.00002951
10	0.0000267	- 0.0001317

Table 4a: Pure Theoretical Generalized Aerodynamic Forces of 1st Elastic Mode Ma=0.8, k=0.5, α=0°

Generalised Forces of First Elastic Mode		
Mode	Ma = 0.8, k = 0.5, α = 6.5 °	
No	Real Part	Imaginary Part
1	- 0.00002837	0.00001523
2	- 0.0002943	0.0001063
3	0.0004135	0.0000525
4	- 0.0004718	0.0001944
5	- 0.0002160	0.0000233
6	0.0001072	- 0.0004658
7	0.000344	- 0.0002962
8	- 0.000370	0.0000867
9	- 0.0006443	0.000268
10	- 0.0002553	- 0.000559

Table 4b: Corrected Generalized Aerodynamic Forces of 1st Elastic Mode Ma=0.8, k=0.5, α=6.5°

Generalised Forces of Second Elastic Mode		
Mode	Ma = 0.8, k = 0.5, α = 0°	
No	Real Part	Imaginary Part
1	- 0.00004183	0.00006174
2	- 0.0005784	0.0007545
3	0.001065	- 0.001135
4	- 0.0009078	0.001279
5	- 0.0004627	0.000459
6	0.000830	- 0.000533
7	0.0007200	- 0.000627
8	0.0006679	- 0.0003566
9	- 0.0008845	0.0007964
10	- 0.0009134	- 0.0003091

Table 5a: Pure Theoretical Generalized Aerodynamic Forces of 2nd Elastic Mode Ma=0.8, k=0.5, α=0°

Generalised Forces of Second Elastic Mode		
Mode	Ma = 0.8, k= 0.5, α = 6.5 °	
No	Real Part	Imaginary Part
1	- 0.0000319	0.000113
2	- 0.000584	0.00128
3	0.001933	- 0.00166
4	- 0.001017	0.00223
5	- 0.000770	0.000732
6	- 0.00144	- 0.00137
7	0.000588	- 0.00134
8	0.001549	- 0.000319
9	- 0.000995	0.00138
10	- 0.003319	- 0.00168

Table 5b: Corrected Generalized Aerodynamic Forces of 2nd Elastic Mode Ma=0.8, k=0.5, α=6.5°

Generalised Forces of First Elastic Mode		
Mode	Ma = 0.8, k = 0.5, α = 0°	
No	Real Part	Imaginary Part
1	- 0.00001568	0.000003261
2	- 0.0001703	0.00002626
3	0.0002131	0.000000468
4	- 0.0002758	0.00004727
5	- 0.0001079	0.000004113
6	0.0001450	- 0.00008669
7	0.0002390	- 0.00004396
8	0.0001117	0.00002989
9	- 0.0002826	0.00002951
10	0.0000267	- 0.0001317

Table 6a: Pure Theoretical Generalized Aerodynamic Forces of 1st Elastic Mode Ma=0.8, k=0.5, α=0°

Generalised Forces of First Elastic Mode		
Mode	Ma 0.8, k = 0.5, α = 8.0 °	
No	Real Part	Imaginary Part
1	- 0.00002067	0.000005742
2	- 0.0002678	- 0.000003112
3	0.0005179	0.000223
4	- 0.0002269	0.00002287
5	- 0.0001302	- 0.00005679
6	0.000233	- 0.0003974
7	0.0003955	- 0.0001993
8	- 0.0004609	0.000232
9	- 0.0006454	0.0000414
10	- 0.0001441	- 0.0006855

Table 6b: Corrected Generalized Aerodynamic Forces of 1st Elastic Mode Ma=0.8, k=0.5, α=8.0°

Generalised Forces of Second Elastic Mode		
Mode No	Ma = 0.8, k = 0.5, α = 0°	
	Real Part	Imaginary Part
1	- 0.00004183	0.00006174
2	- 0.0005784	0.0007545
3	0.001065	- 0.001135
4	- 0.0009078	0.001279
5	- 0.0004627	0.000459
6	0.000830	- 0.000533
7	0.0007200	- 0.000627
8	0.0006679	- 0.0003566
9	- 0.0008845	0.0007964
10	- 0.0009134	- 0.0003091

Table 7a: Pure Theoretical Generalized Aerodynamic Forces of 2nd Elastic Mode Ma=0.8, k=0.5, α=0°

Generalised Forces of Second Elastic Mode		
Mode No	Ma = 0.8, k = 0.5, α = 8.0°	
	Real Part	Imaginary Part
1	- 0.00006028	0.00009879
2	- 0.001182	0.001279
3	0.003109	- 0.002028
4	- 0.001866	0.002335
5	- 0.001205	0.0007689
6	- 0.001888	- 0.0005377
7	0.0008453	- 0.0008769
8	0.002208	- 0.0001753
9	- 0.00147	0.0006049
10	- 0.004434	- 0.001867

Table 7b: Corrected Generalized Aerodynamic Forces of 2nd Elastic Mode Ma=0.8, k=0.5, α=8.0°

Generalised Forces of First Elastic Mode		
Mode No	Ma=0.9, k=0.5, α = 0°	
	Real Part	Imaginary Part
1	- 0.0000165	0.00000429
2	- 0.0001793	0.00003433
3	0.0002345	0.000002205
4	- 0.0002895	0.00006146
5	- 0.0001167	0.000006226
6	0.0001313	- 0.0001167
7	- 0.0002459	- 0.0000678
8	0.00013138	0.0000378
9	- 0.0003019	0.00004408
10	- 0.00001428	- 0,0001696

Table 8a: Pure Theoretical Generalized Aerodynamic Forces of 1st Elastic Mode Ma=0.9, k=0.5, α=0°

Generalised Forces of First Elastic Mode		
Mode No	Ma= 0.9, k= 0.5, α = 7.5°	
	Real Part	Imaginary Part
1	0.000010406	- 0.00000164
2	0.0001033	- 0.0000302
3	- 0.00006217	0.0000759
4	0.0001380	- 0,00003738
5	0.0000293	- 0.00002627
6	- 0.000316	- 0.00000848
7	- 0.0000737	- 0.000005276
8	0.00001303	0.0000654
9	0.0001374	- 0.0000524
10	- 0.0003077	- 0.000125

Table 8b: Corrected Generalized Aerodynamic Forces of 1st Elastic Mode Ma=0.9, k=0.5, α=7.5°

Generalised Forces of Second Elastic Mode		
Mode No	Ma=0.9, k=0.5, α = 0°	
	Real Part	Imaginary Part
1	- 0.0000401	0.0000681
2	- 0.000590	0.000827
3	0.001190	- 0.00123
4	- 0.000918	0.001398
5	- 0.000498	0.000505
6	- 0.0000688	- 0.000629
7	0.000644	- 0.000736
8	0.000793	- 0.000402
9	- 0.000903	0.000917
10	- 0.001279	- 0.000295

Table 9a: Pure Theoretical Generalized Aerodynamic Forces of 2nd Elastic Mode Ma=0.9, k=0.5, α=0°

Generalised Forces of Second Elastic Mode		
Mode No	Ma= 0.9, k= 0.5, α = 7.5°	
	Real Part	Imaginary Part
1	- 0.0000399	0.000000514
2	- 0.000748	0.000111
3	0.001837	- 0.000456
4	- 0.001227	0.000260
5	- 0.000646	0.0002209
6	- 0.000458-	0.000925
7	0.000377	- 0.000348
8	0.001034	- 0.000254
9	- 0.000766	- 0.0000489
10	- 0.00219	0.000366

Table 9b: Corrected Generalized Aerodynamic Forces of 2nd Elastic Mode Ma=0.9, k=0.5, α=7.5°

A Unified Unsteady Aerodynamic Module for Aeroelastic and MDO Applications

P.C. Chen, D. Sarhaddi
ZONA Technology, Inc., Mesa, Arizona 85202

D.D. Liu
Arizona State University, Tempe, Arizona 85287

Summary

Recent advances in the lifting surface methods are attributed to the possible generalization of the Aerodynamic Influence Coefficient (AIC) method to the Transonic and Hypersonic flight regimes. Thus, a unified AIC (UAIC) approach has been developed for aeroelastic/MDO applications in the complete Mach number range.

A typical CFD method usually requires CFD/CSD interfacing in a time-domain aeroelastic analysis, while additional grid generation effort is needed in each MDO design cycle. The former procedure is still underdeveloped and the latter could be costly. Free from these procedures, the present UAIC is fully compatible with classical linear aeroelastic matrix equations. Thus, the UAIC approach as an unsteady aerodynamic module can be readily integrated with current standard FEM systems or into a MDO environment, practiced by aerospace industries. Specifically, the present module consists of four major unsteady aerodynamic codes which jointly cover all flight regimes, thereby rendering the module unified for all Mach numbers. First, the capability of the present aerodynamic module will be discussed. Second, the seamless integration of the present aero module with a MDO software ASTROS is properly defined. Third, cases studied for the validation of the integrated aerodynamic module will be presented. These include: supersonic analysis of a swept untapered wing, a fighter wing with transonic flutter constraint and a rectangular wing in roll with control surface reversal.

Finally, we will present our concept of computational aeroelasticity in terms of Aeroelasticity Modeling Methodology (AIC methods) and Aeroelasticity Simulation Methodology (CFD methods) from the standpoint of industrial application. We believe that these two methodologies, if their practices follow the proposed global strategy, could compliment each other in achieving further computational expediency and with wider applicability.

INTRODUCTION

In recent years, rapid progress in aeroservo-elasticity and multi-disciplinary optimization (MDO) has demanded further improvement of computational aerodynamic methods in their capability to generate s-domain aerodynamics, their compatibility with structural FEM and their expediency for design optimization. Meanwhile, aerodynamic parameters such as wing thickness, body-wing configurations, and Mach number range to cover Transonic and Hypersonic flow regimes are considered as important parameters to be included in a general aerodynamic module, ready to be integrated with a MDO system such as ASTROS[1].

Although current CFD methods have reached a rather mature stage for steady aerodynamic design/analysis, its acceptance by industries for aeroelastic applications is still hampered by the

problems in grid generation, CFD/CSD interfacing and extensive turn around time. For example, without a major modification, the program structure of ASTROS remains totally unfriendly to be interfaced with a time-accurate CFD method[2,3]. On the other hand, panel methods imbedded in the Aero module of ASTROS such as the Doublet Lattice Method[4] (DLM) and the Constant Pressure Method[5] (CPM), albeit fully compatible with the structural FEM, requires further improvement in their robustness, their confinement to lifting surfaces (rather than wing-body systems) and their extendibility to transonic and hypersonic Mach numbers.

Towards this end, during the last few years we have re-examined the above lifting surface methods critically from the viewpoint of program robustness and range of applicability. The result of this re-examination effort is a developmental planning of a unified

aerodynamic influence coefficient (UAIC) approach extending the applicability of our current wing-body AIC methods to the transonic and hypersonic regimes (Fig. 1). This paper attempts to report this UAIC approach and review these methods developed in each valid flight regime accordingly.

A unified unsteady aerodynamic module (hereinafter called ZAERO module) is developed based on the UAIC formulation. The ZAERO module is a stand-alone Aerodynamic module, which can be interfaced with existing FEM programs such as NASTRAN and ASTROS. Under Wright Lab/AF contractual support, a seamless integration of the ZAERO module into ASTROS is being carried out. Fig. 2 shows the integrated ASTROS/ZAERO program architecture.

In what follows, three validation cases for ASTROS/ZAERO will be presented. These include a swept untapered wing analysis in supersonic flow, a fighter wing with transonic flutter constraint and a rectangular wing in roll with control surface reversal.

ZAERO: A UAIC BASED AERODYNAMIC MODULE

The ZAERO module consists of four major unsteady aerodynamic codes that jointly cover the complete domain of all Mach number ranges, namely ZONA7U (formerly ZONA51U), ZONA6, ZONA7 and ZTAIC. As can be seen in Fig 1, the aero modules currently integrated within MSC/NASTRAN and ASTROS only have the purely subsonic and supersonic capabilities.

By contrast, the ZAERO module serves as a unified aerodynamic tool which provides computed data from unsteady pressures to Generalized Aerodynamic Forces (GAF's) throughout all Mach numbers by means of the unified AIC approach. In fact, it is the UAIC of the ZAERO Module that has efficiently provided the k-domain solution. By means of rational-approximation techniques[6,7] the s-domain solution can be obtained from the k-domain solution for the subsequent aeroservoelastic application[16,20,21,22].

The development of the ZAERO module has been the major endeavor of ZONA Technology in the last decade. The following is a brief account of the capability of the computer codes in ZAERO.

ZONA6/ZONA7: Generates Unsteady Subsonic/Supersonic Aerodynamics for Aircraft Configurations with External Stores[8,9]

Prior to 1990, all unsteady aerodynamics methods for aeroelastic computations were based on lifting-surface models (e.g. DLM). The aerodynamic effects due to the presence of bodies and due to wing-body interference were largely ignored. Meanwhile, the coupled external-store wing flutter, a problem that is of frequent concern to modern aeroelasticians, can no longer be resolved by the lifting surface modeling alone. For this reason, development of methods such as ZONA6/ZONA7 is mandatory.

In the following examples, Figs. 3 and 4 are computed by ZONA6 and Fig. 5 by ZONA7. Note that ZONA6 and ZONA7 are based on a higher-order panel formulation, and therefore are more robust than a low-order method like DLM. ZONA6 also includes a body-wake option for treatments of truncated stores.

Fig. 3 presents the out-of-phase pressures on two spanwise stations on a 70° Delta Wing. It is seen that using a typical panel cut, DLM totally breaks down at M=0.8 and k=0.5. Fig. 4 presents the unsteady pressure along the underwing store of a NLR Wing-Tiptank-Pylon-Store configuration. It is clearly seen that a large discrepancy exists between the results of body alone and that of the wing-body.

Fig. 5 presents the spanwise unsteady forces and moments of a NLR wing (F-5 wing) with underwing fin-missile and pylon. It is seen that, in both cases, the discrepancy between the wing-only results and the wing-body results are substantial.

ZONA51U/ZONA7U: Generates Unified Unsteady Hypersonic/Supersonic Aero-dynamics for Lifting Surface Systems[10,11] and Wing-body Configurations

A Unified Supersonic/Hypersonic Lifting Surface Method has been developed recently[10,11]. This method combines the Supersonic Lifting Surface Theory (such as ZONA51[12]) with a nonlinear thickness correction matrix E_{ij}, based on a composite third-order theory, which is rendered uniformly valid throughout the Hypersonic/Supersonic regime, i.e.

$$\{\Delta C_P\} = [D + \mu E]^{-1}\{w\}$$

where D is the linear supersonic downwash matrix provided by ZONA51 and μ is a switching function that operates on the nonlinear thickness matrix E for compression and expansion waves. This correction matrix takes the flow nonlinearity as well as the flow rotationality due to shock waves into account, which covers both the Mach wave and Newtonian limits. For aeroelastic applications, ZONA51U has been applied to various wing planforms with thickness distributions. Superseding ZONA51U, ZONA7 integrates ZONA51U into ZONA7 in that only the lifting surfaces are subject to unified hypersonic/supersonic aerodynamics.

Fig. 6 shows the GAF C_{L_α} of an oscillating wedge by ZONA7U is in good agreement with Euler solution[13]. Fig. 7 shows the flutter results of a 70° Delta Wing. It is found that ZONA7U improves substantially over the linear theory results in terms of pressures, stability derivatives, and provides more conservative flutter boundaries due to the thickness effect. Furthermore, the input format of ZONA7U is nearly the same as that of ZONA7 only with an additional input card on the Wing Profile Slope. The computing time for ZONA7U is also comparable to that of ZONA7.

ZTAIC: Generates Unsteady Transonic Aerodynamics for Lifting Surface Systems[14,15,16]

Since 1985, ZONA has been following up on the development of the Transonic Strip (TES) Method[14,15] for unsteady flow computations of arbitrary wing planforms. The TES method consists of two consecutive steps, to a given nonlinear Transonic Small Disturbance Code such as ZTRAN, namely the chordwise mean flow correction and the spanwise phase correction. Based on the TES concept, ZONA's Transonic Aerodynamic Influence Coefficient (ZTAIC) method is developed to fully automate the computation procedure resulting in a modal-based AIC matrix[16]. The computation procedure requires direct pressure input from a set of computed or measured data. Otherwise, it does not require airfoil shape or grid generation for a given planform. Meanwhile, all the mean-flow shock jumps are properly included in the resulting unsteady aerodynamics through the AIC formulation. The unsteady pressures can be readily solved on the surfaces of a lifting surface system according to the following modal-based AIC formulation, i.e.

$$\{\Delta C_p\} = [MAIC]\{h\}$$

where $[MAIC] = \left[\Delta C_{P_\phi} \cdot \left(\phi^T \phi\right)^{-1} \phi^T\right]$, ϕ is the baseline modes. ΔC_{P_ϕ} is the computed pressure due to ϕ, and h is the given modes which expressed in terms of ϕ.

Computed results of ZTAIC have been validated with existing results for a number of wing planforms. These include: the Lessing Wing[17] at M=0.9 (Fig 8); the LANN Wing[18]; the Northrop F-5 Wing with/without control surface[19] (see Refs. 14, 15 and 16).

Computed flutter results of the AGARD standard 445.6 wing (Fig. 9), the modeled F-16 Wing and the Doggett Wing are presented in Refs. 16, 20, 21, and 22. It is seen in Fig. 9 that the flutter results of ZTAIC and CAPTSD are in good agreement. In contrast to CAPTSD, the essential feature of ZTAIC is that it can provide transonic Modal AIC's, which can be readily adopted by the ASTROS static/dynamic matrix equations. The Modal AIC also serves as the aerodynamic transfer function. Once computed it can be repeatedly used in the ASTROS optimization loop. Furthermore, ZTAIC has a user-oriented input format which is fully compatible with that of DLM.

ZAERO MODULE IN ASTROS

According to the ASTROS/ZAERO program architecture (Fig. 2), database entities (such as MAIC) generated by the ZAERO module are computed during the ASTROS preface phase and need not be recomputed in the ASTROS analysis/optimization loop. Meanwhile, computation of the ZAERO module is triggered by the new bulk data entry MKAEROZ which specifies the Mach number, reduced frequencies, method flags and the mean flow conditions.

With the seamless integration of ZAERO into ASTROS near completion, several validation cases are underway. A case studied by Rodden[23] using MSC/NASTRAN — Aero II and two specific cases studied using ASTROS/CAPTSD by Kolonay[24] and by Andersen et al[25] are selected for present validations of the developed ASTROS/ZAERO.

Swept Untapered Wing: Supersonic Flutter Analysis[21]

Fig. 10 and Table 1 present a validation case on supersonic flutter analysis of a 15° swept untapered wing at M=1.3 and 3.0. In Table 1, computed results of ASTROS/ZONA7 for the no-thickness case and that of Rodden's method

(employing ZONA51 in MSC/NASTRAN) are compared with test data[26]. While the predicted flutter speeds with thickness effect (Case B) due to Rodden and ZONA7U are slightly unconservative at M=1.5, both are found conservative at M=3.0.

Fighter Wing Optimization with Transonic Flutter Constraint[24]
(Figs. 11-13, Tables 2-4)

A fighter wing test case by Kolonay is selected for the present validation of the ZAERO module for transonic aeroelastic analysis/optimization at a design Mach number M=0.93. Fig. 11 shows the FEM and ZAERO aerodynamic models for this wing. The FEM model consists of 86 grid points. 62 membrane (CQDMEM/ CTRMEM) elements are used for modeling the wing skins, 361 shear (CSHEAR) elements for spars and ribs, 111 rod (CROD) elements for sparcaps and shear webs. There are 26 design variables defined for skin, spar, rib, sparcap and shear web design. ASTROS/ZAERO optimization is performed for one flutter constraint, which is: Flutter free from 0 ~ 15,000 in/sec at M=0.93 with mean angle-of-attack of α=0.5°, and density at ρ=6.67E-07 slinch/in^3 (= lb-s^2/in^4).

Three unsteady aerodynamic methods in the ZAERO module are used in conjunction with the ASTROS optimization. These are: ZONA6, (linear subsonic), ZTAIC with CAPTSD[2] steady input (ZTAIC/TSD), and ZTAIC with ENSAERO[3] steady input (ZTAIC/N-S).

The flutter speeds and frequencies of the initial design (at M=0.93, α=0.5°) are presented in Table 2. Here, the flutter speed of the initial design is about 20% below the constrained flutter speed (15,000 in/s). The computed results of ZAERO are compared with those of Kolonay[27] using linear/nonlinear versions of CAPTSD with ASTROS. Overall, flutter results of the linear and nonlinear methods show good agreement. Less than 5% discrepancy in flutter speeds is found between ZTAIC/N-S and nonlinear CAPTSD.

Fig. 12 shows the steady and unsteady pressure distributions of the initial design (at M=0.93, α=0.5° and k=1.0). The steady pressures of CAPTSD show stronger shock strength than that of ENSAERO, as expected. This difference in shock strength does influence somewhat the in-phase and out-of-phase pressures due to first bending and torsion modes. However, it is interesting to note that the corresponding flutter speeds in Table 2 (at M=0.93 but at

different flutter frequency) vary no more than 2%.

Fig. 13 shows the design weight history of the fighter wing using ASTROS/ZAERO. Note that ASTROS optimization achieves converged solutions at the 11th iteration using ZONA6, 9th iteration using ZTAIC/TSD and 8th iteration using ZTAIC/N-S. By converged solution, it is meant that the weight is minimized, while the flutter constraint is satisfied. Table 3 presents the optimized weights and flutter speeds at final design. For final design weight due to the nonlinear methods, the difference between weight percentage change of ZAERO and CAPTSD is about 11% and the trend is acceptable.

By contrast, the final design weight due to the linear methods show opposite trend in weight percentage change. ZONA6 yields a 31.7% weight reduction whereas linear CAPTSD a 1.87% weight increase. The reason for this remains to be clarified.

Table 4 presents a list of local design variables of the final design structure. It is seen that the final structure design using ZTAIC/TSD and ZTAIC/N-S are nearly the same. They are also in good agreement with the results using nonlinear CAPTSD, except at design variables 8, 16 and 21. Again, variance in the percentage of structure changes of the design variables are noticed when using the linear methods.

Rectangular Wing in Roll Performance with Control Surface Reversal[25] *(Figs. 14-17)*

A rectangular wing test case of Andersen et al[25] is selected for the present validation of the ZAERO module for static aeroelastic analysis of the wing in roll with control surface reversal, the Mach number ranges from M=0.7 to 1.5.

Fig. 14 shows the planform and aerodynamic model of the wing with aileron. The FEM model (not shown here) is a beam model consisting of ten equal length beam elements along the one-third chord position. A single aileron spans the outboard half of the wing with the hinge line located at three-quarter chord.

Fig. 15 presents the "equivalent" rigid rolling moment derivatives C_{ℓ_δ} and reversal dynamic pressure $q_{reversal}$ computed by ZONA6, ZONA7 and ZONA7U. Note that C_{ℓ_δ} is aerodynamic related, but $q_{reversal}$ results from aerodynamic-structure interaction of the wing. Good agreement at M=0.85, 0.9, 0.925, 0.95, 0.975, 1.1, 1.2 and 1.5 with the solutions due to the

CAPTSD/linear method is noted. ZONA7U provides the most conservative solution at M=1.5.

Fig. 16 presents the "equivalent" rigid rolling moment derivatives and reversal dynamic pressure computed by ZTAIC/TSD, ZTAIC/N-S and by CAPTSD at five transonic Mach numbers (M=0.85, 0.9, 0.925, 0.95 and 0.975). It is seen that ZTAIC/TSD results are in good agreement with nonlinear CAPTSD. By contrast, different results using ZTAIC/N-S in C_{ℓ_δ} is observed near M=0.975, showing a low value of C_{ℓ_δ} obtained at M=0.975.

The discrepancies between the two ZTAIC solutions in C_{ℓ_δ} at high transonic Mach number is caused by the steady shock solutions of CAPTSD and ENSAERO. The C_p plot of Fig. 17 shows the forward shock location due to ENSAERO, in contrast to the aft shock (of the trailing edge) due to CAPTSD. Consequently, the lifting pressures ΔC_P are impacted by these steady shock solutions as shown by the ΔC_P's on the aileron. The kink in ΔC_P due to ZTAIC/N-S is clearly a result of the steady N-S shock solution. The large departure in these aileron ΔC_P's is known to affect the transonic hinge moment, whose value is sensitive to prediction methods and flow viscosity (Winzell, Ref. 28). Here, the effect of aileron ΔC_P on the rolling moment derivative is apparent.

COMPUTATIONAL AEROELASTICITY

Preference to CFD methods or AIC methods for aeroelastic applications has been the subject of much discussion. Here, we refer both methodologies as a part of the computational aeroelasticity. In general, our concept of computational aeroelasticity consists of Aeroelastic Modeling Methodology, which includes AIC methods, structural FEM, etc., and Aeroelastic Simulation Methodology, which includes CFD methods, closely-coupled CFD/CSD interfacing method, etc. (see Figs 18, 19) In our estimation, there should exist little conflict in the choice of these two methodologies for aeroelastic applications. Rather, they should compliment each other if their practices could follow the proposed strategy as shown in Figs 18 and 19.

On the one hand, AIC methods, as evidenced by the present module, could provide expedient amplitude-perturbation solutions in both the k-domain and s-domain. Consequently, their application to aeroservoelasticity and the MDO environment is straightforward. In terms of

aeroelastic applications, they should provide selected critical conditions for CFD methods to fine tune the unsteady aerodynamics in a confined flow regime, thus saving a substantial computing effort in search of potential flutter solutions.

On the other hand, the utilization of CFD methods is to link up with a structural FEM via a closely-coupled CFD/CSD interfacing, such as the BEM solver[29], as indicated in Figs 18, 19. Clearly, CFD methods are required when more accurate solutions become mandatory in a flow regime where nonlinearity dominates (e.g. thick wing in supercritical flow, high-angle-of-attack flow with vortex dynamics).

For classical-flutter predictions, the flow nonlinearity could be linearized through a robust indicial method routine in conjunction with a proposed modal AIC method[16]. In this way, CFD solutions could be carried over to the k-domain for its subsequent participation to aeroservoelasticity and MDO applications. For applications in static aeroelasticity, the proposed modal AIC method can be an expedient means in utilizing CFD solutions to generate a flexibility correction to the measured rigid load.

Thus, it is in this context that we propose the global strategy for computational aeroelasticity. From the standpoint of industrial application, the utilization of AIC methods and CFD methods should not be mutually exclusive, but rather be complimentary.

CONCLUSIONS

We have presented a unified AIC based unsteady aerodynamic module ZAERO, applicable to all ranges of Mach number, from subsonic to hypersonic. The seamless integration of ZAERO into ASTROS was successfully demonstrated by the present in-depth study on three selected validation cases. However, two specific findings in these cases studies are of some concern. For the fighter wing optimization case, good agreement is found between all methods in the initial design, but not so in the final design. The departure found between the final design results of two linear methods is probably caused by the difference in their aerodynamic sensitivities. Perhaps a standard test cases(s) should be established for applying other CFD methods to ASTROS for further verification of this issue.

For the rectangular wing in roll performance case, the disagreement between our two ZTAIC results in C_{ℓ_δ} using CAPTSD and ENSAERO steady inputs indicates that the inclusion of

viscous effect is crucial to the prediction of transonic static aerodynamic moments, as noted by Winzell.

As the seamless integration of ASTROS/ZAERO near completion, its validation should continue to cover more cases for transonic and hypersonic design and analysis.

ACKNOWLEDGMENT

References

1. Johnson, E.H. and Venkayya, V.B., "Automated Structural Optimization System (ASTROS), Theoretical Manual," AFWAL-TR-88-3028, Vol. 1, December 1988.
2. Batina, J.T., "Unsteady Transonic Small-Disturbance Theory Including Entropy and Vorticity Effects," Journal of Aircraft, Vol. 26, No. 6, June 1989, p. 531.
3. Guruswamy, G.P., "Time-Accurate Unsteady Aerodynamic and Aeroelastic Calculations of Wings Using Euler Equations," AIAA Paper No. 88-2281, April 1988.
4. Albano, E. and Rodden, W.P., "A Doublet-Lattice Method for Calculating Lift Distributions on Oscillating Surfaces in Subsonic Flows," AIAA Journal, Volume 7, February 1969, pp. 279-285.
5. Appa, K., "Constant Pressure Panel Method for Supersonic Unsteady Airfoils Analysis," Journal of Aircraft, Vol. 24, Oct. 1987, pp. 696-702.
6. Karpel, M., "Time-Domain Aeroservo-elastic Modeling Using Weighted Unsteady Aerodynamic Forces," J. Guidance, Control, and Dyn., Vol. 13, No. 1, 1990, pp. 30-37.
7. Karpel, M., and Strull, E., "Minimum-State Unsteady Aerodynamic Approximation with Flexible Constraints," CEAS, Manchester UK, June 1995, pp. 66.1-66.8.
8. Chen, P.C., Lee, H.W. and Liu, D.D., "Unsteady Subsonic Aerodynamics for Bodies and Wings with External Stores Including Wake Effort," Journal of Aircraft, Vol. 30, No. 5, Sept.-Oct. 1993, pp. 618-628.
9. Chen, P.C., Liu, D.D., "Unsteady Supersonic Computation of Arbitrary Wing-Body Configurations Including External Stores," Journal of Aircraft, Vol. 27, No. 2, February 1990, pp. 108-116.
10. Liu, D.D., Yao, Z.X., Sarhaddi, D. and Chavez, F., "From Piston Theory to a Unified Hypersonic-Supersonic Lifting Surface Method," Journal of Aircraft, Vol. 34, No. 3, May-June 1997, pp. 304-312.
11. Liu, D.D., Chen, P.C., Yao, Z.X. and Sarhaddi, D., "Recent Advances in Lifting Surface Methods," the Aeronautical Journal of the Royal Aeronautical Society, Vol. 100, No. 958, Oct. 1996, pp. 327-339.
12. Chen, P.C. and Liu, D.D., "A Harmonic Gradient Method for Unsteady Supersonic Flow Calculations,"

Journal of Aircraft, Vol. 22, No. 5, May 1985, pp. 371-379.
13. Hui, W.H., "Unified Unsteady Supersonic-Hypersonic Theory of Flow Past Double Wedge Airfoils," Journal of Applied Mathematics and Physics, 34, (4), 1983, pp. 458-488.
14. Liu, D.D. and Kao, Y.F., "An Efficient Method for Computing Unsteady Transonic Aerodynamics of Swept Wings with Control Surfaces," AIAA-85-4058, Oct. 1985.
15. Liu, D.D., "Computational Transonic Equivalent Strip Method for Applications to Unsteady 3D Aerodynamics," AIAA-83-0261, Reno, NV, Jan. 10-13, 1983.
16. Chen, P.C., Sarhaddi, D. and Liu, D.D., "Transonic AIC Approach for Aeroelastic and MDO Applications," Presented at the Euromech Colloquium 349 at DLR, Göttingen, Germany, Sept. 16-18, 1996.
17. Lessing, H.C., Troutman, J.L. and Menees, G.P., "Experimental Determination of the Pressure Distribution on a Rectangular Wing Oscillating in the First Bending Mode for Mach Numbers from 0.24 to 1.30," NASA TN D-33, December 1960.
18. Malone, J.B. and Ruo, S.Y., "LANN Wing Test Program: Acquisition and Application of Unsteady Transonic Data for Evaluation of Three-Dimensional Computational Methods," AFWAL-TR-83-3006, Feb. 1983.
19. Sotomayer, W.A. and Borland, C.J., "Numerical Computation of Unsteady Transonic Flow about Wings and Flaps," AIAA Paper 85-1712, 1985.
20. Chen, P.C., Liu, D.D., Sarhaddi, D., Striz, A.G., Neill, D.J. and Karpel, "Enhancement of the Aeroservoelastic Capability in ASTROS," STTR Phase I Final Report WL-TR-96-3119, Sept. 1996.
21. Chen, P.C., Sarhaddi, D., Liu, D.D. and Karpel, M., "A Unified Unsteady Aerodynamic Influence Coefficient Approach for Aeroelastic/Aeroservoelastic and MDO Applications," AIAA 97-1181-CP, Kissimmee, FL, Apr. 7-10, 1997.
22. Chen, P.C., Sarhaddi, D., Liu, D.D., Karpel, M., Striz, A.G. and Jung, S.Y., "A Unified Unsteady Aerodynamic Module for Aeroelastic, Aeroservoelastic and MDO Applications," CEAS, Vol. 2, Rome, Italy, Jun. 17-20, 1997.
23. Rodden, W.P., "Correction Factors for Supersonic Thickness Effects," MSC/NASTRAN, WPR-3, April 1, 1991.
24. Kolonay, R.M., "Unsteady Aeroelastic Optimization in the Transonic Regime," AIAA-96-3983-CP, Bellevue, WA, Sept. 4-6, 1996.
25. Andersen, G, Kolonay, R.M. and Eastep, F., "Control-Surface Reversal in the Transonic Regime," AIAA-97-1385, Kissimmee, FL, Apr. 7-10, 1997.
26. Tuovila, W.J. and McCarty, J.L., "Experimental Flutter Results for Cantilever-Wing Models at Mach Numbers Up to 3.0," NACA RM L55E11, 1955.
27. Kolonay, R.M., Private Communication.
28. Winzell, B., "Recent Applications of Linear and Nonlinear Unsteady Aerodynamics for Aeroelastic Analysis," AGARD SMP, Transonic Unsteady Aerodynamics, Paper 5, Oct. 1991.
29. Chen, P.C. and Jadic, I., "CFD/CSD Interfacing via an Innovative Structural Boundary Element Method," AIAA-97-1088CP, Kissimmee, FL, Apr. 7-10, 1997.
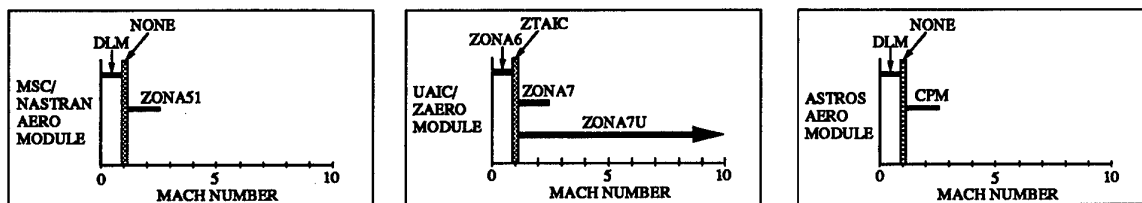
Figure 1. *ZAERO* and Other Aerodynamic Modules.
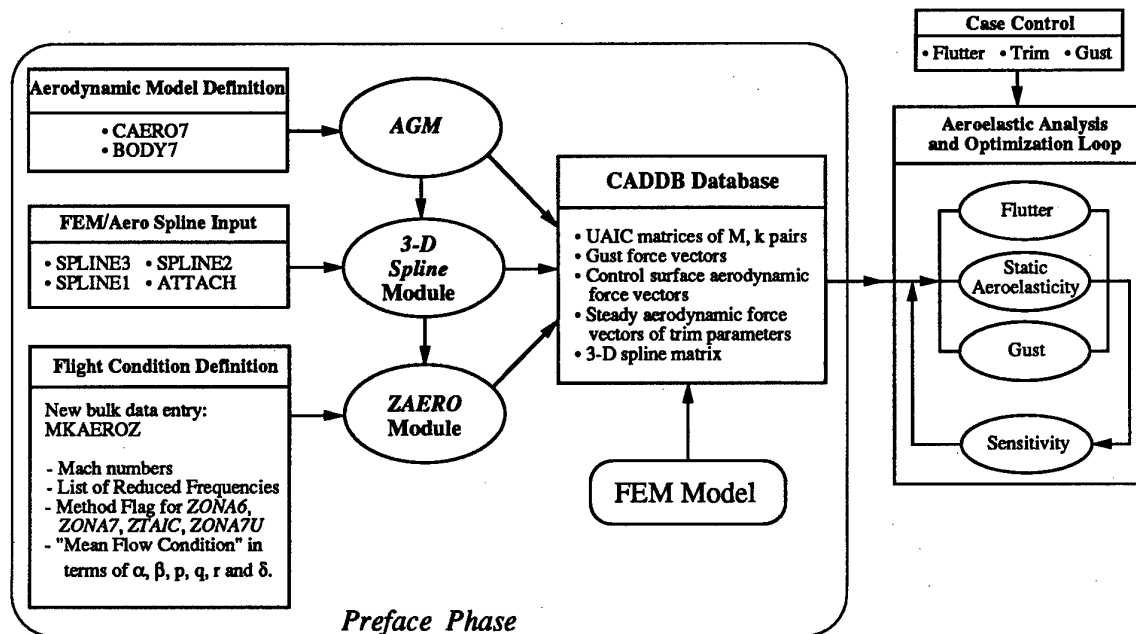
Figure 2. *ASTROS/ZAERO* Program Architecture.
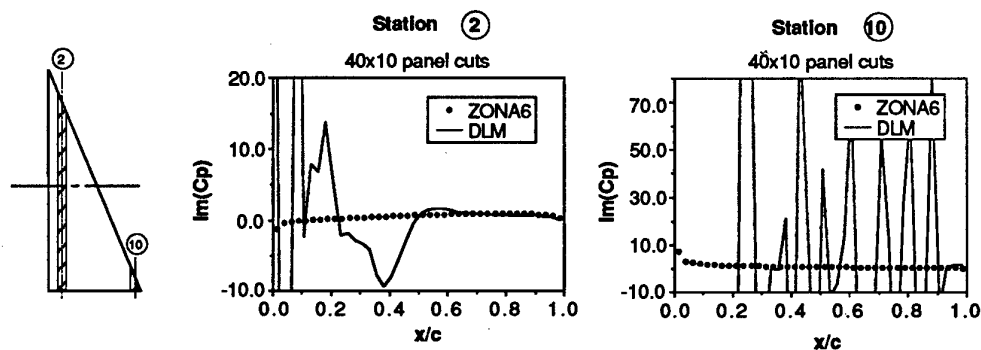
Figure 3.   Out-of-Phase Pressures on Two Spanwise Stations.
70° Delta Wing at M=0.8, k=0.5, Pitch Axis=0.5c_R.
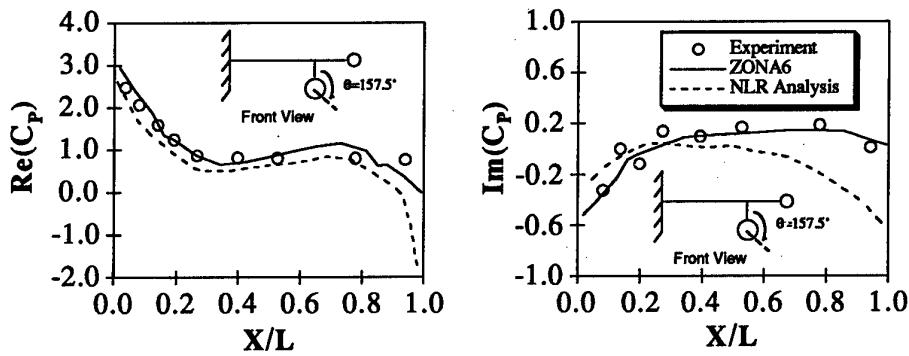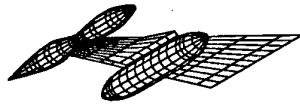
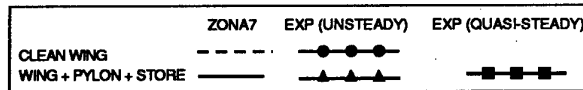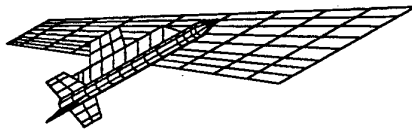Figure 4.   Unsteady Pressures Along Store of NLR Wing-Tiptank-Pylon-Store Configuration at M=0.45, k=0.3055, Pitch Axis=$0.5c_R$.
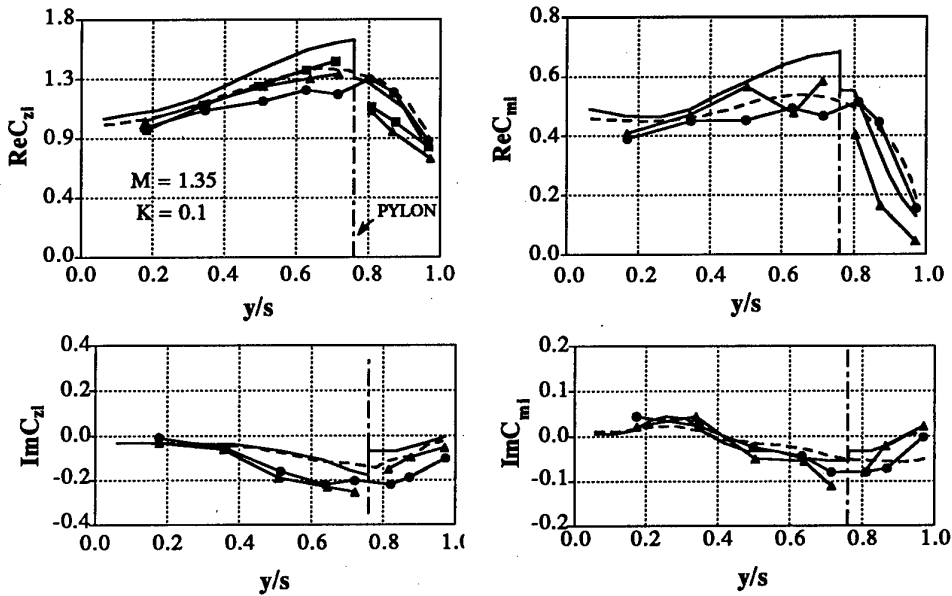
Figure 5.   Spanwise Normal Force and Pitching Moment for the Clean F-5 Wing and F-5 Wing with Underwing Store Configuration at M=1.35 and Reduced Frequency k=0.1, pitch axis=$0.5c_R$.
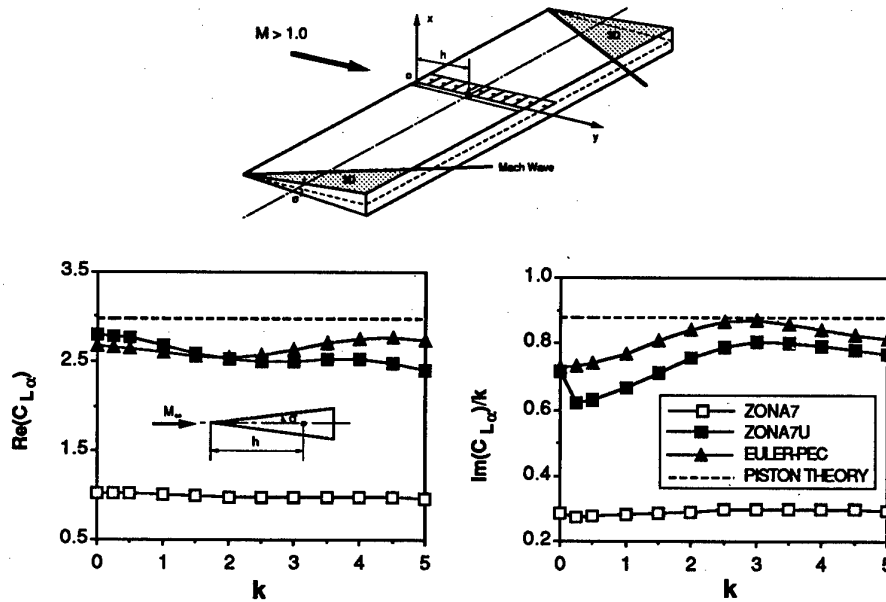
Figure 6.   GAF $C_{L\alpha}$ and $C_{M\alpha}$ of a Rectangular Wing with Wedge Profile at Various Reduced Frequencies (M=4.0, σ=15°, h=0.25c).
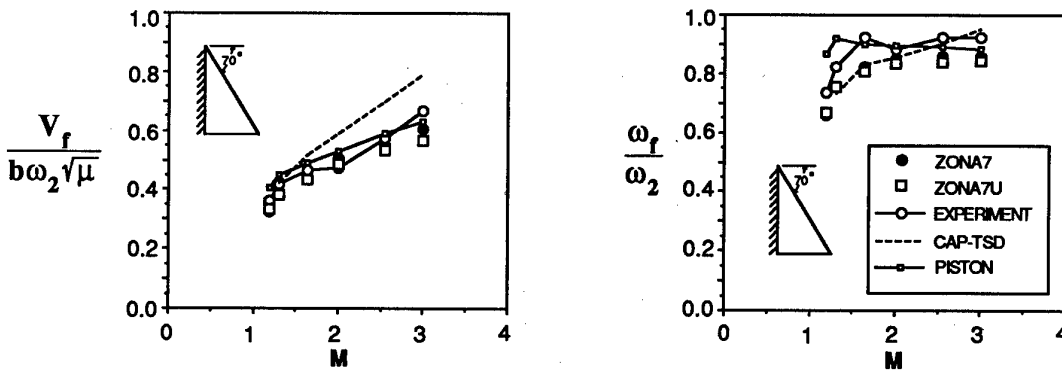
Figure 7.   Flutter Speeds and Frequencies of a 70° Delta Wing vs. Mach Number.
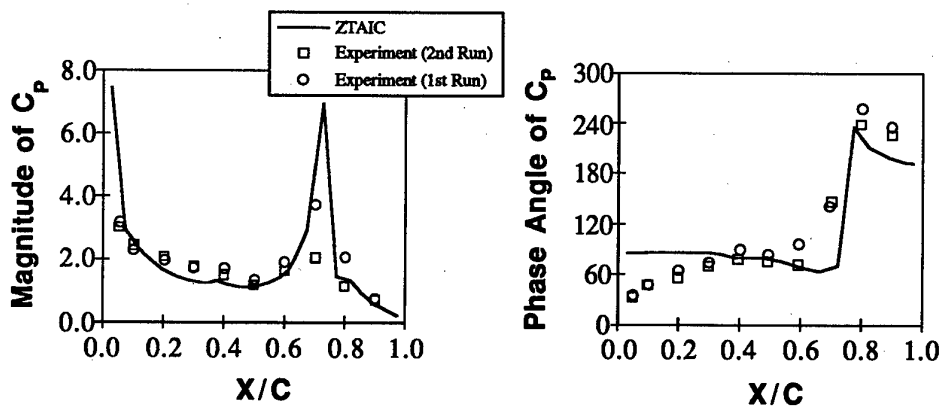
Figure 8.   Lessing Wing Oscillating in First Bending Mode at M=0.9, k=0.13.
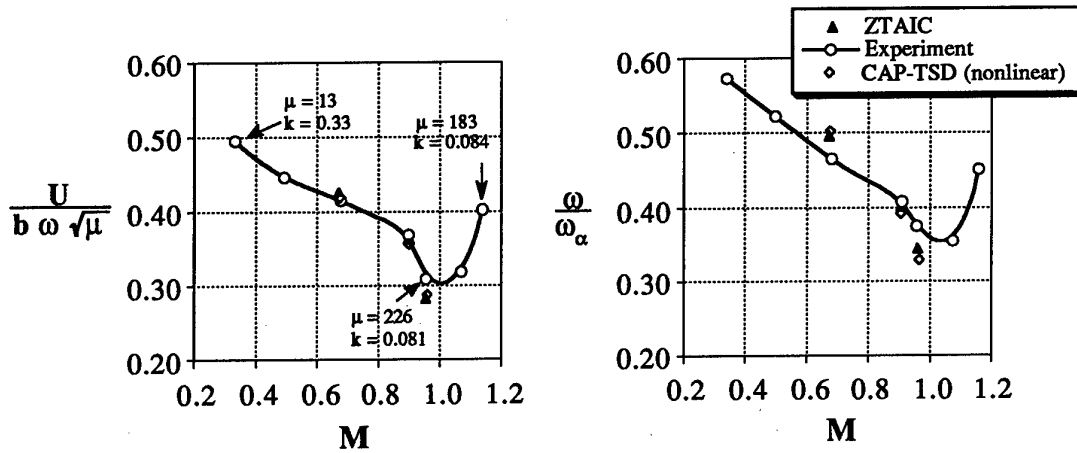
Figure 9. Flutter Boundary of AGARD 445.6 Wing at M=0.678, 0.90 and 0.95.
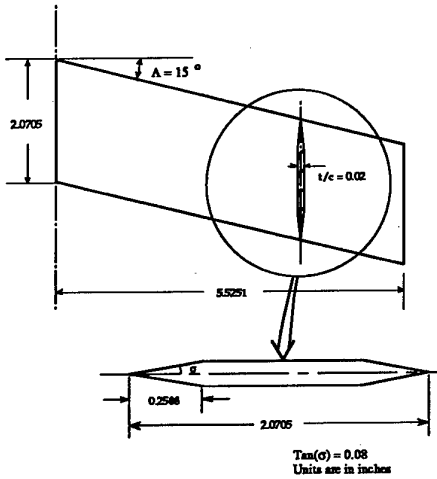
Figure 10. 15° Swept Untapered Wing
Showing Dimensions.

Table 1. Flutter Results of a 15° Swept Untapered Wing With
and Without Thickness Effect.

Flutter Results of Case HA145FB (With/Without Thickness)

| | $\sigma = 0.20606$ | | $\sigma = 0.391$ | |
| | M=1.3 | | M=3.0 | |
	V_f(ft/s)	f_f(Hz)	V_f(ft/s)	f_f(Hz)
Test	1280	102	2030	146
Rodden	1397	124	1913	149
ASTROS (ZAERO) K-Method/P-K Method				
ZONA7	1583/1601	132/130	2369/2448	158/154
ZONA7U	1415/1426	123/122	1859/1923	156/152

$\sigma = \rho/\rho_{sea\ level}$
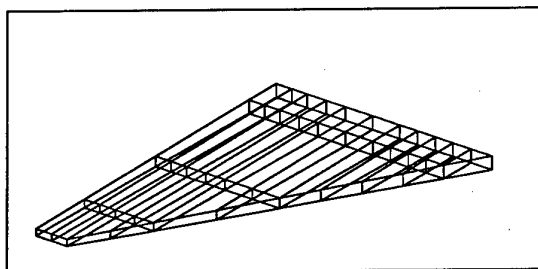
FEM Model
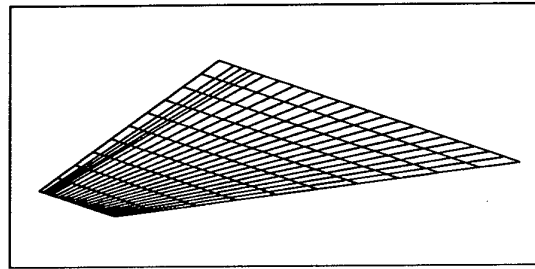
ZAERO Model

Figure 11. Structural/Aerodynamic Models of a Fighter Wing Test Case: Optimization with Transonic Flutter
Constraints at M=0.93 (Kolonay, Ref. 24).

Table 2. Flutter Speeds of the Initial Design: Fighter Wing Optimization.

	Linear Method		Nonlinear Method		
	Kolonay (Linear CAP-TSD)	ASTROS/ZAERO (ZONA6)	Kolonay (Nonlinear CAP-TSD)	ASTROS/ZAERO (ZTAIC/TSD)	ASTROS/ZAERO (ZTAIC/N-S)
Flutter Speed (in/s)	12,492	12,309	12,137	11,734	11,550
Flutter Frequency (Hz)	19.72	19.71	19.64	19.61	19.55

M=0.93, α=0.5°
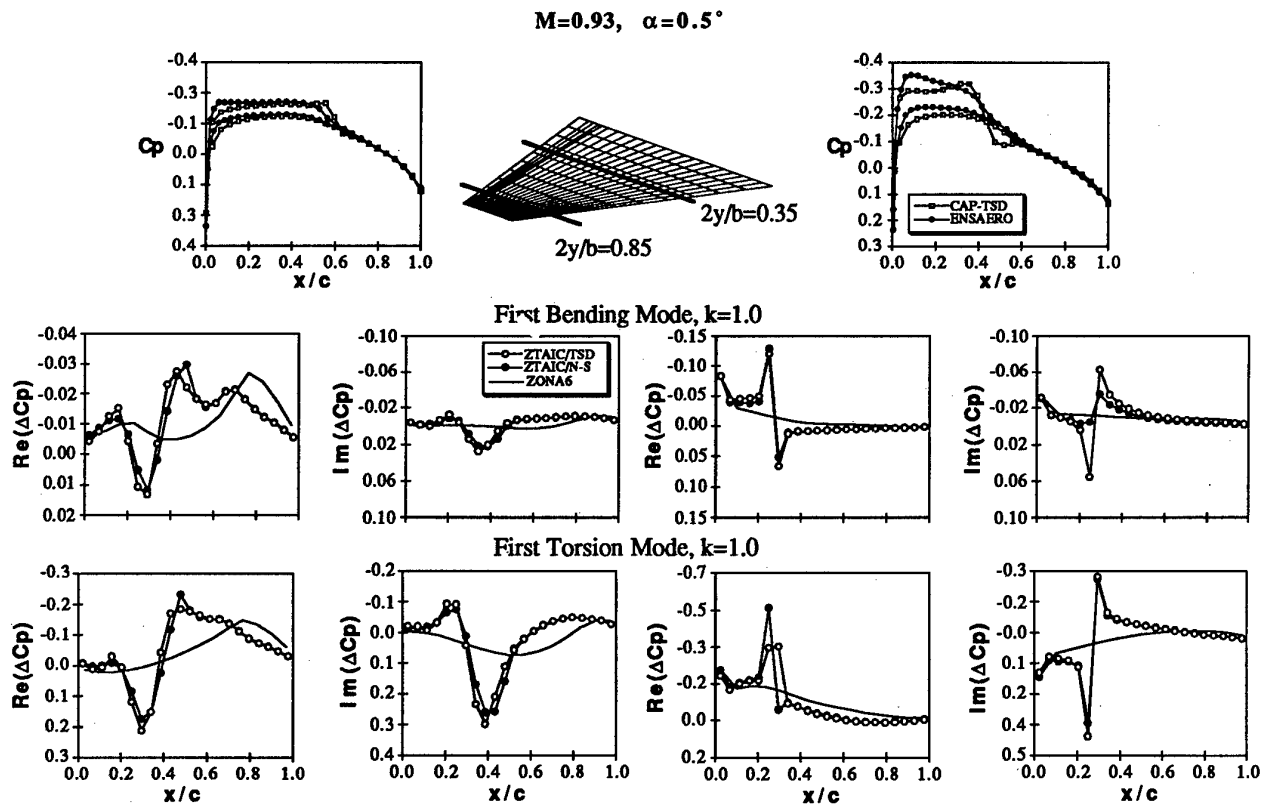
Figure 12. Unsteady/Steady Pressure Distributions of the Initial Design: Fighter Wing Optimization.
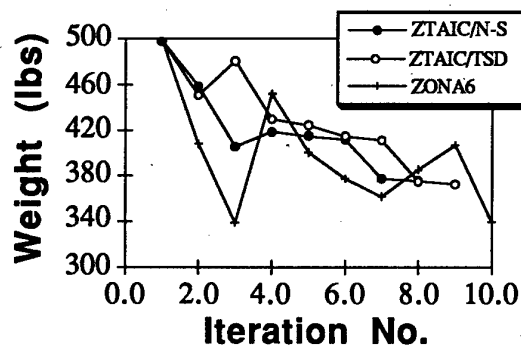
Figure 13. *ASTROS/ZAERO* Design Weight History: Fighter Wing Optimization.

Table 3. Design Weight and Flutter Speeds of the Final Design: Fighter Wing Optimization.

a) Weight at Final Design:

	Linear Method		Nonlinear Method		
	Kolonay (Linear CAP-TSD)	ASTROS/ZAERO (ZONA6)	Kolonay (Nonlinear CAP-TSD)	ASTROS/ZAERO (ZTAIC/TSD)	ASTROS/ZAERO (ZTAIC/N-S)
Final Weight (lbs)	507	340	427	373	376
Weight Change (%)	+1.87	-31.7	-14.22	-25.1	-24.5

Initial Weight = 497.7 lbs

b) Flutter Speed of Final Design (ρ=6.76E-07 slinch/in^3).

	ZAERO(ZONA6)	ZAERO(ZTAIC/TSD)	ZAERO(ZTAIC/N-S)
Flutter Speed (In/s)	15,000	15,100	15,000
Flutter Frequency (Hz)	17.07	17.08	17.05
Flutter Speed Increase (%)	21.8	28.0	29.8

Table 4. Final Design Structure: Fighter Wing Optimization.

			% Change of Property from Initial Values				
Global Design Variable	Local Design Variable	Initial Property Value	Linear Methods		Nonlinear Methods		
			Kolonay/ CAPTSD	ZONA6	Kolonay/ CAPTSD	ZTAIC/ TSD	ZTAIC/ N-S
1	CROD 101-131	0.050 in^2	-75.46	-88.88	-82.07	-90.0	-90.0
2	CSHEAR 309, 310,312 ,314,316, 318, 312, 324, 328, 332	0.075 in	-75.0	-75.0	-75.0	-75.0	-72.7
3	CSHEAR 311, 313, 315, 317, 319, 322, 325, 329, 333	0.065 in	-75.0	-75.0	-75.0	-75.0	-75.0
4	CSHEAR 320, 323, 326, 330, 334	0.050 in	24.21	-71.14	-70.05	-75.0	-75.0
5	CSHEAR 327, 331, 335	0.030 in	50.0	50.0	50.0	50.0	50.0
6	CROD 134 - 153	1.000 in^2	-89.39	-90.0	-84.05	-90.0	-90.0
7	CROD 164 - 181	0.750 in^2	-90.0	-90.0	-88.92	-90.0	-90.0
8	CROD 188 - 197	0.600 in^2	25.0	25.0	25.0	-4.25	-5.23
9	CROD 204 - 209	0.500 in^2	25.0	25.0	25.0	25.0	25.0
10	CSHEAR 340 - 361	0.080 in	50.0	50.0	50.0	50.0	50.0
11	CTRMEM 1, 2	0.250 in	-87.6	-90.0	-88.9	-90.0	-90.0
12	CTRMEM 23, 24	0.188 in	-87.29	-90.0	-87.75	-90.0	-89.8
13	CTRMEM 43, 44	0.080 in	-87.75	-90.0	-88.9	-90.0	-90.0
14	CTRMEM 55, 56	0.040 in	50.0	50.0	50.0	50.0	50.0
15	CQDMEM1 3 - 22	0.250 in	27.24	-90.0	-73.36	-90.0	-90.0
16	CQDMEM1 25 - 42	0.188 in	50.0	0.08	50.0	30.3	30.3
17	CQDMEM1 45 - 54	0.080 in	50.0	50.0	50.0	50.0	50.0
18	CQDMEM1 57 - 62	0.040 in	50.0	50.0	50.0	50.0	50.0
19	CSHEAR 300, 336	0.135 in	50.0	50.0	50.0	50.0	50.0
20	CSHEAR 301 - 304, 337	0.120 in	50.0	50.0	50.0	50.0	50.0
21	CSHEAR 305, 306, 338	0.090 in	50.0	0.0	-3.34	-62.5	-66.66
22	CSHEAR 307, 308, 339	0.050 in	50.0	50.0	50.0	50.0	50.0
23	CROD 132, 133, 154, 155	1.750 in^2	25.0	25.0	25.0	25.0	25.0
24	CROD 156 - 163, 182, 183	1.350 in^2	-89.52	-90.0	-88.91	-90.0	-90.0
25	CROD 184 - 187, 198, 199	1.050 in^2	25.0	25.0	25.0	25.0	25.0
26	CROD 200 - 203, 210, 211	0.880 in^2	25.0	25.0	25.0	25.0	25.0
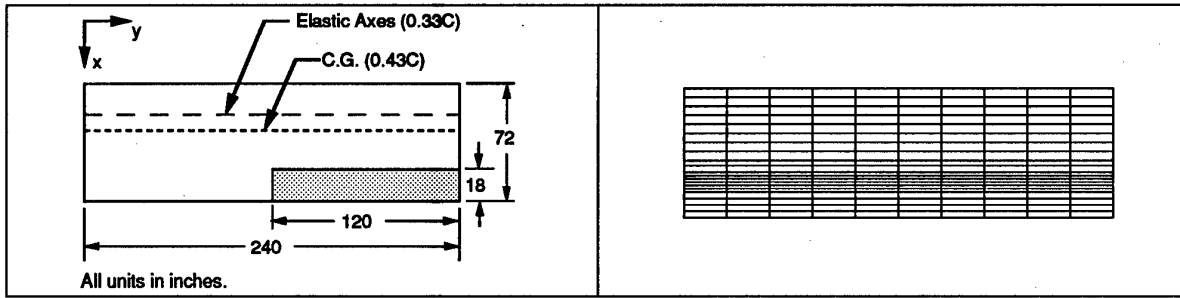
Figure 14. Planform and Aerodynamic Model of a Rectangular Wing Test Case: Transonic Roll Performance with Control Surface Reversal (Andersen et al, Ref. 25).
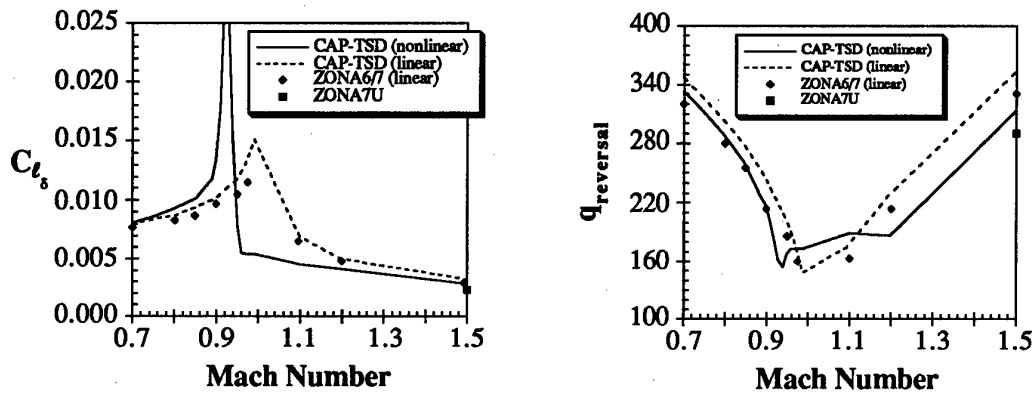
Figure 15. Rigid Rolling Moment Derivative and Reversal Dynamic Pressure of the Rectangular Wing: *ZONA6/7/7U* vs *CAPTSD*.
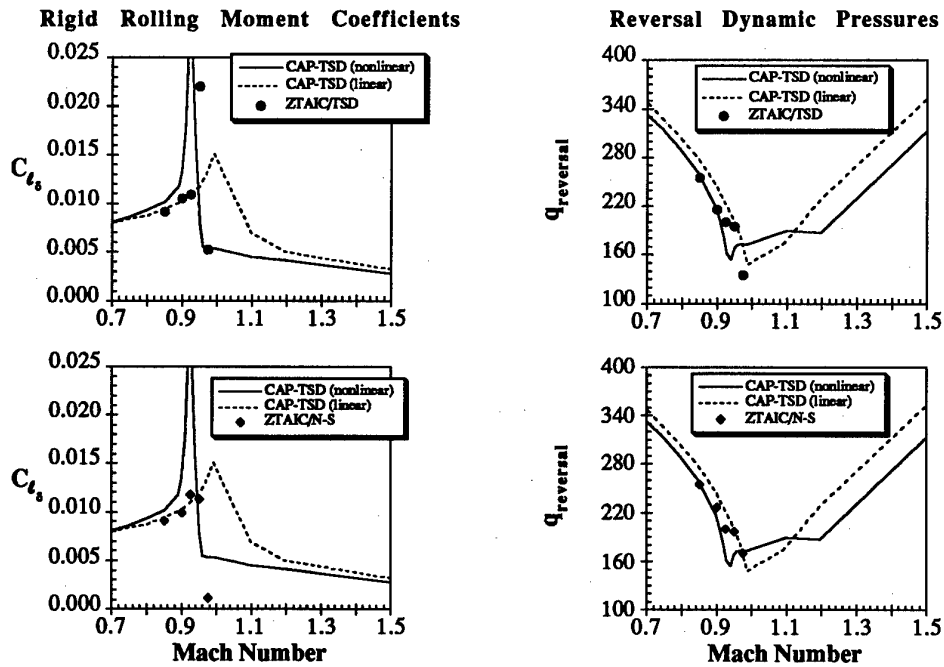
Figure 16. Rigid Rolling Moment Derivative and Reversal Dynamic Pressure of the Rectangular Wing: *ZTAIC* vs *CAPTSD*.

Steady Pressure at 85% Span   **ΔC_P Due to Unit Aileron Deflection**
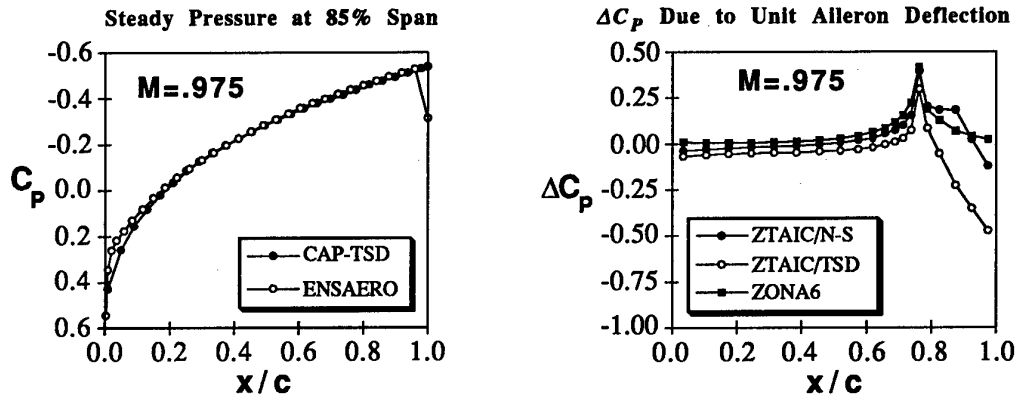
Figure 17. Rectangular Wing Pressure Distributions at M=0.975: Steady Lifting Pressures.

Aeroelastic Modeling
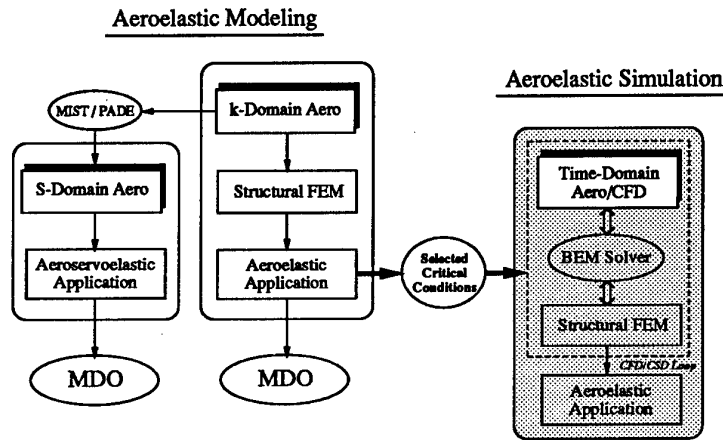
Figure 18. Computational Aeroelasticity: A Global Strategy.

Aeroelastic Modeling
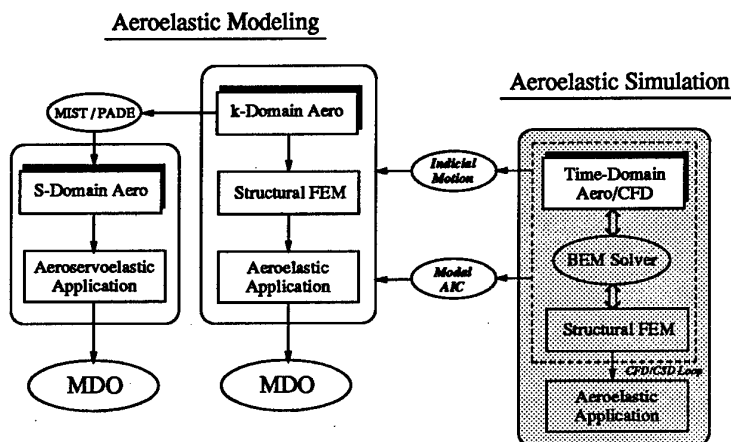
Figure 19. Computational Aeroelasticity for MDO Applications.

Experience With Unsteady Aerodynamics Computation for Saab Aircraft

by

Bo Franzen, Bo Nilsson and Bengt Winzell
Flutter and Loads Department
SAAB AB
S-58188 Linkoping, Sweden

SUMMARY.

Unsteady aerodynamics plays a vital role in the design of an aircraft. Already in the initial phase it is necessary to have reliable estimates of flutter boundaries and to supply information for control system software and hardware. Thus speed and accuracy of unsteady aerodynamic computation are required. In practise, it is natural to depend mainly on computations based on linear theory. There are situations where speed of computation and accuracy are contradictory, and then one must resort to previous experience and correction strategies.

The elastic modern aircraft is becoming more and more aero-servo-elastic. The quality of simulation of the numerous feedback mechanisms is highly depending on the accuracy of control surface aerodynamics. Moreover, the frequent application of multi-disciplinary optimization puts new strong demands on unsteady aerodynamic accuracy.

In this paper we will show examples of validating experiments and computations, and discuss applications of classical and new methods for real civil and military aircraft.

INTRODUCTION.

Modern aircraft are flexible structures which easily respond to aerodynamic unsteadiness. While experience of previous projects and flight testing plays a fundamental role in the clearance of a new design, there is a fundamental and ever increasing role of computation for flutter and response.

At Saab we saw the advent of computer programs for unsteady aerodynamics more than 40 years ago. Since then the efficiency and accuracy of the linear aerodynamics modeling have reached considerable heights, now enabling whole design concepts to be analyzed in a fraction of the time that was possible before. Recently, more complicated modeling of the flow in terms of non-linear equations for the Full Potential, Euler's and even Navier-Stokes' equations have been introduced. It is not always true, however, that an increase of precision in the prediction have compensated the computational effort of more sophisticated methods. Moreover, the accuracy of the sophisticated methods is itself subject to suspicion and doubt.

Although classical bending/torsion flutter seems to be accurately predicted by existing computational meth-ods, and thus can be excluded already in the early design phase, there are many aspects of airforce computation which are less mature. For instance the control surface effectiveness and hinge moments are difficult to calculate correctly and such data are important for successful prediction of the coupled aerodynamics - elasticity - controls system. The installation of a large number of weapons under the wings and even at wing tips lead to considerable change in the elastic and aeroelastic properties of an aircraft. This challenges both the aerodynamics and the structural dynamics analysis to accurately predict these properties, in particular as we are looking for an "optimal design".

COMPUTER PROGRAMS.

The corner stone in flutter and response analysis is the AEREL[1] system, once introduced by Stark. It contains a linear unsteady potential boundary element method for subsonic flow, ADE, and another method for supersonic flow. Recently we have included ZONA51[2] enabling a common modeling of the full configuration aircraft in the whole speed range. The program package contains pre and post processing tools for loads, generalized aerodynamic forces, flutter analysis and means for checking data and results. The linear methods work in the frequency plane.

Mainly for analyzing single wing transonic phenomena, an unsteady aerodynamics method based on the full potential equation was introduced[3]. This method steps in time, using transpiration technique for the time varying deformation input and for strip wise boundary layer correction. It also couples the aerodynamics solution directly with the equations of motion for the deforming wing.

Through close cooperation with FFA (the Swedish Aeronautical Research Institute in Stockholm) we have recently introduced the multi purpose CFD program EURANUS in industrial applications. The EURANUS[4] program was developed by FFA and VUB (Vrije Universiteit Brussel) for steady state Euler and Navier-Stokes flow, capable of handling multi-block structured grids. It was made time accurate by FFA[5] through a dual time step technique and introduction of a moving grids option. A pilot version of a direct coupling of aerodynamics and structures was introduced by Saab.

APPLICATIONS FOR MILITARY AIRCRAFT

During ten years, considerable work including analysis, tests and experiments for the JAS 39 Gripen aircraft was carried out. Careful modeling of the aircraft as a set of planar thin surfaces for the AEREL[1] system enabled complete flutter analysis of many weapons configurations, including the effect of the digital control system. The analysis was based both on Finite Element mode shapes and mode shapes measured in ground vibration tests. The subsequent flight test program essentially verified the flutter calculations. We will briefly discuss, however, a case where the flight test program showed a difference in damping, compared with calculations.

Unsteady aerodynamics modelling

A multi-role aircraft such as Gripen suggests a large set of different weapons configurations. It turns out, however, that very few cases require actual aerodynamic modeling of under wing stores. The tip installation is of higher aero-elastic importance, and thus the bulk of computations have used an aerodynamic model for the complete aircraft, including its wing tip configuration, but with few exceptions under wing storage has entered the computations only via the mode shapes.

Example of full aircraft geometric modelling for AEREL.
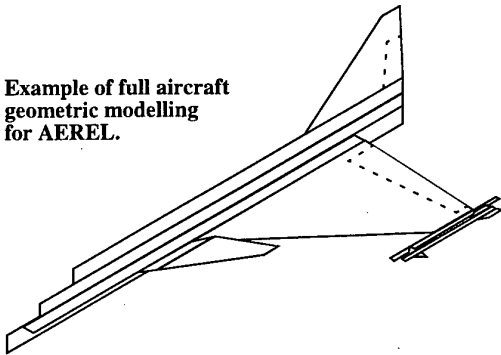
The model is trimmed such that typical aerodynamic derivatives match available data in the aerodynamic design data base. This usually requires correction factors for control surfaces.

Aerodynamic influence matrices in a reasonably fine grid are computed for a set of subsonic and supersonic Mach numbers and a range of reduced frequencies. These matrices are stored and reused for repeated generalized aerodynamic forces calculations for multiple configuration elastic mode shapes. The generalized forces are treated as aerodynamic transfer functions in flutter analysis, aero-servo-elastic analysis and response analysis.

Aero-servo-elastic analysis and flutter test excitation method.

The Gripen aircraft has a fly-by-wire control system with feedback control to overcome its basic longitudinal instability in subsonic flight. The feed back signals are given by accelerometers and rate gyros, and these pick up any motion in the rigid but also the elastic aircraft. Hence this aircraft is an aero-servo-elastic system and must be treated as such in flutter analysis and dynamic

response analysis. In particular this requires the elastic mode shapes to be computed or measured also at the gyro position. In most cases, however, the impact of the control system feedback on flutter stability is rather weak.
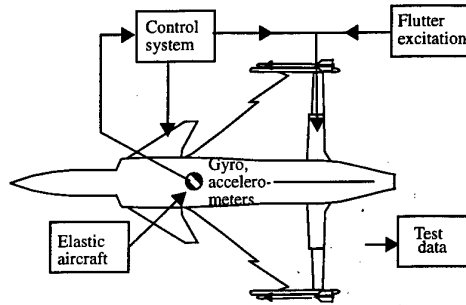
The control surface servos are used for flutter excitation. A repeated sine sweep of the elevons, the rudder and the canards excite the aircraft, and the response at several locations on the aircraft is measured by accelerometers. The signals are telemetrized to the ground control for on-line examination and are recorded for detailed post flight evaluation. An example of the response at the wing tip launcher is presented below.
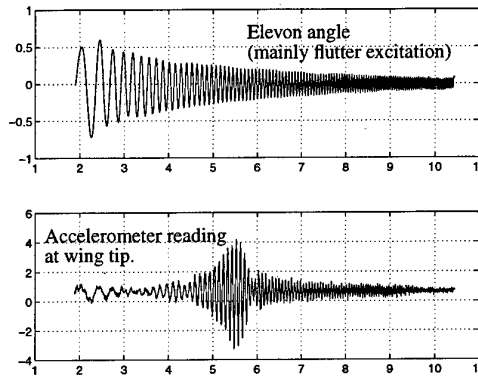
To verify stability for the aero-servo-elastic (ASE) system the following steps are taken:

- Calculate, at specified flight conditions and for different aircraft configurations, the response of the aircraft and the autopilot sensors for a harmonic motion of the control surfaces. In this calculation the same aerodynamic and structural model of the aircraft as in the flutter analysis is used.

- Calculate the resulting control surface commands due to the sensor response. In this calculation a reduced model of the autopilot is used

- From the open loop gains it can be verified whether the stability requirements are fulfilled. If not, requirements on body-bending attenuation filters and maximum autopilot gains are fed back to the flight systems department.

The ASE-analyses as described above are carried out by the flutter department for every relevant change of the aircraft configuration and every new version of the autopilot. The elastic contribution to the sensor response can, depending on the sensor location, be considerable

and affect the stability of the flight control system as described above.

To reduce the number of iterations in the autopilot design process, the flight systems department get at an early stage approximate correction factors for the transfer functions between control surface deflection and autopilot sensors. These correction factors account for the elastic contributions to the transfer functions.

The theoretical analyses are checked by extensive testing both on ground and in flight. The ground testing is used for calibration of the structural model i. e. the mode shapes, modal deflection at the autopilot sensors and mass couplings to the control surfaces. In the response calculations measured structural damping is used. The figure below shows a comparison between measured and calculated response of the pitch rate gyro to pitch command. The reduced model of the autopilot is checked by measuring the different transfer functions between sensor outputs and control surface commands.

GVT. Pitch rate vs pitch cmd deg/sec/rad Mach 0
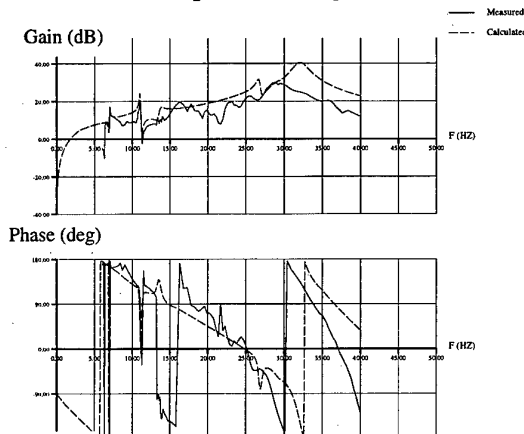
The ASE-flight testing which is performed in connection with flight flutter testing is used for verification of the calculated stability margins. The accuracy of the ASE-process depends to a large extent on the unsteady aerodynamic calculations especially on the control surface aerodynamics. This is most often over-predicted which calls for the use of correction factors. The figure below shows a Nyquist diagram with a comparison

Pitch rate vs δ_e deg/sec/deg Mach 0.6 6 km
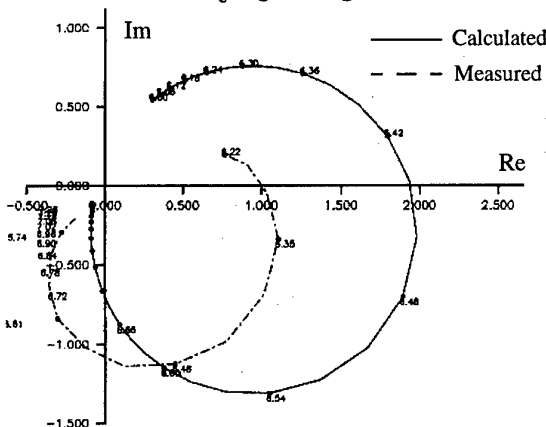
between calculated and measured pitch rate to elevator deflection.

Flutter analysis and flight test.

Flutter analysis is done with the p-k method. Hence one iterates in the equation

$$[p^2 \cdot M + p^* \cdot C + K + A(Im(p^*)) + S(p^*)]q = 0$$

$$p^* = p$$

to find the eigen solutions q and the eigenvalues p of the coupled aerodynamic-structures-controls system. Here M is the mass matrix, C is a damping matrix, $A(\omega)$ is the matrix of aerodynamic transfer functions defined for pure harmonic oscillation and S is the resultant transfer functions matrix for the control system. The solution $p = d + i\omega$ of the non-linear eigenvalue problem thus contains the increment d/ω and the frequency ω.

We are generally using Mach number and altitude as parameters in the analysis and present the flutter analysis in a set of diagrams of damping versus flight speed at different altitudes. Similarly frequency versus speed is given for different altitudes.

During testing it was found that there is a difference between computed and measured damping rates for high transonic Mach numbers.
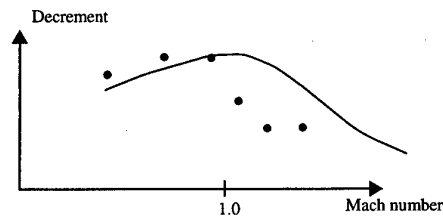
This discrepancy was unexpected and considered too large not to be explained. An investigation of the cause of the non-conservative prediction was initiated. The damping is for a mode involving the tip missile motion and the flexible wing tip. The following hypotheses were put forward:

- Transonic dip phenomena due to shock waves etc. As will be discussed below, the conclusion was that no strong transonic effects could be detected when replacing linear theory unsteady aerodynamics by Euler computations.

- Could there be flow separation over the wing, and was this an effect similar to the LCO-phenomena discussed by Cunningham and Meijer[6]? As will be discussed in the next subsection, the conclusion was that the wing is very well shaped, not admitting any flow separation at normal angles of attack in this speed range.

- Spurious feedback control?

Although not necessary for the clearance of the present

aircraft, an explanation is important to have confidence in the unsteady aerodynamics.

It is difficult to measure unsteady aerodynamic forces in flight but in this case such data were obtained to validate the linear unsteady aerodynamic forces at the wing tip. Indeed, exciting the aircraft at resonance frequency and measuring shear force and pitching moment close to the wing tip, we could compare computed aerodynamic forces with measured ones and found good correlation. The diagrams below compare (in the frequency plane) measured data at a supersonic free stream Mach number with computations. The motion of the wing tip was used as input for the computed aerodynamics.

Comparing measured (solid line) and computed (dashed) shear force for the aircraft excited at resonance frequency.
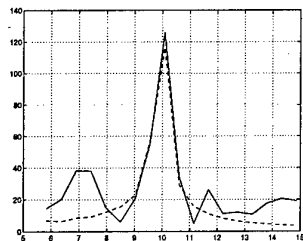
Comparing measured (solid line) and computed (dashed) pitching moment for the aircraft excited at resonance frequency.
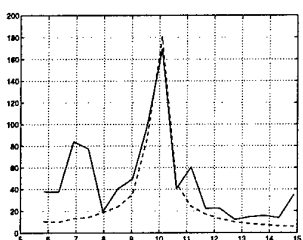
CFD application

In order to estimate the strength of transonic effects on the flutter characteristics of the Gripen aircraft we applied the CFD program EURANUS[4,5]. A detailed grid around the wing with its complex wing tip geometry was created by the MULCAD module of ICEM/CFD[7].
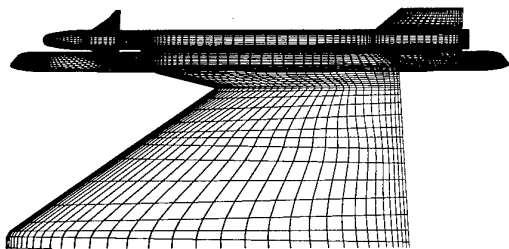
The grid consisted of a little more than 1,000,000 points in 194 blocks. A reason for such a large number of blocks is that EURANUS works in structured meshes and that the geometry has many details, such as depicted in the figure below.

solid walls
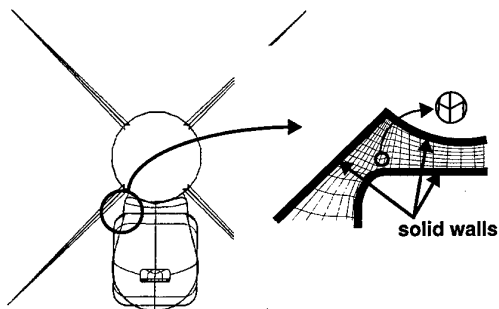
An example of Mach number distribution about part of the wing tip is shown below for a free stream Mach
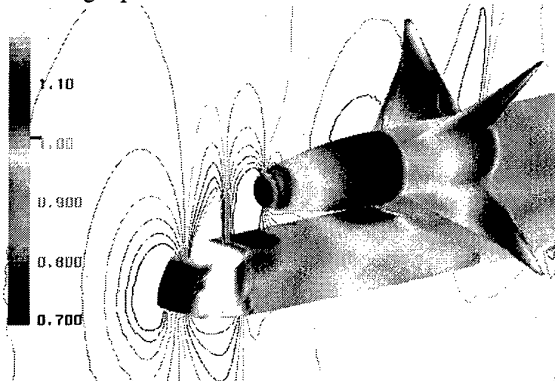
number of M = 0.95. The whole grid was then deformed according to the elastic mode shapes, one by one. The amplitude of this deformation was a pulse of "one minus cosine" type. The transient response in pressure distribution was computed, and because of the small maximum amplitude in the perturbation, air force matrices were obtained using Fourier analysis. Using these transonic aerodynamic forces in flutter analysis somewhat reduced the damping compared to linear analysis, but this reduction was global in speed and of much smaller magnitude than the difference to flight data. We rather attributed this difference in damping to the tendency of inviscid analysis to over emphasize transonic effects. No transonic effect was detected.

So far we have not applied unsteady Navier-Stokes analysis for the Gripen aircraft. However, in an attempt to spot any signs of possible flow separation on the wing, *steady* viscous CFD analysis was carried out for several
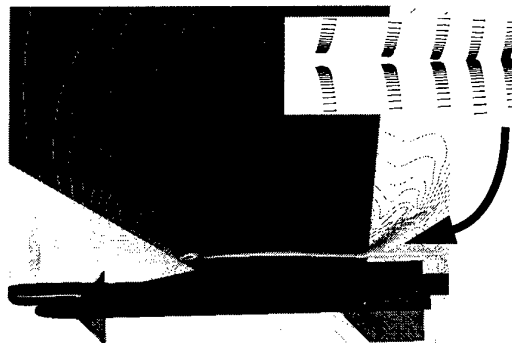
Iso Mach lines in a vertical section and velocity vectors at the trailing edge.
M = 1.05, α = 5°.

transonic and supersonic Mach numbers, M ≥ 0.9, and for angles of attack up to 5 degrees. The snapshot above demonstrates the attached flow character that we found to be typical for the JAS Gripen wing. This supports the experience from flight tests that the flow over the wing is of very high quality.

Use of CFD in project work seems still to be almost forbiddingly time consuming. This is partly due to the many man weeks or even months it takes to create structured grids around complex geometries. However, the gridding problem should be less time consuming in the next generation of CFD codes, using various types of more freely distributed blocks or even unstructured grids. But also the computing time is considerable. At present our experience in the work on Gripen is that for flutter, linear analysis does a reasonably good job and that the effects of transonic unsteady aerodynamics are less pronounced.

APPLICATIONS FOR CIVIL AIRCRAFT

We will briefly discuss two examples of applications for the Saab 2000 aircraft. The first example concerns control surface aerodynamics and dynamics of dampers. The second example is for gust load evaluation.

Flutter stability of a spring tab system.

The initial design of Saab 2000 had a mechanical control system for the elevator. The concept was later abandoned for a power controlled elevator. The change in design was motivated by the flight mechanics longitudinal stability which had to be increased in certain extreme configurations. The flutter stability was well proven both in test and analysis.

The mechanical control system consisted of aerodynamically balanced control surfaces with tabs which also had an aerodynamic balance. The tab was a so called spring tab.

Tab input affects the main
surface through aerodynamics
· and spring/damper.
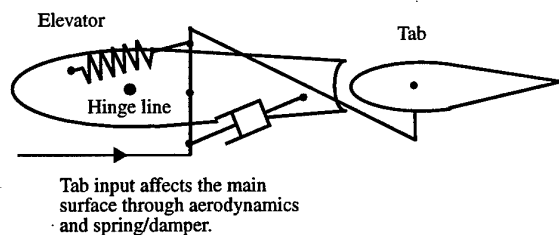
The unsteady aerodynamics for the spring tab system was obtained from a combination of linear potential theory and specially designed flight tests to obtain reliable correction factors to the computed forces. Control surface aerodynamics is rather difficult to compute, and in this case both the tab and the main control surface were aerodynamically balanced. In such a configuration, the hinge moments is the difference of two large but almost equal numbers, and the resultant force enters the delicate stability equations. Measuring tab loads in flight gave quasi-steady data and with the help of this, corrections to the linear potential analysis could be obtained. In the flutter analysis, a variation of these factors was

made to certify the robustness of the prediction.

It turned out that in order to prove flutter stability in the extended flight envelope (20% increased speed range), spring tab dampers had to be introduced. These were of hydraulic type, and influenced the dynamics of the elevator and tab considerably.

Usually a damper is a pure damper only in a narrow frequency band. In the diagram below we show measured characteristics of the damper that was used in the aircraft. It shows a stiffness component and a damping

Stiffness component.   *Damping rate component.*
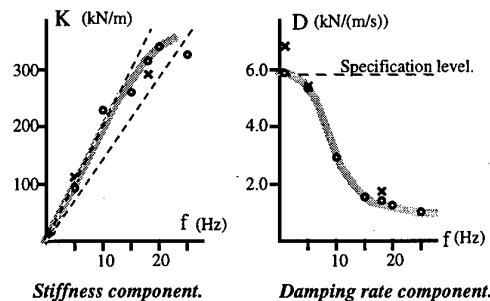
component of the total impedance. The interesting, and as it turns out, most beneficial effect of the spring tab flutter damper is the stiffness it adds at higher frequencies. It separates the two (or more) basic control surface frequencies. The "tab frequency", which without damper is in the order of 15 Hz, was raised to above 25 Hz. Thus the elevator mode, which on ground has a low frequency, but becomes stiffer due to the aerodynamic spring with increasing dynamic pressure, is unable to couple with the tab mode. This is clearly demonstrated in the diagrams below.
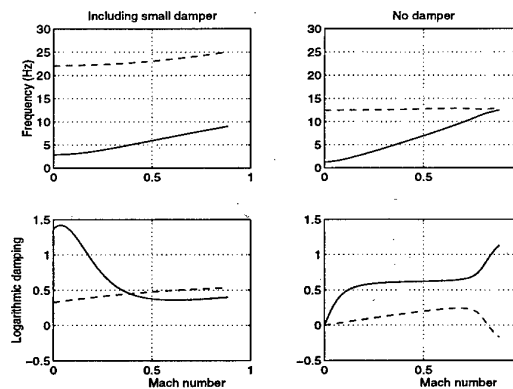

This analysis is an example of how, in addition to the difficulty to get the unsteady aerodynamics right, the flutter analyst also has to consider all other dynamic ingredients in the model.

Unsteady aerodynamics for dynamic loads.

Unsteady aerodynamics plays an important part in gust loads calculations. Considerable work is spent on developing a reliable computational model for the unsteady linear potential theory. Since gust loads are obtained in a global model of the aircraft and the equations of motion for the whole rigid and elastic aircraft are to be solved,

the basic aerodynamic derivatives have to be well repro- duced and the quasi-steady aerodynamic loads distribu- tion over fuselage and lifting surfaces must be correct. Since modern aircraft also have feed back control, the inclusion of any control system is important and there- fore also the control surface effectiveness.

Linear theory has to be corrected for numerous effects which are not usually covered by the linear theory. This includes the relaxation of the Kutta condition on non- lifting surfaces and the control surface effectiveness. Means for such corrections were included in the AEREL[1] package.
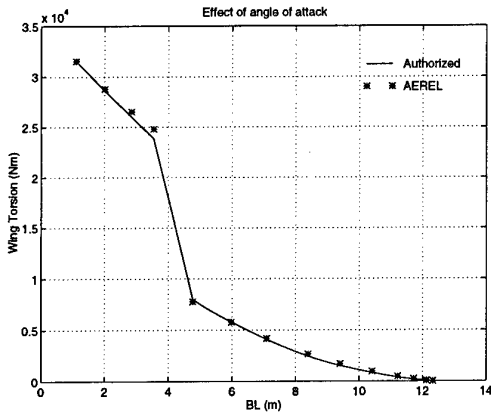
The diagram above is an example of how the computa- tional model is trimmed to closely reproduce detailed air loads on the aircraft. This is the wing torsion distri- bution due to change in angle of attack. In particular, the jump in load across the engine nacelle is a crucial fea- ture. The authorized loads data were obtained from a combination of wind tunnel experiments, computations and similarity with other aircraft. Our experience is that the detailed trimming of the computational model sel- dom calls for any drastic deviations from just plain geo- metric corner coordinate data in the aircraft definition.

EXPERIMENTS AND VALIDATION

Nonlinear methods for unsteady aerodynamics can be accepted for industrial application only when proven accurate and ready to use in such applications where a better analysis than the classical methods is needed. Unfortunately our experience is, that many times the cases which call for the more complicated analysis also are complicated with respect to geometry or flow condi- tion. The geometry can be too complicated to enable enough detailed grids for appropriate resolution, or the flow conditions may be highly vortical or contain sepa- rated flow and there we have less confidence in the abil- ity of new methods to really pick up the true physics. So, overall, unsteady CFD methods are considered with suspicion since it appears that in the cases where you really would need them, they are not ready for use.

However, anticipating the methods to mature we have ongoing programs to investigate the accuracy one can achieve and the ease by which the methods can be han- dled in the industrial environment. We will discuss three rather simple cases here.

Unsteady air loads on a pitching delta wing.

Jointly with VAC (Volvo Aero Corporation) and FFA (Swedish Aeronautical Research Institute) we have taken part in a series of experiments and computations of unsteady pressure on a cropped delta wing with a 55 degree leading edge sweep. The model was built in two different sizes, one three times the other. The larger model was equipped with a part span trailing edge con- trol surface. One chord was instrumented with dynamic pressure transducers.

The larger model[9]
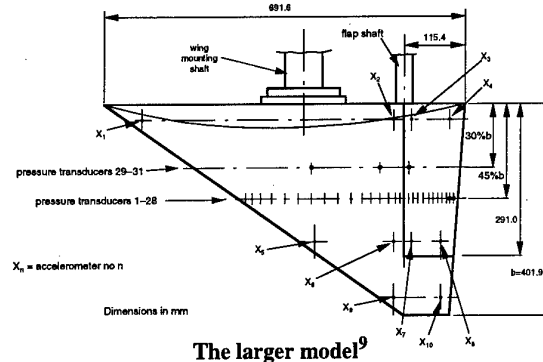
With a NACA64A006 section this wing is purely sub- sonic for M = 0.7 and moderate angles of attack. There- fore unsteady pressures, measured in a transonic 0.5 m x 0.5 m wind tunnel at VAC should match the ones com- puted with linear potential theory. The figure below indeed verifies this. For the computations we have used Stark's ADE method[1]. The frequency of 285 Hz for this model with a root chord of 23 cm corresponds to a reduced frequency of about 1.0, based on the chord where the measurements were taken.

Unsteady Cp due to pitch oscillation

M = 0.7
f = 285 Hz
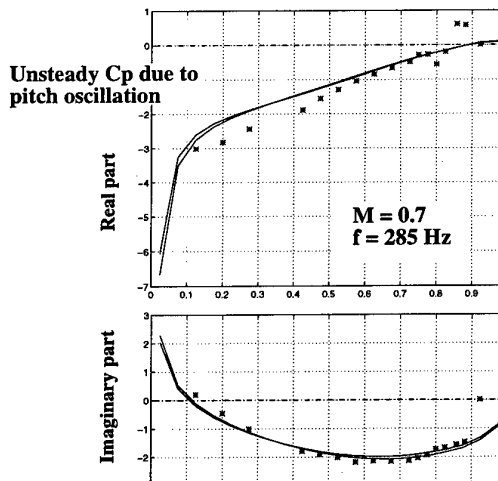
For M = 0.95 (actual tunnel reading was M = 0.97, but it was later discovered that the Mach number over the wing was less) the flow is transonic already at $\alpha = 0^\circ$. The computation is thus carried out with an unsteady full potential analysis, including a simple boundary layer correction. Here the reduced frequency based on local chord is about 0.25.

Unsteady Cp due to pitch oscillation
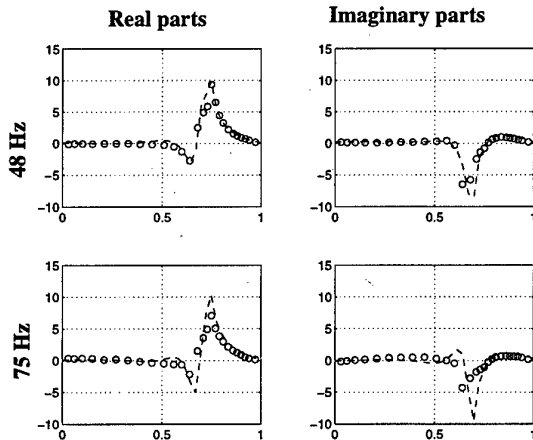
M = 0.95
f = 95 Hz

Real part

Imaginary part
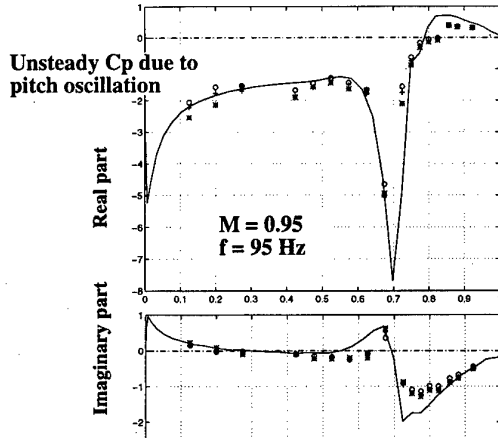
The experimental data in the figure above was obtained with three different levels of pitch amplitude, ranging from 0.2 to 0.7 degrees. There is a spread in the data, but there is no evidence that this is due to physical nonlinearity. It is probably more an estimate of the tolerances in the measurement.

The comparison seems to indicate that the measurements were correct (agreement with linear theory for subsonic flow) and the transonic case supports the use of the transonic full potential method for mild transonic flow and pitch motion. Without boundary layer correction, however, the results were inadequate. More about this is published in Reference 8. This experiment will be followed by one in the larger T1500 wind tunnel at FFA, this time with a variation in mean angle of attack.

Unsteady air loads due to oscillating control surface.

The larger model of the delta wing was tested at FFA in the wind tunnel T1500[9]. The trailing edge control surface was oscillated around different mean angles and with different frequencies and amplitudes. For the subsonic free stream Mach number, M = 0.7, the comparison with theory is rather good. For higher Mach numbers, with well developed transonic flow conditions, the comparison between theory and measurements is reasonable as long as the theory can handle the tran-

sonic flow and if the mean control surface angle is not too large. A large deflection angle resulted in separated flow over a large part of the control surface.

In the figure above we plot unsteady pressure measurements (symbols), compared with unsteady Euler computations (lines) for the subcritical case, M = 0.94, in which the shock is located just ahead of the hinge line.

For M = 0.97, the shock is stronger and located slightly behind the hinge line. Because EURANUS was used in the inviscid Euler mode, the shock location in the computation is too far aft, and this of course worsens the comparison. The peaks are also much higher in the com-

Real part   Imaginary part

Unsteady pressure due to control surface oscillation. M = 0.97, $\delta = 0°$.
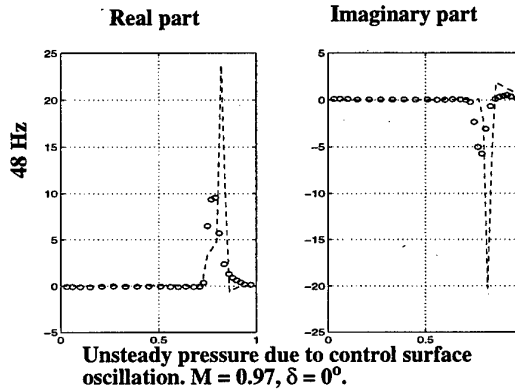
putation. The height of such peaks depends on amplitude and sampling rate in tests and on grid size in the computations. Therefore global quantities, like the lifting force, can be reasonable even if the detailed pressure plot shows bad agreement. In this case, however, the hinge moments must be completely different in the test and in the computation.

When the control surface is further deflected, the shock moves further aft in the test until the flow separates. This physical phenomenon has a great effect on the control surface effectiveness, but so far a CFD analysis has not been successfully applied. The figure below presents steady pressure distribution for a sequence of increasing control surface deflection angles. Notice the fully supersonic character of the pressure ahead of the hinge line and also the classical behavior of pressure on a ramp in supersonic flow behind the hinge line. The classical formula $\Delta C_p = \dfrac{Slope}{\sqrt{M_{loc}^2 - 1}}$ suggests an M_{loc} of about 1.08

Real parts   Imaginary parts

Unsteady pressure due to control surface oscillation. M = 0.94.

$\delta = 10.25°$
$\delta = 8.25°$
$\delta = 6.26°$
$\delta = 4.30°$
$\delta = 2.29°$
$\delta = 0.29°$
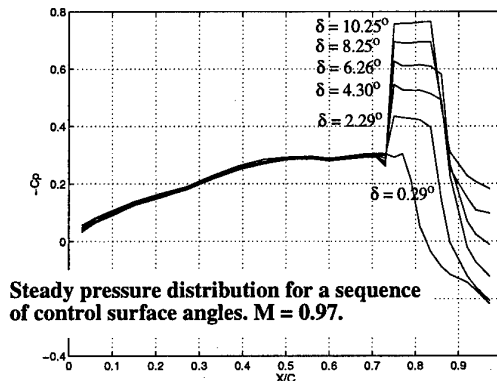
Steady pressure distribution for a sequence of control surface angles. M = 0.97.

here, and that is about what corresponds to the local Cp of about 0.25-0.3 ahead of the control surface.

## Flutter analysis for the 445.6 elastic wing model.

Previous investigations comparing measured flutter data with linear theory predictions and also full potential analysis have shown that for thin wings and small angle of attack, already linear theory is enough to get reasonable to good agreement with experiments. This was presented in References 10 and 11. If for instance there is a transonic dip, linear theory appears to miss that, and if the dip is at a subsonic Mach number, well below Mach one, a typical recovery of flutter speed after the dip is not predicted at all by linear analysis. However, full potential analysis predicted such a recovery at too early a Mach number[11], a dangerous result.

Here we will present recent analysis for the AGARD 445.6 wing[12], tested in NASA Langley's Transonic Dynamics Tunnel. So far only linear analysis and full potential calculations have been carried out. We intend to follow up by Euler and Navier-Stokes computations in the near future.

The 445.6 wing is very thin. The flutter data were obtained at zero angle of attack. This wing therefore is relevant for validation of methods which will be used in military aircraft design. There is a transonic dip, but the dip is located in the speed range close to Mach one. Hence the shift in aerodynamic characteristics between subsonic and super sonic flow could be expected to be similar to the reduction of flutter speed at a transonic Mach number and the subsequent recovery for higher Mach numbers. The occurrence of the phenomenon should however be somewhat earlier in the test than in the linear analysis. Indeed this seems to be the case.

Dynamic pressure at flutter, linear theory and measurements
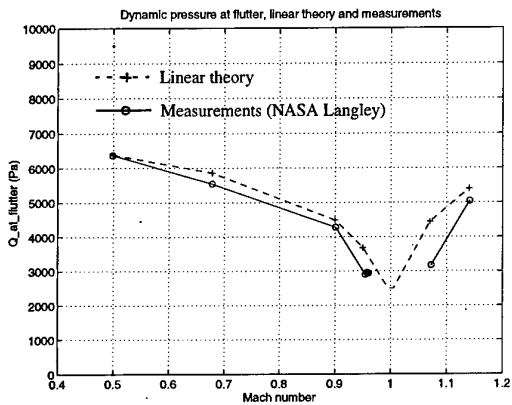
In the diagram above we have plotted the measured data by ring symbols, joined by the solid line. The linear theory prediction is given by plus symbols, and an "engineer's concept" of the transonic dip is introduced as a dashed line. The prediction is somewhat non-conservative, but on the supersonic side it is far better than what was achieved by full potential analysis:

Dynamic pressure at flutter
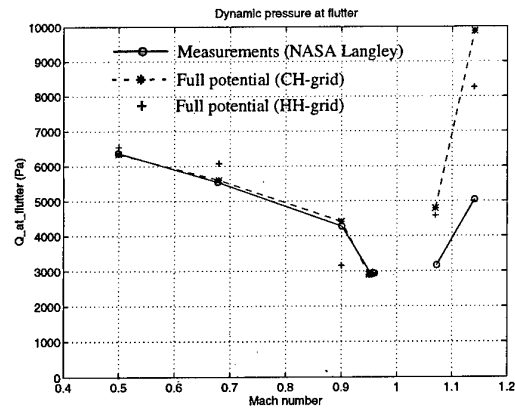
The full potential program can work in two different grid structures. The CH-grid prediction, which is given by star symbols, joined by dashed lines, agrees very well with test data for the subsonic free stream Mach numbers, but on the supersonic side the discrepancy is intolerable. There is a strong influence of grid on the results. The plus symbols are predictions made using an HH-grid instead of the CH-grid. The normal strategy is to use HH-grid for high Mach numbers and CH-grid for low speed. The result above supports this, but the difference is too large to ensure confidence in any of the results.

Another question mark should be raised for the flutter frequency estimates. Below we plot the experimental data (solid lines and ring symbols) together with linear theory (dashed line), CH-grid (stars) and HH-grid (pluses) full potential predictions. Usually we expect the linear theory to predict the low speed data with high accuracy. The discrepancy here for M = 0.5 indicates that the coupling mechanism between the structural modes is not correct. This could for instance be due to the mode shapes which are computed rather than measured.

Flutter frequency
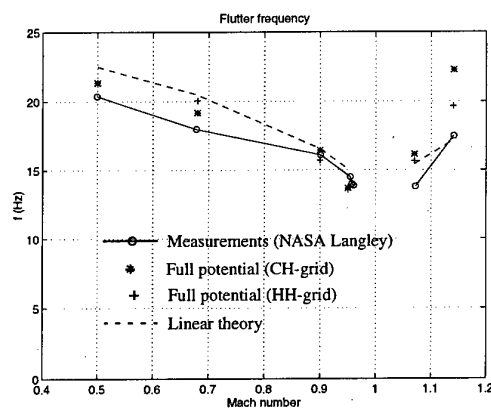
Our conclusion is, as so many times before, that the linear theory, the faults and weaknesses of which we are quite familiar with, seems to be the better tool when assessing the flutter stability in the whole speed range. On the other hand, the nonlinear CH-grid prediction is very good up to M = 0.95, and therefore it is important to find out what the reason for the non-conservative

A. S.: *Further studies of harmonic gradient method for supersonic aeroelastic applications*, Proc. European Forum on Aeroelasticity and Structural Dynamics, 1989, Paper 89.

3 Winzell, B.: *Applications of the unsteady full potential equation for wings*, Proc. European Forum on Aeroelasticity and Structural Dynamics, 1989, pp. 65-83.

4 Rizzi, A., Eliasson, P., Lindblad, I., Hirsch, C., Lacor, C. and Haeuser, J.: *The engineering of multi-block/multigrid software for Navier-Stokes flows on structured meshes*, Comp. Fl., 22(2/3), pp. 341-367, 1993.

5 Eliasson, P. and Nordström, J.: *The development of an unsteady solver for moving meshes*, FFA TN 1995-39, Stockholm 1995.

6 Meijer, J. J. and Cunningham, A. M.: *Outline and applications of a semi-empirical method for predicting transonic limit cycle oscillation characteristics of fighter aircraft*, Proc. International Forum on Aeroelasticity and Structural Dynamics, 1995, Paper 75.

7 ICEM™ CFD/CAE MULCAD Reference Manual, Control Data, Oct. 1993.

8 Johansson, U. and Winzell, B.: *Steady and unsteady pressure measurements on a 55° delta wing and comparison with computation*, Proc. International Forum on Aeroelasticity and Structural Dynamics, 1995, Paper 45.

9 Karlsson, A., Winzell, B., Eliasson, P., Nordström, J., Torngren, L. and Tysell, L.: *Unsteady control surface pressure measurements and computations*, Proc. 14th AIAA Applied Aerodynamics Conference, 1996, Paper 96-2417.

10 Stark, V.: *Flutter calculations for flutter models of JAS 39 Gripen*, ICAS Paper 88-4.10.1

11 Winzell, B.: *Recent applications of linear and non-linear unsteady aerodynamics for aeroelastic analysis*, Paper 5 in AGARD CP-507, 1991.

12 Yates, E. Carson, Jr.: *AGARD standard aeroelastic configurations for dynamic response. Candidate configuration I. - Wing 445.6*, NASA TN D-100492, 1987.

REPORT DOCUMENTATION PAGE

1. Recipient's Reference	2. Originator's Reference	3. Further Reference	4. Security Classification of Document
	AGARD-R-822	ISBN 92-836-0054-1	UNCLASSIFIED/ UNLIMITED

5. Originator	Advisory Group for Aerospace Research and Development North Atlantic Treaty Organization 7 rue Ancelle, 92200 Neuilly-sur-Seine, France

6. Title	Numerical Unsteady Aerodynamic and Aeroelastic Simulation

7. Presented at/sponsored by
The 85th Meeting of the AGARD Structures and Materials Panel, held in Aalborg, Denmark 14-15 October 1997.

8. Author(s)/Editor(s)	9. Date
Multiple	March 1998

10. Author's/Editor's Address	11. Pages
Multiple	198

12. Distribution Statement	There are no restrictions on the distribution of this document. Information about the availability of this and other AGARD unclassified publications is given on the back cover.

13. Keywords/Descriptors

Unsteady flow	Scale effect
Aerodynamics	Euler equations of motion
Aeroelasticity	Navier-Stokes equations
Computerized simulation	Flutter
Mathematical models	Buffeting
Finite element analysis	Aerodynamics loads
Computational fluid dynamics	Aerodynamic stability
Viscocity	Dynamic response

14. Abstract

Computational unsteady aerodynamics (CUA) is a critical element in the prediction of flutter stability and dynamic response of aircraft. Linear aerodynamic methods are still the most widely used, but more advanced methods are receiving increased attention.

The purpose of this Workshop was to review methods in use and to give exposure to other methods which are currently available or are in the development process.

AGARD

NATO -⊕- OTAN

7 RUE ANCELLE • 92200 NEUILLY-SUR-SEINE

FRANCE

Télécopie 0(1)55.61.22.99 • Télex 610 176

DIFFUSION DES PUBLICATIONS

AGARD NON CLASSIFIEES

L'AGARD détient un stock limité de certaines de ses publications récentes. Celles-ci pourront éventuellement être obtenus sous forme de copie papier. Pour de plus amples renseignements concernant l'achat de ces ouvrages, adressez-vous à l'AGARD par lettre ou par télécopie à l'adresse indiquée ci-dessus. *Veuillez ne pas téléphoner.*

Des exemplaires supplémentaires peuvent parfois être obtenus auprès des centres de diffusion nationaux indiqués ci-dessous. Si vous souhaitez recevoir toutes les publications de l'AGARD, ou simplement celles qui concernent certains Panels, vous pouvez demander d'être inclus sur la liste d'envoi de l'un de ces centres.

Les publications de l'AGARD sont en vente auprès des agences de vente indiquées ci-dessous, sous forme de photocopie ou de microfiche. Certains originaux peuvent également être obtenus auprès de CASI.

CENTRES DE DIFFUSION NATIONAUX

ALLEMAGNE
Fachinformationszentrum Karlsruhe
D-76344 Eggenstein-Leopoldshafen 2

BELGIQUE
Coordonnateur AGARD - VSL
Etat-major de la Force aérienne
Quartier Reine Elisabeth
Rue d'Evere, B-1140 Bruxelles

CANADA
Directeur - Gestion de l'information
(Recherche et développement) - DRDGI 3
Ministère de la Défense nationale
Ottawa, Ontario K1A 0K2

DANEMARK
Danish Defence Research Establishment
Ryvangs Allé 1
P.O. Box 2715
DK-2100 Copenhagen Ø

ESPAGNE
INTA (AGARD Publications)
Carretera de Torrejón a Ajalvir, Pk.4
28850 Torrejón de Ardoz - Madrid

ETATS-UNIS
NASA Center for Aerospace Information (CASI)
Parkway Center, 7121 Standard Drive
Hanover, MD 21076

FRANCE
O.N.E.R.A. (Direction)
29, Avenue de la Division Leclerc
92322 Châtillon Cedex

GRECE
Hellenic Air Force
Air War College
Scientific and Technical Library
Dekelia Air Force Base
Dekelia, Athens TGA 1010

ISLANDE
Director of Aviation
c/o Flugrad
Reykjavik

ITALIE
Aeronautica Militare
Ufficio Stralcio AGARD
Aeroporto Pratica di Mare
00040 Pomezia (Roma)

LUXEMBOURG
Voir Belgique

NORVEGE
Norwegian Defence Research Establishment
Attn: Biblioteket
P.O. Box 25
N-2007 Kjeller

PAYS-BAS
Netherlands Delegation to AGARD
National Aerospace Laboratory NLR
P.O. Box 90502
1006 BM Amsterdam

PORTUGAL
Estado Maior da Força Aérea
SDFA - Centro de Documentação
Alfragide
P-2720 Amadora

ROYAUME-UNI
Defence Research Information Centre
Kentigern House
65 Brown Street
Glasgow G2 8EX

TURQUIE
Millî Savunma Başkanliği (MSB)
ARGE Dairesi Başkanliği (MSB)
06650 Bakanliklar - Ankara

AGENCES DE VENTE

NASA Center for AeroSpace Information (CASI)
Parkway Center, 7121 Standard Drive
Hanover, MD 21076
Etats-Unis

The British Library Document Supply Division
Boston Spa, Wetherby
West Yorkshire LS23 7BQ
Royaume-Uni

Les demandes de microfiches ou de photocopies de documents AGARD (y compris les demandes faites auprès du CASI) doivent comporter la dénomination AGARD, ainsi que le numéro de série d'AGARD (par exemple AGARD-AG-315). Des informations analogues, telles que le titre et la date de publication sont souhaitables. Veuiller noter qu'il y a lieu de spécifier AGARD-R-nnn et AGARD-AR-nnn lors de la commande des rapports AGARD et des rapports consultatifs AGARD respectivement. Des références bibliographiques complètes ainsi que des résumés des publications AGARD figurent dans les journaux suivants:

Scientific and Technical Aerospace Reports (STAR)
STAR peut être consulté en ligne au localisateur de
ressources uniformes (URL) suivant:
    http://www.sti.nasa.gov/Pubs/star/Star.html
STAR est édité par CASI dans le cadre du programme
NASA d'information scientifique et technique (STI)
STI Program Office, MS 157A
NASA Langley Research Center
Hampton, Virginia 23681-0001
Etats-Unis

Government Reports Announcements & Index (GRA&I)
publié par le National Technical Information Service
Springfield
Virginia 2216
Etats-Unis
(accessible également en mode interactif dans la base de
données bibliographiques en ligne du NTIS, et sur CD-ROM)

AGARD

NATO -⊕- OTAN

7 RUE ANCELLE • 92200 NEUILLY-SUR-SEINE

FRANCE

Telefax 0(1)55.61.22.99 • Telex 610 176

DISTRIBUTION OF UNCLASSIFIED
AGARD PUBLICATIONS

AGARD holds limited quantities of some of its recent publications, and these may be available for purchase in hard copy form. For more information, write or send a telefax to the address given above. *Please do not telephone.*

Further copies are sometimes available from the National Distribution Centres listed below. If you wish to receive all AGARD publications, or just those relating to one or more specific AGARD Panels, they may be willing to include you (or your organisation) in their distribution.

AGARD publications may be purchased from the Sales Agencies listed below, in photocopy or microfiche form. Original copies of some publications may be available from CASI.

NATIONAL DISTRIBUTION CENTRES

BELGIUM
Coordonnateur AGARD - VSL
Etat-major de la Force aérienne
Quartier Reine Elisabeth
Rue d'Evere, B-1140 Bruxelles

CANADA
Director Research & Development
Information Management - DRDIM 3
Dept of National Defence
Ottawa, Ontario K1A 0K2

DENMARK
Danish Defence Research Establishment
Ryvangs Allé 1
P.O. Box 2715
DK-2100 Copenhagen Ø

FRANCE
O.N.E.R.A. (Direction)
29 Avenue de la Division Leclerc
92322 Châtillon Cedex

GERMANY
Fachinformationszentrum Karlsruhe
D-76344 Eggenstein-Leopoldshafen 2

GREECE
Hellenic Air Force
Air War College
Scientific and Technical Library
Dekelia Air Force Base
Dekelia, Athens TGA 1010

ICELAND
Director of Aviation
c/o Flugrad
Reykjavik

ITALY
Aeronautica Militare
Ufficio Stralcio AGARD
Aeroporto Pratica di Mare
00040 Pomezia (Roma)

LUXEMBOURG
See Belgium

NETHERLANDS
Netherlands Delegation to AGARD
National Aerospace Laboratory, NLR
P.O. Box 90502
1006 BM Amsterdam

NORWAY
Norwegian Defence Research Establishment
Attn: Biblioteket
P.O. Box 25
N-2007 Kjeller

PORTUGAL
Estado Maior da Força Aérea
SDFA - Centro de Documentação
Alfragide
P-2720 Amadora

SPAIN
INTA (AGARD Publications)
Carretera de Torrejón a Ajalvir, Pk.4
28850 Torrejón de Ardoz - Madrid

TURKEY
Millî Savunma Başkanliği (MSB)
ARGE Dairesi Başkanliği (MSB)
06650 Bakanliklar - Ankara

UNITED KINGDOM
Defence Research Information Centre
Kentigern House
65 Brown Street
Glasgow G2 8EX

UNITED STATES
NASA Center for Aerospace Information (CASI)
Parkway Center, 7121 Standard Drive
Hanover, MD 21076

SALES AGENCIES

NASA Center for AeroSpace Information (CASI)
Parkway Center, 7121 Standard Drive
Hanover, MD 21076
United States

The British Library Document Supply Centre
Boston Spa, Wetherby
West Yorkshire LS23 7BQ
United Kingdom

Requests for microfiches or photocopies of AGARD documents (including requests to CASI) should include the word 'AGARD' and the AGARD serial number (for example AGARD-AG-315). Collateral information such as title and publication date is desirable. Note that AGARD Reports and Advisory Reports should be specified as AGARD-R-nnn and AGARD-AR-nnn, respectively. Full bibliographical references and abstracts of AGARD publications are given in the following journals:

Scientific and Technical Aerospace Reports (STAR)
STAR is available on-line at the following uniform resource locator:
    http://www.sti.nasa.gov/Pubs/star/Star.html
STAR is published by CASI for the NASA Scientific and Technical Information (STI) Program
STI Program Office, MS 157A
NASA Langley Research Center
Hampton, Virginia 23681-0001
United States

Government Reports Announcements & Index (GRA&I)
published by the National Technical Information Service
Springfield
Virginia 22161
United States
(also available online in the NTIS Bibliographic Database or on CD-ROM)